X-RAY ANALYSIS AND MODELING OF NGC 3227

by

Jared James Newman

A dissertation submitted in partial fulfillment
of the requirements for the degree

of

Doctor of Philosophy

in

Astrophysics

MONTANA STATE UNIVERSITY
Bozeman, Montana

May 2022

ACKNOWLEDGEMENTS

I would like to thank a number of people who have been an enormous help. Dr. Sachiko Tsuruta for years of assistance, guidance, and flexibility. Dr. Andrew C. Liebmann for teaching me much of the technical side of the research and general guidance. Dr. Hideyo Kunieda of Nagoya University and Dr. Yoshita Haba of the Aichi University of Education for their assistance and suggestions pertaining to the earlier observations. My committee consisting of Doctors Yves Idzerda, Dana Longcope, Jiong Qiu, and Charles Kankelborg for their teaching expertise and suggestions to improve my thesis. Finally, all of the friends and family that never lost faith in me, even when I struggled to find it in myself.

TABLE OF CONTENTS

TABLE OF CONTENTS – CONTINUED

TABLE OF CONTENTS – CONTINUED

LIST OF TABLES

LIST OF FIGURES

LIST OF FIGURES – CONTINUED

Figure Page

LIST OF FIGURES – CONTINUED

Figure Page

LIST OF FIGURES – CONTINUED

Figure Page

ABSTRACT

The 1.5 Seyfert galaxy NGC 3227 has been observed by several X-ray missions. We carried out combined analysis of the data from a total of twenty one observations. Six of the observations were preformed by Suzaku, eight by XMM-Newton, and seven by NuStar.

A unified model was constructed which is consistent with all twenty one of the observations by the three satellites with large intensity and spectral changes. The model consists of a hard power law which is interpreted as the Comptonized emission from the corona above an accretion disk. In the high flux states an additional soft excess component dominates, which is consistent with a model with either a steeper power law or a warm Comptonization component. These emissions from the central engine are absorbed by multiple distinct absorbers at various ionization levels. A reflection component and several emission lines are also present. This is the most robust model of this source to date.

1

INTRODUCTION

Active galactic nuclei (AGN) are relatively compact regions at the center of galaxies that are incredibly luminous. They are large, complex systems with multiple structures and processes that emit light of different energies across all major energy bands. Thus, to understand these objects they must be observed in as many different energy bands as possible. The X-ray band is of interest for studying high energy processes that occur in the more energetic portions of the system. In the last few decades, methods of focusing and detecting X-ray photons have substantially improved. The higher quality data allow us to form more accurate models to explain the system and observe short term events that occur within observations.

When viewed across multiple observations, the spectral features of a single source can change substantially. However, the overall system itself does not undergo drastic changes during our lifetimes. Instead, changes in the spectrum should be explained by local behaviour that affects photons along the line of sight. For example, large changes in absorption features can be explained by the motion of absorbing clouds relative to the line of sight, or changes in the ionization levels of those clouds. Changes in intrinsic luminosity can be explained by alterations to the accretion rate, the expansion or contraction of X-ray emitting regions, the formation and dissapation of hot spots on the accretion disk, etc.

This thesis focuses on the AGN contained within NGC 3227, an intermediate spiral galaxy. This is a well studied AGN with observations in multiple energy bands. It displays characterisitics typical of other Seyfert 1.5 AGN including an obvious hard X-ray power law, Fe Kα emission, and absorption features. Initially, I was drawn to this source due to the number of available observations. Most other AGN lack the amount of observations, and

thus the amount of data, that are available for NGC 3227. Furthermore, the data are from modern satellites and thus are higher quality compared to data from earlier observatories. After extracting, processing, and observing the data, I also noticed that these observations viewed the source at significantly different luminosities. The shapes of the spectra of different observations were also substantially different. Noting that some characteristics of the source must remain constant, I became interested in what variable parameters could produce such spectral variety. While previous spectral modeling had been done on these observations, the efforts were confined to a single observation or multiple observations that were part of a campaign. Explaining all available observations with a single model had not been attempted. In addition, other authors produced models that were inconsistent with each other and/or ignored part of the available energy band in their work. From this, an outstanding question arose. What is the best model to describe the characterisitics of this source?

Thus, the purpose of this work is to form a single, robust model that is capable of explaining current and future X-ray observations of this source, on both short and long timescales, with minor adjustments. It includes the longest timespan of available observations (2000 - 2017) of current efforts to model the source. It also utilizes the full energy band of quality data available (0.3 - 50 keV). This approach would create a model of the source that is free from the inconsistencies present in previous work, yeilding the best representation of the physical parameters to date.

To this end, we employ several strategies for analysing the data gathered from NGC 3227. Timing analysis focuses on the count rate of the photons received by the satellite. It gives information on the flux variability of the source and locates events that cause rapid changes in flux levels. The total energy band observable by the satellite can be segregated to energy bands for further scrutiny. Spectral analysis focuses on the count rate of each energy bin. Time averaged analysis takes the data from the entire observation and averages them into a single spectrum for use in modeling. Time resolved analysis instead takes a smaller

time slice of the observation and averages it, allowing us to focus on events or local trends within the observation. This thesis is structured in the following way.

Chapter 2 gives an overview of the history and structure of the AGN system and the characteristics of the various AGN subclasses. A breif overview of the basic accretion physics of AGN are given, followed by a discussion of spectral features of AGN. It also presents a summary of the unified model of AGN. Afterwards, it discusses the satellites responsible for taking the observations used in this dissertation. The history, structure, and operation of the satellite and its insturments are presented. The chapter ends with a summary of the software used for processing and analyzing the data.

Chapter 3 covers the time averaged analysis of eight observations of NGC 3227. Six of them were Suzaku observations while the other two came from XMM-Newton. The work of previous authors on these observations yeilded models that were inconsistent with one another. The primary focus of Chapter 3 is to create a model that is consistent with all eight observations, thereby being a more robust model than previous efforts. How characterisitics of the source change with luminosity are also explored.

Chapter 4 presents the time averaged analysis of thirteen additional observations of NGC 3227. Six from NuStar and six from XMM-Newton were part of a joint observation campaign in late 2016. On the dates of the joint observations both satellites observed the source albeit with different start and end times. The result was a series of partially simultaneous observations that produced data that could be used in tandem. A seventh observation was taken by NuStar in early 2017 that was also included for completeness. The primary focus of Chapter 4 is to adapt and apply the model formed in Chapter 3 to these new observations. This tests how well our model is able to adapt to new observations.

Chapter 5 covers the time resolved analysis of the higher luminosity Suzaku and XMM-Newton observations. One Suzaku and seven XMM-Newton observations were suitable for this analysis. The purpose of the chapter is twofold. First, to test if our time averaged

model is capable of explaining the source on shorter timescales. Second, to identify and study events that occur within the observation, such as a flare.

Chapter 6 presents the conclusion for the thesis.

Appendix A presents a list of the abbreviations used in this thesis.

Appendix B summarizes the XSPEC models used in this thesis.

ACTIVE GALACTIC NUCLEI, SATELLITES, AND SOFTWARE

2.1 AGN Environment Overview

In the center of all active galactic nuclei (AGN) is a supermassive black hole. In accretion powered AGN, the black hole is surrounded by an accretion disk extending from the innermost stable circular orbit (ISCO) out to tens of light days. Energy released from the infall of material from the disc is the primary source of power for the system in accretion powered AGN. Above the accretion disk, a corona of free electrons exist that reprocess the optical/UV emission into X-ray energies via inverse Compton scattering. Surrounding the disc are clouds of material in various stages of ionization. Those closer to the black hole move fast enough that their emission and absorption lines are broadened by doppler effect and are contained within the Broad Line Region (BLR). Clouds farther away do not have broadened spectral lines and lie within the Narrow Line Region (NLR). A large dusty torus (a few parsecs thick) surrounds the system. The gas and dust within the torus are primarily responsible for the infrared emission. Radio-loud AGN have a pair of jets extending from the poles of the black hole. These jets lead to the radio lobes that are the primary source of radio emission via syncrotron radiation. A diagram of a typical AGN system is displayed in Figure 2.1. A radio image showing the lobes of a radio load AGN is displayed in Figure 2.2.

2.2 Types of AGN

2.2.1 Seyferts

Seyferts are one of the two largest groups of AGN and the first to be discovered. They were first detected in 1908 by E. A. Fath using the Lick Observatory in California. Originally thought to be a spiral nebula, NGC 1068 exhibited bright emission lines associated with nebulae (Fath 1909). Nine years later, V. M. Slipher produced a higher quality spectrum of

NGC 1068 at Lowell Observatory (Slipher 1917). In 1926, E. Hubble looked at the emission lines of NGC 1068 and other "nebulae" and classified them as extragalactic objects. Carl Seyfert studied a group of six galaxies in 1943: NGC 1068, NGC 1275, NGC 3516, NGC 4051, NGC 4151, and NGC 7469. All of these galaxies are spiral galaxies with a bright, stellar-like core and emission lines from highly ionized atoms. Emission lines in the optical band were notably broad (Seyfert 1943).

Additional Seyfert galaxies were discovered over the years and in 1974 Khachikian & Weedman (1974) classified Seyferts into two groups: Seyfert 1 and Seyfert 2. They were separated based on the relative widths of forbidden lines and Balmer lines. If the Balmer lines were broader, the galaxy was classified as Seyfert 1. If both types of lines were similar in width, the galaxy was a Seyfert 2. Later, Seyferts with characteristics between the two classifications prompted further subdividing the galaxies into Seyfert 1, 1.2, 1.5, 1.8, 1.9, and 2 (Osterbrock & Koski 1976; Osterbrock & Martel 1993). As the classification number increases, the broad lines get progressively weaker compared to the narrow line components. In addition to the emission lines, Seyfert 1s are luminous at UV and X-ray energies, while Seyfert 2s are bright in infrared. NGC 1068 is the prototype Seyfert 2, and the polarization of its light indicates that its core emission is reflected off a dust cloud. This supported the idea that the core is obscured by a dust torus, with gas and dust above and below the torus reflecting the core emission (Barthel 1991).

A notable subgroup of Seyfert 1s are Narrow Line Seyfert 1s (NLS1). They produce much narrower Balmer lines than Seyfert 1s and strong Fe II emission. The X-ray continuum slope tends to be steeper than standard Seyfert 1s (Boller et al. 1996). They are unobscured AGN with relatively low black hole mass ($\lesssim 10^8 M_\odot$) and high Eddington ratio. NLS1s are thought to be young AGN that are growing and evolving (Mathur 2000), or older AGN that have been rejuvenated by a recent merger (Mathur et al. 2012). Many NLS1s are radio-quiet, but some are radio-loud and characterized by strong, rapid variability (Foschini et al. 2015).

A candidate for another subtype of AGN are Low Ionization Emission-Line Region galaxies (LINERS). Identified by Heckman (1980), they spectroscopically resemble Seyfert 2 galaxies except that the low ionization lines (e.g. [O I] λ6300, [N II] λ6548) are relatively strong. Some LINERs appear to be very low luminosity Seyfert 2s, but some models can produce LINER-type spectra from cooling flows, starburst-driven winds, and shock-heated gas (Heckman 1987).

2.2.2 Quasars

During the radio surveys of the 1950s a number of radio sources of unknown origin were discovered that could not be matched with optical galaxies. When identified at visible wavelengths in photographs, they appeared as faint, star-like points of light. They were described as quasi-stellar radio sources (QSRs) or quasars for short.

In California, M. Schmidt viewed the radio source 3C 273 with the Palomar Observatory. He noticed that a series of prominent emission lines could be explained by highly redshifted (z = 0.158) Balmer lines. This interpretation was also supported by a Mg II line. He concluded that 3C 273 is either a star with a radius on the order of 10 km to produce the lines via gravitational redshift, or the nuclear region of a galaxy with cosmological redshift. The latter interpretation implied 3C 273 was at a distance of $\sim$ 500 Mpc, and that the nuclear region would be about 100 times brighter optically ($\sim 10^{59}$ ergs) than the luminous galaxies that had been identified with radio sources. He correctly concluded that the extragalactic explaination was more plausable (Schmidt 1963). Soon after, Greenstein & Schmidt (1964) found similar characteristics with the quasar 3C 48. Utilizing redshifted lines, additional quasars would be discovered.

Matthews & Sandage (1963) showed that quasars displayed an "ultraviolet excess" when compared to standard stars on a color-color (U-B, B-V) diagram. A search technique involving exposures in U and B recorded on the same plate allowed much more rapid

idenitification of quasars than previous methods. The majority of quasars discovered in this manner lacked radio emission. They became known as quasi-stellar objects (QSOs). Today, the term quasar often refers to both QSRs and QSOs, and the radio emission is identified as a radio-loud or radio-quiet quasar.

The importance of X-ray spectra were revealed later, with the Uhuru satellite that launched in 1970 and operated for three years. A few AGN were observed to be strong X-ray sources (Gursky et al. 1971; Tucker et al. 1973). Additional observations from Ariel V (Elvis et al. 1978) and HEAO-1 (Mushotzky et al. 1980) established AGN as luminous X-ray sources.

Quasar spectra are similar to Seyfert 1s but are much more luminous. Quasars also have weaker narrow emission lines and stellar absorption features. As light emitted by these sources must travel through the intergalactic medium (IGM), the spectrum contains information about both the source emission and IGM characteristics. The oldest known quasars display a Gunn-Peterson trough (Gunn & Peterson 1965); an absorption feature associated with neutral hydrogen absorption. This feature, as well as the Lyman α forest displayed by younger quasars, provides important information reguarding the Epoch of Reionization in cosmology (Zaroubi 2013).

2.2.3 Radio Galaxies

Radio galaxies are highly luminous radio sources that are matched with a host galaxy. These sources are almost always giant elliptical galaxies (Adams 1977). The radio emission is smooth and strongly polarized, and is thought to arise from syncrotron radiation. They come in two varieties: core dominated and lobe dominated. Core dominated radio galaxies have compact ($\lesssim$ 15 kpc) radio morphologies. They often display a flat spectrum core component with additional weak extended emission. The core components are usually resolved as compact core-jet features (Barthel et al. 2000).

Lobe dominated radio galaxies exhibit radio emission in the core, but they also have large radio emitting structures. Their name arises from a pair of somewhat symmetrical radio emitting lobes that appear in many of the sources (see Figure 2.2). These lobes can contain emission hot spots. The lobes are commonly a few hundred kiloparsecs, but in some cases can be megaparsec scales (Machalski et al. 2008). Some lower luminosity radio galaxies instead have more elongated structures known as plumes. The plumes or lobes are powered by flows of high-energy particles and magnetic fields from the AGN. They can also be bent due to ram pressure as the source moves through a cluster. In many sources, one or two radio emitting jets are beamed from the core. These jets are thought to be the observable manifestation of the flow. In some sources, particularily those of high luminosity, one jet is not visible. There still are two lobes, so the one that does not have a visible jet must be powered somehow. The reason for this is not well understood. This may be due to relativistic beaming causing the radiation focused in a narrow cone opposite to the line of sight, rendering the jet effectively invisible (Blandford & Königl 1979; Kellermann & Owen 1988a). Alternatively, the jet could simply be radiating much fainter for some reason, or that there is a single jet that alternates sides (Kellermann & Owen 1988b; Rudnick & Edgar 1984).

Fanaroff & Riley (1974) created the Fanaroff-Riley classification to distinguish lobe dominated galaxies based on their radio luminosity in relation to their hosting environment. Class I (FR-I) sources are brightest towards their central galaxy. Towards the outer region of the lobes they are fainter and the spectra are steepest, indicating that the radiating particles have aged the most. About 80% of FR-Is contain jets that are two sided and often end in plumes. FR-I sources are associated with large, bright galaxies that have a flatter light distribution than a typical elliptical galaxy (Kellermann & Owen 1988c).

Class II (FR-II) sources contain hotspots in the lobes, farther away from the host galaxy than FR-Is. FR-IIs are highly luminous, producing about an order of magnitude more optical

line emission than FR-Is. They are also more luminous in radio at the core and jets, but the lobes are so much brighter that the interior structures are fainter by comparison. Jets in FR-IIs are frequently one sided. They are often associated with mostly normal giant elliptical galaxies, except with nuclear and extended emission line regions (Fanaroff & Riley 1974; Kellermann & Owen 1988c).

2.2.4 Blazars

The blazar catagory is a small subgroup of AGN that includes BL Lac Objects, High Polarization Quasars (HPQ), Flat-Spectrum Radio Quasars (FSRQ), and Optically Violently Variable (OVV) quasars. They comprise less than 1% of all AGN. Blazars are highly variable, radio loud sources that differ from other quasars by their relatively featureless non-thermal emission continuum.

BL Lac Objects are named after BL Lacertae, an AGN discovered by Cuno Hoffmeister in 1929 (Cuno 1929). It was originally thought to be a variable star, but it exhibited highly polarized light and a spectrum nearly devoid of the emission lines associated with stars. It was later identified as a bright, variable radio source in 1968 when matched with the radio object VRO 42.22.01 (Schmitt 1968). BL Lacertae became the prototype for similar sources known as BL Lacertae Objects or BL Lacs. Oke & Gunn (1974) later showed that BL Lacertae was in fact an AGN with a redshift of z = 0.07 by analyzing absorption lines from the elliptical host galaxy.

The remaining blazars display continuum emission very similar to Bl Lacs, but have emission lines more similar to quasars. These three classifications (HPQ, FSRQ, and OVV) refer to the same class of objects but differ based on the classification schemes used: optical variability (OVV), optical polarization (HPQ), or radio spectral index (FSRQ). They exhibit rapid variability, high and variable polarization, and radio structures dominated by compact radio cores. Today, they are more often referred as FSRQ (Urry & Pdovani 1995).

2.3 AGN Accretion Basics

A comprehensive discussion of AGN accretion physics is beyond the scope of this work, thus a synopsis of the simplified physics is presented. As the name implies, accretion powered AGN are assumed to be powered by the infall of material from the accretion disk to the black hole. The rate of gravitational potential energy released by this process is given by

$$\frac{dE_g}{dt} = \frac{GM\dot{M}}{r} \tag{2.1}$$

for black hole mass M, accretion rate $\dot{M}$, and radial distance from the black hole r. The Virial theorm states that half of this energy heats the gas while the other half is radiated. Approximating an accretion disk as a flat disk at temperature T, radiative energy loss rate is

$$\frac{GM\dot{M}}{2r} = \begin{cases} 2\pi r^2 \sigma T^4, & \text{if } R_{In}<r<R_{max} \\ 0, & \text{otherwise} \end{cases} \tag{2.2}$$

where R_{In} and R_{max} are the inner and outer radii of the disk respectively. Solving for T, we find

$$T = \left(\frac{GM\dot{M}}{4\pi\sigma r^3}\right)^{1/4} \tag{2.3}$$

for the same limits of r. However, this approach neglects other heat sources such as viscosity. Shakura & Sunyaev (1973) shows that a more accurate derivation yields the following equation.

$$T_{eff}(r) = \left(\frac{3GM\dot{M}}{8\pi\sigma r^3}\left(1 - \sqrt{\frac{R_{In}}{r}}\right)\right)^{1/4} \tag{2.4}$$

The blackbody spectral radiance B_ν is then

$$B_\nu(r) = \frac{2h}{c} \frac{\nu^3}{exp\left(\frac{h\nu}{kT_{eff}(r)}\right) - 1} \tag{2.5}$$

As the temperature is radius dependent, we arrive at the multicolor disk model. The blackbody spectrum is a series of nested rings that have peak emission in the optical band for the outer disk and UV-EUV for the inner disk. For a typical Seyfert of $M{\sim}10^7 M_\odot$ and $\dot{M}$ $\sim 0.3 M_\odot$ year^{-1} the overall blackbody portion of the spectrum will peak in UV.

2.4 Spectral Features

A summary of spectral features for Seyferts and QSO AGN are given in this section. Blazar spectra are significantly different and are not the focus of this dissertation, although they will be mentioned. This is because the spectra of other AGN are due to the full AGN system while Blazar spectra are dominated by the emission from the relativistic jet. This will begin with radio waves and cover increasingly energetic bands. A representation of the typical spectra of AGNs is displayed in Figure 2.3.

2.4.1 Radio

Radio emission from AGN is produced in either compact or extended sources. Compact sources are unresolved ($<$ 1") or barely resolved at a few arcsec and are often associated with syncrotron radiation in optically thick portions of the AGN nucleus. More recently, radio emission in radio-quiet AGN has been shown to be consistent with star formation processes (Bonzini et al. 2013; Maini et al. 2016; Padovani 2011). Many compact sources produce flat radio spectra over several orders of magnitude in frequency, but a number of compact steep-spectrum sources have been identified (Fanti et al. 1990).

Extended radio sources are optically thin and include the radio lobes, jets, and plumes

of radio galaxies and radio-loud quasars. The spectra are steeper than compact sources. For more detail see Section 2.2.3. The low energy cutoff for the non-thermal syncrotron based radio emission is due to syncrotron self-absorption.

2.4.2 Infrared

The infrared continuum is thought to be thermal radiation from the dust in the torus that surrounds the nucleus. In radio-loud and Blazar-like objects synchrotron radiation can also be a significant contribution (Edelson & Malkan 1986; Sanders 1999). Evidence supporting the dust explaination includes extinction features in the far IR and an excess in the near infrared continuum. The extinction is consistent with the presence of dust grains of sizes between 0.003 and 1.0 microns (Draine & Lee 1984). The excess IR emission forms an "IR bump" around ~ 2 μm that corresponds to the spectral peak for optically thin emission from graphite grains at 1500 K (Barvainis 1987). Infrared variability is frequently correlated with optical/UV variability but with a time delay. The delay is thought to be due to light travel time. The source of optical/UV emission is the disk, which travels outwards a few parsecs towards the torus. Dust in the torus is warmed by this light, and reradiates as the IR bump.

2.4.3 Optical

The optical emission is primarily due to thermal emission from the accretion disk. As the disc is progressively hotter the closer to the center, the disk appears as a series of concentric rings at different temperatures. The superposition of the rings forms the optical (and UV) spectrum that appears to be a power law shape. This multidisk model is responsible for both the optical and UV continuum.

Optical emission lines produced by clouds of photo-ionized gas are used to divide Seyferts into subclasses. They originate in different regions of the AGN environment. The most important set is the Balmer series. Seyfert 1s produce both broad and narrow

emission lines while Seyfert 2s produce only the narrow lines. While all lines are produced by clouds of photo-ionized gas, their location in the AGN system is responsible for the different characteristics. The broad lines originate in clouds closer to the central black hole in the Broad Line Region (BLR) and are broadened by Doppler shift due to the orbital motion of the clouds. The narrow lines are produced farther away in the Narrow Line Region (NLR). At the NLR distance, the clouds are moving much slower and thus are not Doppler shifted nearly to the extent of the broad lines. Furthermore, the NLR exists outside the dusty torus that obscures the BLR for Seyfert 2s. Osterbrock & Ferland (2006) provides a discussion of these regions. Variability on the order of hours/days is independent, while variability on longer time scales is strongly correlated with UV.

2.4.4 Ultraviolet

Similar to the optical band, the UV emission is largely a series of blackbody rings that comprise the inner accretion disk, conforming to the multidisk model. However, there exists a prominent feature that does not appear at optical energies: the big blue bump (BBB). Unfortunately, the peak of the BBB lies in an unobservable region that suffers from absorption by neutral galactic hydrogen (13.6 eV - 0.1 keV). The source of the BBB is thought to be thermal in nature, either optically thick thermal radiation from the accretion disk (Sheilds 1978) or optically thin thermal bremsstralung radiation (Barvainis 1993a). The shape and the peak of the BBB would provide critical information on the inner accretion disk and ionizing flux that powers emission lines. The tails are observable with the low energy end in UV while the high energy end extends into soft X-rays. The unobservable gap also obscures neutral hydrogen lines from the AGN. Short time scale variability (less than a day) tends to be independent, but longer scale variability is tied to optical variations.

2.4.5 X-ray

Above ∼2 keV the spectrum is dominated by a power law shape. Black body emission alone is insufficient to explain this behaviour. As this system is energetic and ionized, free electrons are expected. Above the accretion disk there exists a region of free electrons known as the corona. Thermally emitted photons from the disc travel through the corona and encounter electrons. If the electrons have sufficiently high energy, inverse Compton scattering will occur (Haardt & Maraschi 1991; Haardt et al. 1994). The scattered photons will be at higher energy and the electrons cooled, opposite of standard Compton scattering. Consider a power law energy distribution of the electrons

$$N_e(\gamma) = \begin{cases} K_e \gamma^{-p}, & \text{if } \gamma_0 < \gamma < \gamma_m; \\ 0, & \text{otherwise} \end{cases} \tag{2.6}$$

Where N_e is the number of electrons, K_e and p are appropriate constants for the distribution, the electron energy is γmc^2, and γ_0 and γ_m are the low and high cutoffs of the distribution respectively. For radio quiet sources, the high energy cutoff is in the range of 100-200 keV (Zdziarski et al. 1995). Blumenthal & Gould (1970) shows that the resulting inverse Compton spectrum will also be a power law in photon energy ϵ.

$$\frac{dN_{tot}^2}{dtd\epsilon} = \frac{r_0^2}{\pi\hbar c^2} K_e (kT)^{(p+5)/2} F(p) \epsilon^{-(p+1)/2} \tag{2.7}$$

Where N_{tot} is the total number of photons, r_0 is the classical electron radius, and the parameter $F(p)$ is

$$F(p) = 2^{p+3} \left[\frac{p^2 + 4p + 11}{(p+3)^2(p+1)(p+5)} \right] \times \Gamma[\frac{1}{2}(p+5)] \zeta[\frac{1}{2}(p+5)] \tag{2.8}$$

for the Γ function and Riemann ζ function. This supports inverse Compton scattering as

the source of the power law spectrum at X-ray energies. While the energy source for the hot electrons is not well understood, magnetic reconnection and magnetohydrodynamic shocks provide a plausable way of injecting energy into this region (Cheng et al. 2020).

In addition to the power law continuum, there exists an obvious Fe Kα flourescent emission line. The Kα line occurs when an electron transitions from a p orbit of the L shell (n = 2) to a vacancy in the K shell (n = 1). Standard equivalent widths for this line are 5 - 300 eV (Mushotzky et al. 1993). This line is caused by coronal X-rays shining back onto the disc, causing the cool Fe within to flouresce. The existence of this line also signals the presence of a Compton reflection component. Continuum photons above 2 keV encounter an optically thick slab, and either reflect off of it or are absorbed by it (Guilbert & Rees 1988; Lightman & White 1988). Short term variations average out when the light-travel time is considered but this component can vary on longer time scales.

If the hard X-ray power law observed in the $>$ 2 keV band is extended below 2 keV, positive model residuals are sometimes seen. More common in brighter observations of a source, this "soft excess" indicates the existence of additional emission source(s). One explaination is thermal in nature; the soft excess is the high energy edge of the big blue bump. Another explaination could be inverse Compton scattering off of a population of electrons that are separate and cooler than those that exist in the corona. Thermal bremsstrahlung is also a candidate. This is radiation released when electrons coulomb scatter off of other electrons or ions. Barvainis (1993b) showed that bremsstrahlung is a plausible source of the BBB, and similar to the thermal case the soft excess would then be the high energy edge. Saxton et al. (1993) also successfully modeled the soft excess in several quasars using bremsstrahlung that occurs in the inner regions of the accretion disk.

While the previous models are thermal in nature, the soft excess could instead be due to reflection and reprocessing. Ross and Fabian's blurred relativistic ionized reflection model (Ross & Fabian 1993, 2005; Ross et al. 1999) considers an X-ray source (corona) above

the disk that is shining onto the disc. The X-rays photoionize material which then produce emission lines. H and He like C, N, O, Ne, and M shell Fe produce lines within a few 100 eV in the soft excess band. As this process occurs in the inner regions of the disk, the lines are relativistically smeared together due to the proximity of the material to the black hole. Miniutti & Fabian (2004) identifies three regimes in which the reflection-dominated component and the Fe line is correlated, nearly independent, and anticorrelated with the direct continuum based on the height of the X-ray source. Low flux states are associated with low X-ray source heights ($h_s \lesssim 2 - 4r_g$ for source height h_s and gravitational radius r_g). Much of the X-ray continuum and reprocessed light are lost due to light bending from the black hole, and the reflection dominated component is correlated with the flux. As the height of the source rises to $2 - 4r_g \lesssim h_s \lesssim 7 - 13r_g$ the reflection component has largely constant flux while the power law can vary by a factor of 3$\sim$4. At larger heights the source struggles to effectively illuminate the disc and the reflection component is anticorrelated with the flux. At heights above $h_s \geq 30r_g$, the continuum and reflection components tend towards their asymptotic values. This model has the advantage of accounting for the hard X-ray hump and also the broad Fe Kα line with sufficiently high Fe abundance (greater than solar). However, it is not appropriate for all sources (e.g. Boissay et al. (2016) and this dissertation). Of course, the soft excess could also be comprised of the sum of multiple of the emission sources discussed.

Alternatively, the soft excess could not be an emission source at all, but rather an artifact of absorbing material. Gierliński & Done (2004, 2006) showed that an opacity jump between 0.7 and 2 keV associated with partially ionized O and Fe can give rise to an apparent soft excess through reflection, transmission, or both. This approach requires a strong velocity shear to relativistically smear narrow atomic features together, as well as the ionization level of the material to respond to luminosity changes in the continuum. This method indicates that the intrinsic spectrum is significantly different than that assumed by

other models (see Gierliński & Done (2004) Figure 3) which becomes the observed spectrum when complex absorption is applied.

In addition to the primary emission mechanisms, absorption features and emission lines are commonly seen in the spectrum. The absorbing clouds can be either neutral or ionized (warm absorbers). Furthermore, the clouds themselves may not fully obscure the line of sight, leading to partially covering absorber models such as those used in this dissertation. The warm absorbers tend to be less relevant than the neutral ones above 4 keV but are critical in explaining spectral features below 1 keV. The warm absorber was originally proposed to explain a spectral feature in some quasars (Halpern 1984) but was later observed in Seyferts (Ulrich 1984). Today, the warm absorber is a common feature in many Seyfert galaxies. Initially, they were characterized by absorption edges of O VII (0.74 keV) and O VIII (0.87 keV) but more recent observations have detected many elements are present within them. Furthermore, an absorption trench between $\sim 730 - 775$ eV that could not be explained by the O absorption edges was detected in multiple sources (Kaspi et al. 2002; Sako et al. 2001; Stenbrugge et al. 2003). The transitions of M-shell Fe I - Fe XVI (n = 2 - 3) occur at these energies and the emission lines are so close together that current instruments are not able to resolve them. This unresolved transition array (UTA) can explain the trench (Netzer 2004).

AGN X-ray emission is strong in both intensity and variability. X-ray variability on the order of hours is often seen, such as some observations presented in this dissertation. On longer timescales (days or longer), X-ray variability can be correlated with optical and UV emission (Buisson et al. 2016; Jin et al. 2012).

2.4.5 Gamma rays

Gamma ray emission from AGNs are often simlar to X-ray emission, but with a higher spectral power law index ($\Gamma \geq 2$). Significant γ-ray detection is often associated with AGNs

that contain strong relativistic jets such as blazars, radio-loud NLS1s, and radio galaxies. In a few cases, TeV energies have been detected. In this regime, the additional γ-ray emission is thought to be due to inverse Compton scattering of soft photons off of the ultrarelativistic electrons present in the jet (Abdo et al. 2010; Ackermann et al. 2012). Otherwise, the γ-ray emission may simply be an extention of the inverse Compton scattering responsible for the hard X-ray power law, cutting off at a couple hundred keV and being indistinguishable from noise.

2.5 The Unified Model of AGN

Active galactic nuclei are classified based on their differences, but share similarities as well. Attempts have been made to explain the diversity of AGN using a small number of physical parameters. The oldest and simplest unification scheme combines the subclasses of AGN using two parameters: luminosity of the source and inclination in the line of sight (Antonucci 1993; Urry & Pdovani 1995; Urry 2003). Emission from AGN is altered by reflection, scattering, and absorption from material as it escapes the system. This can occur in the torus, the host galaxy, in outflows, or in BLR and NLR.

The luminosity explaination attempts to combine Seyfert 1s and QSOs into a single group. Initially, these sources were thought to be distinct, but additional observations revealed a large number of identical features between them. Eventually, the most significant difference between them was their luminosity; quasars are brighter by a couple orders of magnitude. The luminosity of accretion powered AGN is largely dependent on the mass of the central black hole and the accretion rate. Thus, Seyfert 1s are simply QSOs with significantly lower black hole mass and accretion rate.

Extragalactic sources can be viewed from any angle. In addition, AGN are thought to be a non-isotropic system (see Figure 2.1). Thus, the inclination angle is expected to affect our observations of these sources. The inclination explanation attempts to combine Seyfert

1s and Seyfert 2s, as well as combine blazars with other radio-loud AGN. For Seyferts, we return to the classification scheme where Seyfert 1s have both broad and narrow emission lines while Seyfert 2s only display narrow lines. Furthermore, Seyfert 2s are more numerous and less luminous than Seyfert 1s. From these characteristics, it was proposed that Seyfert 1s and 2s are the same type of source, but Seyfert 2s are viewed at an angle such that the torus obscures the AGN core. Emission from the BLR is absorbed and reprocessed by the torus, preventing us from observing the broad lines. The narrow lines are produced in a region not enclosed by the torus (NLR) and thus are unaffected. Furthermore, the NLR acts as a scattering medium which scatters and polarizes light from the BLR and central engine (Osterbrock 1978).

In radio-loud AGN, we observe jets extending from the core of the source. At most viewing angles, these jets are pointed away from us. Should the jet be aligned or nearly aligned with the line of sight, the emission from the jet will be heavily enhanced. Blazars are theorized to have this property. We observe blazar spectra as significantly different than other radio-loud AGN, which can be explained by the enhanced jet emission. Furthermore, the small amount of viable viewing angles is supported by the low number of blazars (Blandford & Rees 1978).

Ultimately, inclination and luminosity are not able to explain all of the features of AGN. More recently, it has been suggested to split AGN into "radiative mode" and "jet mode" AGN (Heckman & Best 2014). In radiative mode, the majority of the energy output is electromagnetic radiation emitted as a result of accretion through an optically thick accretion disk. This is the scenario discussed previously in this dissertation. Seyferts and QSOs fall into this catagory. Their Eddington ratios are $L \leq 0.1 L_{edd}$. About 10% are radio-loud sources with one or two jets, so long as the accretion flow is the primary energy source (Netzer 2015).

In jet mode AGNs the primary energy output takes the form of bulk kinetic energy transported in two-sided jets. They have a much smaller Eddington ratio and the jets

are possibly powered by a radiatively inefficient accretion flow (RIAF). These flows occur when the accretion rate is low. If the density of the accretion flow is low enough, radiative processes (generally scale with ρ^2) cannot keep up with dissapation (scales with ρ) (Begelman 2014; Shakura & Sunyaev 1973). Alternatively, the jets could potentially be powered by extracting rotational energy from the black hole using magnetic fields. Magnetohydrodynamic simulations in a general relativistic framework produce jets by tapping into the spin of the black hole via the Blandford-Znajek mechanism. This produces jets where the collimation and jet power depend on the black hole spin (Blandford & Znajek 1977; Heckman & Best 2014; McKinney & Gammie 2004; Netzer 2015).

2.6 Satellites

This dissertation uses data collected from three satellites. The first, Suzaku, is a joint mission from JAXA and NASA. The second, XMM-Newton, was launched by the ESA. Finally, NuSTAR was launched by NASA. In addition to the data gathered by the observatories, software is necessary to process and analyze the data.

2.7 Suzaku

On 10 February 2000 the Astro-E mission was launched with the M-V rocket from Kagoshima Space Center. Unfortunately, a failure of the first stage motor resulted in the loss of the mission. Five years later, the recovery mission Astro-EII was successfully put into orbit on 10 July 2005 and named Suzaku (Mitsuda et al. 2007). Suzaku launched with five X-ray Telescopes (XRT) for the X-ray Spectrometer (XRS-2) and four X-ray Imaging Spectrometers (XIS). In addition, a Hard X-ray Detector (HXD) was attached to the side of the spacecraft. The spacecraft is powered by a solar array. Unfortunately, a series of cooling system malfunctions caused the liquid helium (He) reserves to boil off by 8 August 2005. This

rendered the primary instrument, XRS-2, inoperable. Additional damage was suffered by the spacecraft from micro-meteorite impacts which caused the loss of XIS2 in November 2006 and part of XIS0 in June 2009 (Mitsuda 2003, 2009). The Suzaku observations concerned in this dissertation were taken in 2008, and thus omit XRS-2 and XIS2 while using XIS0, 1, 3, and the HXD. The Suzaku spacecraft is shown in Figure 2.4. From early June 2015 the Suzaku satellite experienced intermittent ground communications and on 26 August 2015 JAXA declared that the satellite would be retired (Release 2015).

2.7.1 X-ray Telescope (XRT)

Suzaku has five aluminum (Al) XRTs, each with nested conical gold (Au) foil as the reflector. One is reserved for the XRS (XRT-S) while the other four are used for the four XIS (XRT-I0, I1, I2, and I3 for XIS 0, 1, 2, and 3 respectively). The four XRT-Is are designed to be identical while the XRT-S is similar. The four XRT-Is have a focal length of 4.75 m and contain 1400 Au foil reflectors with radii from 118 mm to 399 mm. The XRT-S has a focal length of 4.5 m and contains 1344 reflectors with radii from 119 mm to 400 mm. The orientation of the XRTs is displayed in Figure 2.5 (Serlemitsos et al. 2007). The reflectors are a thin (≥ 1000 $\AA$) gold layer transferred to an Al substrate with epoxy adhesive (Serlemitsos & Soong 1996). In order to prevent contamination from X-ray sources outside the field of view, pre-collimators are installed on top of each XRT. These contain a series of nested Al blades (175 for XRT-Is, 168 for XRT-S) with effective height of 30 mm which minimize light that enters the reflectors at undesirable angles (Mori et al. 2005). Finally, a thermal shield is applied to protect the XRTs from space and the spacecraft interior, keeping the XRT temperature within 293 ± 7.5 K. The sheild consists of an Al frame with thirteen spokes with a stainless-steel mesh adhered with epoxy to the top of the frame. A polyethylene teleftalate film coated with an Al layer is ahered to the mesh (Kunieda et al. 2001; Serlemitsos et al. 2007).

2.7.2 X-ray Imaging Spectrometer (XIS)

The XIS sensors are comprised of a CCD and a camera body. A cross section diagram of the XIS is displayed in Figure 2.6. The camera body is split into a hood, bonnet, and base and acts to contain the components and sheild them from radiation while in orbit (Koyama et al. 2007).

2.7.3 XIS Sensors and Housing

The camera body hood contains five baffles to block unwanted light. The bonnet has a vacuum valve, an optical block filter (OBF), iron (^{55}Fe) calibration sources, a pressure sensor, a paraffin actuator, and a door. The vacuum valve was used immediately after the launch to create a vacuum in the body to protect the OBF, then closed to avoid contamination from the thruster fuel. A pressure sensor is installed to track the pressure of the body. The OBFs are located 20 mm above the imaging area of the CCDs and act to sheild them from optical and UV light. They are made of a polyimide ($C_{22}H_{10}N_2O_4$) film with aluminum on both sides. They are largely ($\geq$80% transmission above 0.7 keV) transparent to X-rays while being opaque to optical and UV photons (Kitamoto et al. 2004). Eighteen days after launch, the paraffin actuator opened the door and allowed for data observation. The bonnet and hood are both made of aluminum with a black surface finish (Koyama et al. 2007).

The base includes an X-ray CCD mounted on an alumina substrate and attached to a copper heat sink. A Peltier (thermo-electric cooler TEC) cooler in the heat sink cools the detector to its 183 K operating temperature. A cover sheild protects the CCD. The frame-store region of the CCD is protected by an aluminum sheild with gold-plated nickel treatment. The surfaces of the substrate, heat sink, and cover sheild are also gold plated. The inside of the base is nickel plated except for the gold plated feed-through plate.

The XIS sensors are metal oxide semiconductor (MOS) type three phase CCDs operated in the frame transfer mode. Each CCD consists of four (A, B, C, and D) segments with their

own read-out nodes. A schematic of the XIS CCD is shown in Figure 2.7. Three of the sensors (XIS0, 2, and 3) are front-illuminated (FI) CCDs while XIS1 is back-illuminated (BI). The FI CCDs have thicker depletion layers than the BI CCD. This yeilds a lower quantum efficiency below ∼4 keV, making the BI CCD superior for softer X-rays. However, the BI CCD suffers from reduced charge collection efficiency near the back surface of the device. Thus, the FI CCDs are superior above ∼4 keV (Koyama et al. 2007). The quantum efficiencies as a function of energy for the CCDs are displayed in Figure 2.8.

2.7.4 XIS Electronics

Electronics for control and processing of XIS are comprised of analog electronics/thermo-electric cooler control electronics (AE/TCE) and digital electronics (DE). The DE has both pixel processing units (PPU) and main processing units (MPU). The AE/TCE are installed in two boxes, and are paired with two PPUs each. Each pair of AE/TCE and PPU is responsible for two XIS sensors. The AE/TCE01 and PPU01 handle XIS0 and XIS1, while AE/TCE23 and PPU23 are for XIS2 and XIS3. One MPU is connected to all AE/TCEs and PPUs.

The AE/TCE controls the CCD temperature via the thermo-electric cooler (TEC), generates CCD clock signals, and processes CCD signals into digital data. The TEC warms and cools the CCD as needed, keeping the chip at 183 K. The clock signals are generated in the AE with 1/48 pixel cycle steps with a pixel rate fixed at 24.4 μs pixel^{-1}. The CCD output is sampled at 16 bits, but 12 are sent to the PPU. These 12 bits cover the full energy scale in the normal setting of the gain.

The PPU applys corrections to the digital data supplied by the AE/TCE. The data from the AE/TCE may include light leakage through the OBF, electric offsets due to CCD position and time, and/or pulse height (PH) offsets due to dark current. Light leak is a pixel region that is updated every frame to compensate rapid changes of PH offset. Prior

to 20 January 2006 the region was 64 × 64 pixels, and afterwards it was changed to 256 × 114 pixels. The dark level is the average output of a pixel with no irradiation. If the PPU identifies pixels with PHs exceeding a threshold, they are registed as "hot" and excluded from the event extraction process. When a charge pattern consistent with X-rays is detected, it declares it an event and sends the event data to the MPU. The MPU controls the PPUs and AE/TCEs, generates telemetry, and decodes commands. The MPU compiles event or diagnostic data from the PPU and housekeeping data from the AE/TCE and sends them to the satellite data processor (DP).

The XISs are run in two clocking modes. The clocking modes are normal and P-sum. Normal mode reads all the pixels in the CCD over 8 s, producing 1024 × 1024 pixel data. Two options, window and burst, can also be applied to the normal mode. The burst option introduces artificial dead time which can avoid photon pile-up in bright, extended sources. The window option reads a selected part of the CCD and is useful for avoiding pileup for bright point sources. The P-sum mode sums multiple rows of data at the bottom of the imaging area and generates 1-dimensional data. All observations concerned in this dissertation use normal mode without either burst or window options.

Four editing modes are used. Normal mode uses 5 × 5, 3 × 3, and 2 × 2 modes while the P-sum uses timing mode. When an X-ray photon is absorbed by the CCD, it produces a small charge cloud of 2 × 2 pixels or less. If a charged particle encounters the CCD, it will produce a larger charge cloud. The PPU is able to reject most charged particle events by recognizing this difference. When a valid event is determined, the local maximum PH dictates which pixel is the event center. The 5 × 5 and 3 × 3 modes send the PHs and X,Y coordinates of the 25 and 9 pixels, respectively, centered on the event to the telemetry. The 2 × 2 mode extracts 4 pixels from the 3 × 3 region and sends the PHs and X,Y coordinates. The timing mode searches the 1-dimensional data for a 1 × 3 pixel row event. Total PH, X coordinate, and grade of the event are sent to the telemetry (Koyama et al. 2007).

2.7.5 Hard X-ray Detector (HXD)

The HXD is a collimated, non-imaging instrument included with Suzaku. The basic design is the same as the HXD for the Astro-E mission with some sensor and analog electronic improvements (Kamae et al. 1996; Tashiro et al. 2002). The system is composed of the sensor part (HXD-S), an analog electronic system (HXD-AE), and a digital electronic system (HXD-DE). A block diagram of the HXD is displayed in Figure 2.9. Events are detected by the HXD-S, which sends analog signals to the HXD-AE. Valid events are selected by the HXD-AE, digitized, then sent to the HXD-DE. The HXD-DE formats the data packets and sends them to the satellite data processor (DP) which in turn sends the packets back to Earth. Commands to the instrument are supplied by the satellite data handling unit and received by the peripheral interface module (PIM). The PIM then transmits the commands to the HXD-DE. The instrument is designed to operate at $\sim$253 K and receives power from a local power-supply unit (HXD-PSU) (Takahashi et al. 2007).

2.7.6 HXD Sensor Array and Housing (HXD-S)

The HXD-S consists of sixteen well units arranged in a 4 $\times$ 4 array for detecting 10-600 keV events surrounded by twenty anti units primarily for sheilding and MeV detection. The configuration of the HXD-S is displayed in Figure 2.10. The well unit consists of a Bismuth germanate crystal (BGO; $Bi_4Ge_3O_{12}$), four Gadolinium silicate crystals (GSO; Gd_2SiO_5(Ce)), four silicon PIN diodes, a photomultiplier, and front-end electronics. The bottom of the BGO is a block that the detector elements (GSO crystals and PIN diodes) rest upon. The top of the BGO crystal forms the well and has a cross-shaped plate that divides the well into four narrow collimators. At the base of the well are the four PIN diodes arranged beneath the collimators. The PIN diodes absorb X-rays below $\sim$70 keV, acting as the detector for those energies. Above $\sim$70 keV the PIN diodes become progressively transparent to harder X-rays, allowing them to reach the GSO detector beneath. The

photomultiplier (HAMAMATSU R6231-07) is attached to the unit to collect light from the GSO and BGO scintillators. Signals from the photomultiplier and PIN diodes are processed by the electronics.

The anti units are ∼2.6 cm BGO rods which reduce the flux on the detectors by an order of magnitude. Each is viewed by a photomultiplier. They provide hit pattern information (see Section 2.7.7) to the well units. In addition, with an effective area of ∼400 cm^2, they are capable of detecting γ-ray bursts between 50 keV and 5 MeV (Takahashi et al. 2007).

The housing for the HXD-S holds the 36 detector units and mechanically protects them, minimizes temperature differentials, and reduces electrical noise. The top lid and central body are made of carbon fiber reinforced plastic (CFRP) while the bottom is made of magnesium alloy. The lid has 64 square openings for each well unit and is covered by another thin (400μm) plate of CFRP (Nakazawa et al. 1999; Takahashi et al. 2007).

2.7.7 HXD Electronics (HXD-AE & HXD-DE)

Once the HXD-S detects an event, it sends analog signals to the HXD-AE. The HXD-AE are comprised of a control board (Analog Control Unit ACU), four signal processing boards for the well units (Well Processing Unit WPU), and four signal processing boards for the anti units (Transient Processing Unit TPU). The ACU receives power from the HXD-PSU and controls the power to other HXD-AE boards and the HXD-S. In addition, it tracks house keeping data such as voltage values, temperatures, ect. Each WPU and TPU handles four well units and five anti units respectively.

Each of the 36 units notifies the others of detected events though electronics on the backplane of the HXD-AE. This information, called hit pattern, allows the HXD-AE to reject Compton events that occur in the HXD-S and would otherwise contaminate the data. A signal from the HXD-S photomultiplier is fed into anode and dynode amplifiers within a WPU. Since the scintillation decay times are different between the GSO and BGO, the GSO

will produce greater anode output pulse heights than the BGO for the same energy input. This allows the HXD-AE to discriminate GSO signals from BGO events.

When an event from a well unit is considered valid by the HXD-AE, all analog outputs from the well unit are digitized by analog to digital converters, edited into event data, and sent to the HXD-DE. The HXD-DE act as the primary interface with the satellite data processor for command and telemetry, control the procurement and formatting of data from the HXD-AE, and react to energetic events such as γ-ray bursts. The HXD-DE have two CPU boards, with one functioning and the other idle and acting as backup. The boards contain 512 KB of SRAM for a programmable region, 512 KB of SRAM for a direct memory access buffer, and 512 KB of EEPROM for program storage. The rate of tolerance is 4000 events s^{-1}. While in orbit, irradiation from charged particles can cause memory errors. Potential malfunctions due to this are mitigated by the process called Memory-Patrol which verifies the memory byte by byte. The HXD-DE also include an error correction code that repairs 1-bit errors and reports those of multiple bits (Takahashi et al. 2007).

2.8 XMM-Newton

On 10 December 1999 the ESA's X-ray Multi-Mirror Mission (XMM-Newton) was launched by an Ariane 504 rocket from the Guiana Space Centre. Over the next six days on-board propulsion systems set the satellite from its initial launch orbit (850 km $\times$ 114,000 km at 40° inclination) into its final orbit with an increased perigee of 7000 km (ESA 2019). The satellite is split into four main regions: the Focal Plane Assembly (FPA), the Telescope Tube, the Mirror Support Platform (MSP), and the Service Module (SVM). The FPA consists of the Focal Plane Platform and the attached instruments: one European Photon Imaging Camera (EPIC) pn detector, two EPIC MOS detectors, two Reflection Grating Spectrometer (RGS) cameras, and the power and data handling units for the cameras. The EPIC and RGS are cooled via radiators. The Telescope Tube is a 6.8 m carbon fiber tube that maintains the

position between the MSP and FPA. The upper half also includes two venting and outgassing doors and the outgassing baffle to create a sufficient vacuum in the tube. It contains three telescopes, each reserved for one EPIC detector. The MSP includes a support platform, three mirror assemblies, the Optical Monitor (OM), and two star trackers. The mirror assemblies consist of the mirror modules, the entrance and exit baffles, mirror doors, and two RGS grating boxes. The SVM contains the spacecraft subsystems including thermal control, altitude and orbit control, on-board data handling, two S-band radio antennae for ground communications, and the electrical power subsystem. Two solar arrays and the Telescope Sun Sheild are also attached to the SVM (ESA 2021a,b). A schematic of the XMM-Newton Payload is displayed in Figure 2.11.

2.8.1 XMM-Newton X-ray Telescopes

Each of the three telescopes consist of the mirror assembly door, the entrance baffle, the X-ray baffle, the Mirror Module, an electron deflector, and the exit baffle. The two telescopes that focus onto the EPIC MOS also contain Reflection Grating arrays. A schematic of the telescope configuration is displayed in Figure 2.12. The mirror assembly door protected the optics during pre-launch, launch, and early orbit. The entrance baffle surpresses stray light at angles above 47°. The X-ray baffle is located in front of the Mirror Module and acts as a collimator and reduces stray light. The electron deflector produces a circumferential magnetic field that prevents low energy electrons reflected by the mirrors from reaching the detectors. The Reflection Grating Array is part of the RGS instrument and is discussed in more detail in Section 2.8.6. The exit baffle aids in temperature regulation (ESA 2021c; Jansen et al. 2001).

The Mirror Modules consist of 58 Wolter I mirrors nested in a coaxial, confocal configuration. The grazing incidence angles range between 17 and 42 arcmin. They have a 7.5 m focal length and the diameter of the largest mirrors is 70 cm. The mirrors were formed

from gold coated mandrels using nickel electroforming (Gondoin et al. 1994). The mirrors are bonded to the entrance aperture to the sixteen spokes of a spider made from Inconel. The spider is attached to the support platform by an Al Mirror Interface Structure. This structure consists of an outer cylinder and an interface ring (ESA 2021c; Jansen et al. 2001).

2.8.2 European Photon Imaging Cameras (EPIC)

Each EPIC camera is split into three sections: the stand-off structure, the cryostat section, and the radiator. The stand off structure contains the filter wheel, door, calibration sources, the radiation sheild, the internal vacuum bulkhead, and the interface to the spacecraft. It is identical for all three EPIC cameras. The cryostat section contains the CCDs and electronic interfaces. The radiator cools the CCDs.

The stand-off structure is a Ni-plated cylindrical Al structure with a vacuum bulkhead containing feed-through for the electronic connections and filter wheel drive. The vacuum protects the CCDs from contamination prior to launch and acoustic damage during launch. The filter wheel is located on the vacuum side of the bulkhead. It has six filter locations and six additional apatures that allow the calibration source to shine onto the CCDs. Four of the filter slots hold filters of different thicknesses, one is open, and one is closed. The thin and medium filters are a poly-imide film with Al deposited on the side, with the medium filter having about twice as much Al. The thick filter for the MOS cameras is made of Polypropylene, tin (Sn), and one layer of Al while the pn camera's thick filter has the Polypropylene and tin between two Al layers (Strüder et al. 2001; Turner et al. 2001). The calibration source is mounted on the vacuum side of the bulkhead. The door was closed prior to and during launch, later opening to allow X-rays to reach the CCDs. The radiation sheilding is an internally mounted Al sheild between the bulkhead and the CCDs, and a separate sheild that is mounted on the spacecraft focal plane bulkhead (Turner et al. 2001).

2.8.3 EPIC pn

The pn camera housing is primarily Al, with Si, Fe, copper (Cu), manganese (Mn), magnesium (Mg), chromium (Cr), zinc (Zn), and titanium (Ti) comprising about 10% of its mass. The main components of the pn-CCD system are the radiator, cold finger, proton shield, circuit board with preamplifiers, and the pn-CCD mounted on an invar ring. The interconnections between the CCD and electronics are ∼900 individually coated wedge bonds. The camera head is supported by a spider structure pressed onto the PC board (Strüder et al. 2001).

The EPIC pn camera contains twelve pn-CCDs. It achieves spatially uniform detector quality due to the fabrication of all twelve 3 × 1 cm CCDs on a single Si wafer. The instrument is split into four quadrants, each with three pn-CDDs with a format of 200 × 64 pixels that are operated in parallel. The relevant X-ray Telescope also has a field of view (FOV) of 6 × 6 cm. The pn array covers ∼97% of the FOV, with some of the CCD's sensitive area outside of the FOV for background study. The pixel size is 150 × 150 μm with a position resolution of 120 μm which yeilds an angular resolving capability of 3.3 arcsec for a single photon (ESA 2021d; Strüder et al. 2001).

The pn-CCD functions by X-rays hitting the detector from the back contact (see Figure 2.13). When an X-ray interacts with the Si atoms, a number of electrons and holes are produced proportional to the energy of the photon. Strong electric fields inside the detector separate the electrons and holes before they are able to recombine. The positively charged holes migrate to the negatively biased back side and are 'absorbed'. Electrons drift to the potential minimum and are captured in potential wells 10 μm below the surface. They can be transferred to the readout nodes upon command, conserving charge distribution patters in the process. A readout amplifier terminates the CDD line. The quantum efficiency of the EPIC pn is displayed in Figure 2.14 (ESA 2021d; Strüder et al. 2001).

2.8.4 EPIC MOS

The EPIC MOS cryostat is a conical Ni plated Al structure attached to the stand-off structure. The cold finger is supported by Al and glass fiber reinforced polymer (GFRP). This forms a doubly insulated structure with a secondary thermal shield that is linked to the outer radiator. The CCDs are bonded to a silicon substrate, which is bonded to an invar plate that is bolted and bonded to an Al block. The block slides into a channel in the mounting plate at the end of the cold finger. Heaters are included in the mounting plate to ensure the CCDs remain at their operation temperature ($\sim$170 K). An external mounted multi-layer polychlorinated biphenyl board (PCB) contains the relevant electrical components. The PCB is also the vacuum feed-through, providing signals and power to the cryostat (Turner et al. 2001). The cryostat is passively cooled by three nested conical radiators (Goodall et al. 2001). The flanged cones are truncated at an angle to match the slope of the sheilded zone. The inner radiator is attached to the CCD via the cold finger and has no contact with the outer two radiators. The middle radiator is connected to the thermal shroud surrounding the CCD. The outer radiator has exterior insulation on its outer face and the middle radiator on its inner face (Turner et al. 2001).

The EPIC MOS camera consists of seven EEV type 22 front illuminated CCDs. The central CCD is at the focal point of the optical axis of the telescope, and the surrounding six CCDs are stepped by 4.5 mm to follow the focal plane curvature. The CCDs are buttable and adjacent CCDs are stepped by $\sim$1 mm to overlap by 300 μm. Since the CCDs have dead region gaps of $<$300 μm, this minimizes the dead space of the detector. "The imaging section has 600 $\times$ 600, 40 micron square, pixels; one pixel covers 1.1 $\times$ 1.1 arc seconds on the field of view" (Turner et al. 2001). The readout registers have two sections, each ending in a readout node. The CCD image can be read using either node or both. The two MOS cameras are arranged on the spacecraft such that they are orthogonal, resulting in the gaps of the outer CCDs in one detector being covered by the other detector. The gaps around

the central CCD overlap, but the pn detector is angled at 45° to the MOS detectors, thus fully covering the field of view (ESA 2021d; Turner et al. 2001).

The MOS CCDs are three-phase frame transfer devices on epitaxial Si with an open-electrode structure. The epitaxial layer is 80 μm thick (p-type) and has a resistivity of $\sim$400 Ω-cm. One of the three electrodes is enlarged and holes have been etched through it. This area has a high transmission for soft X-rays that would have been absorbed by the electrodes.

The preamplifiers for the MOS CCDs are mounted on the cyrostat PCB. This interfaces to the analogue electronics (EMAE). The EMAE condition the signal and are partially redundant; reading out the seven CCDs with a set of eight channels. They also contain the clocking sequencers which generate pulses to transfer the charge released by the X-rays to the readout nodes. The control and recognition unit (EMCR) converts the image read from each CCD onto an event list (Ferrando et al. 1999; Pigot et al. 2000; Turner et al. 2001). This identifies geometric patterns of pixels and distinguishes between X-rays and events from cosmic rays. It also sums the charge over the pattern to determine X-ray energy. The EMCR also stores and transmits CCD clock sequences to the EMAE, controls signals to the filter wheel, and timestamps CCD frames. The voltage controller (EMVC) receives power from the spacecraft and provides the necessary voltage and currents to all other boxes and is fully redundant. The data handling system (EMDH) receives data from the EMCR and processes it for the telemetry (Turner et al. 2001; Villa et al. 1996). It receives and executes commands to the system and is the interface to the spacecraft for software upload and data handling. A block diagram for the EPIC MOS electronics is displayed in Figure 2.15 (Turner et al. 2001).

2.8.5 EPIC Radiation Monitor (ERM)

The ERM detects radiation belts and solar flares. The data are used to provide particle environment information for proper operation of the EPIC cameras and to monitor the space

environment. The latter is useful for development of detectors for future missions. The ERM is split into three sections: the detection head (ERMD) and accompanying thermal cover, the electronics for data handling and interfacing with the spacecraft (ERME), and the harness (ERH) between the ERMD and ERME.

The ERM has three Si diode detectors, one for lower and two for higher energies. It contains both a nominal (A) and redundant (B) setup assembled on a single structure. All ERM detectors have a surface area of 0.85 cm^2 and thickness of 500 mm. The lower energy detector is sensitive between 50 keV and 5 MeV while the high energy detectors register events between 500 keV and 12 MeV. When sufficient ambient radiation is detected, the ERM sends an alert signal every 4 seconds to the EPIC telemetry. This triggers the closing of the EPIC cameras in order to protect them during high radiation instances such as solar flares or when the spacecraft enters Earth's radiation belts (ESA 2021d). A block diagram of the ERM is displayed in Figure 2.16.

2.8.6 Reflection Grating Spectrometer (RGS)

The two telescopes that are pointed at the EPIC MOS detectors have RGSs behind them. Each RGS is a reflection grating array which intercepts about half of the X-ray light and diffracts it onto a strip of CCD detectors offset from the telescope focal plane. The remaining light shines upon the EPIC MOS detectors. The RGS instruments have fist order spectral resolving power of 150 - 800 over a 0.33 - 2.5 keV range. They consist of a Reflection Grating Array unit (RGA), a Focal Plane Camera unit (RFC), an Analogue Electronic unit (RAE), and two Digital Electronic units (RDE, one RDE is for redundancy). A schematic of the RGS is displayed in Figure 2.17. The dispersion equation 2.9:

$$m\lambda = d(\cos(\beta) - \cos(\alpha)) \tag{2.9}$$

yeilds the wavelength for incident angle α, dispersed angle β, spectral order m, and groove

spacing d (see Figure 2.17). The high resolution ($E/\Delta E = 100$ to 500) makes the RGS instrument useful for determining composition of the X-ray source environment. It is particularily good at detecting K-shell transitions of Carbon (C), Nitrogen (N), Oxygen (O), Neon (Ne), Magnesium (Mg), and Si, and L-shell transitions of Iron (Fe) (Brinkman et al. 1998; den Herder et al. 2001; ESA 2021e).

One RGA contains 182 identical gratings while the other has 181 due to a fabrication problem. The gratings are mounted in the classical configuration, meaning the incident and diffracted x-rays lie in a perpendicular plane to the grating grooves. The gratings are arranged such that the incident angle α (see Figure 2.17) at the center of the grating is the same for all gratings in the array. All gratings lie on the Rowland circle, and each RGA has six rows of gratings. The grating substrates are 1 mm silicon carbide (SiC) with five ribs at the back. The gratings are covered with Au. The RGA support structure is made of Beryllium (den Herder et al. 2001).

The RFC is comprised of nine back illuminated CCDs mounted according to the curvature of the Rowland circle and four calibration sources (see Figure 2.17). The CCDs are GEC/EEV with an image and storage section of 384×1024 pixels with each pixel being 27×27 μm^2. The CCDs are operated in frame transfer mode. A thin Al sheild (75 nm for the two closest CDDs to optical axis, 68 nm for the next three, and 45 nm for the further four) guards the CCDs from optical light. The calibration sources are an α emitter (^{244}Cm), and either an Al target or a Teflon target. The targets produce Al Kα or Flourine (F) Kα flourescence. These illuminate two of the CDDs offset from the source image. The CCDs are cooled to 193 K by a two-stage cooler and three nested thermal shells (den Herder et al. 2001).

The electronic processing consists of the RAE and RDE. A block diagram of the RFC, RAE, and RDE is displayed in Figure 2.18. They are under control of the Instrument Controller (IC) which set the bias settings of the CCDs and commands the Clock Sequence

Generator (CSG), which handles the clock drivers for the CCDs. All interfaces with the On-board Data Handling bus (OBDH) go through the IC as well. The CCD readouts are sent through two output nodes resulting in different gains and offsets for each node. The signals are amplifed and digitized in the RAE using a correlated double sample (CDS). All data are then sent to the RDE Data Pre-Processor (DPP). The RDE also control the temperature of the bench and contain the Power Supply Unit (PSU) (den Herder et al. 2001).

Three operating modes are available for the RGS: Spectroscopy, High Time Resolution, and Diagnostic. Spectroscopy reads out the nine CCDs sequentially and rejects hot pixels and columns. The remaining pixel data are sent to a programmable processor that rejects pixels above a signal threshold as well as complex structure pixels which are typical of cosmic rays. Remaining data are considered valid. The High Time Resolution mode sums the image over 74 pixels. This has the shortest accumulation time but higher background contamination compared to Spectroscopy. The Diagnostic mode ignores data processing and sends the entire image to Earth. It is used for dark current and noise verification (den Herder et al. 2001).

2.8.7 Optical/UV Monitor (OM)

The Optical/UV Monitor is attached to the MSP near the mirror modules. It observes 170 nm - 650 nm of the central 17 arc min X-ray field of view. The OM contains a Telescope Module for the optics and detectors, and two Digital Electronics Modules for data processing and power supply. The Telescope Module has two detectors for redundancy. The second Digital Electronics module is also included for redundancy.

The Telescope Module is a 2 m tube housing a 30 cm Ritchey-Chretien telescope with a 3.8 m focal length. Incident light is reflected by a 0.3 m primary mirror, onto a secondary hyperboloid mirror, then onto a third mirror at 45° angle which finally reflects the light onto a detector. A filter wheel is installed in front of the detector and contains filters, grisms, and

a magnifier (ESA 2021f; Mason et al. 2001). This dissertation focuses on the X-ray spectra above 0.3 keV and thus does not utilize this instrument. This brief section was included for completeness.

2.9 NuSTAR

The Nuclear Spectroscopic Telescope Array (NuSTAR) launched on 12 June 2012 in the skies above the Kwajalein Atoll. A Pegasus rocket carrying the satellite was loaded onto a Stargazer L-1001 aircraft and dropped at 40,000 ft. Five seconds later, the three-stage rocket motor on board the Pegasus ignited and took the payload to space. Thirteen minutes later, NuSTAR separated from the rocket and achieved its final low Earth orbit (Release 2012). An extendable mast was deployed to gain the 10.14 m instrument focal length nine days after launch. The spacecraft is powered by a solar array extending from the section containing the focal plane bench. The science instrument consists of two Wolter-I conical approximation mirrors which focus onto two detector arrays. All optics and detectors are designed to be identical. The benches that support the optics and focal plane systems are separated by a mast which requires corrections to keep the alignment of the benches. To this end, a star camera mounted to the optics bench and two laser metrology units measure the translation, tilt, and rotation between the benches. These data are used during data processing to remove image blur and create proper response files. Four star cameras are used to determine the instrument and spacecraft altitude. Three are mounted on or near the spacecraft bus and are used with other sensors to control altitude and determination. The fourth is mounted on the optics bench and is combined with the laser metrology units to align and point the instruments. A picture of the observatory is displayed in Figure 2.19 (Harrison et al. 2013).

The mirror assemblies are 133 nested shells in a conical approximation to Wolter-I geometry. Each shell is aligned at grazing incidence and comprised of either 12 or 24

formed glass segments, depending on the radius. The segments are coated with depth-graded multilayer structures which increase the graze angle and thus field of view for energies above ∼15 keV compared to standard metal coatings. The coating materials vary as a function of shell radius to optimize the energy response and field of view. The inner 89 shells are platinum (Pt) and carbon (C) layers while the outer 44 shells are coated with tungsten (W) and Si layers (Harrison et al. 2013).

The two telescopes are paired with two focal plane modules (FPMA and FPMB). Each module is a solid state detector array comprised of cadmium (Cd), zinc (Zn), and telurium (Te) (Harrison et al. 2010) surrounded by a caesium iodide (CsI) sheild. The detector array contains four CdZnTe pixel detectors with the optical axis being ∼1' offset from the chip gap. Each pixel has an independent discriminator and individual X-ray events trigger readout. Each FPM has an on board processor that identifies the row and column of the largest pulse height. The pulse heights of that pixel, as well as the surrounding eight pixels, are then read out. The processing time per event is 2.5 ms, limiting the read out rate to 300-400 events s^{-1} $module^{-1}$. The FPM detectors are enclosed by a CsI anti-coincidence sheild. Events that produce energy deposition in both the sheild and the detectors are rejected as background. Apature stops deployed post-launch reduce the opening angle of the sheild to a 4° full width at zero intensity (FWZI) field. While these stops significantly reduce stray light compared to the sheild's base 15° FWZI, some remains which dominates the background below 10 keV (Harrison et al. 2013).

2.10 Software

Two software suites were used in the research presented in this dissertation: Scientific Analysis System (SAS) and High Energy Astrophysics Software (HEASoft). The SAS was created by the ESA specifically to reduce and analyze data collected by XMM-Newton. It is a collection of scripts and libraries that process the raw data files into ones capable of being

using in data analysis. HEASoft is a general use spectral analysis suite made by NASA. For Suzaku and NuStar, HEASoft contained the necessary scripts and libraries to process the data. Suzaku data were processed using XSELECT and NuStar data were processed using the "nuproducts" command included in HEASoft. Once the data of all three satellites were processed, they were analyzed using HEASoft programs XSELECT and XSPEC. Both software suites are open source and kept up to date.

The HEASoft package XANADU contains three programs for data analysis: XSPEC, XRONOS, and XIMAGE. All spectral analysis and plotting was done using XSPEC, discussed in greater detail in the next section. Timing analysis can be done with XRONOS and image analysis with XIMAGE but neither were used in this dissertation. The FTOOLS packages contains tools to manipulate FITS files while FITSIO contains libraries responsible for reading and writing FITS files. It also includes "fv", a FITS file browser and plotter. The XSELECT package contains tools for filtering event files and generating light curves and spectra. The Astronomical Imaging and Data Visualization Application: DS9 was used to ensure that the programs were drawing data from the correct region of the detectors. Many of the ionized (warm) absorbers used in spectral modeling were constructed using the XSTAR package (Kallman 2021).

2.10.1 XSPEC

Prior to the creation of the XSPEC program, X-ray spectra fitting programs were written specifically for the experiment where the data were analyzed. In 1983 R. Shafer began work on a spectral fitting program that would be independent of the instrument. So long as the spectra and detector response are formatted into a FITS file, it can be used with XSPEC. Since then, continued development of XSPEC by R. Shafer, F. Haberl, A. Tennant, and others has raised XSPEC to be the global standard for astronomical X-ray spectroscopy. Given a theoretical model and a detector response file, the program is able to simulate a

spectrum. The simulated spectrum can then be compared to the data using a goodness of fit statistic (χ^2). If the statistics are insufficient, models can be added and/or removed and the individual parameters of those models can be changed. A flow chart of the fitting process is displayed in Figure 2.20 (Arnaud 1996).

XSPEC has a wide variety of models built into its installation. As of the writing of this dissertation, over 150 models come with the installation. Some stand alone while others have variations (e.g. redshifted and non-redshifted versions of the model). In addition, table models can easily be used by the program so long as the table is an N-dimension grid of spectra for N model parameters and the file contains the necessary information to communicate with XSPEC. The warm absorber models (multiplicative table models) created using XSTAR were applied to the spectral model this way. In addition, XSPEC can be used to analyze spectra in the optical, UV, EUV, and γ-ray wavebands and is well suited to multiband studies of sources (Arnaud 1996). All XSPEC graphics use the PLT interface (Tennant 1991) to the PGPLOT package (Pearson 1995). Both XSPEC and PGPLOT are primarily written in Fortran (Arnaud 1996; Pearson 1995).

2.11 Chapter 2 Figures

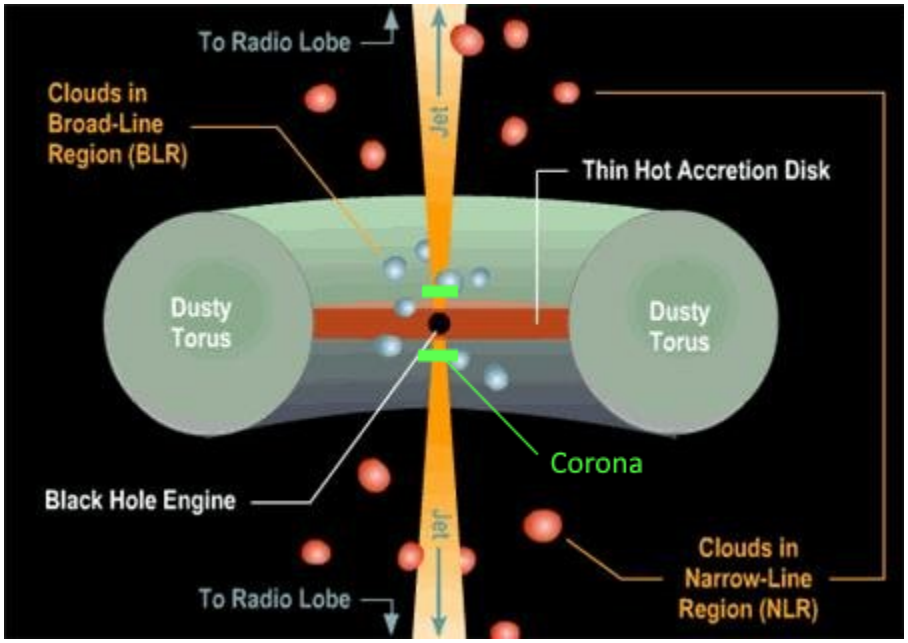

Figure 2.1: Diagram of a radio loud AGN system. Not to scale. Modified from a figure present in Sujová et al. (2008).

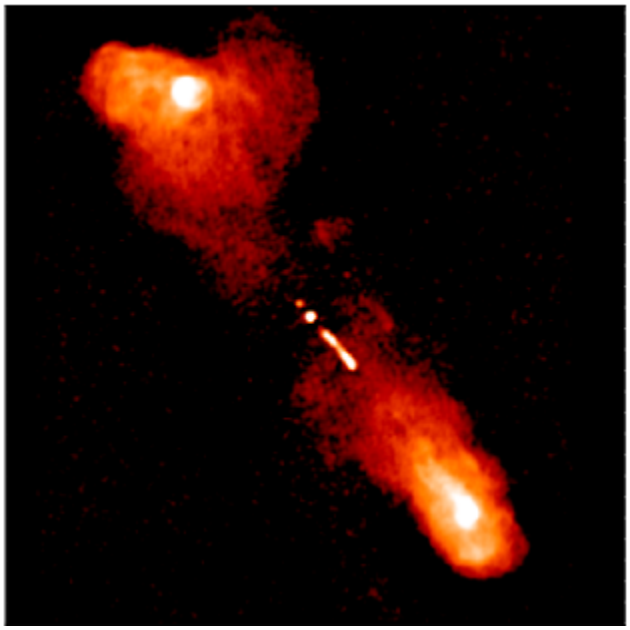

Figure 2.2: Radio image of 3C219 with radio lobes clearly visible. The black hole is in the central region (Clark et al. 1992; Hardcastle & Croston 2020).

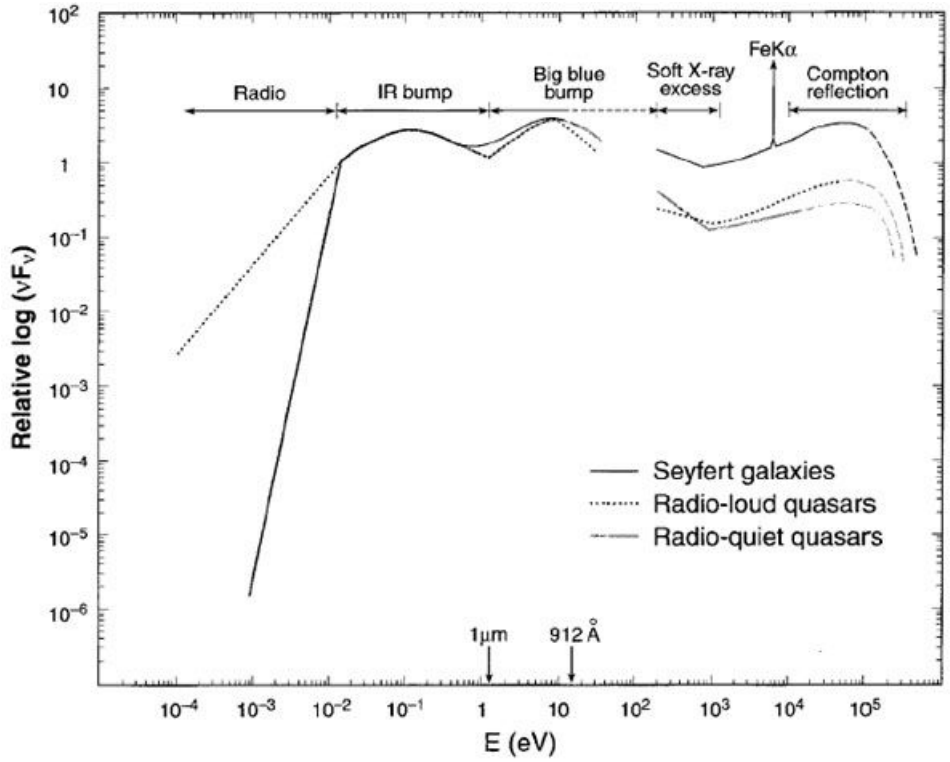

Figure 2.3: Schematic representation of the broad band spectrum for various AGN (Koratkar & Blaes 1999).

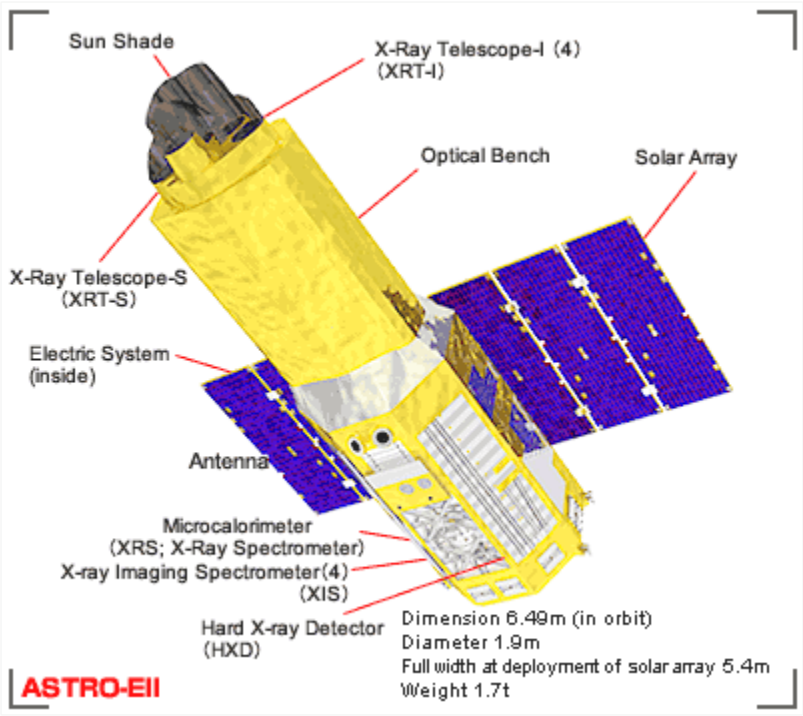

Figure 2.4: Suzaku spacecraft schematic (JAXA 2003).

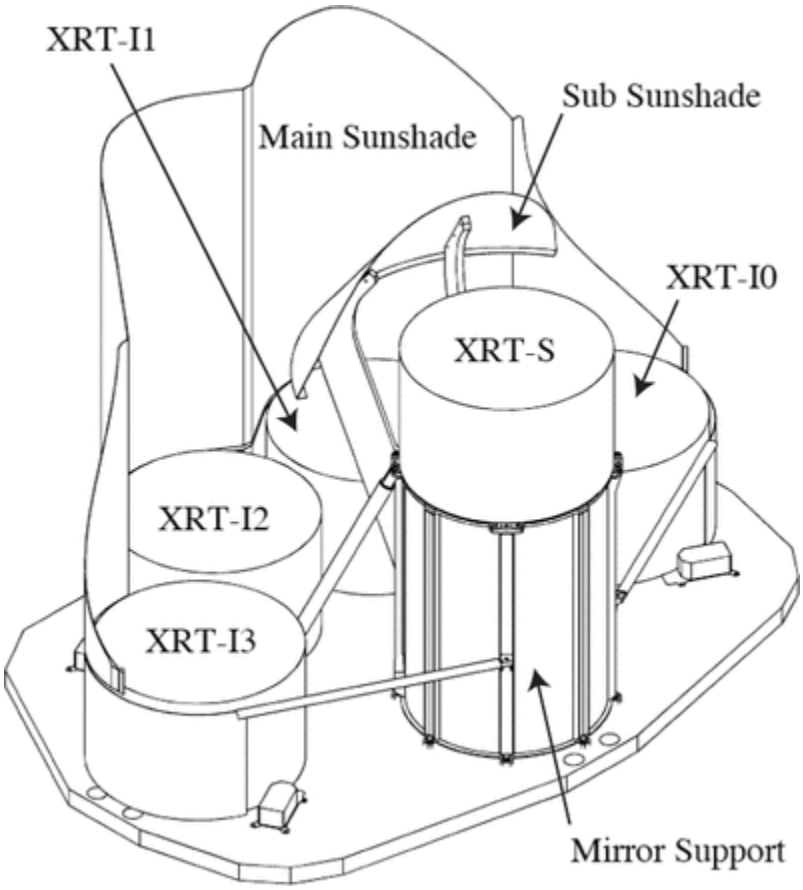

Figure 2.5: Suzaku XRT schematic (Serlemitsos et al. 2007).

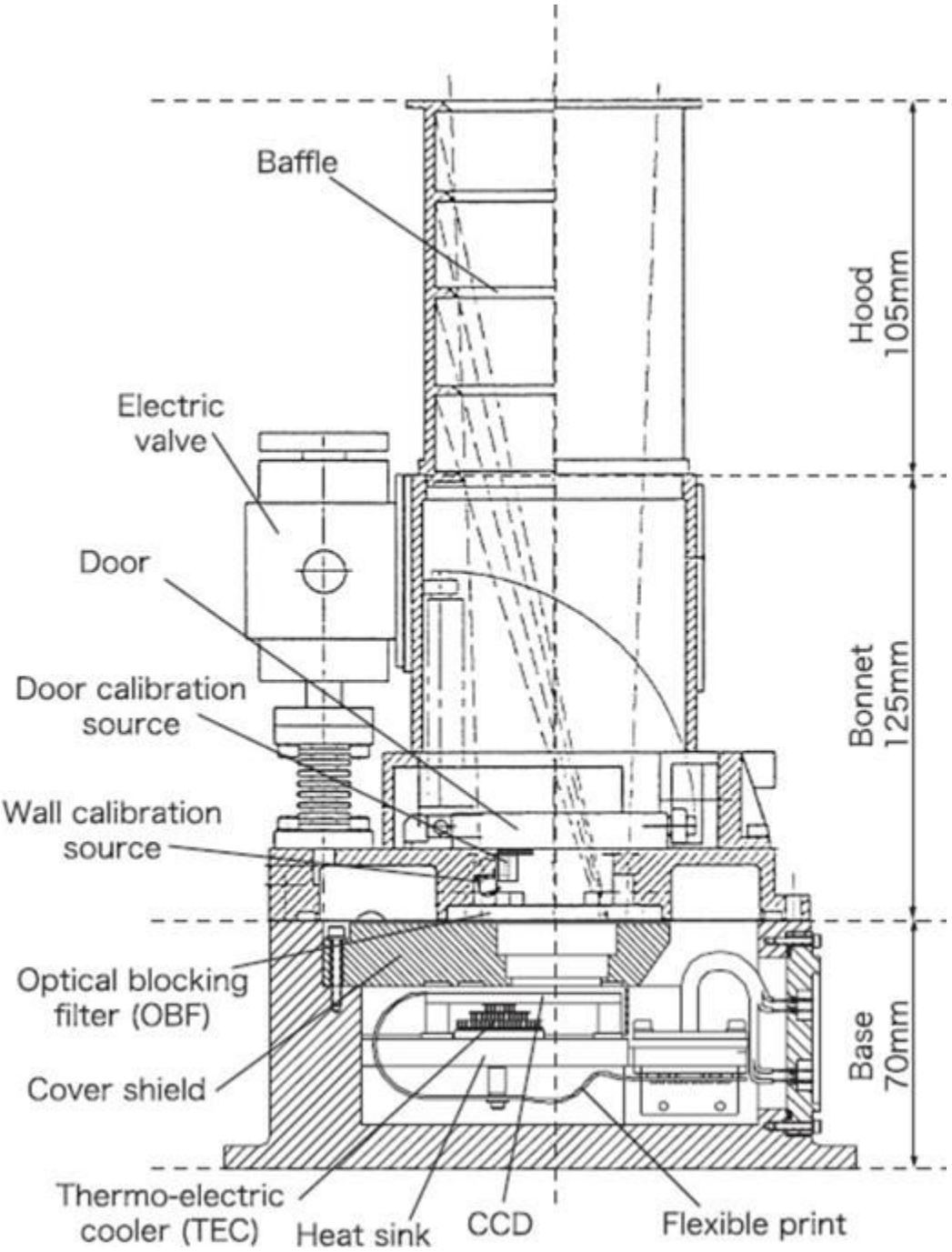

Figure 2.6: Cross sectional diagram of an XIS sensor (Koyama et al. 2007).

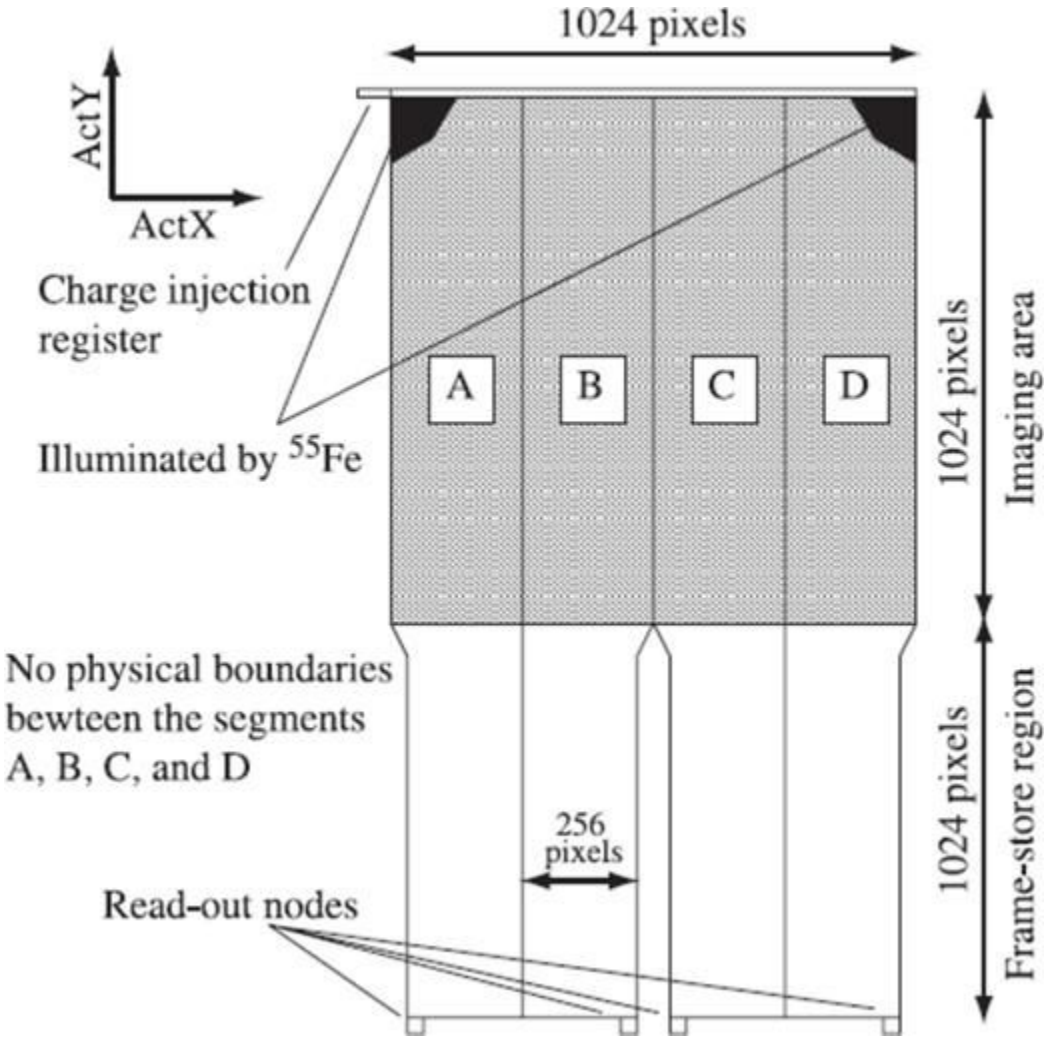

Figure 2.7: Top view schematic of an XIS CCD. Each segment (A, B, C, and D) has its own read out node (Koyama et al. 2007).

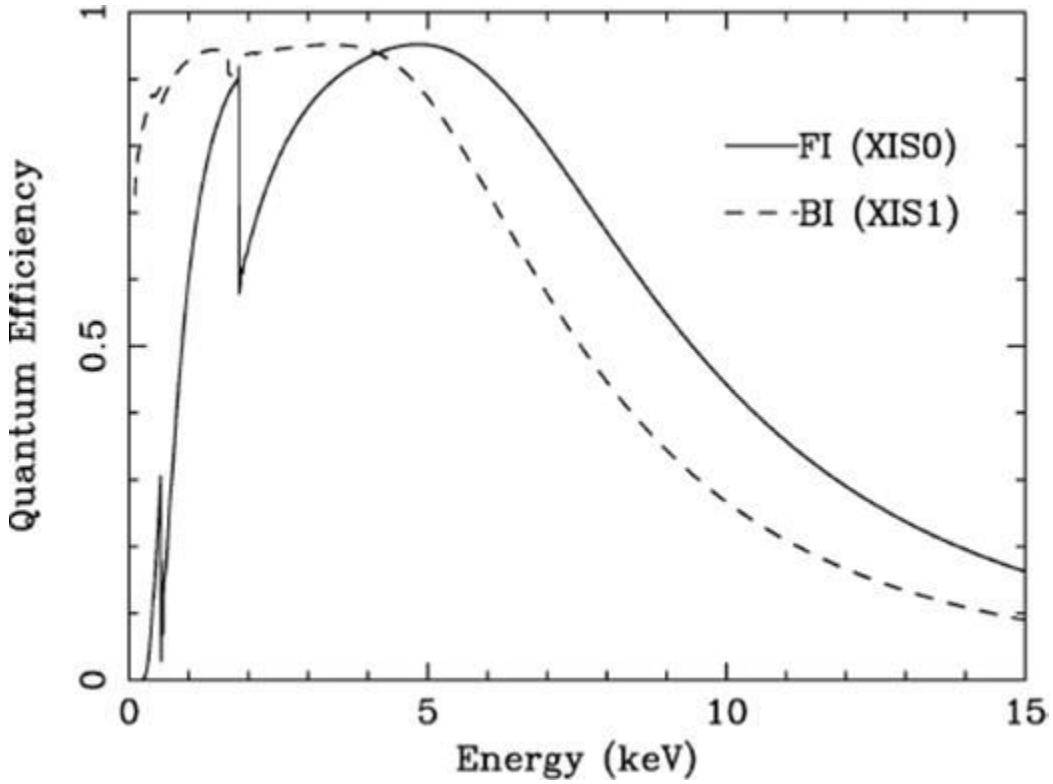

Figure 2.8: Quantum efficiency of the XIS FI and BI CCDS. Note that the FI is superior in the high energy range while the BI is better for softer X-rays (Koyama et al. 2007).

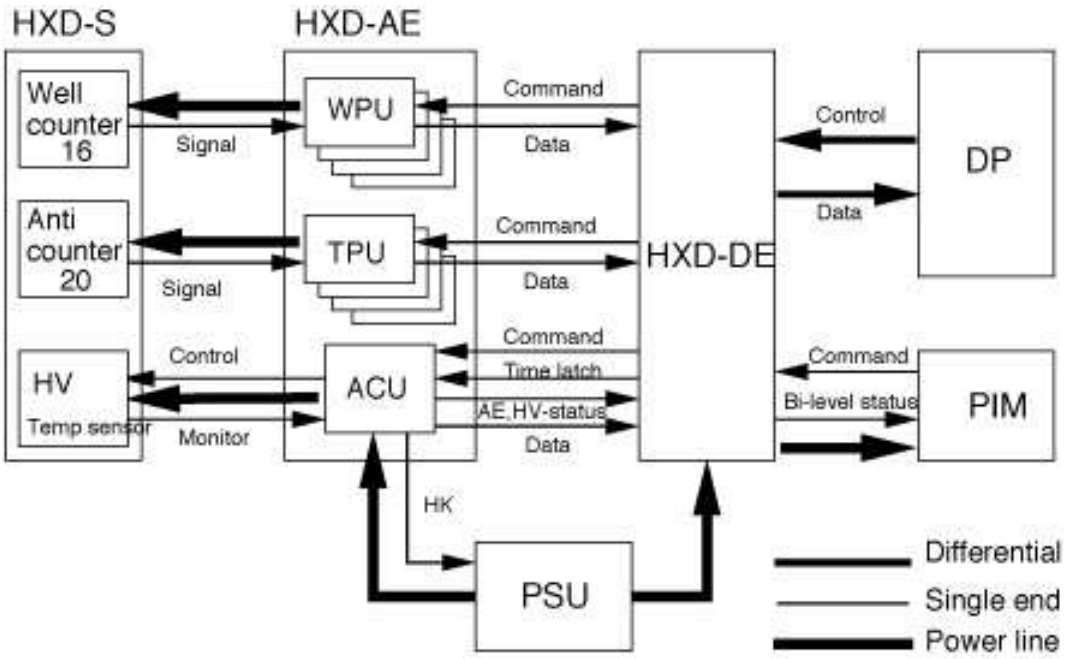

Figure 2.9: Block diagram of HXD and signal flow (Takahashi et al. 2007).

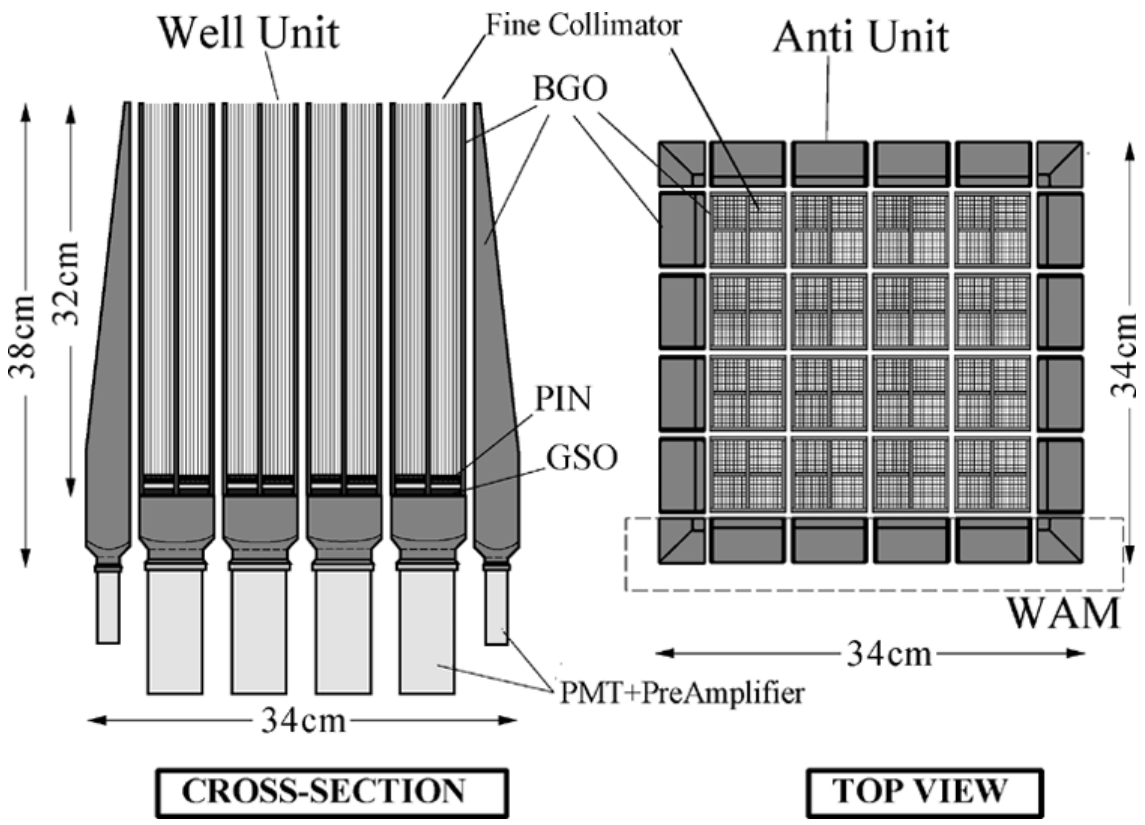

Figure 2.10: HXD-S schematic. The instrument consists of 16 well units sheilded by 20 anti units. The detectors are the GSO scintillator and the PIN diodes located in front of it (Takahashi et al. 2007).

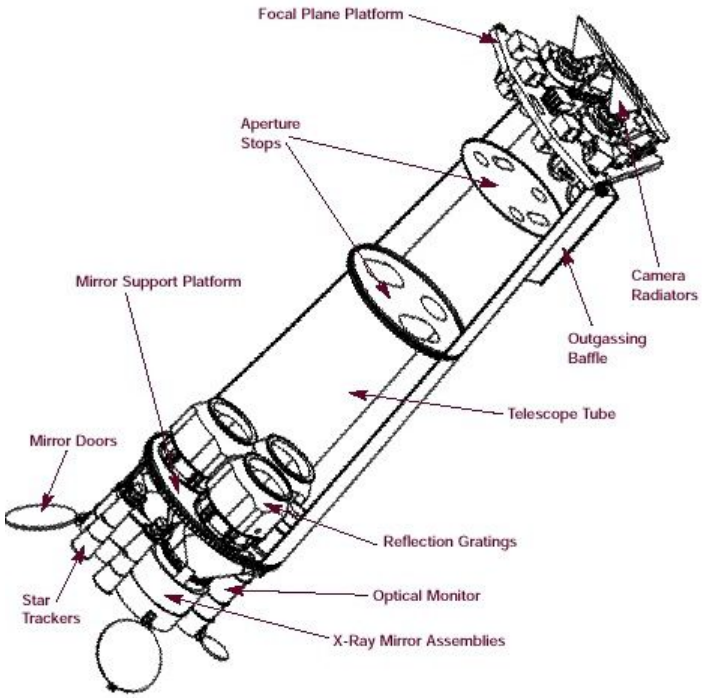

Figure 2.11: XMM-Newton payload schematic showing the FPA, Telescope Tube, MSP, and SVM (ESA 2021a).

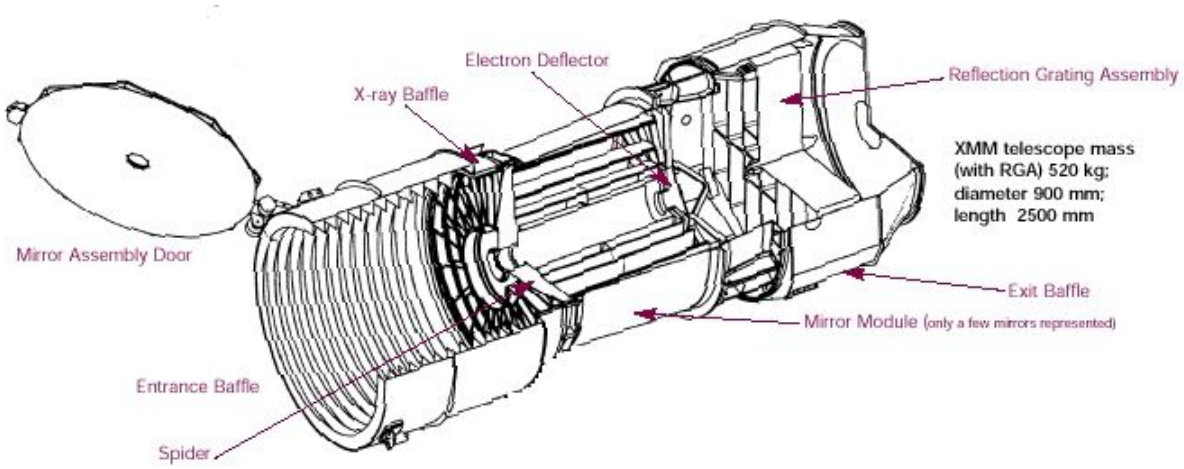

Figure 2.12: XMM-Newton Telescope schematic (ESA 2021c).

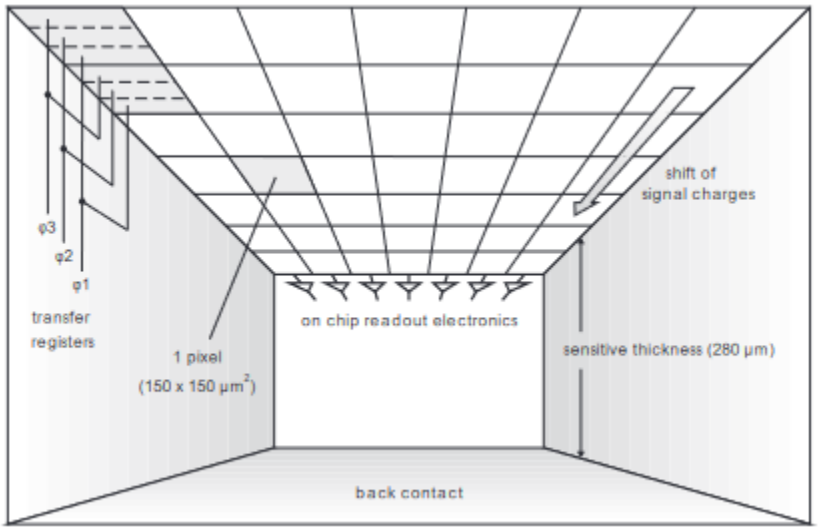

Figure 2.13: EPIC pn schematic (Strüder et al. 2001).

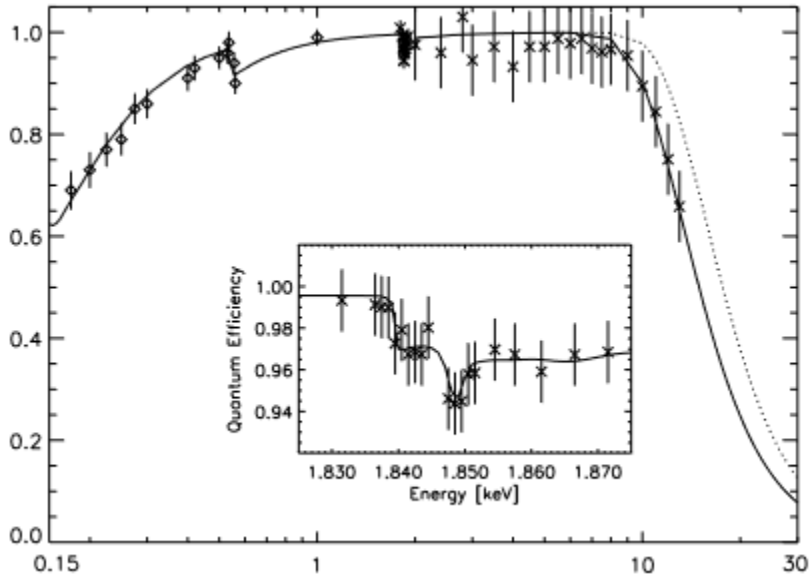

Figure 2.14: EPIC pn quantum efficiency (Strüder et al. 2001).

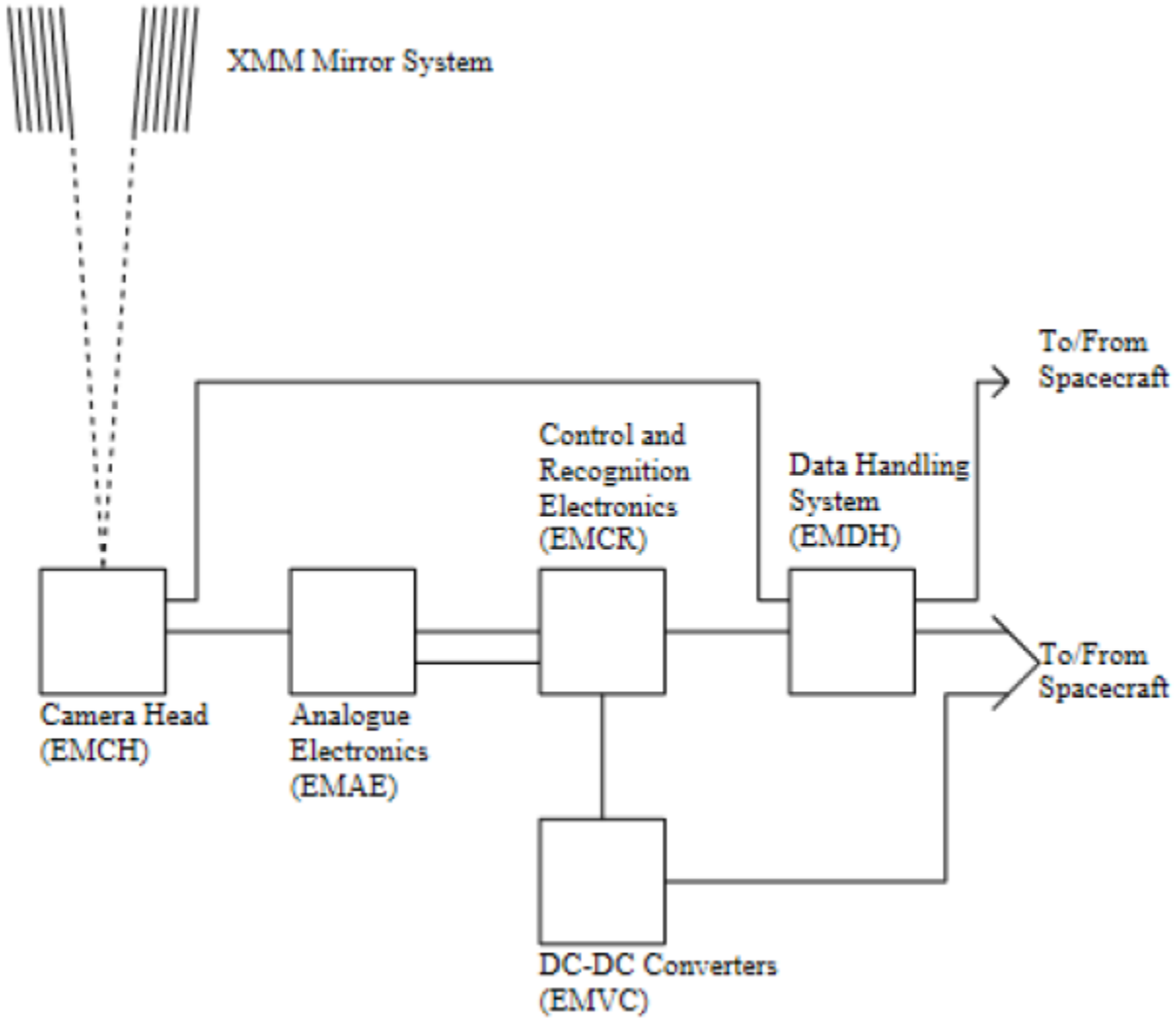

Figure 2.15: EPIC MOS electronic block diagram (Turner et al. 2001).

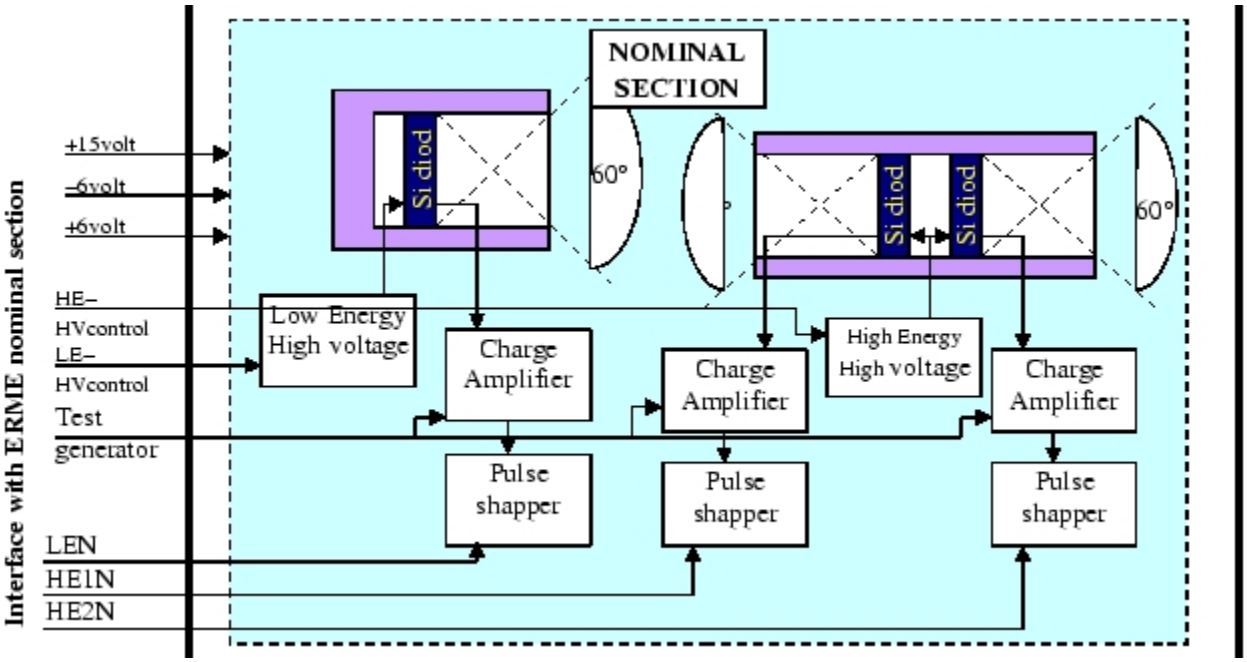

Figure 2.16: XMM-Newton EPIC Radiation Monitor (ERM) block diagram. Displayed here in the diagram for the nomial section with the redundant section being identical (ESA 2021d).

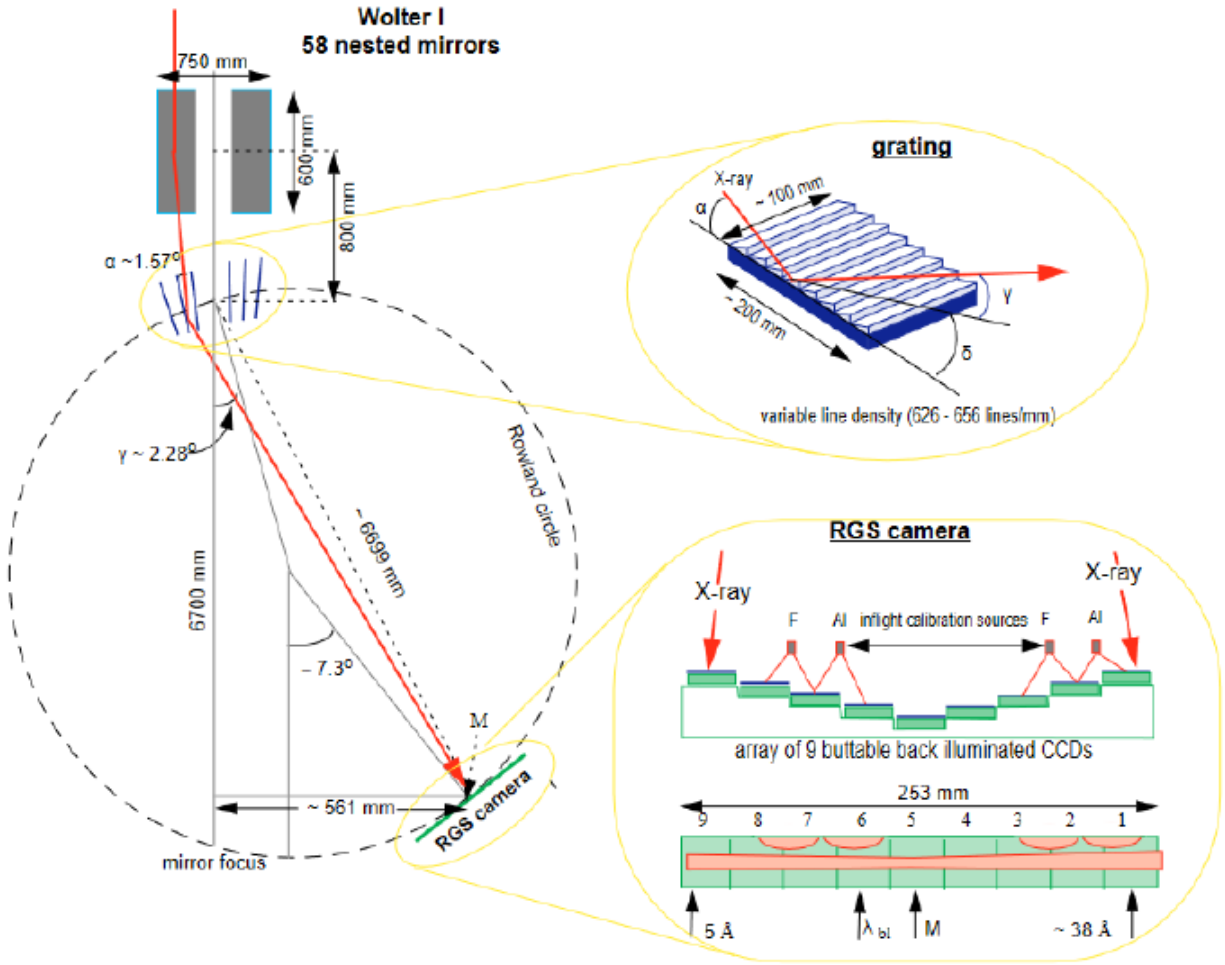

Figure 2.17: XMM-Newton RGS schematic. Note that EPIC MOS is at the mirror focus but not displayed in this figure (Brinkman et al. 1998).

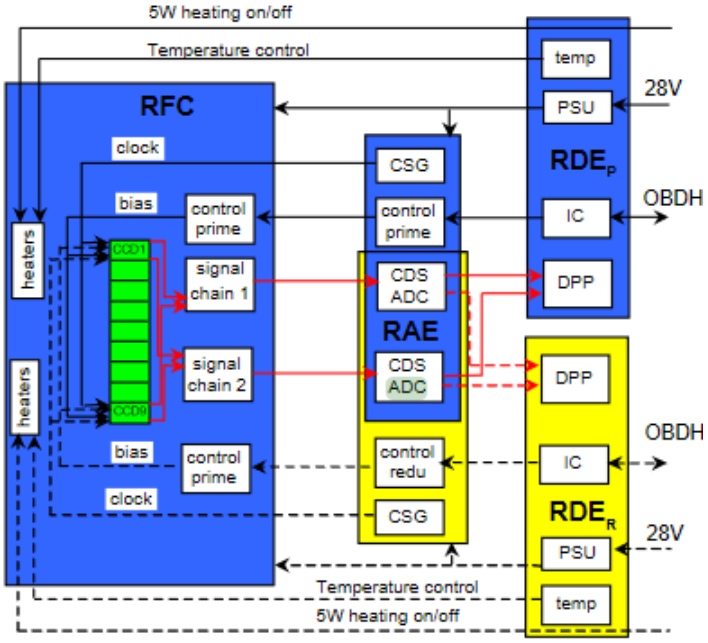

Figure 2.18: XMM-Newton RGS electric block diagram. Note the primary RDE (RDE$_P$) and redundant RDE (RDE$_R$) (Brinkman et al. 1998).

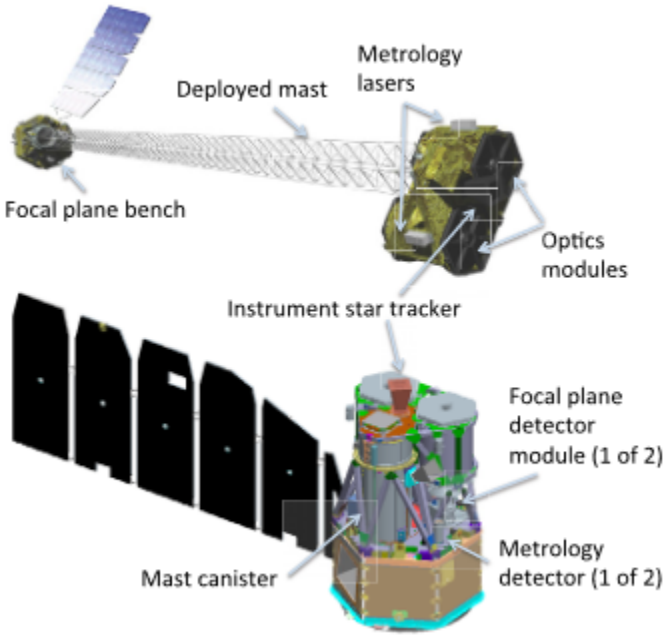

Figure 2.19: NuSTAR spacecraft shown in the extended (top) and compact (bottom) configurations (Harrison et al. 2013).

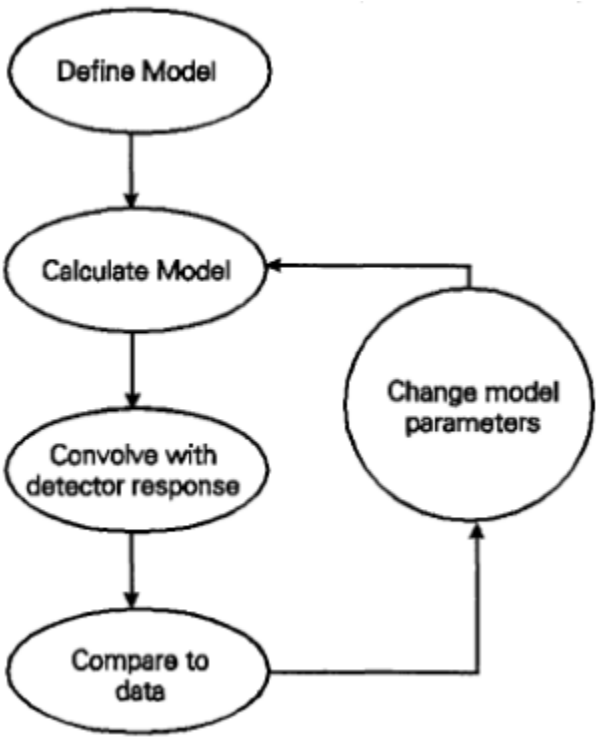

Figure 2.20: XSPEC flow chart for data analysis. First, data are loaded and a theoretical spectral model is defined by the user. Then, the program calculates the model and convolves it with the detector response file(s). The resulting simulated spectrum is then compared to the data and improvements can made by the user (Arnaud 1996).

NGC 3227 TIME AVERAGED ANALYSIS PART I: THE SUZAKU AND EARLY XMM-NEWTON OBSERVATIONS

This chapter, "NGC 3227 Time Averaged Analysis Part I: The Suzaku and Early XMM-Newton Observations", is an adaptation and expansion of published material. The paper titled "Combined Analysis of X-Ray Spectra of NGC 3227" was published in The Astrophysical Journal (volume 907, page 45, J. Newman with co-authors A. C. Liebmann, S. Tsuruta, H. Kuneida, and Y. Haba) (Newman et al. 2021). It is similar in content and source material. However, it has been expanded and formatted to meet Montana State University thesis standards. Some aspects are explained in greater detail, such as the definitions of statistical values and the explaination of model parameters. A brief section involving the XMM-Newton RGS instrument (Section 3.5.3) has been added. The data, anaylsis, and conclusion are the same as in Newman et al. (2021).

3.1 Introduction

The analysis and interpretation of NGC 3227 observations have been performed by various authors throughout the years. Earlier X-ray observations from the Advanced Satellite for Cosmology and Astrophysics (ASCA) taken in 1993 and 1995 and those by Röntgen Satellite (ROSAT) in 1993 gave evidence supporting the presence of both warm and neutral absorbers (George et al. 1998; Komossa & Fink 1997; Netzer et al. 1994; Ptak et al. 1994). In the optical range the Hα/Hβ ratio for both broad and narrow lines shows a degree of reddening consistent with the presence of dust (Cohen 1983; González-Delgado & Pérez 1997; Komossa 2002; Mundell et al. 1995; Rubin & Ford 1968; Shull & van Steenberg 1985; Winge et al. 1995). Komossa & Fink (1997) suggested the dust was part of the warm absorber similar to the concept of a "dusty warm absorber" of IRAS 13349+2438 presented by Brandt et al. (1996). Kraemer et al. (2000) proposed that the warm absorber was too highly ionized

to contain the dust. These authors suggested instead the presence of a second warm absorber at low ionization. The presence of this additional absorber was later supported by a Hubble Space Telescope (HST)-STIS observation which detected intermediately ionized C, N, and Si in the optical/UV band (Crenshaw et al. 2001).

More recently, XMM-Newton observed NGC 3227 for 40 ks in 2000 and 108 ks in 2006. Subsequently, Suzaku observed this source six times with about a week between observations in 2008. Gondoin et al. (2003) gave a model for the 2000 XMM-Newton observation with power law continuum emission absorbed by a fully covering neutral absorber, a partially covering neutral absorber, and a fully covering warm absorber. A Gaussian emission line to model the Fe Kα line and an absorption edge around 7.6 keV for the Fe absorption edge were also added. Markowitz et al. (2009) presented a model for the 2006 XMM-Newton observation of this source. It consists of a flatter primary hard power law emission with neutral absorption and an additional steeper power law soft excess. Two zones of fully covering warm absorbers were applied to both. They also included Fe Kα emission and an Fe absorption edge, as well as several emission lines. Noda et al. (2014) proposed a model for the six Suzaku observations. In their model, the primary continuum emission consists of two power law components with different slopes; one steep with $\Gamma \sim 2.3$ and another flatter with $\Gamma \sim 1.6$ in the 2 - 50 keV band with no soft excess. The flat power law component is more absorbed while the steeper component is less absorbed. Among the six observations, the first is in a bright state while the rest are in the dim state. The flatter power law component appears in both dim and bright states while the steep power law appears and dominates in the bright state. These authors interpret this behavior as a phase transition from a dim state to a bright state which involves a change from flatter to steeper power law due to increased accretion rates, analogous to the stellar mass black hole case.

The models presented for the two XMM-Newton observations are somewhat different but they are still consistent with each other, noting that the source was in significantly

different states. During the 2000 XMM-Newton observation the source was in a substantially dim state and it is heavily absorbed by dense material in the line of sight. However, during the 2006 XMM-Newton observation the source was in a brighter phase with much less absorption.

On the other hand, we note that the Markowitz et al. (2009) model for the 2006 XMM-Newton observation and the Noda et al. (2014) model for the first of Suzaku observations, although both cases are during a similar bright phase, are very different. For instance, in the bright state the primary hard power law continuum for XMM-Newton (2006) by Markowitz et al. (2009) is flatter while for Suzaku by Noda et al. (2014) it is steep. Moreover the model by Markowitz et al. (2009) has additional soft excess while it is missing in the Noda et al. (2014) case. Two models for similar bright states of the same source are not consistent with each other. Therefore, it will be worthwhile to carry out detailed combined analysis of all observations, two from the XMM-Newton and six from Suzaku, to explore a model for NGC 3227 which will be consistent with multiple observations from different missions combined. That is the main goal of this chapter.

NGC 3227 is an active galactic nucleus situated at RA 10h 23m 30.58s, Dec +10d 51m 4.18s (Anderson & Ulvestad 2005). The galaxy has a redshift of z = 0.00386 and central black hole mass of $M_{bh} = 4.22 \times 10^7 \mathrm{M}_\odot$ (Peterson et al. 2004).

Section 3.2 explains the data reduction and Section 3.3 gives timing analysis. Section 3.4 is devoted to spectral analysis of the Suzaku observations and Section 3.5 presents spectral analysis of the XMM-Newton observations. Alternative ways to model the soft excess emission seen in Sections 3.4 and 3.5 are explored in Section 3.6. Model parameter and luminosity trends are discussed in Section 3.7. Section 3.8 gives discussions where a unified model is constructed based on the analysis and its comparison with other major earlier proposed models. Summary and concluding remarks are given in Section 3.9. Tables and Figures are displayed at the end of the chapter.

3.2 Observations and Data Reduction

Two XMM-Newton observations were taken six years apart in 2000 and 2006. Eight Suzaku observations were taken in 2008 with about one week in between each observation. Summary of observation start times, end times, and usable exposure times are given in Table 3.1 for both Suzaku and XMM-Newton.

The range of 0.3 - 10 keV was used for the European Photon Imaging Camera (EPIC) pn for the XMM-Newton observations. The Metal Oxide Semi-conductor (MOS) cameras were not used as this dissertation focuses on the pn camera. For Suzaku, the 0.5 - 10 keV range was used for the X-ray Imaging Spectrometer (XIS) cameras and the 15 - 50 keV range for the Hard X-ray Detector (HXD)-PIN. For the pn and XIS cameras the 1.7 - 2.1 keV range was omitted due to calibration uncertainties. All spectra were analyzed using XSPEC version 12.9.0i (Arnaud 1996).

All Observational Data Files (ODF) were downloaded using the w3browse HEASARC tool from the NASA website. The observations are numbered in sequential order based on the date of observation. Furthermore, an "X" prefix is used if observed by XMM-Newton or an "S" prefix if performed by Suzaku (e.g., X1, S3 etc.). XMM-Newton ODF data were processed using the xmmextractor command as included in Scientific Analysis System (SAS) version 16.0.0. Suzaku data were processed using XSELECT version 2.4c. Non X-ray background files were taken from the HXD-PIN tuned non X-ray background database from the NASA website. All Suzaku extraction regions were a circle of 130" for the source and an annulus of inner radius 200" and outer radius of 300" for the background. The first XMM-Newton observation (X1) used a circular region of 40" for the source and an annulus of inner radius of 60" and outer radius of 82.46" for the background, while the second observation (X2) used a source circle of 40" and a background annulus with inner and outer radii of 60" and 96.01" respectively.

In order to simultaneously use the XIS and HXD-PIN data, a calibration constant is needed. This constant is obtained by using the method described in Walton et al. (2013) and the X-ray Telescope (XRT) response given by Maeda et al. (2008). The XIS-PIN calibration constant is a multiple of the XIS1-XIS03 calibration constant and 1.16. The XIS1-XIS03 calibration constant is found by fitting a galactic absorbed broken power law to each Suzaku observation. The regions 1.7 - 2.4 keV and 4 - 7 keV are ignored to remove calibration uncertainties and Fe contamination respectively. A constant is multiplied by the model. All parameters between XIS0 & 3 and XIS1 are tied with the exception of the constant. After fitting, the value of the XIS1 constant is the XIS1-XIS03 calibration constant.

Our models adopt $H_o = 70, q_o = 0.0$, and $\Lambda_o = 0.73$. For the Suzaku observations the XIS0 and XIS3 data sets are combined as both are front illuminated. In each model all components are attenuated with a neutral hydrogen column density of $N_H = 1.99 \times 10^{20}$ cm^{-2} reported by the Galactic Column Density HEASARC tool (Angelini & Sabol 2021), with data taken from Kalberla et al. (2005). All fit parameters are given in the source rest frame and errors are reported at the 90% confidence level ($\Delta\chi^2 = 2.7$) unless otherwise stated.

3.3 Timing Analysis

3.3.1 Light Curves

Initially, we extracted the light curves of all observations. Figures 3.1, 3.2, 3.3, 3.4, 3.5, and 3.6 show the light curves for the Suzaku observations using all 3 XIS cameras in sequencial order. Figures 3.7 and 3.8 display the XMM-Newton pn camera light curves for X1 and X2 respectively. The Suzaku light curves used 0.5 - 10 keV while the XMM-Newton light curves used 0.3 - 10 keV. Both Suzaku and XMM-Newton light curves exhibit similar characteristics. The variability increases with flux intensity. In the lowest flux states (S4 and X1) light curves are nearly flat with little variability. In low but slightly brighter states

(S2, S5, and S6) the fluxes show some variability. The moderate flux state (S3) shows significant changes in count rates. Both of the highest flux states S1 and X2 are highly variable. Furthermore, the later half of S1 exhibits higher flux and variability within the observation. The two highest states S1 and X2 are variable enough to perform time-resolved analysis (see Chapter 5). Note that both XMM-Newton observations exhibited a similar intensity of variability ($\sim 30\%$) despite having significantly different fluxes.

3.3.2 Flux-Flux Plot

After extracting light curves of the data, we formed flux-flux plots for the source in order to examine spectral characteristics of the soft and hard bands. The 0.5 - 2 keV range is used for the soft band and 2 - 10 keV for the hard band. The vertical and horizontal axes are flux of the hard and soft bands respectively. The flux-flux plot for Suzaku was formed by summing data from all three XIS detectors while the flux-flux plot for XMM-Newton was created using the pn camera. The flux-flux plots are displayed in Figures 3.9 and 3.10 for Suzaku and XMM-Newton, respectively.

The flux-flux plot for Suzaku shows two distinct branches. The left branch (dim branch) has a steeper slope and shows the source in a low flux state. In the right branch (bright branch), the count rates of the soft band start to show a larger increase than the hard band. The transition between the two branches occurs between 0.6 - 1.8 counts s^{-1} for the soft band and 2.2 - 3.1 counts s^{-1} for the hard band. The only two observations that encounter this transition are S1 and S3. With further increase in intensity the source enters the bright branch which corresponds to a high flux state. This branch has a flatter slope than the dim branch.

With only two observations, XMM-Newton was unable to observe the transition phase. However, it was able to see the source in its dim state during X1 and in its bright state during X2. The results are consistent with the Suzaku flux-flux plots. The dim state showed

a steeper slope while the bright state had a more gradual trend.

The property and implication of these distinct two branches will be further examined and discussed in Sections 3.4 and 3.8. Note that both of the observations that showed high temporal variability, S1 and X2, spent most or all of their time in the bright state. The slope flattening in the bright branch suggests an excess of emission in the soft band. This soft excess emission is highly variable. This highly variable soft excess emission will be examined further in Chapter 5 where the time-resolved analysis will be applied.

3.4 Suzaku Spectral Analysis

Spectral analysis was performed with the six Suzaku observations obtained by the three functional XIS cameras as well as the HXD-PIN. First, the 2.1 - 10 keV range of the XIS was considered and a model fit of that range was made. Then, the 15 - 50 keV HXD-PIN data were added. Once an acceptable fit for the 2.1 - 50 keV range was achieved, this model was extended down to 0.5 keV to form our final best fit broadband model. As a measurement of goodness of fit, we used the χ^2 test included in XSPEC. The χ^2 value is a measurement of how well the model fits the data is and given by Equation 3.1.

$$\chi^2 = \sum_{i=1}^{n} \frac{(y_i - m_i)^2}{\sigma_i^2} \tag{3.1}$$

Where χ^2 is the fit statistic, y_i is the observed value of data point i, m_i is the value of data point i predicted by the model, and σ_i is the error of data point i. Negative changes in this value ($\Delta\chi^2$) are an improvement to the fit. The degrees of freedom (DOF) are also listed, which is the number of spectral bins minus the number of parameters (Arnaud 2018). For the XSPEC program, goodness of fit is determined by χ^2/DOF and its associated p-value. Ideally, the χ^2/DOF is as close to 1 as possible. A p-value is our ability to reject the null hypothesis and is also reported by XSPEC. The smaller the p-value, the stronger the

evidence for rejection. For XSPEC, the null hypothesis is the probability of the observed data being drawn from the model. Since this allows the model to recreate the data, a higher p-value ($p \geq 0.05$) is favorable.

3.4.1 Suzaku 2.1 - 50 keV Band Analysis

The spectral fits were started with the S1 data between 2.1 and 10 keV and the residual of the data from the model for S1 is plotted in Figure 3.11. Assumed model is the simple redshifted power law (model "zpowerlw") to the 2.1 - 10 keV spectrum. The model parameters are the photon index Γ and the normalization (total photons keV^{-1} cm^{-2} s^{-1}). Galactic absorption (model "phabs") is applied to the power law. The "phabs" model is a cloud of neutral material fully obscuring the line of sight and is included to account for gas and dust within our own galaxy. The only parameter is the column density of the cloud. Note that all models except this galactic absorption were redshifted to the value ($z = 0.00386$) of NGC 3227. This showed significant residuals around 6.4 keV and below 3 keV (see Figure 3.11a).

The residuals below 3 keV are consistent with absorption. The model that most successfully dealt with the residuals below 3 keV was "zxipcf", an ionized partial covering model. The model parameters are the column density, ionization parameter (ξ) of the material, and the covering fraction (see Figure 3.11b). The ionization parameter is defined by Equation 3.2.

$$\xi = \frac{L}{nr^2} \tag{3.2}$$

Where L is the integrated incident luminosity, n is the density of the material, and r is the distance of the material from the illuminating source (Done et al. 1992). The covering fraction ($0 \leq f \leq 1$) represents the portion of the line of sight that is obscured by the material. The remainder $(1 - f)$ of the emission is not absorbed by this model.

The 6.4 keV residuals were assumed to be Fe Kα emission. These were modeled with a redshifted gaussian model ("zgauss"). The model parameters are the gaussian line energy, the line width, and the normalization (total photons $cm^{-2}s^{-1}$). In this manner, the best model in the 2.1 - 10 keV band was formed (see Figure 3.11c).

Afterwards, the 15 - 50 keV HXD-PIN data were included with the appropriate calibration constant (model "constant"). Refer to Section 3.2 as to the method for creating this calibration constant. Since the residuals to the HXD data suggested a reflection component, an accretion disk reflection model ("Xillver" Garcia et al. (2013)) was added (see Figure 3.12). This model gives both the primary hard power law (replacing the "zpowerlw" model) as well as reflection of that power law off of the accretion disk. As the Fe Kα line is reflection based, the reflection portion of this model accounts for it. The model parameters are the photon index, Fe abundance, high energy cutoff, ionization parameter, inclination, reflection fraction, and the normalization. The photon index Γ is the power law of the incident spectrum. The Fe abundance is the ratio of Fe in the disc compared to Solar abundace. We set this value to 1. The high energy cutoff $20 < E_{cut} < 300$ is the energy at which the power law stops in keV. The ionization parameter ξ is equal to the ionization parameter defined given by Equation 3.2 with an assumed density $n = 10^{15}$ cm^{-3}. The inclination is the viewing angle with respect to the disk's normal and is set to 60° for this work since NGC 3227 is a Seyfert 1.5 galaxy. Reflection fraction is defined in the frame of the source as the ratio of coronal intensity illuminating the disk to the coronal intensity that reaches the observer (Dauser et al. 2016; Garcia et al. 2013). Similar to the power law model, the normalization is total photons keV^{-1} $cm^{-2}s^{-1}$ and evaluated at 1 keV.

After adding Xillver, some small residuals persisted around 7 keV. To model them an absorption edge (model "zedge") at 7.11 keV was added, which is the location of the Fe K edge. The model parameters are the energy at which the absorption is strongest (7.11 keV in this case) and the depth. The depth (τ) is the strength of the absorption. There

existed a narrow absorption residual at ∼7 keV which was modeled by an inverse gaussian for $\Delta\chi^2 = -25.14$ for 4 DOF. This is most likely systemic error as it was not seen in most other observations. A similar residual was found in S5 but was not as strong. It is most likely due to Xillver overestimating Fe contribution at this energy. In this way, the best fit 2.1 - 50 keV model was acquired.

The same procedure was applied to all data from the six Suzkau observations and similar results were obtained. Furthermore, in S4 the Fe Kα line was broader than the Xillver parameters anticipated. An additional gaussian at 6.4 keV fit the residual with $\Delta\chi^2 = -30.24$ for 3 DOF.

3.4.2 Suzaku Phenomenological Broad Band 0.5 - 50 keV Analysis

To model the full 0.5 - 50 keV broad band data, the 2.1 - 50 keV band model obtained in Section 3.4.1 was extended down to 0.5 keV. The 1.7 - 2.1 keV band was omitted due to calibration uncertainties. On the lower energy side the residuals showed a large trench centered near 0.9 keV consistent with warm absorption. Other work such as Komossa & Fink (1997) have also found evidence for warm absorption. For our warm absorber, we used an XSTAR table (XSTAR v2.39 Kallman (2021)). For all XSTAR tables, an α parameter was used which is equivalent to the hard X-ray power law index. Most other parameters using the "xstar2xspec" command were left as the default values including the velocity (v_{turb} = 300 km s^{-1}). The range of allowed column densities was expanded as needed. Though one fully covering warm absorber was applied to the data, significant residuals still remained. The second warm absorber at higher ionization was added. The parameters of the high ionization warm absorber were less constrained. Although less significant than the low ionization warm absorber, this second warm absorber was necessary to properly model S1. Other observations did not strictly require the high ionization warm absorber for an acceptable fit but were improved by including it. The one exception was S4 which did not

require a second warm absorber. A single warm absorber was sufficient to form an acceptable fit and attempting to force a second warm absorber only worsened the fit. Henceforth, all references to the high ionization warm absorber and low ionzation warm absorber refer to these two fully covering zones instead of the partially covering absorber. In addition, the low ionization and high ionization warm absorbers will occasionally be referred to as LIWA and HIWA respectively.

In the brightest state (S1) this model underestimated the 0.5 - 1.4 keV range. Therefore, a power law was added to model the extra soft emission. This soft power law is much steeper ($\Gamma_{Soft} = 3.31^{+0.11}_{-0.11}$) than the hard power law contained within the Xillver parameters. In other observations the additional soft excess features were absent.

With the warm absorbers added there now existed positive residuals around 0.58 keV in S3, S4, S5 and S6, which are consistent with an O VII line. A gaussian emission feature was introduced with energy at 0.58 keV and narrow width ($\sigma = 10^{-5}$) to model this. All gaussian emission lines below 2 keV remove 2 DOF. This improved the fit by $\Delta\chi^2 = -15.86$ for S3, $\Delta\chi^2 = -4.18$ for S4, $\Delta\chi^2 = -7.6$ for S5, and $\Delta\chi^2 = -9.38$ for S6. Note that the O VII line was detected by XIS1 only. This is because XIS1 is more sensitive to softer X-rays compared to XIS0 & 3. All other emission lines were also modeled with thin redshifted gaussians. In S3, S4, and S5 there were residuals around 0.9 keV which is consistent with a Ne IX line. Adding a gaussian fixed at 0.922 keV improved the fit by $\Delta\chi^2 = -12.83$ for S3, $\Delta\chi^2 = -11.92$ for S4, and $\Delta\chi^2 = -32.95$ for S5. In S4 there existed emission residuals around 1.02 keV which are consistent with a Ne X line. This was modeled with a gaussian fixed at 1.022 keV, which improved the fit by $\Delta\chi^2 = -10.38$. Note that this may be systemic as we did not detect this line in other observations. However, Ne X absorption at this energy appeared in the Reflection Grating Spectrometer (RGS) analysis of X2 performed by Markowitz et al. (2009) (see their Section 5) as well as our own (see Section 3.5.3) suggesting presence of this Ne species. Emission from O VII and Ne IX were detected during the Turner et al. (2018)

RGS analysis of this source. Markowitz et al. (2009) also detected absorption from those same three species. Ne IX and Ne X emission are often associated with starburst activity in galaxies. Starburst activity was found by Rodrìguez-Ardila & Viegas (2003) as well as Davies et al. (2006) and evidenced by the detection of the 3.3 μm Polycyclic Aromatic Hydrocarbon feature by Imanishi (2002). Thus, we consider starburst activity to be the source of this Ne emission in NGC 3227. We note that S1 did not detect any of the lines. This is most likely because the soft excess emission has outshined the lines and made them not visible. Including these lines in S2 did not have a meaningful effect on the fit (combined Ne IX and O VII $\Delta\chi^2 = -0.3$) and were omitted from the model. Emission line energies were verified using the online atomic database AtomDB version 3.0.9.

As an alternative to using gaussian emission lines we considered utilizing the "mekal" model (Liedahl et al. 1995; Mewe et al. 1985, 1986). While a plasma temperature of ∼700-1000 eV gave respectable fits they were worse than using individual emission lines for the Suzaku observations. For X1, it signficantly worsened the fit with $\Delta\chi^2 = +48.03$. For this reason we have chosen to use emission lines.

The 0.5 - 50 keV broad band spectral models thus obtained for observations S1 to S6 are displayed in Figures 3.13, 3.14, 3.15, 3.16, 3.17, and 3.18. Model parameters are listed in Table 3.2. In addition to χ^2/DOF, the p-values for the fits are listed.

3.5 XMM-Newton Spectral Analysis

The EPIC pn spectra of two XMM-Newton observations X1 and X2 were analyzed by using XSPEC. As with Suzaku, both cases included galactic hydrogen column density. In both observations, initially an acceptable model was fitted to the 2.1 - 10 keV data, and then it was extended to the band of 0.3 - 10 keV and modified to achieve a good fit.

Analysis of the RGS data from XMM-Newton X2 observation has been performed thoroughly by Markowitz et al. (2009) and as such our own analysis was simpler (see Section

3.5.3). They found evidence supporting the existence of two separate warm absorbers and details of their analysis are contained within Markowitz et al. (2009) Section 5. The X1 observation took place during a dim state and hence the data were not good enough for RGS analysis.

3.5.1 XMM-Newton 2.1 - 10 keV Band Analysis

First attempt for a single power law model fit to the X1 data did not provide a good fit with residuals across the majority of the band, while the power law provided a decent fit to X2 except for residuals around the Fe line. To keep consistency with the Suzaku observations the power law model was replaced with the Xillver model, which includes the Fe Kα line and reflection features.

At this point X1 still had significant residuals below 4 keV and required some absorption feature. These residuals were reduced by an ionized partial covering model as was found in Suzaku spectral analysis. On the other hand, the X2 spectrum was reasonably well fitted with just the photo-absorbed Xillver model. Partial covering model required a covering fraction > 0.95, so a fully covering neutral absorber model ("zphabs") was introduced instead. This is the redshifted version of the "phabs" model and thus the only parameter is the column density. Using an ionized absorber instead worsened the fit.

3.5.2 XMM-Newton Phenomenological Broad Band 0.3 - 10 keV Analysis

After obtaining the 2.1 - 10 keV band best fit model it was extended to the broader 0.3 - 10 keV band. The 1.7 - 2.1 keV band was omitted due to calibration uncertainties. For X1, the negative residuals in the soft band were consistent with the warm absorbers (Komossa & Fink 1997). After applying the low ionization warm absorber emission residuals remained near 0.42 keV. This energy is consistent with a N VI emission line. A narrow gaussian fixed at 0.42 keV provided a good fit by $\Delta\chi^2 = -94.94$. There remained residuals around 0.9 keV, and thus a 0.922 keV (Ne IX) gaussian was added which improved the fit by $\Delta\chi^2 = -14.97$.

For observation X2, distinct positive residuals were found below 1.7 keV, which suggested a second continuum power law to model this excess soft X-ray emission as was seen for S1. Additional second power law of index $\Gamma_{Soft} = 3.83^{+0.02}_{-0.02}$ significantly improved the fit. Since the residuals seemed to be consistent with warm absorption, two zones of warm absorber model were applied. With this change most of the residuals had dropped to an acceptable level. There remained emission residuals near 0.58 keV and absorption residuals around 0.74 keV. The 0.58 keV residual is most likely O VII emission and was also detected by Markowitz et al. (2009). This was modeled with a gaussian which improved the fit by $\Delta\chi^2 = -62.2$. Compared to Suzaku's XIS cameras, the pn has better spectral resolution at this energy which is why it was able to detect this line while S1 could not. Attempting to force this line into X1 significantly worsened the fit ($\Delta\chi^2 = +40.98$). The 0.74 keV absorption feature was modeled with a redshifted absorption edge and is consistent with O VII edge absorption and possibly the Fe unresolved transition array (UTA) (Markowitz et al. 2009; Sako et al. 2001). This is most likely part of the warm absorbers and its inclusion improved the fit by $\Delta\chi^2 = -473.32$ for 2 DOF.

Modeled spectra are shown in Figures 3.19 and 3.20 for X1 and for X2 respectively. Model parameters are listed in Table 3.3.

3.5.3 XMM-Newton RGS Analysis of X2

To observe the composition of the warm absorbers we analyzed the 0.3 - 2 keV data from the two Reflection Grating Spectrometer instruments (RGS1 and RGS2) onboard XMM-Newton. To begin, we fit a simple power law over the two spectra and applied gaussian absorber models (model "gabs") in order to locate absorption lines. We detected C VI Lyα (368 eV), C VI Lyβ (436 eV), N VII (500 eV), O VII (0.574), O VIII Lyα (653 eV), Fe XVIII (853 eV), Ne IX Lyα (905 eV), Ne IX (922 eV), Ne X (1022 eV), and Mg XI (1352 eV).

Afterwards, we abandoned the simple model and proceeded to fit the RGS spectrum using the model described in Section 3.5.2. All parameters between the two RGS spectra were tied except for their normalizations. Since data above 2 keV were critical to fitting the Xillver parameters, we fixed those parameters to the values of the best fit pn model. All other parameters were initially allowed to vary. The 0.58 keV O VII line was not apparent, but a sharp emission feature at 0.5 keV appeared. This is the location of the N VII line and its inclusion improved the fit by $\Delta\chi^2 = -74.02$. Since this line appeared as an absorption feature previously, it is likely that our warm absorber models have overestimated the amount of N VII absorption at this energy. The spectra proved largely insensitive to the high ionization warm absorber, so its parameters were also tied to the best fit pn model. The best fit to the RGS spectra was rougher than the pn best fit with $\chi^2/\mathrm{DOF} = 3767.08/2923$. Model parameters are displayed in Table 3.4. The soft X-ray power law had a higher best fit value of $4.01^{+0.14}_{-0.14}$ but the lower end of the error bars is close to the best fit pn model. The densities of both the neutral absorption and low ionization warm absorber were somewhat lower while the ionization parameter was higher. In addition, the optical depth of the absorption edge was stronger. Overall, the results are consistent with the 0.3 - 10 keV pn best fit. The differences in parameter values can be explained by the RGS being a different instrument than the pn. As a result, we are confident in our use of warm absorbers in our Suzaku and XMM-Newton models. The model and detected absorption lines are displayed in Figure 3.21.

3.6 Alternative Models for Soft Excess

Extra soft excess emission appears only during the S1 and X2 observations. In Sections 3.4.2 and 3.5.2 it was shown that a steep power law (steeper than the primary power law in the higher energy bands) adequately explains the data. Here, additional alternative possible models for this soft excess are considered: blackbody, warm comptonization, thermal

bremmstralung, and ionized reflection.

The redshifted blackbody (BB) model "zbbody" has two parameters: peak blackbody temperature (kT) and normalization given by Equation 3.3.

$$Norm._{bb} = \frac{L_{39}}{D_{10}(1+z)^2} \tag{3.3}$$

Where L_{39} is luminosity in 10^{39} ergs s^{-1}, D_{10} is distance in 10 kpc, and z is the redshift. This produced a good fit for S1 with χ^2/DOF = 1807.13/1755 and X2 with χ^2/DOF = 691.98/605. Our best fits give kT = $113.57^{+5.60}_{-5.37}$ eV for S1 and kT = $87.78^{+0.74}_{-0.74}$ eV for X2. These values are too high as a more reasonable temperature is closer to kT = 10 eV (see Bechtold et al. (1987); Gierliński & Done (2004)). We do not consider blackbody to be a physically plausible explanation of the soft excess emission.

Next, a warm Compontization model was considered (model "compST" Sunyaev & Titarchuk (1980)). In this model, the soft X-ray emission is due to Comptonization of seed photons (UV or EUV) emitted by the accretion disk in the warm atmospheres of the inner regions of the disk. The model parameters are temperature (kT), optical depth (τ), and normalization. The mean free path (λ_l) of Compton scattering is given by Equation 3.4.

$$\lambda_l = \frac{1}{n_e \sigma_t} \tag{3.4}$$

For electron number density n_e and Thompson cross section σ_t. The optical depth is defined as the size of the region (l) divided by this value and is given by Equation 3.5.

$$\tau = \frac{l}{\lambda_l} = l n_e \sigma_t \tag{3.5}$$

The normalization is given by Equations 3.6 and 3.7.

$$Norm._{comp} = \frac{Nf}{4\pi d^2} \tag{3.6}$$

Where N is the total number of photons from the source, d is the distance from the source, and f is the factor given by Equation 3.7.

$$f = \frac{\alpha(\alpha+3)y^2\Gamma(\alpha)}{\Gamma(2\alpha+4)} \tag{3.7}$$

Where α is the spectral index, y is the injected photon energy in units of temperature, and Γ is the incomplete gamma function.

This model shows a good fit for S1 with χ^2/DOF = 1813.98/1754 and an acceptable fit with χ^2/DOF = 670.14/602 for X2. The fit parameters were $\tau = 22.67^{+0.19}_{-0.75}$, kT = $363.50^{+14.72}_{-13.96}$ eV for S1 and $\tau = 14.92^{+0.09}_{-0.09}$, kT = $479.77^{+4.31}_{-4.28}$ eV for X2.

Then, a redshifted bremsstrahlung model ("zbremss", Karzas & Latter (1961); Kellogg et al. (1975)) was applied to the data. The model parameters are the plasma temperature (kT) and the normalization. The normalization is given by Equation 3.8.

$$Norm._{bremss} = \frac{3.02 \times 10^{-15}}{4\pi D^2} \int n_e n_i \, dV \tag{3.8}$$

Where D is the distance to the source, n_e is the electron number density, and n_i is the ion number density.

A good fit was obtained (with χ^2/DOF = 1810.62/1755) for S1 but not for X2 (χ^2/DOF = 791.49/623). We do not consider this model further.

Finally, an ionized relativistic reflection (IRR) model (model "reflionx" Ross & Fabian (2005); Ross et al. (1999)) blurred in the Laor model shape (model "kdblur" Laor (1991)) was considered. The reflionx parameters were the Fe abundance, illuminating photon index, ionization parameter, and normalization. The Fe abundance was set to solar, the illuminating

photon index (Γ_{Hard}) was tied to the same value given by Xillver, the ionization parameter (ξ) is given by Equation 3.2, and the normalization is total photons keV^{-1} cm^{-2} s^{-1} evaluated at 1 keV. For kdblur, the parameters are the index (I), the inner and outer radii of the disc (R_{in} and R_{out} respectively), and the inclination. The index is the power law dependance of emissivity and was set to 3 for our models. We adopted radii of $R_{in} = 1.5$ and $R_{out} = 300$ in units of gravitational radii. Similar to Xillver, the inclination was set to 60°. A good fit for S1 was obtained with χ^2/DOF = 1800.40/1756, but it was not acceptable for X2 with χ^2/DOF = 1604.85/604.

With these results it appears that warm Comptonization is acceptable as an alternative option despite the p-values for X2 being inferior to the two power law model. Model parameters are displayed in Table 3.5 for S1 and Table 3.6 for X2.

3.7 Luminosity and Model Parameter Relation

Once the broadband models for all of the observations were formed, analysis was carried out on how model parameters changed with the intrinsic luminosity of the source. Intrinsic luminosity was estimated using the unabsorbed 0.5 - 10 keV luminosity reported by the XSPEC "lumin" command. Henceforth, all references to luminosity refer to the intrinsic luminosity.

A Spearman's rank correlation was applied to the parameters. To define Spearman's rank correlation, we must first define the Pearson correlation coefficient. The Pearson correlation coefficient (r_p) is defined as the covarience of two variables (X and Y) divided by the multiple of their standard deviations (σ_x and σ_y respectively). It is a parametric measure of the linear correlation between the two variables and is given by Equation 3.9 (Pearson 1895).

$$r_p = \frac{cov(X,Y)}{\sigma_x \sigma_y} \tag{3.9}$$

To form the Spearman's rank correlation (ρ), we must first rank the data points. This is a simple task. For example, if we had ten data points the highest value would be rank 1 and the lowest rank 10. An important note is that if there are duplicate values each will have the same rank which is equidistant between the integer ranks. For example, if two values are the same and would take ranks 5 and 6, each value would have rank 5.5. Spearman's rank correlation is a version of the Pearson correlation coefficient applied to ranked values and is defined by Equation 3.10 (Spearman 1904)

$$\rho = \frac{cov(R(X), R(Y))}{\sigma_{R(x)} \sigma_{R(y)}} \tag{3.10}$$

for ranked values R(X) and R(Y) and their standard deviations $\sigma_{R(x)}$ and $\sigma_{R(y)}$. The benefit to using Spearman's rank correlation in this context is that it is nonparametric and measures how well the variables can be described using a monotonic function which makes it more flexible. The ρ and corresponding p-value are displayed in Table 3.7. The emission line intensity did not show any clear correlation with luminosity.

Here we would like to present how some parameters behave with luminosity. The hard photon index (Figure 3.22) displayed a weak (ρ = 0.431) correlation with luminosity. On average, the higher luminosity states had a higher index than the lower ones, although S1 had a markedly low index for its luminosity. Figure 3.23 displays the reflection fraction against luminosity. There is a generally strong (ρ = -0.810) negative trend implying reflection is a stronger component for the lower luminosity observations. Since high reflection fraction yeilds a broader Fe Kα line, this may be due to the X-ray Baldwin effect (Iwasawa & Taniguchi 1993). That paper shows that the equivalent width of the Fe Kα line decreases with increasing luminosity (see their Figure 1). Noting that NGC 3227 was one of the sources

Iwasawa & Taniguchi (1993) used to present this correlation (see their Table 1a), we consider this to be an explanation of the reflection fraction trend.

Figures 3.24 - 3.26 plot components of the ionized partial covering model against luminosity for the Suzaku observations. In general, Markowitz et al. (2009) in their warm absorber analysis report that from their velocity data the high and low ionization warm absorber clouds are located at around the broad line region (BLR) and narrow line region (NLR). Cold absorbers are expected to be further away. Therefore, it is unlikely that the partially covering clouds have changed significantly over the six Suzaku observation periods which were taken only within several weeks span. On the other hand, XMM-Newton observations were taken a few years apart from each other and the Suzaku observations, which is enough time for absorption features to change. For this reason X1 is absent from Figure 3.24 - 3.26. X2 is absent from those Figures as it did not use a partial covering model.

In Figure 3.24 partial covering fraction is plotted against luminosity. The fraction seems to be similar and higher among five Suzaku observations S2 - S6 in the lower flux phase, while it is very low for S1 in the bright phase. A very weak (ρ = -0.21) negative trend may be present. The column density of the Suzaku observations showed a strong negative correlation (ρ = -0.943) with the luminosity which is shown in Figure 3.25. The same treatment was applied to the ionization parameter of the partial coverer (Figure 3.26) but no trend was visible (ρ = -0.116). These Suzaku trends will be discussed further in Section 3.8.1.

Figures 3.27 - 3.30 display the parameters of the warm absorbers (column density and ionization parameter) against luminosity. The column density of the low ionization warm absorber (Figure 3.27) showed a positive correlation (ρ = 0.786) with luminosity. However, the ionization parameter of that absorber (Figure 3.28) did not (ρ = 0). A similar result was obtained for the high ionization warm absorber, with a positive trend on the column density (ρ = 0.821, Figure 3.29) and no correlation with the ionization parameter (ρ = 0, Figure 3.30).

3.8 Discussion

3.8.1 The Unified Model

Referring to the flux-flux plots in Section 3.3.2 (Figures 3.9 and 3.10) the lower flux states show a steep slope for our chosen bands while high flux states show a more gradual slope. Note that only S1 and X2 are in the bright branch where soft excess is dominant. As the hard band (2 - 10 keV) increases to about twice as high, the soft band (0.5 - 2 keV) goes up about five times as high (see Figure 3.9). The best fit spectral models achieved in Sections 3.4.2 and 3.5.2 indicate that only S1 and X2 have soft excess, which is consistent with our flux-flux analysis.

Based on these results we propose a unified model which is consistent with all eight observations by the two satellite missions. In this model in the lower states (Suzaku S2 to S6 and XMM-Newton X1) the intrinsic radiation directly from the central power house is the hard power law emission from a hot corona above an accretion disk, which is the conventional Compton model for Seyfert nuclei. This interpretation is consistent with what Yang et al. (2014) found in their studies of correlation between the photon index and X-ray luminosity. Their results show that the photon index increases with luminosity when the X-ray emission comes from the corona in the disk-corona model, and moreover that for fainter objects within this class the power law index can be as low as $\sim$ 1.4 - 1.7 (see their Figure 2). The source NGC 3227 is a relatively low luminosity ($\sim 10^{42}$ ergs s^{-1}) Seyfert where the photon index of the hard X-ray power law emission is rather low, around 1.4 - 1.7.

This hard power law emission continues to the high states (S1 and X2). However, in these high states the total emission is dominated by an additional strong highly variable soft excess. We identify the location of this soft excess emission tentatively as the warm atmospheres of the accretion disk. The data of this component is consistent with an additional steep power law with $\Gamma \sim$ 3.3 - 3.85. The analysis carried out in Section 3.6

shows that the warm Compton model is consistent with the data. Using the time scale of time variability to estimate the size of the emission region, we calculate the size as $\leq 10^{15}$ cm ($80R_g$). In this scenario the soft excess is caused by Comptonization of photons in the warm atmospheres of the accretion disk closer to the center of the disk. The energy for the atmosphere electrons is possibly sourced by magnetic effects in a thin layer on the surface of the accretion disk (Zhong & Jiancheng 2013). Magnetic microflares could also play a roll in the soft excess emission, but work adapting them to the AGN environment has not been carried out.

These primary continuum emissions from the central power house are absorbed by various cold and warm materials further out in the line of sight. There is also an additional reflection component as evidenced by the narrow Fe Kα emission. Consider the relationship between the behavior of partially covering absorbers and luminosity found for the Suzaku observations in Section 3.7 (see Figures 3.24 and 3.25). The column density of the partially covering absorber generally decreased with luminosity (see Figure 3.25). Furthermore, the brightest state (S1) has a significantly lower covering fraction than in the lower states (see Figure 3.24). The partially covering absorber and fully covering neutral absorber (X2) should be located further away than fully covering ionized absorbers which were found to be located at least as far away as the BLR while some are in the NLR, from the velocity data noted in Markowitz et al. (2009). As there are years between the individual XMM-Newton observations and Suzaku observations, the partial covering absorber can be different for X1 and the Suzaku observations and different than the neutral absorber for X2. A timescale of years is enough time for the clouds to drift out of line of sight. However, there is only about a week between individual Suzaku observations, and thus the same partial covering absorber is most likely obscuring the central emissions during the six Suzaku observations.

Therefore, we offer the following explanation. The size of the emission region increases with luminosity in a similar way as described by Haba et al. (2008) for NGC 4051. In this

scenario, the partially covering cloud is lumpy and moreover denser near the center above the primary emission region. Due to this, the lowest flux observation (S4) when the primary emission region is small requires both a high covering fraction and high column density as found. As the source becomes brighter, the size of the emission region increases. The emission region is still obscured but the outer parts of it are absorbed by a less dense portion of the outer parts of the clouds. This can still yield a relatively high covering fraction (e.g. S3) but should yield a lower average column density (both S3 and S1) than S4. In the highest luminosity state (S1), the outermost parts of the emission site has become so extended that they are hardly obscured by the cloud. The part of the emission region that is still obscured is mostly covered by the lower density outer regions of the absorber. This yields a low covering fraction and a low column density for the absorber in S1. In this model, the size of the corona where the primary power law is emitted increases with luminosity. That is consistent with other work on the size of the corona by, e.g. Kara et al. (2019).

3.8.2 Comparison With Other Work

Gondoin et al. (2003) analyzed the 2000 XMM-Newton data of NGC 3227. The spectrum above 4 keV is well fitted by a hard power law continuum with $\Gamma \sim 1.5$ and an absorption edge at 7.6 keV. In addition, a narrow Fe K emission line is detected at 6.4 keV. The continuum is heavily absorbed at soft band by dense neutral gas with $N_H = 6.6^{+0.1}_{-0.1} \times 10^{22}$ cm^{-2} covering $\sim 90\%$ of the central source. The soft continuum is also attenuated due to ionized material with $N_H = 8.9^{+0.9}_{-0.9} \times 10^{21}$ cm^{-2}. They also noted variability in the continuum emission with a few ks timescale. Our analysis of this observation (X1) agrees with their results although their warm absorber had a higher density.

Markowitz et al. (2009) presented results of a 2006 XMM-Newton observation of NGC 3227. Their best-fit model to the EPIC pn spectrum consists of a moderately flat hard X-ray power law with Γ of 1.57 absorbed by cold gas with $N_H = 2.9^{+0.3}_{-0.8} \times 10^{21}$ cm^{-2}, and

a strong soft excess with steep power law with Γ of 3.35. Both were absorbed by cold gas with $N_H = 8.7^{+0.6}_{-0.5} \times 10^{20}$ cm^{-2}. The hard X-ray power law was consistent with the standard disk-corona model, although these authors commented that the power law index was rather low. These authors discussed the possible origin of the soft excess, but did not come up with a definite physical model. They find the data to be consistent with the warm Compton model also, but noted that the variability behavior of the soft excess is different from the UV variability. In this model, the UV seed photons coming from regions further away are supposed to be comptonized in the warm atmosphere of the disk closer to the center. They also commented on a possibility of a jet as the origin if this component is steep power law, but then they noted that this source does not have any radio jets.

We carried out independently the analysis of multiple observations by two different missions in the broad energy range from 0.3 to 50 keV, and found a common model which can explain all eight observations in various flux levels. On the other hand, Markowitz et al. (2009), as well as others, studied only one or a limited number of our observation targets. The main focus of our studies is on the central power house itself, while Markowitz et al. (2009) concentrated mostly on the detailed studies of the effects of the surrounding material. Our unified model is consistent mostly with the model by Markowitz et al. (2009), although there are some minor differences. For instance, our results from a rather simple warm absorber model gave somewhat thicker high ionization absorber. As stated in Section 3.4.2 we find that a rather low index value for the hard power law is acceptable. As to the nature of the soft excess Markowitz et al. (2009) did not specify any definite physical model. Our suggestion is that the steep power law could be due to some magnetic activity in the warm atmosphere above the accretion disk. If it is warm Comptonization, our suggestion is that the seed photons could be from the extreme ultraviolet (EUV) region closer to the center than ultraviolet (UV). This interpretation can avoid the conflict with the possible discrepancy between soft excess and UV variability reported by Markowitz et al. (2009).

The major focus of Markowitz et al. (2009) is the detailed analysis of absorbing material, especially the warm absorbers, by utilizing both EPIC and RGS. They found two absorbing layers with similar column densities of $\sim 1 - 2 \times 10^{21}$ cm^{-2} but with different ionization states, one at a high state with $\log(\xi_{hi}) = 2.93^{+0.15}_{-0.09}$ erg cm s^{-1} and another at a low state with $\log(\xi_{lo}) = 1.45^{+0.16}_{-0.07}$ erg cm s^{-1}. The outflow velocities are detected with 2060^{+240}_{-170} km s^{-1} and 420^{+430}_{-190} km s^{-1} for the high and low ionized absorbers, respectively. This information gives the estimated location of the high ionization clouds at the BLR and the NLR for the low ionization clouds.

Noda et al. (2014) studied all six of Suzaku 2008 observations of NGC 3227 in the energy range from 2 - 50 keV. In their model the primary continuum emission in the lower luminosity states S2 to S6 is absorbed flatter power law emissions with $\Gamma \sim 1.6$, while the most luminous state S1 is dominated by less absorbed steeper power law continuum with $\Gamma \sim 2.3$ although a weaker flatter power law still exists. In addition, there is a cold reflection component which is evidenced by the narrow Fe Kα line which appears all through the six observations. Their interpretation is that the source undergoes a low to high state transition similar to the case of stellar mass black holes. In this model, as the accretion rate and hence luminosity increase the disk system physically changes from an optically thin, geometrically thick ion torus to an optically thick, geometrically thin disk with a corona at a critical accretion rate. The observations S2 to S6 in the lower states belong to the torus system while S1 is in a high state with the disk-corona system where the torus still exists but it is greatly diminished only to the central region. The corona emits the steep power law while the torus is responsible for the flatter power law.

The Noda et al. (2014) model is substantially different from our unified model and also the model presented by Markowitz et al. (2009). In the high luminosity state (S1) their primary hard X-ray continuum is dominated by steep power law, but both in the model by Markowitz et al. (2009) and ours in the high state it consists of one flatter power law. The

main reason is that their analysis is confined to the 2 - 50 keV range. However, the effects of warm absorption, various emission features, and soft excess are crucial mostly in the lower bands below 2 keV, and therefore the model obtained by excluding these low energy bands will fail to give a better understanding of the source. When their model was extended to below 2 keV it did not yield acceptable fits in these soft bands.

More recently, NGC 3227 was observed by XMM-Newton and NuSTAR for six times during 2016 Nov. 9 - 2016 Dec. 9 and additionally by NuSTAR on 2017 Jan. 21. Lobban et al. (2020) carried out X-ray variability analysis of the data from these observations, while Turner et al. (2018) concentrated on the last two observations of the 2016 campaign. During all these observations NGC 3227 was in the bright state. Their primary emission is a power law with Γ of 2 in Turner et al. (2018) while 1.4 - 1.7 in Lobban et al. (2020), with a black body (Turner et al. 2018) or Comptonized disk blackbody (Lobban et al. 2020) added as a soft excess. The primary emission model by Lobban et al. (2020) is essentially consistent with our model at the bright state, while the Turner et al. (2018) model is somewhat simpler. Both of these authors agree with our finding on the primary emission from the center: (i) softer when brighter behavior of the power law component, (ii) the bulk of the short variability being continuum driven, and (iii) presence of a strong variable soft excess.

On the other hand, their major focus is the effects of the reprocessing surrounding gas, which is responsible for additional complicated absorption and emission features mostly caused in the BLR but some in the NLR clouds, as well as the neutral reflection from material further away. But some of the reprocessing material are outflow winds from regions closer, e.g., near the accretion disk. Lobban et al. (2020) analyzed all of the XMM-Newton and NuSTAR data from the 2016 campaign. These clouds are mostly observed as outgoing winds. There are three zones for the warm absorbers with different ionization states. These authors found a strong low frequency hard lag and evidence for a soft lag at higher frequencies. They may be considered to arise from outflowing disk winds via energy-dependent scattering.

Turner et al. (2018) mainly investigated the large dip in the light curve exhibited near the end of the 2016 observations, which was also identified by Lobban et al. (2020). It is proposed that this dip is due to a cloud passing through the line of sight in the region near the inner edge of the BLR. In conclusion, these papers concentrated mostly on variability in the order of days which are produced by the clouds further away from the central primary source.

These authors did not discuss the shorter (less than $\sim$ days) variability originating in the central source close to the black hole, while the major focus of our studies, on the other hand, is the central source. However, our current studies of the earlier observations also included the effects of the surrounding absorbing/emitting and reflecting material. The new observations took place much later, $\sim$ 10 years, after the observations treated in the current chapter, but our preliminary study shows that our current model is consistent with the newer observations also. In subsequent chapters we will report in detail our spectral and temporal analysis of the data from these observations.

3.9 Summary and Concluding Remarks

We carried out the time-averaged spectral analysis of the combined data for NGC 3227, from two earlier XMM-Newton and six Suzaku observations. A unified model was constructed which is consistent with all of these observations in a broad energy band from 0.3 - 50 keV. The model consists of the central power house with a hard power law continuum emission and in the brighter phase an additional soft excess, a reflection component, and the system is covered by cold and warm absorbers.

- The primary hard X-ray emission comes from a corona above an accretion disk where softer photons from the colder disk are Comptonized by hot electrons in the hot corona.
- During the bright state an additional soft excess modeled by a steeper power law or warm Comptonization appears. This may occur in the warm atmosphere of the inner

part of the accretion disk and be due to magnetically driven processes or additional warm Comptonization. It dominates behavior below 2 keV. This component is highly variable and its behavior is complex. Therefore, the detailed studies of its behavior, such as its short variability in luminosity and spectra, will be carried out separately in Chapter 5 where time-resolved analysis will be applied.

- The clouds responsible for the ionized partial covering absorption are dense near the center while less dense toward the edges.

- The size of the central emission region increases with luminosity. This causes, during the bright phase, the outer emission region to be obscured by the less dense outer regions of the absorber or obscured hardly at all.

Chapter 3 Tables

Table 3.1: NGC 3227 observation summary: start time (UTC), end time (UTC) and exposure times (ks) are given. For the exposure times XIS and HXD-PIN of Suzaku while the pn for XMM-Newton was used.

Observation	Year	Start Time (UTC)	End Time (UTC)	XIS/pn Exposure Times (ks)	HXD Exposure Times (ks)
703022010 (S1)	2008	Oct. 28 08:12:52	Oct. 29 00:34:49	58.92	48.07
703022020 (S2)	2008	Nov. 4 03:36:31	Nov. 4 18:31:01	53.7	46.74
703022030 (S3)	2008	Nov. 12 02:48:55	Nov 12. 18:31:47	56.57	46.68
703022040 (S4)	2008	Nov. 20 17:00:00	Nov. 21 10:56:08	64.57	43.43
703022050 (S5)	2008	Nov. 27 21:29:20	Nov. 28 19:33:11	79.43	37.42
703022060 (S6)	2008	Dec. 2 14:28:03	Dec. 3 04:44:04	51.41	36.91
0101040301 (X1)	2000	Nov. 28 18:15:41	Nov. 29 05:26:33	27.28	
0400270101 (X2)	2006	Dec. 3 01:53:31	Dec. 4 08:09:51	89.77	

Table 3.2: Suzaku 0.5-50 keV time averaged model parameters.

Component	Parameter	S1	S2	S3	S4	S5	S6
Partial Cov.	N_H $\left(10^{22} cm^{-2}\right)$	$1.70^{+0.08}_{-0.07}$	$12.86^{+0.36}_{-0.36}$	$6.12^{+0.11}_{-0.10}$	$15.66^{+0.64}_{-0.63}$	$8.36^{+0.15}_{-0.09}$	$11.94^{+0.32}_{-0.32}$
	Cov. Frac.	$0.46^{+0.02}_{-0.02}$	$0.81^{+0.01}_{-0.01}$	$0.89^{+0.01}_{-0.01}$	$0.74^{+0.01}_{-0.01}$	$0.88^{+0.01}_{-0.01}$	$0.90^{+0.01}_{-0.01}$
	Log ξ	$0.30^{+0.13}_{-0.20}$	$0.78^{+0.11}_{-0.11}$	$0.60^{+0.05}_{-0.05}$	$0.30^{+0.20}_{-0.10}$	$1.16^{+0.02}_{-0.02}$	$1.07^{+0.03}_{-0.07}$
Xillver[a]	Γ_{Hard}	$1.50^{+0.01}_{-0.01}$	$1.47^{+0.01}_{-0.01}$	$1.69^{+0.01}_{-0.01}$	$1.43^{+0.01}_{-0.01}$	$1.59^{+0.01}_{-0.01}$	$1.52^{+0.01}_{-0.01}$
	Log ξ	$0.70^{+0.04}_{-0.18}$	$1.83^{+0.09}_{-0.06}$	$1.36^{+0.17}_{-0.20}$	$1.65^{+0.09}_{-0.12}$	$1.65^{+0.06}_{-0.09}$	$1.54^{+0.14}_{-0.11}$
	Ref. Frac.	$0.73^{+0.05}_{-0.05}$	$1.53^{+0.11}_{-0.08}$	$1.23^{+0.08}_{-0.07}$	$2.57^{+0.19}_{-0.18}$	$1.22^{+0.07}_{-0.08}$	$0.96^{+0.12}_{-0.08}$
	XIS 03 Norm. $\left(10^{-4}\right)$	$2.06^{+0.01}_{-0.01}$	$1.33^{+0.01}_{-0.01}$	$1.62^{+0.01}_{-0.01}$	$0.69^{+0.01}_{-0.01}$	$1.33^{+0.01}_{-0.01}$	$1.22^{+0.01}_{-0.01}$
	XIS 1 Norm. $\left(10^{-4}\right)$	$1.90^{+0.02}_{-0.02}$	$1.26^{+0.01}_{-0.01}$	$1.37^{+0.01}_{-0.01}$	$0.69^{+0.01}_{-0.01}$	$1.29^{+0.01}_{-0.01}$	$1.17^{+0.01}_{-0.01}$
O VII[b]	XIS 1 Norm. $\left(10^{-4}\right)$			$8.37^{+3.47}_{-3.47}$	$1.46^{+0.97}_{-0.97}$	$3.33^{+2.18}_{-2.18}$	$4.24^{+2.36}_{-2.36}$
Ne IX[b]	XIS 03 Norm. $\left(10^{-5}\right)$			$30.76^{+14.78}_{-17.22}$	< 4.33	$18.41^{+6.86}_{-6.86}$	
	XIS 1 Norm. $\left(10^{-5}\right)$			$31.68^{+14.78}_{-14.78}$	$5.64^{+2.72}_{-2.72}$	$14.61^{+7.90}_{-7.90}$	
Ne X[b]	XIS 03 Norm. $\left(10^{-5}\right)$				$2.65^{+1.78}_{-1.78}$		
	XIS 1 Norm. $\left(10^{-5}\right)$				$2.42^{+1.45}_{-1.45}$		
Fe Edge	Depth	$0.15^{+0.02}_{-0.02}$					
HIWA	N_H $\left(10^{21} cm^{-2}\right)$	$49.08^{+30.04}_{-19.52}$	$11.09^{+2.16}_{-1.72}$	$31.68^{+10.34}_{-12.96}$		$32.98^{+3.09}_{-2.87}$	$28.98^{+21.02}_{-15.70}$
	Log ξ	$2.58^{+0.08}_{-0.08}$	$2.90^{+0.09}_{-0.09}$	$2.93^{+0.09}_{-0.08}$		$2.31^{+0.02}_{-0.02}$	$2.56^{+0.32}_{-0.05}$
LIWA	N_H $\left(10^{21} cm^{-2}\right)$	$6.16^{+0.44}_{-0.42}$	$1.65^{+0.19}_{-0.17}$	$3.94^{+0.21}_{-0.20}$	$1.38^{+0.22}_{-0.19}$	$1.66^{+0.20}_{-0.17}$	$2.60^{+0.29}_{-0.26}$
	Log ξ	$1.47^{+0.04}_{-0.04}$	$1.33^{+0.11}_{-0.12}$	$1.06^{+0.08}_{-0.08}$	$1.25^{+0.13}_{-0.41}$	$0.84^{+0.11}_{-0.11}$	$1.47^{+0.11}_{-0.11}$
Power Law[a]	Γ_{Soft}	$3.31^{+0.11}_{-0.11}$					
	XIS 03 Norm. $\left(10^{-3}\right)$	$1.63^{+0.09}_{-0.09}$					
	XIS 1 Norm. $\left(10^{-3}\right)$	$1.73^{+0.09}_{-0.09}$					
XIS-PIN	Constant	1.154	1.217	1.212	1.206	1.206	1.160
	χ^2/DOF	1807.68/1751	1325.03/1317	243.89/219	163.07/148	1102.49/1033	596.85/562
	P-value	0.1688	0.4329	0.1928	0.1877	0.0655	0.1495

[a]Xillver and power law normalizations are photons $\mathrm{keV}^{-1}\mathrm{cm}^{-2}\mathrm{s}^{-1}$ at 1 keV.

[b]Gaussian normalization is total photons $\mathrm{cm}^{-2}\mathrm{s}^{-1}$ in the line of sight.

Table 3.3: XMM-Newton pn 0.3-10 keV time averaged model parameters.

Component	Parameter	X1	X2
Ionized Partial Covering	N_H $\left(10^{22} cm^{-2}\right)$	$6.30^{+0.17}_{-0.17}$	
	Covering Fraction	$0.94^{+0.01}_{-0.01}$	
	Log ξ	$0.32^{+0.07}_{-0.07}$	
Full Covering Absorption	N_H $\left(10^{20} cm^{-2}\right)$		$10.34^{+0.20}_{-0.20}$
Xillver[a]	Γ_{Hard}	$1.52^{+0.01}_{-0.01}$	$1.56^{+0.01}_{-0.01}$
	Log ξ	$1.30^{+0.06}_{-0.16}$	$0.70^{+0.14}_{-0.14}$
	Reflection Fraction	$1.71^{+0.19}_{-0.16}$	$0.69^{+0.04}_{-0.04}$
	pn Norm. $\left(10^{-5}\right)$	$6.44^{+0.07}_{-0.07}$	$26.74^{+0.05}_{-0.05}$
O VII Emission Line[b]	pn Norm. $\left(10^{-4}\right)$		$3.37^{+0.41}_{-0.41}$
N VI Emission Line[b]	pn Norm. $\left(10^{-4}\right)$	$5.62^{+1.30}_{-1.30}$	
Ne IX Emission Line[b]	pn Norm. $\left(10^{-4}\right)$	$1.05^{+0.35}_{-0.35}$	
Absorption Edge	Edge Energy (keV)		$0.84^{+0.01}_{-0.01}$
	Depth		$0.18^{+0.01}_{-0.01}$
High Ion. Warm Abs.	N_H $\left(10^{21} cm^{-2}\right)$	$13.01^{+11.89}_{-8.68}$	$36.51^{+15.24}_{-20.76}$
	Log ξ	$3.08^{+0.49}_{-0.29}$	$3.00^{+0.58}_{-0.15}$
Low Ion. Warm Abs.	N_H $\left(10^{21} cm^{-2}\right)$		$3.15^{+0.08}_{-0.07}$
	Log ξ		$1.30^{+0.03}_{-0.03}$
Soft X-Ray Power Law[a]	Γ_{Soft}		$3.83^{+0.02}_{-0.02}$
	pn Norm. $\left(10^{-3}\right)$		$2.85^{+0.02}_{-0.02}$
	χ^2/DOF	472.26/439	677.10/623
	P-value	0.1319	0.0656

[a]Xillver and power law normalizations are photons $\mathrm{keV}^{-1}\mathrm{cm}^{-2}\mathrm{s}^{-1}$ at 1 keV.

[b]Gaussian normalization is total photons $\mathrm{cm}^{-2}\mathrm{s}^{-1}$ in the line of sight.

Table 3.4: XMM-Newton X2 RGS 0.3-2 keV model parameters.

Component	Parameter	X2 RGS
Full Covering Absorption	N_H $\left(10^{20} cm^{-2}\right)$	$8.32^{+0.71}_{-0.72}$
N VII Emission Line[a]	RGS 1 Norm. $\left(10^{-3}\right)$	$1.14^{+0.29}_{-0.29}$
	RGS 2 Norm. $\left(10^{-3}\right)$	$1.20^{+0.37}_{-0.37}$
Absorption Edge	Edge Energy (keV)	$0.85^{+0.01}_{-0.01}$
	Depth	$0.25^{+0.03}_{-0.03}$
Low Ion. Warm Abs.	N_H $(10^{21} cm^{-2})$	$2.76^{+0.19}_{-0.18}$
	Log ξ	$1.48^{+0.04}_{-0.04}$
Soft X-Ray Power Law[b]	Γ_{Soft}	$4.01^{+0.14}_{-0.14}$
	RGS 1 Norm. $\left(10^{-3}\right)$	$1.14^{+0.06}_{-0.06}$
	RGS 2 Norm. $\left(10^{-3}\right)$	$1.30^{+0.06}_{-0.06}$
	χ^2/DOF	3692.54/2919

[a]Gaussian normalization is total photons $\mathrm{cm}^{-2}\mathrm{s}^{-1}$ in the line of sight.

[b]Power law normalization is photons $\mathrm{keV}^{-1}\mathrm{cm}^{-2}\mathrm{s}^{-1}$ at 1 keV.

Table 3.5: S1 alternative model parameters.

Component	Parameter	BB Model	CompST Model	Bremss Model	IRR Model
Ionized Partial Covering	N_H $\left(10^{22} cm^{-2}\right)$	$0.78^{+0.09}_{-0.8}$	$1.10^{+0.07}_{-0.06}$	$1.08^{+0.07}_{-0.09}$	$2.97^{+0.13}_{-0.12}$
	Covering Fraction	$0.23^{+0.01}_{-0.01}$	$0.37^{+0.03}_{-0.03}$	$0.30^{+0.02}_{-0.02}$	$0.38^{+0.01}_{-0.01}$
	Log ξ	$0.24^{+0.22}_{-0.35}$	$0.29^{+0.16}_{-0.26}$	$0.30^{+0.20}_{-0.23}$	
Xillver[a]	Γ_{Hard}	$1.47^{+0.01}_{-0.01}$	$1.51^{+0.01}_{-0.01}$	$1.48^{+0.01}_{-0.01}$	$1.59^{+0.01}_{-0.01}$
	Log ξ	< 1.15	$0.71^{+0.28}_{-0.13}$	$1.02^{+0.31}_{-0.30}$	$0.56^{+0.13}_{-0.18}$
	Reflection Fraction	$0.59^{+0.04}_{-0.04}$	$0.66^{+0.05}_{-0.05}$	$0.62^{+0.05}_{-0.05}$	$0.73^{+0.07}_{-0.05}$
	XIS 0 & 3 Norm. $\left(10^{-4}\right)$	$2.17^{+0.01}_{-0.01}$	$2.09^{+0.01}_{-0.01}$	$2.15^{+0.01}_{-0.01}$	$2.18^{+0.01}_{-0.01}$
	XIS 1 Norm. $\left(10^{-4}\right)$	$2.03^{+0.01}_{-0.01}$	$1.94^{+0.01}_{-0.01}$	$2.00^{+0.01}_{-0.01}$	$2.08^{+0.02}_{-0.02}$
High Ion. Warm Abs.	N_H $\left(10^{21} cm^{-2}\right)$	$81.11^{+12.06}_{-10.65}$	$80.06^{+10.84}_{-9.69}$	$74.90^{+14.16}_{-12.05}$	$2.12^{+0.13}_{-0.13}$
	Log ξ	$2.40^{+0.01}_{-0.01}$	$2.38^{+0.01}_{-0.01}$	$2.42^{+0.01}_{-0.01}$	$2.33^{+0.02}_{-0.02}$
Low Ion. Warm Abs.	N_H $\left(10^{21} cm^{-2}\right)$	$5.95^{+0.20}_{-0.19}$	$6.13^{+0.46}_{-0.44}$	$6.34^{+0.37}_{-0.35}$	$3.96^{+0.13}_{-0.13}$
	Log ξ	$1.44^{+0.02}_{-0.02}$	$1.44^{+0.05}_{-0.04}$	$1.41^{+0.05}_{-0.04}$	$1.41^{+0.02}_{-0.02}$
Blackbody[b]	kT (eV)	$113.57^{+5.60}_{-5.37}$			
	XIS 0 & 3 Norm. $\left(10^{-5}\right)$	$6.22^{+0.71}_{-0.71}$			
	XIS 1 Norm. $\left(10^{-5}\right)$	$6.94^{+0.53}_{-0.53}$			
Comptonized Component[c]	kT (eV)		$363.50^{+14.72}_{-13.96}$		
	Depth		$22.67^{+0.19}_{-0.75}$		
	XIS 0 & 3 Norm. $\left(10^{-3}\right)$		$1.84^{+0.10}_{-0.10}$		
	XIS 1 Norm. $\left(10^{-3}\right)$		$1.91^{+0.09}_{-0.09}$		
Bremsstrahlung[d]	kT (eV)			$343.46^{+21.83}_{-20.04}$	
	XIS 0 & 3 Norm. $\left(10^{-2}\right)$			$1.26^{+0.08}_{-0.08}$	
	XIS 1 Norm. $\left(10^{-2}\right)$			$1.34^{+0.07}_{-0.07}$	
Reflionx[a]	ξ				$48.63^{+2.73}_{-5.13}$
	XIS 0 & 3 Norm. $\left(10^{-6}\right)$				$1.47^{+0.53}_{-0.53}$
	XIS 1 Norm. $\left(10^{-6}\right)$				$1.98^{+0.90}_{-0.90}$
	χ^2/DOF	1807.13/1755	1813.98/1754	1810.62/1755	1800.40/1756
	P-value	0.1888	0.1556	0.1735	0.1733

[a]Xillver and Reflionx normalizations are photons keV^{-1}cm^{-2}s^{-1} at 1 keV.

[b]Blackbody normalization is $L_{39}/[D_{10}(1+z)^2]$, L_{39} is luminosity in 10^{39} ergs s^{-1}, D_{10} is distance in 10 kpc.

[c]CompST normalization is $Nf/4\pi D^2$ where N is the total number of photons, D is the distance, $f = \alpha(\alpha+3)y^2\Gamma(\alpha)/\Gamma(2\alpha+4)$, α is the spectral index, y is the injected photon energy in units of temperature, and Γ is the incomplete gamma function.

[d]Bremsstrahlung normalization is $3.02 \times 10^{-15}/4\pi D^2 \int n_e n_I dV$ where D is the distance in cm, and n_e and n_I are the electron and ion densities in cm^{-3}

Table 3.6: X2 alternative model parameters.

Component	Parameter	BB Model	CompST Model	Bremss Model	IRR Model
Full Covering Absorption	N_H $\left(10^{20} cm^{-2}\right)$	$7.28^{+0.22}_{-0.22}$	$10.02^{+0.25}_{-0.25}$	$6.67^{+0.24}_{-0.23}$	
Xillver[a]	Γ_{Hard}	$1.61^{+0.01}_{-0.01}$	$1.60^{+0.01}_{-0.01}$	$1.64^{+0.01}_{-0.01}$	$1.64^{+0.01}_{-0.01}$
	Log ξ	$0.30^{+0.04}_{-0.10}$	$0.81^{+0.22}_{-0.29}$	$1.00^{+0.02}_{-0.07}$	$1.00^{+0.01}_{-0.08}$
	Reflection Fraction	$0.75^{+0.04}_{-0.04}$	$0.67^{+0.04}_{-0.04}$	$0.84^{+0.04}_{-0.04}$	$0.96^{+0.05}_{-0.05}$
	pn Norm. $\left(10^{-4}\right)$	$1.78^{+0.01}_{-0.01}$	$2.55^{+0.01}_{-0.01}$	$2.36^{+0.01}_{-0.01}$	$1.68^{+0.01}_{-0.01}$
OVII Emission Line[b]	pn Norm. $\left(10^{-4}\right)$	$1.29^{+0.30}_{-0.30}$	$2.93^{+0.41}_{-0.41}$		
Absorption Edge	Energy (keV)		$0.84^{+0.01}_{-0.01}$	$0.83^{+0.01}_{-0.01}$	$0.85^{+0.01}_{-0.01}$
	Depth		$0.17^{+0.01}_{-0.01}$	$0.12^{+0.01}_{-0.01}$	$0.09^{+0.01}_{-0.01}$
High Ion. Warm Abs.	N_H $\left(10^{21} cm^{-2}\right)$	$2.35^{+0.16}_{-0.18}$	$8.17^{+8.63}_{-6.58}$	> 3.78	$5.72^{+0.12}_{-0.11}$
	Log ξ	$2.05^{+0.04}_{-0.02}$	$2.54^{+0.72}_{-0.13}$	$2.99^{+0.80}_{-0.19}$	$1.68^{+0.01}_{-0.02}$
Low Ion. Warm Abs.	N_H $\left(10^{21} cm^{-2}\right)$	$2.20^{+0.05}_{-0.07}$	$3.23^{+0.07}_{-0.07}$	$3.91^{+0.07}_{-0.07}$	$0.61^{+0.02}_{-0.02}$
	Log ξ	$1.28^{+0.02}_{-0.02}$	$1.27^{+0.03}_{-0.03}$	$1.13^{+0.03}_{-0.02}$	$0.10^{+0.01}_{-0.01}$
Blackbody[c]	kT (eV)	$87.78^{+0.74}_{-0.74}$			
	pn Norm $\left(10^{-4}\right)$	$1.85^{+0.02}_{-0.02}$			
Comptonized Component[d]	kT (eV)		$479.77^{+4.31}_{-4.28}$		
	Optical Depth		$14.92^{+0.09}_{-0.09}$		
	pn Norm. $\left(10^{-3}\right)$		$2.37^{+0.02}_{-0.02}$		
Bremsstrahlung[e]	kT (eV)			$264.91^{+0.28}_{-0.28}$	
	pn Norm. $\left(10^{-2}\right)$			$4.30^{+0.28}_{-0.28}$	
Reflionx	ξ				< 10.80
	XIS 0 & 3 Norm. $\left(10^{-6}\right)$				$4.18^{+0.60}_{-0.88}$
	χ^2/DOF	691.98/605	670.14/602	791.49/623	1604.85/604
	P-value	0.0080	0.0279	$4.96E(-6)$	$9.46E(-92)$

[a]Xillver normalization is photons $\mathrm{keV}^{-1}\mathrm{cm}^{-2}\mathrm{s}^{-1}$ at 1 keV.

[b]Gaussian normalization is total photons $\mathrm{cm}^{-2}\mathrm{s}^{-1}$ in the line of sight.

[c]Blackbody normalization is $L_{39}/[D_{10}(1+z)^2]$, L_{39} is luminosity in 10^{39} ergs s^{-1}, D_{10} is distance in 10 kpc.

[d]CompST normalization is $Nf/4\pi D^2$ where N is the total number of photons, D is the distance, $f = \alpha(\alpha+3)y^2\Gamma(\alpha)/\Gamma(2\alpha+4)$, α is the spectral index, y is the injected photon energy in units of temperature, and Γ is the incomplete gamma function.

[e]Bremsstrahlung normalization is $3.02 \times 10^{-15}/4\pi D^2 \int n_e n_I dV$ where D is the distance in cm, and n_e and n_I are the electron and ion densities in cm^{-3}

Table 3.7: Spearman's rank correlations.

Parameter	ρ	P-Value
Hard Γ	0.431	0.286
Reflection Fraction	-0.810	0.022
Partial Covering Fraction	-0.210	0.714
Partial Covering N_H	-0.943	0.017
Partial Covering Log ξ	-0.116	0.844
Low Ion. Warm Abs. N_H	0.786	0.048
Low Ion. Warm Abs. Log ξ	0	1
High Ion. Warm Abs. N_H	0.821	0.034
High Ion. Warm Abs. Log ξ	0	1

Chapter 3 Figures

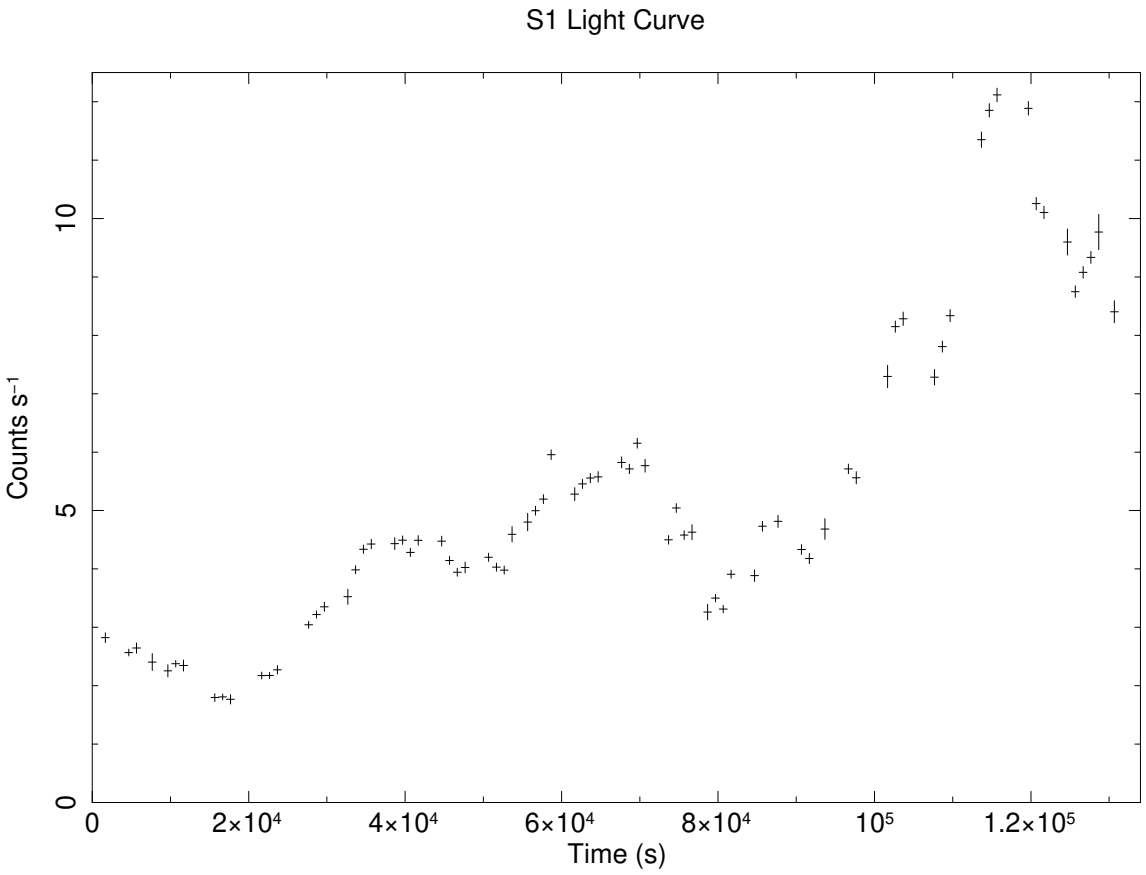

Figure 3.1: Summed XIS0, 1, and 3 light curve for S1. Since the intensity of S1 is high, the vertical axis is expanded compared to the other observations.

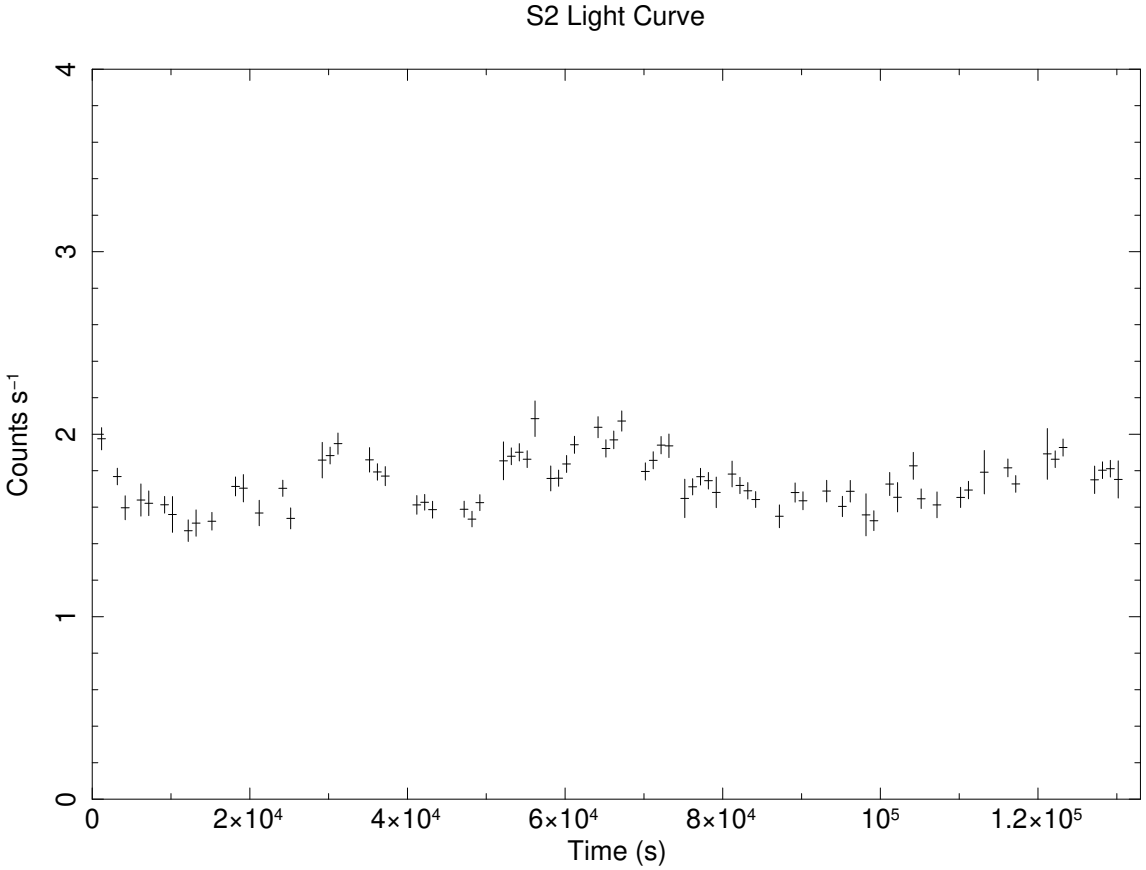

Figure 3.2: Summed XIS0, 1, and 3 light curve for S2. Low flux state.

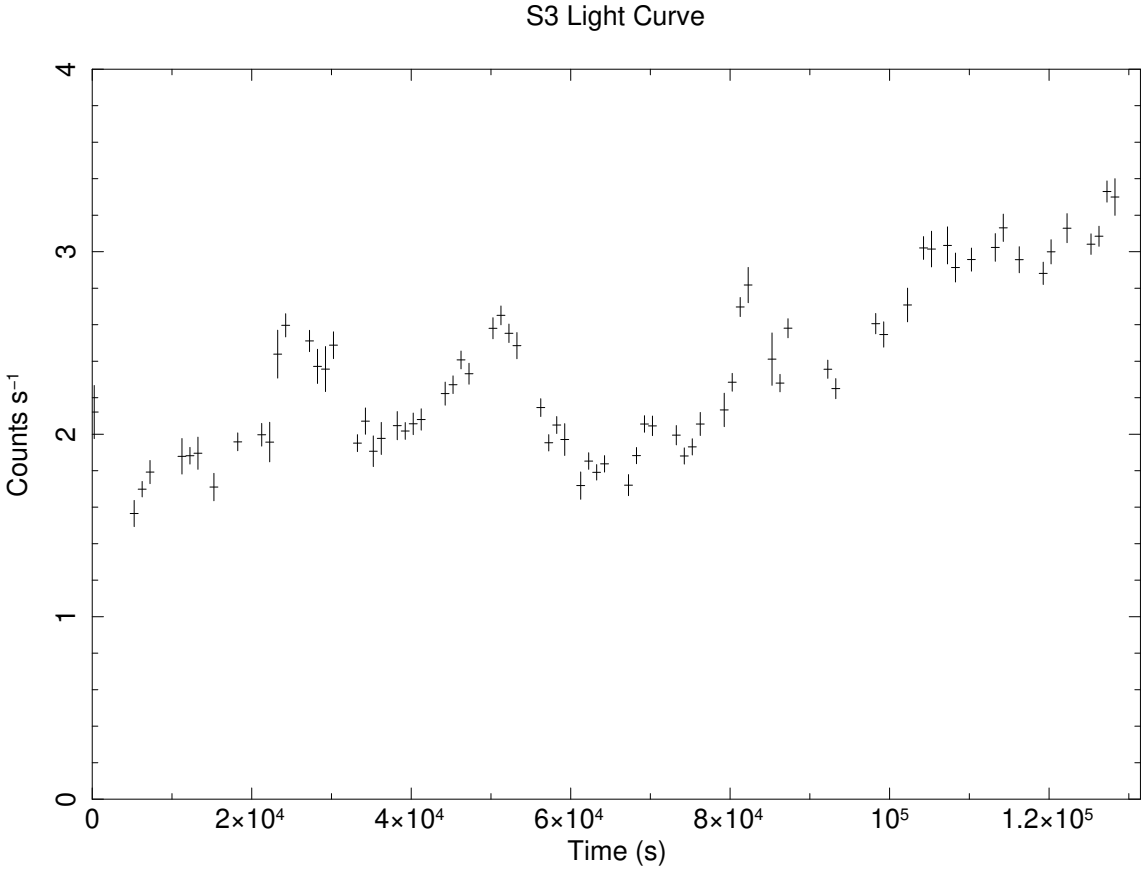

Figure 3.3: Summed XIS0, 1, and 3 light curve for S3. Moderate flux state.

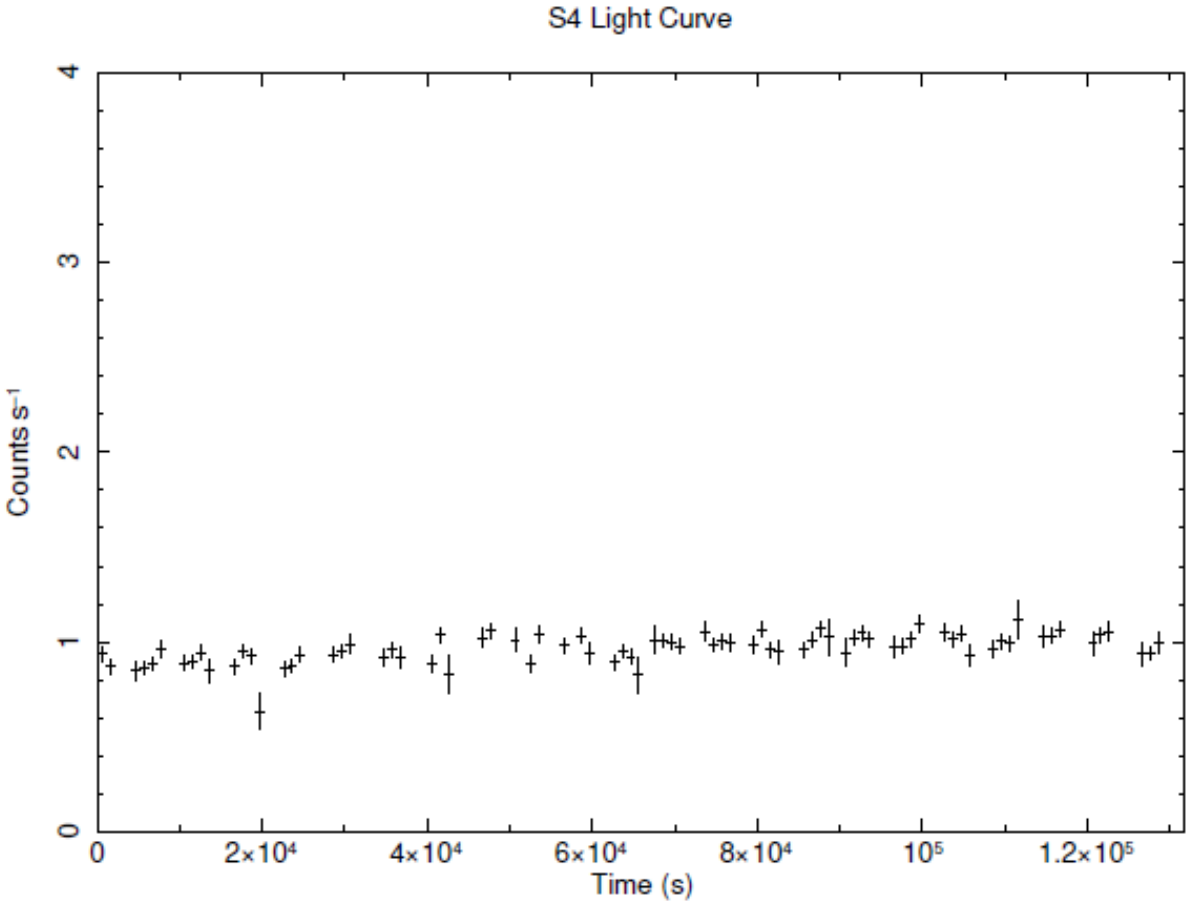

Figure 3.4: Summed XIS0, 1, and 3 light curve for S4. Lowest flux of the Suzaku observations.

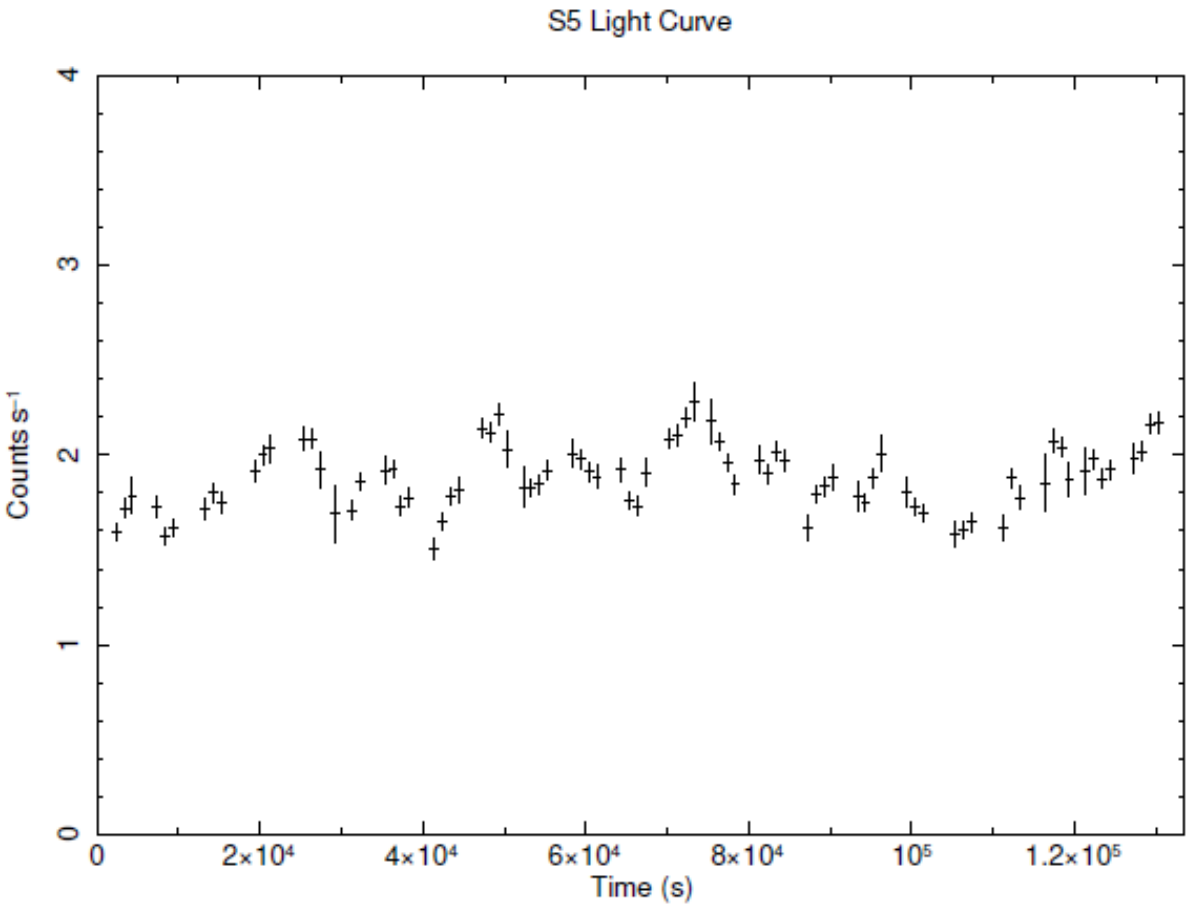

Figure 3.5: Summed XIS0, 1, and 3 light curve for S5. Low flux state.

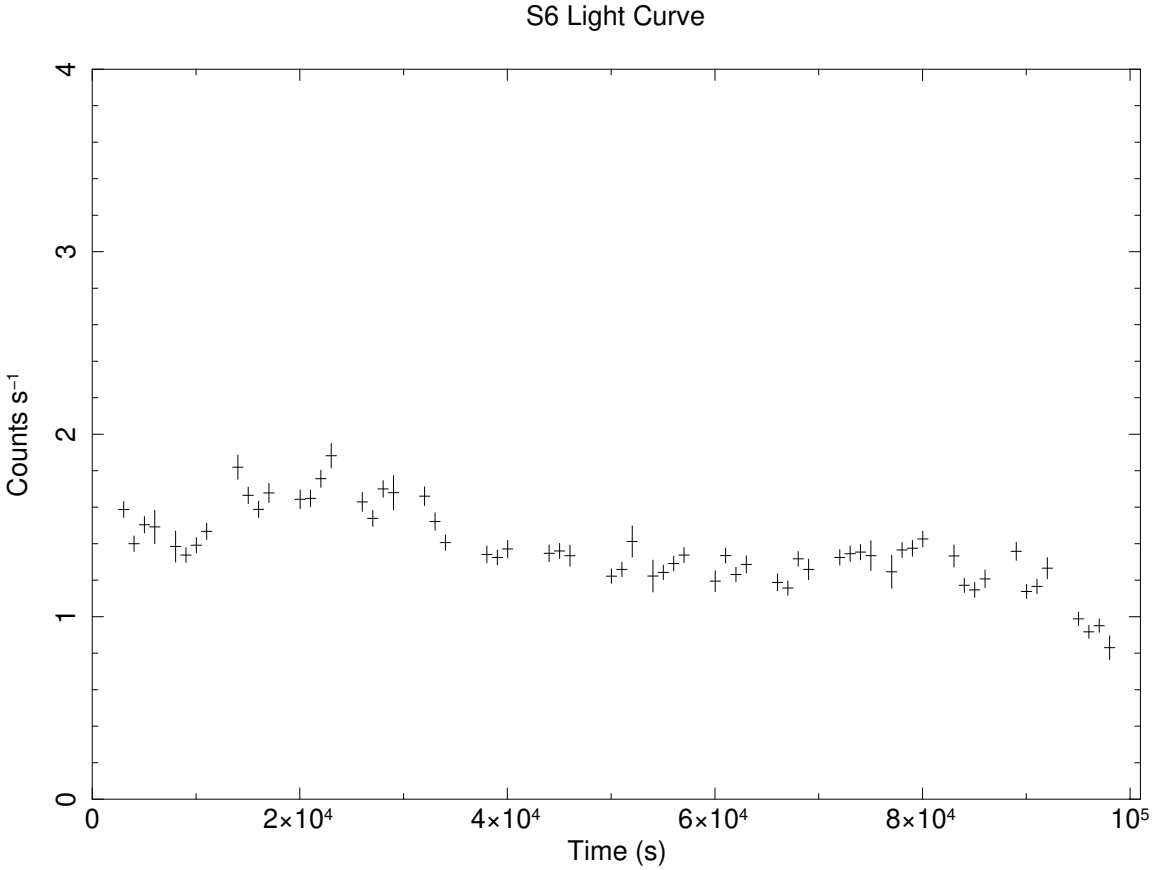

Figure 3.6: Summed XIS0, 1, and 3 light curve for S6. Low flux state.

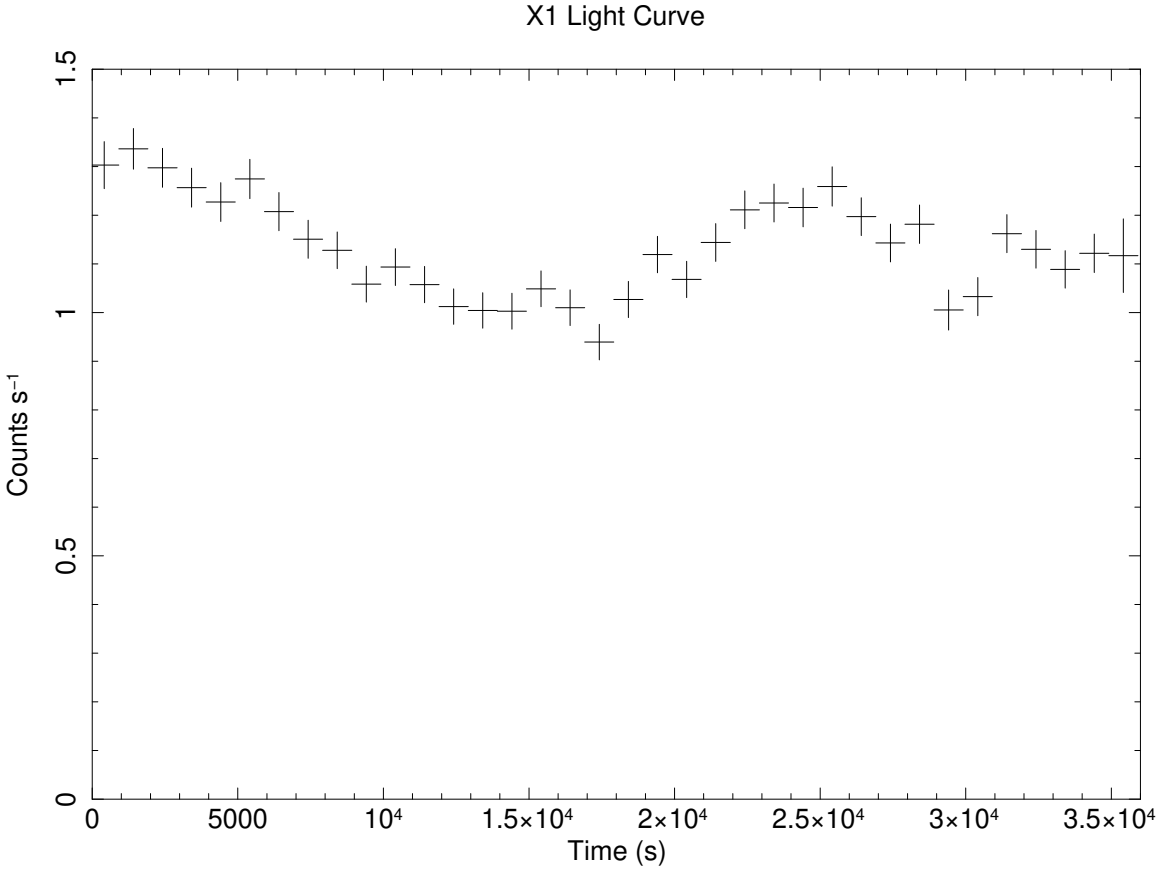

Figure 3.7: Pn light curve for X1 in the low state.

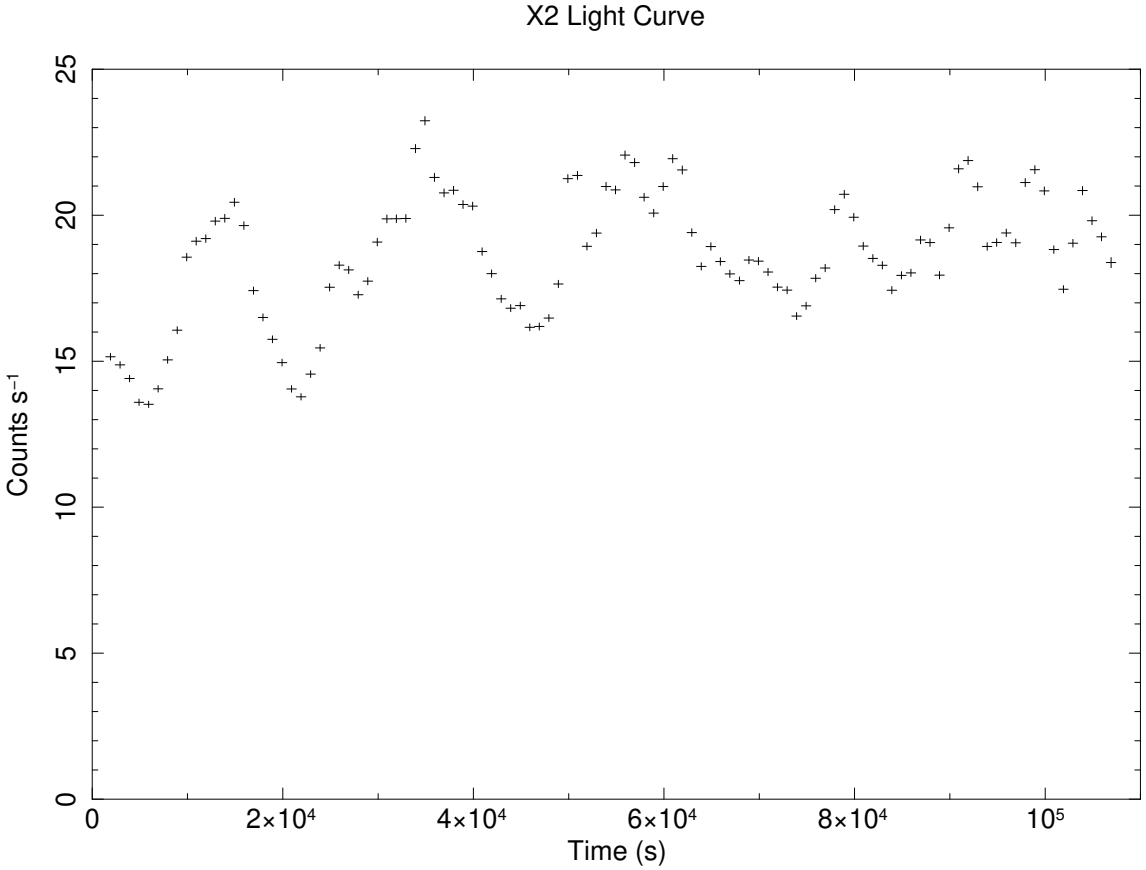

Figure 3.8: Pn light curve for X2 in the high state. Note that the vertical axis is expanded compared to X1.

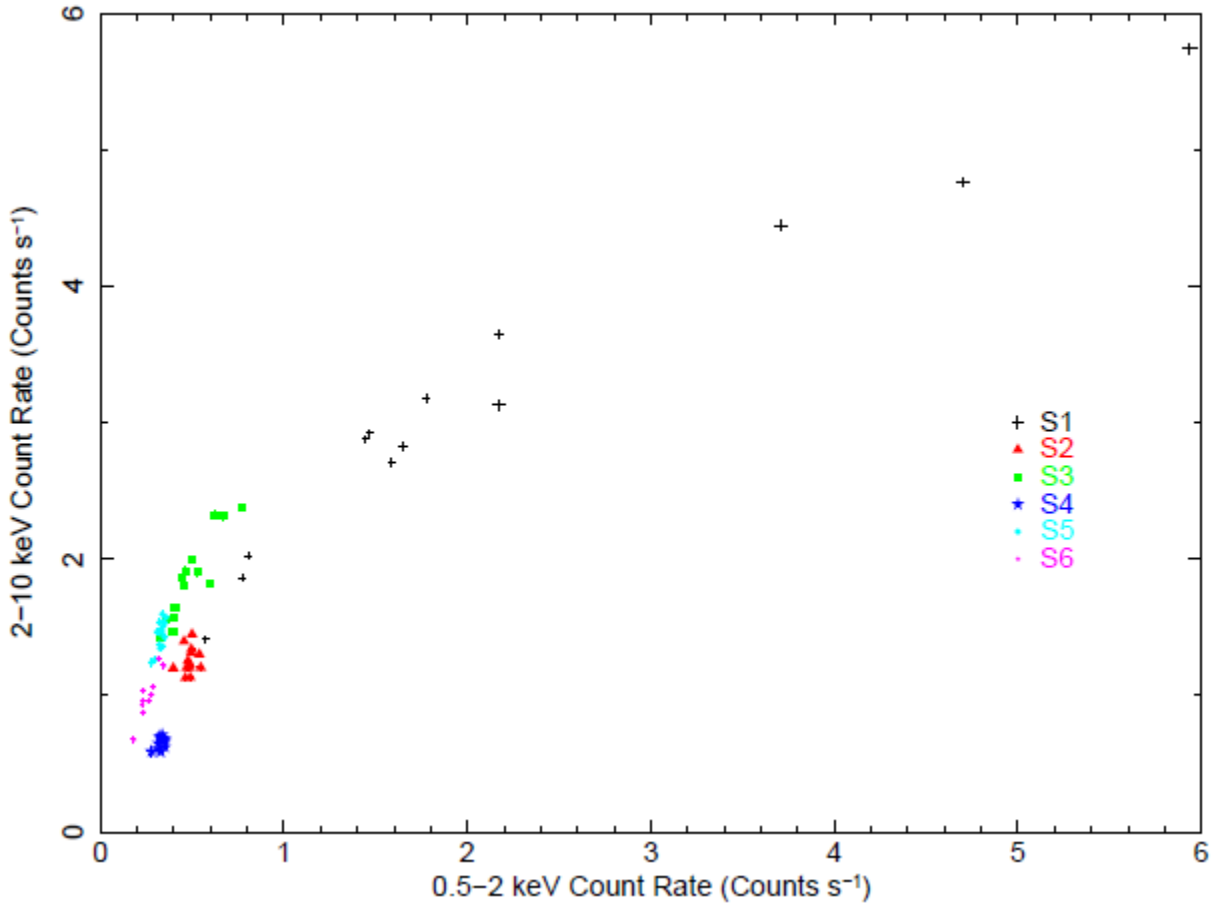

Figure 3.9: The 2 - 10 keV vs 0.5 - 2 keV flux-flux plot is shown for all Suzaku observations S1 to S6. Since the slope from the origin to the data point tells the hardness ratio, the brighter phase S1 has a softer spectrum compared with other fainter phases with steeper slope.

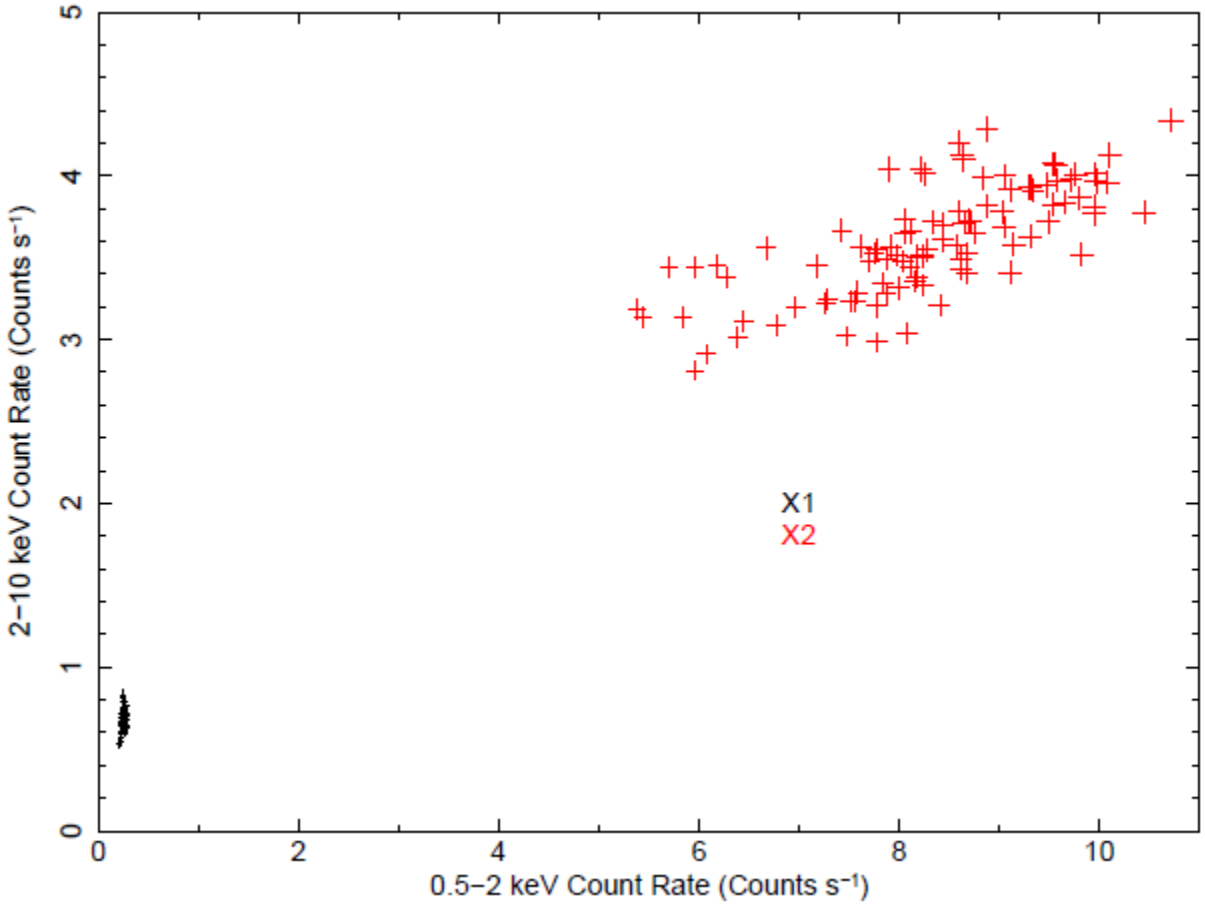

Figure 3.10: The 2 - 10 keV vs 0.5 - 2 keV flux-flux plot for two XMM-Newton observations X1 and X2.

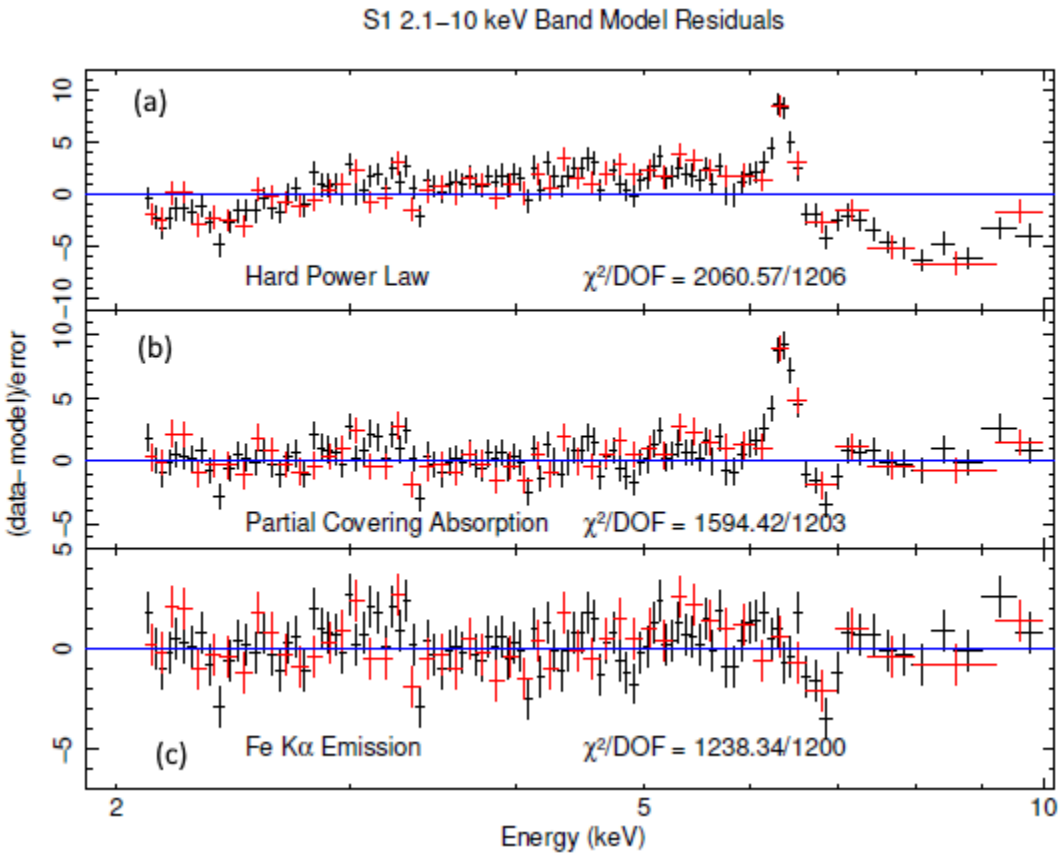

Figure 3.11: S1 hard X-ray band (2.1 - 10 keV) spectral fits. The ratio of the data to the model is shown. XIS0 & 3 are the black data and XIS1 is red. At first a simple power law was applied with the galactic absorption (3.11a). Then an ionized partial covering was added (3.11b). A gaussian at 6.4 keV was introduced to eliminate the residual due to the Fe Kα line (3.11c).

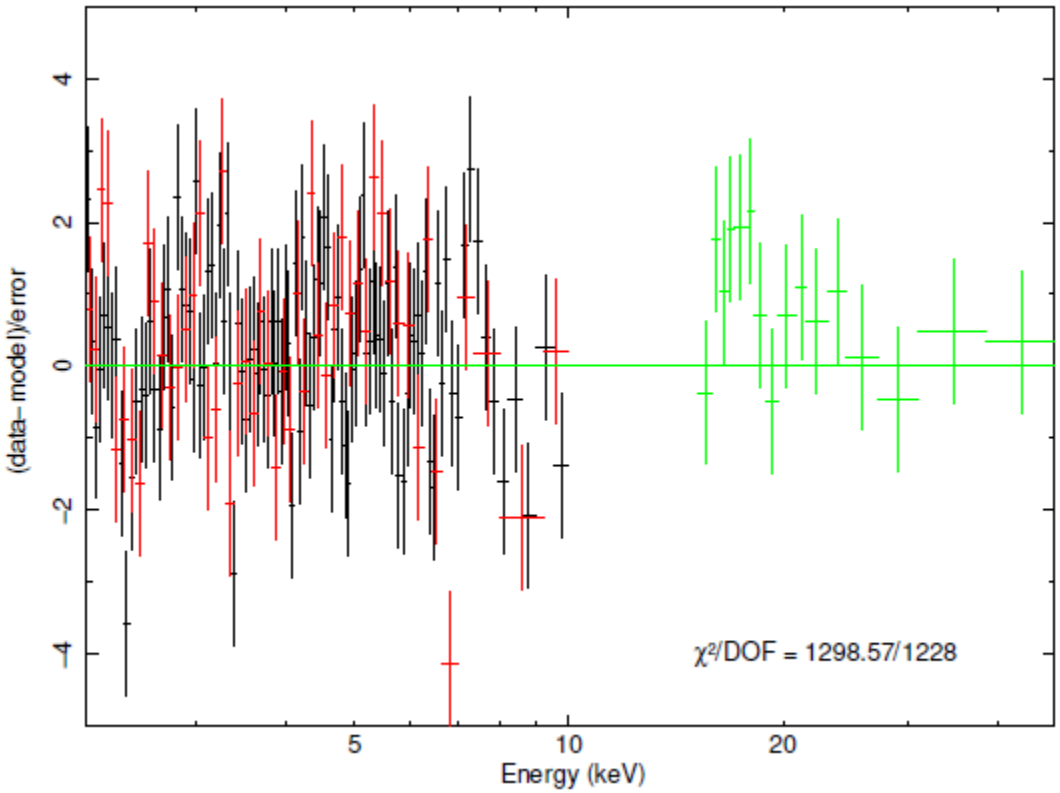

Figure 3.12: S1 Broader hard X-ray band (2.1 - 50 keV) spectral fit residuals. The ratio of the data to the model is shown. XIS0 & 3 are the black data, XIS 1 is red, and HXD-PIN is green.

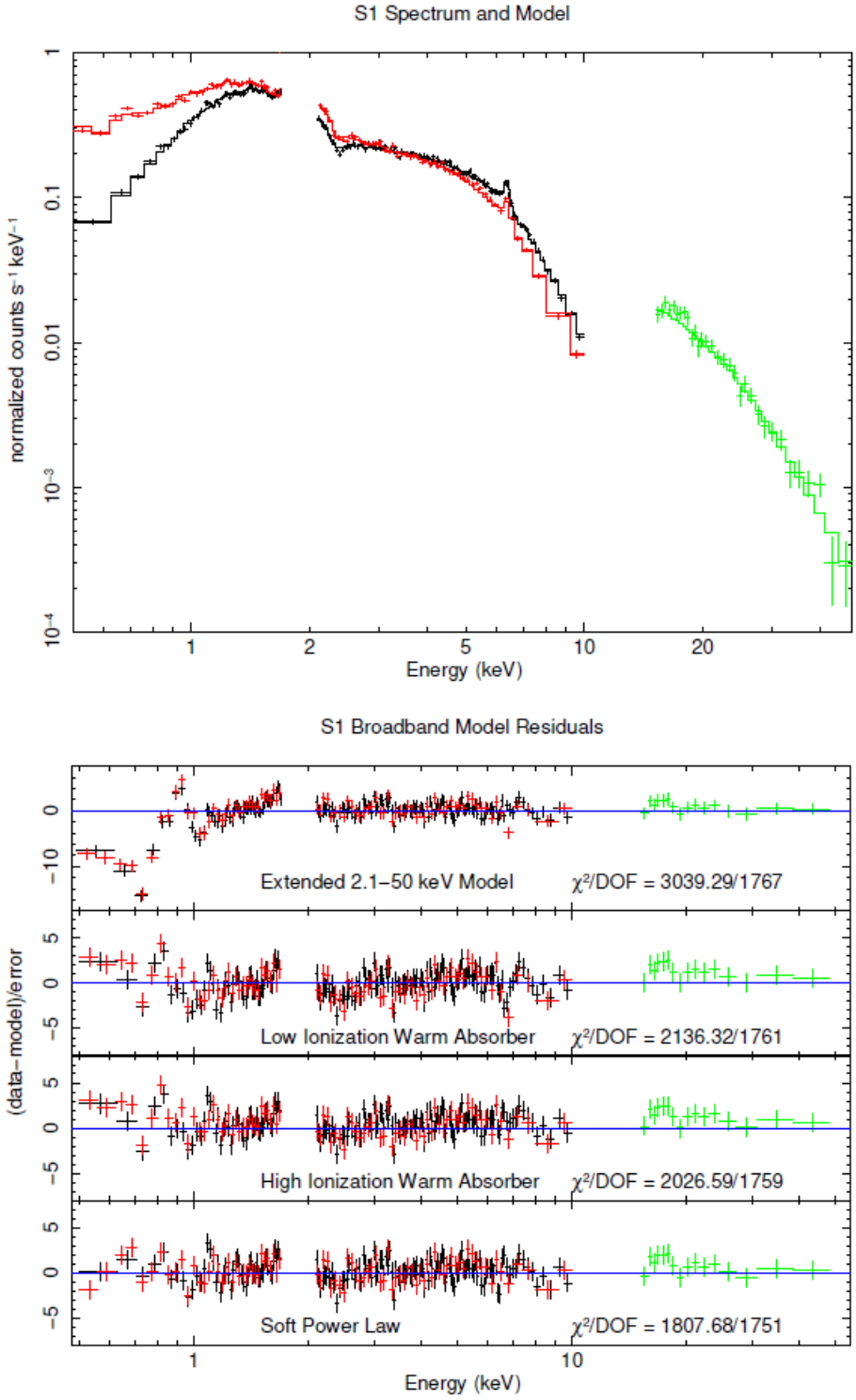

Figure 3.13: S1 Full X-ray band (0.5 - 50 keV) spectrum and fit residuals. The ratio of the data to the model is shown. XIS0 & 3 are the black data, XIS1 is red, and HXD-PIN is green. S1 contains both warm absorbers and the soft power law.

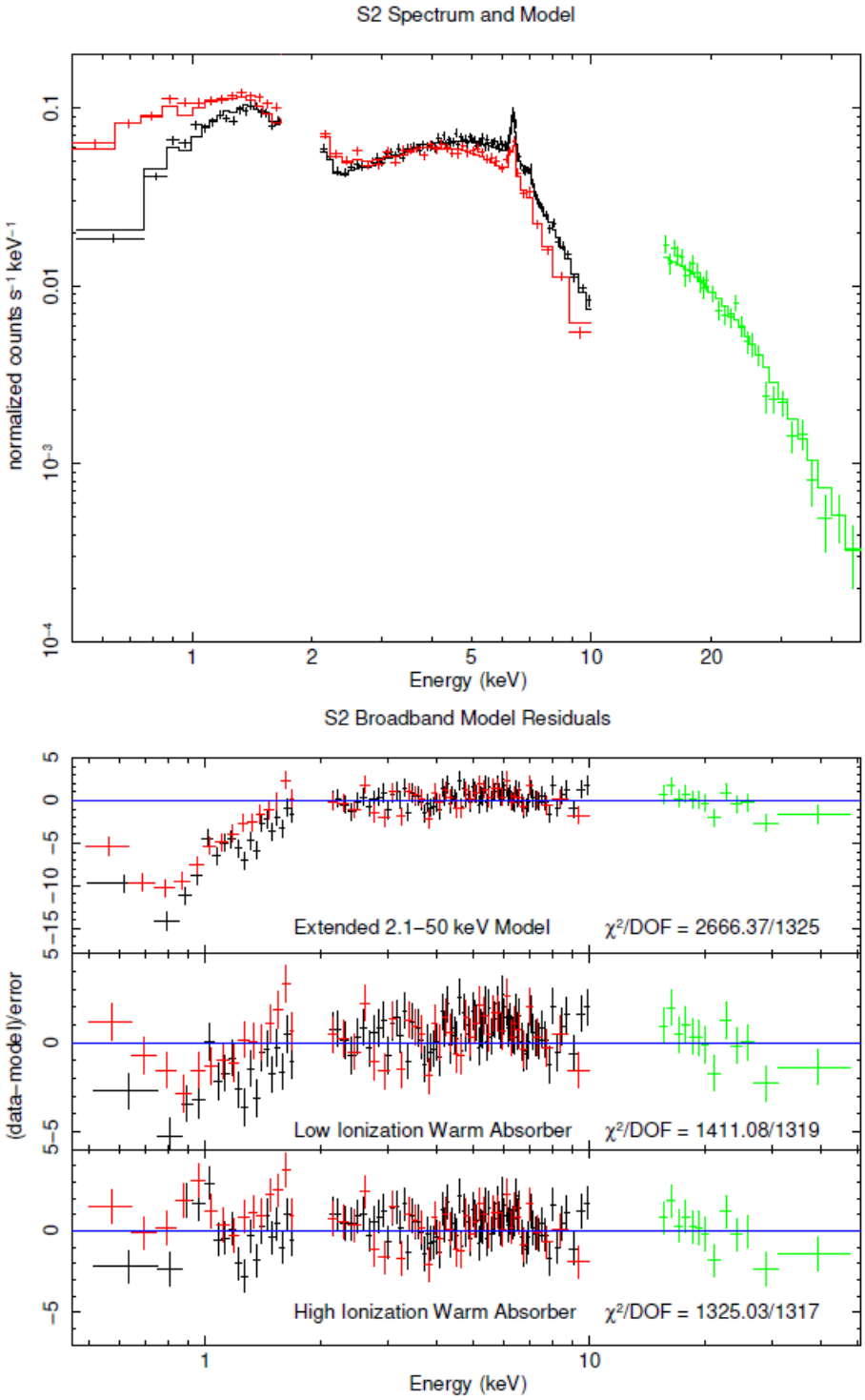

Figure 3.14: S2 Full X-ray band (0.5 - 50 keV) spectrum and fit residuals. The ratio of the data to the model is shown. XIS0 & 3 are the black data, XIS1 is red, and HXD-PIN is green. S2 contains both warm absorbers but no emission lines.

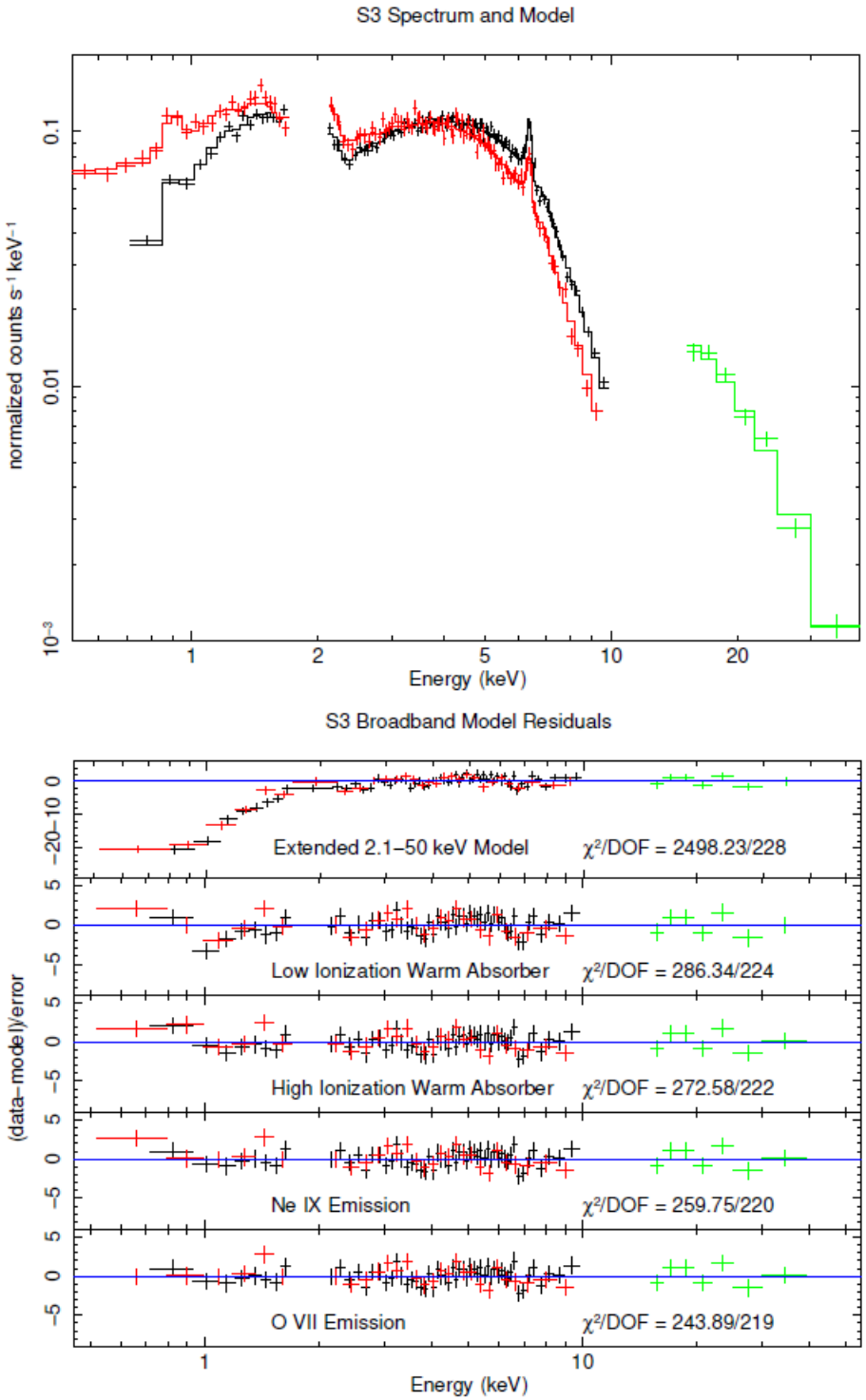

Figure 3.15: S3 Full X-ray band (0.5 - 50 keV) spectrum and fit residuals. The ratio of the data to the model is shown. XIS0 & 3 are the black data, XIS1 is red, and HXD-PIN is green. S3 contains both warm absorbers, the O VII line, and the Ne IX line.

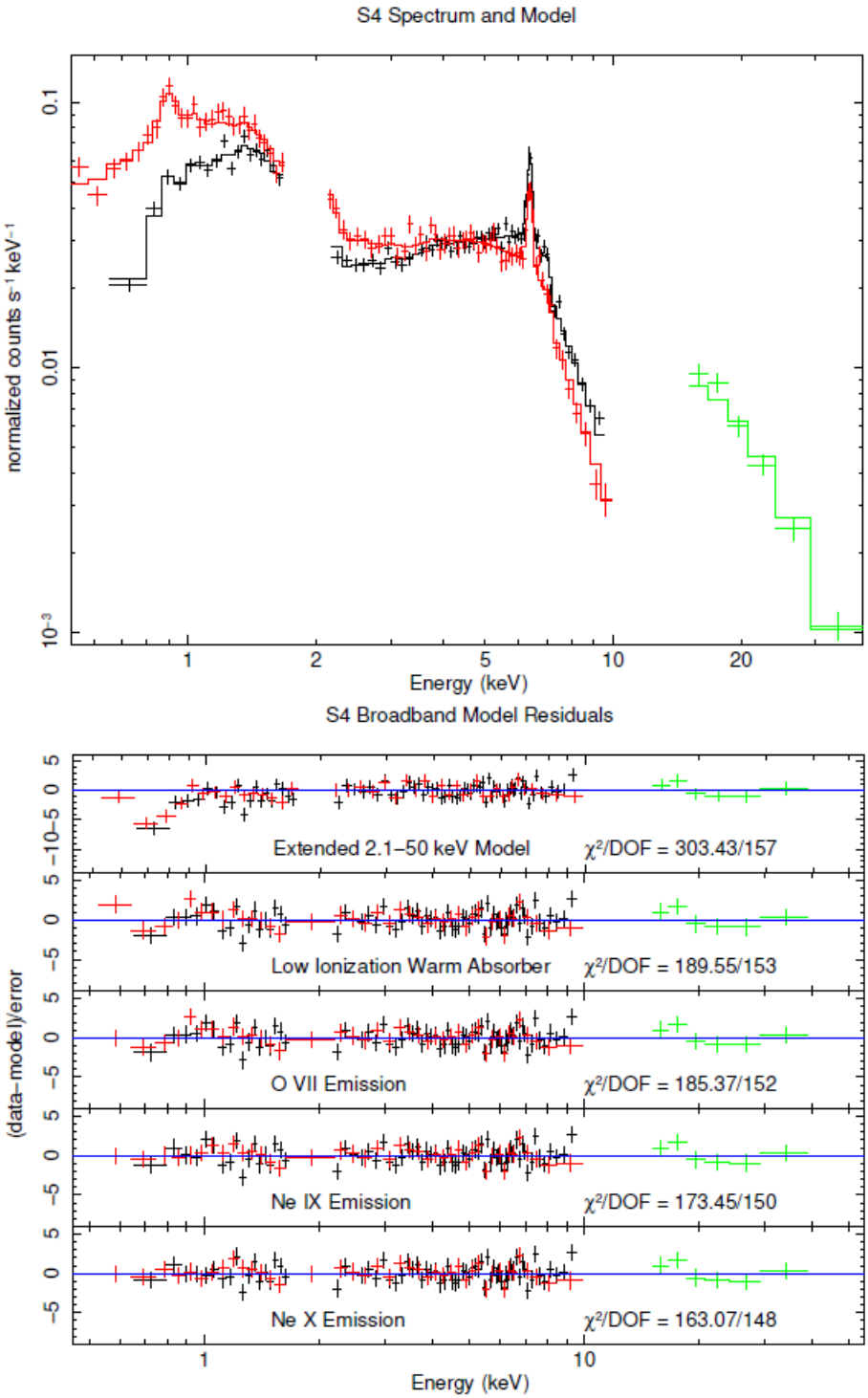

Figure 3.16: S4 Full X-ray band (0.5 - 50 keV) spectrum and fit residuals. The ratio of the data to the model is shown. XIS0 & 3 are the black data, XIS1 is red, and HXD-PIN is green. S4 contains the low ionization warm absorber and all three added emission lines.

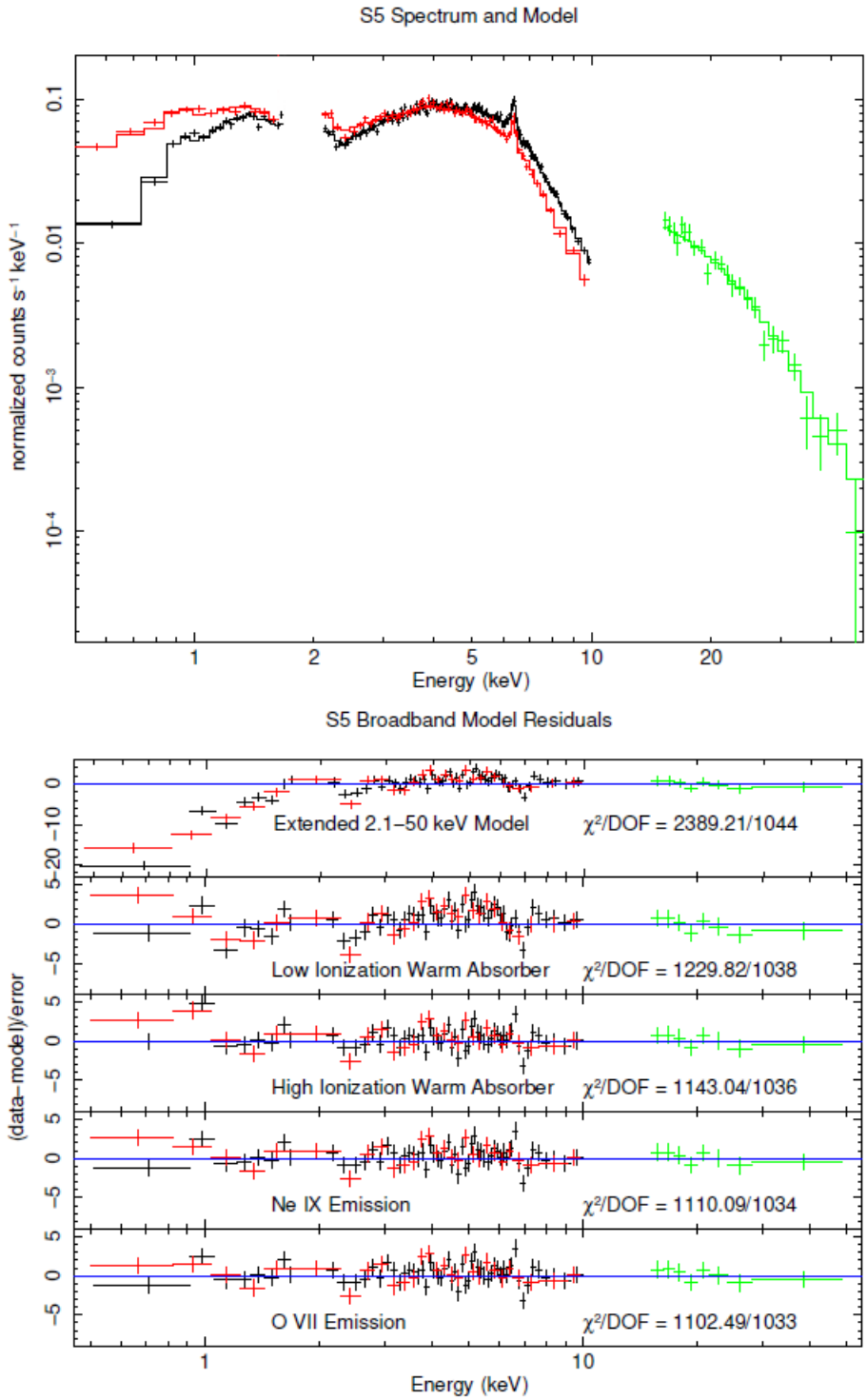

Figure 3.17: S5 Full X-ray band (0.5 - 50 keV) spectrum and fit residuals. The ratio of the data to the model is shown. XIS0 & 3 are the black data, XIS1 is red, and HXD-PIN is green. S5 contains both warm absorbers, the O VII line, and the Ne IX line.

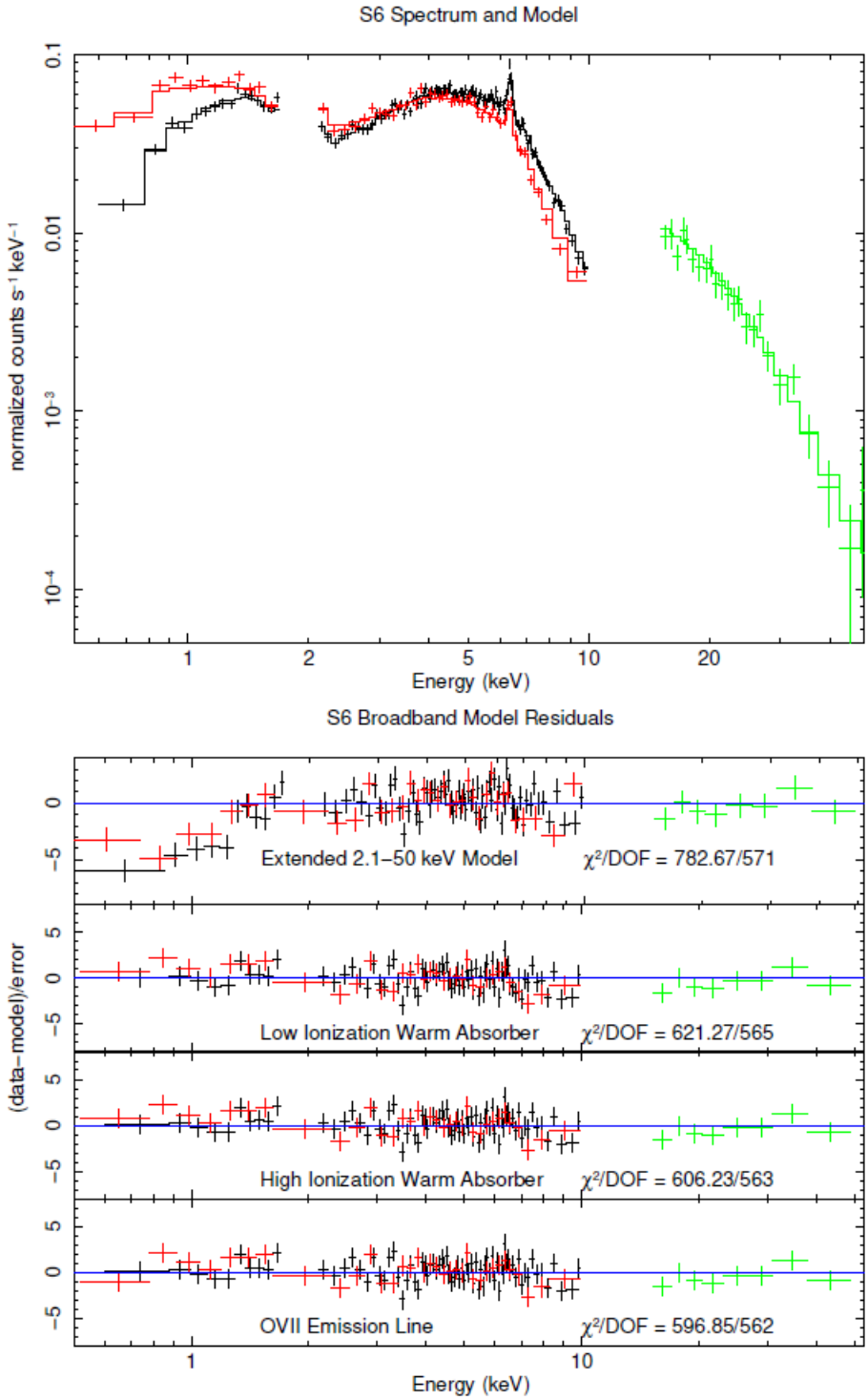

Figure 3.18: S6 Full X-ray band (0.5 - 50 keV) spectrum and fit residuals. The ratio of the data to the model is shown. XIS0 & 3 are the black data, XIS1 is red, and HXD-PIN is green. S5 contains both warm absorbers and the O VII line.

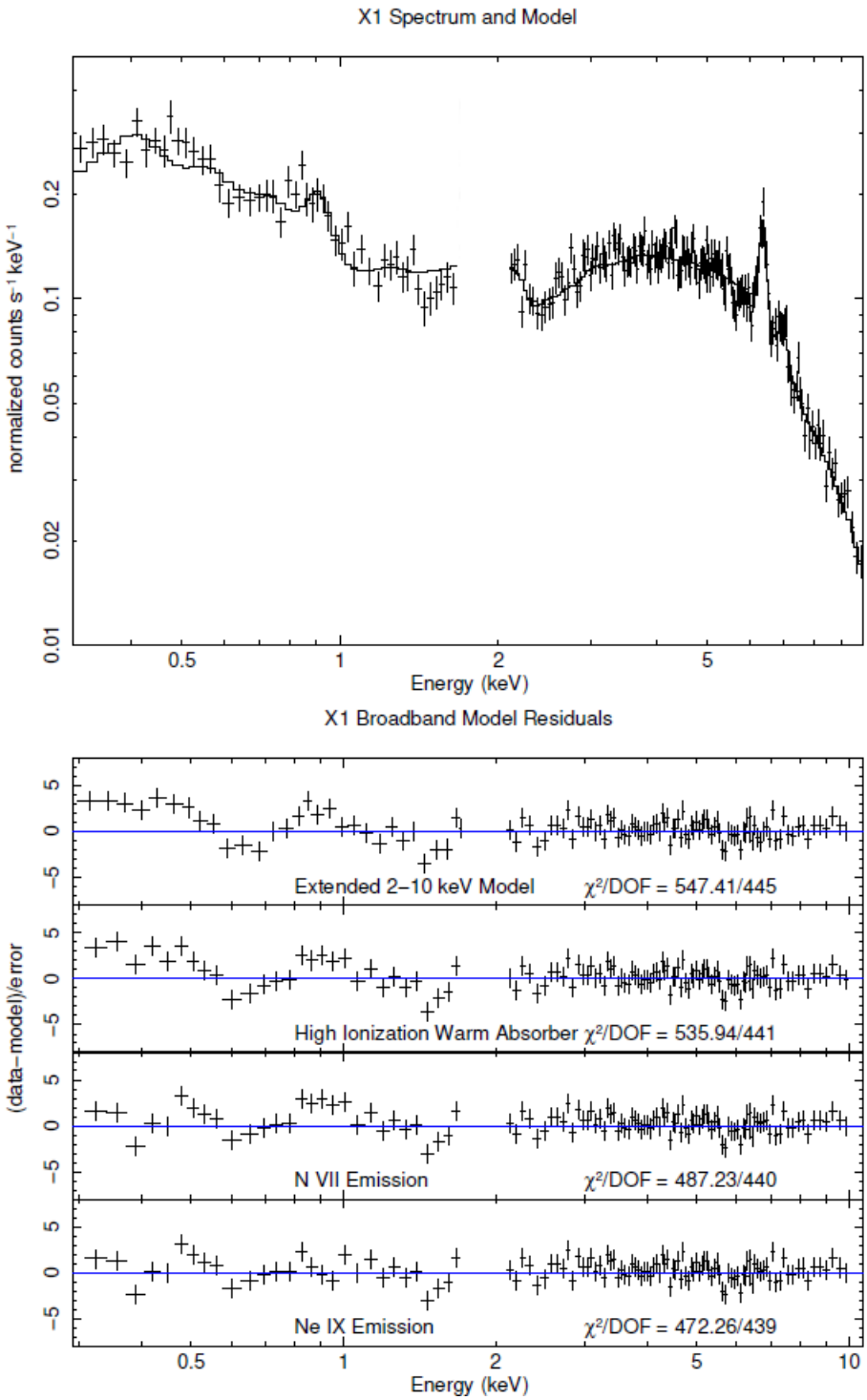

Figure 3.19: X1 Full X-ray band (0.3 - 10 keV) pn spectrum and fit. The ratio of the data to the model is shown. X1 contains the high ionization warm absorber, the N VI line, and the Ne IX line.

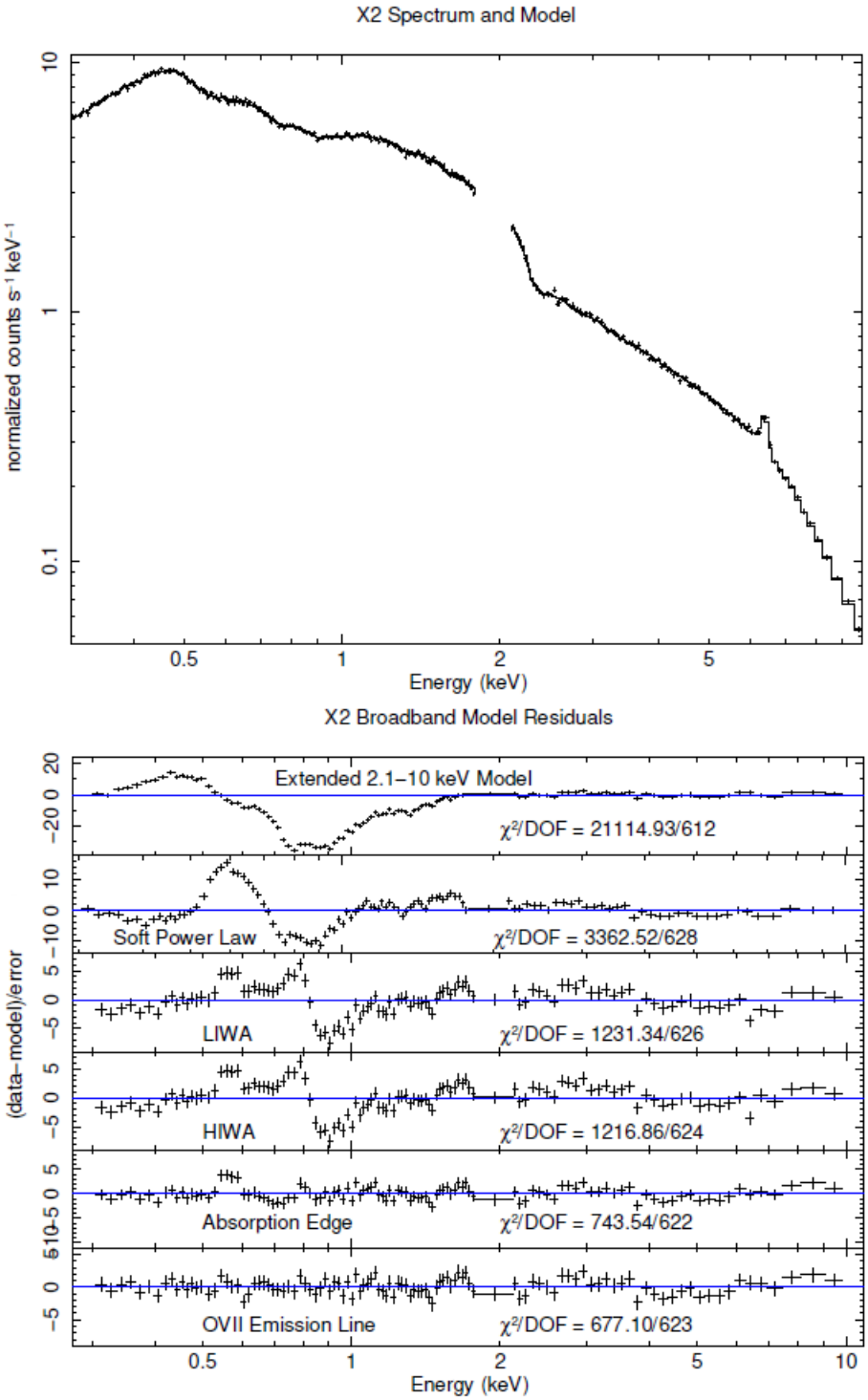

Figure 3.20: X2 Full X-ray band (0.3 - 10 keV) pn spectrum and fit. The ratio of the data to the model is shown. X2 contains both warm absorbers, the soft power law, an absoprtion edge, and the O VII line.

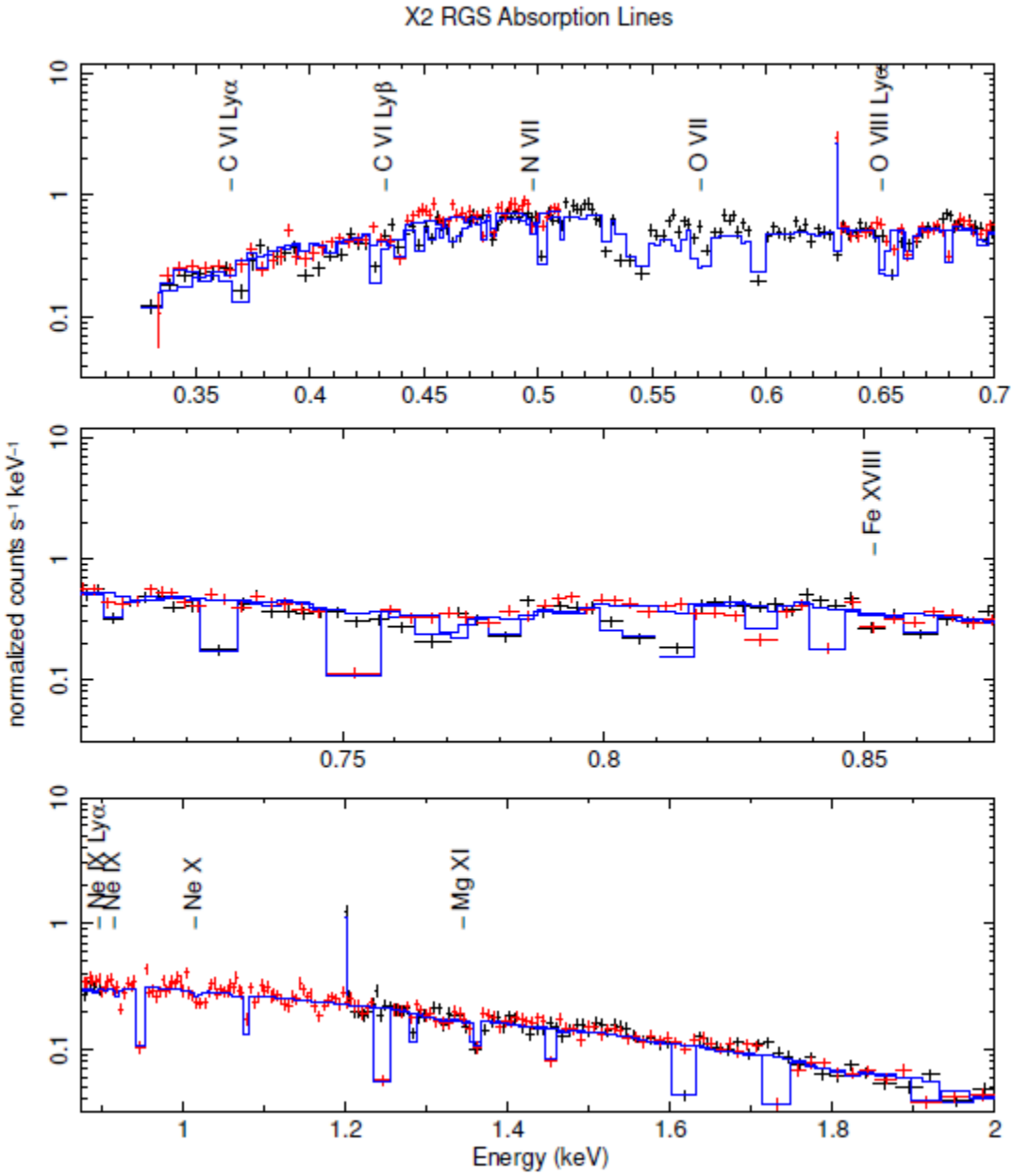

Figure 3.21: Absorption lines detected during the X2 RGS analysis. The 0.3 - 2 keV band is split into three regions. The top panel is 0.3 - 0.7 keV, the middle panel is 0.7 - 0.875, and the bottom panel is 0.875 - 2 keV. RGS1 data are black, RGS2 data are red, and the model is blue.

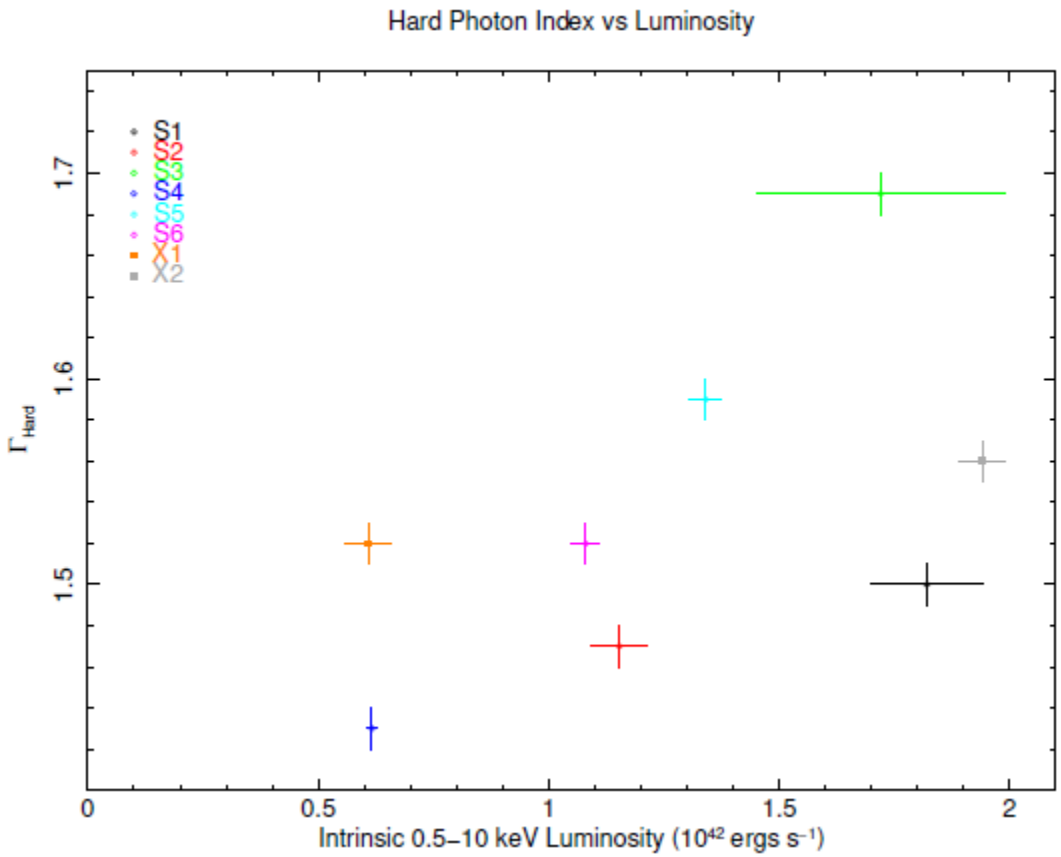

Figure 3.22: Hard photon index plotted against intrinsic luminosity. Displays a weak positive correlation.

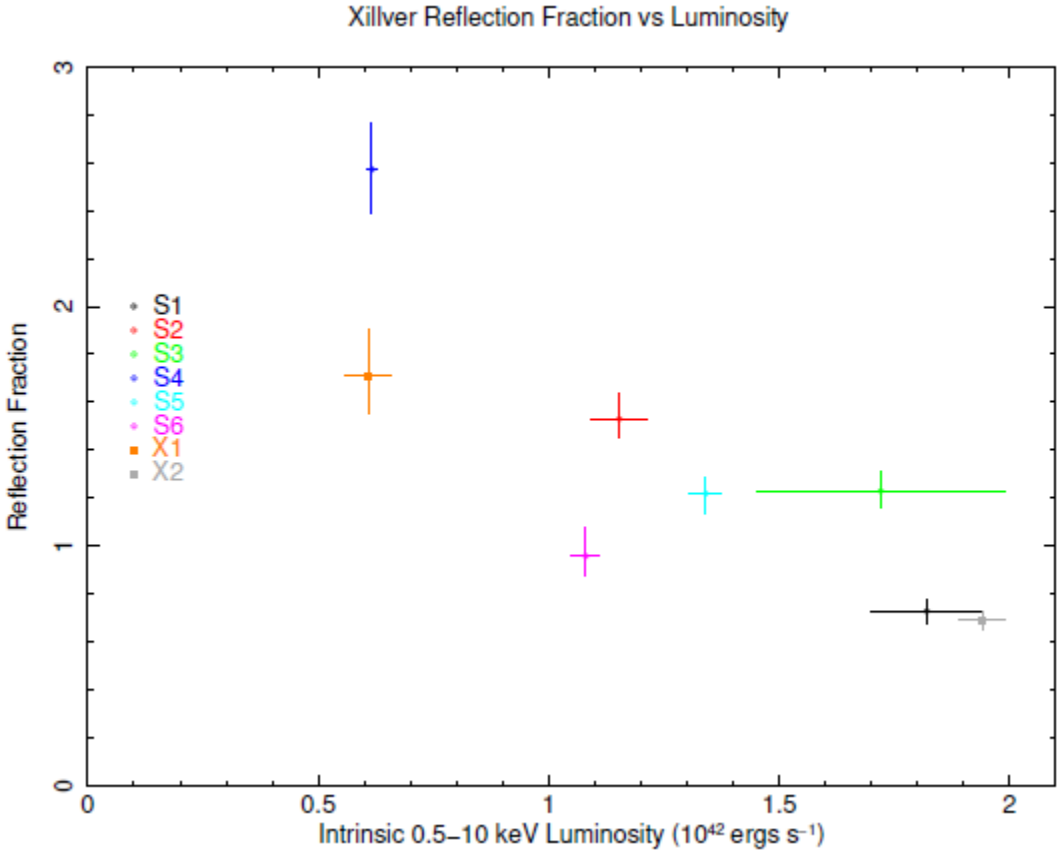

Figure 3.23: Reflection fraction plotted against intrinsic luminosity. Displays a negative correlation.

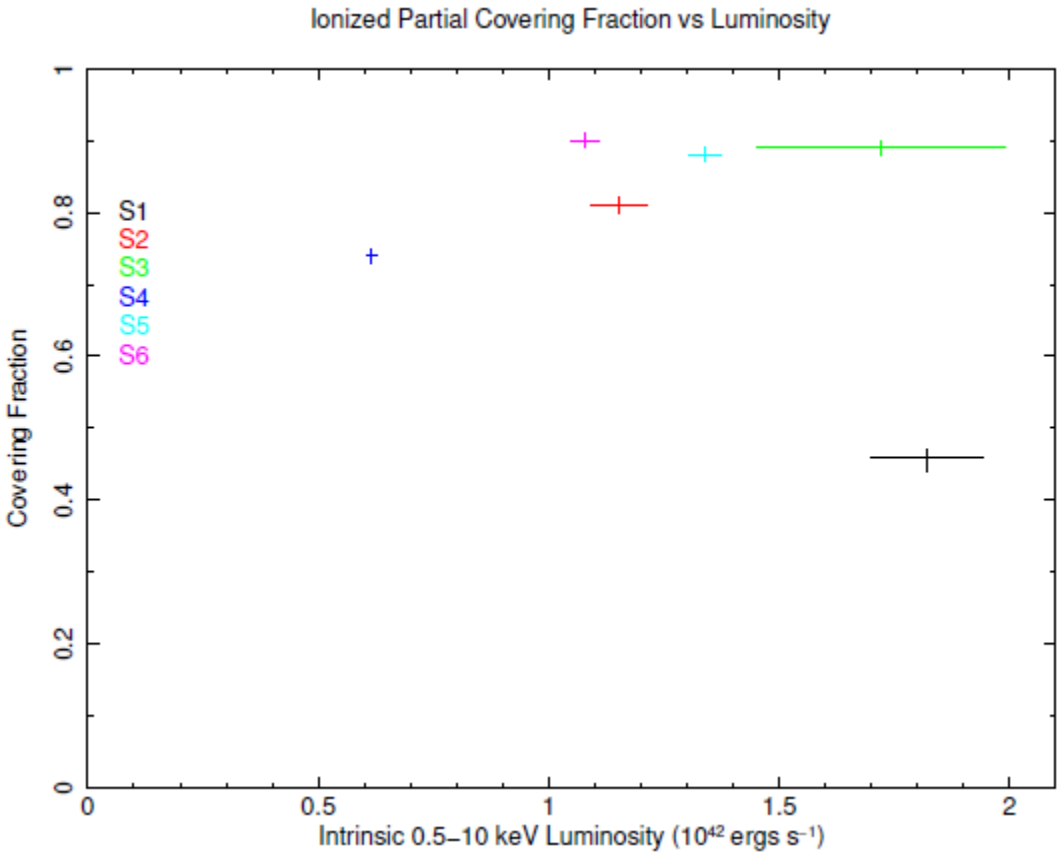

Figure 3.24: Ionized partial coverer covering fraction plotted against intrinsic luminosity. The covering fraction is nearly constant and high for less bright states, while it drops significantly for the brightest state S1.

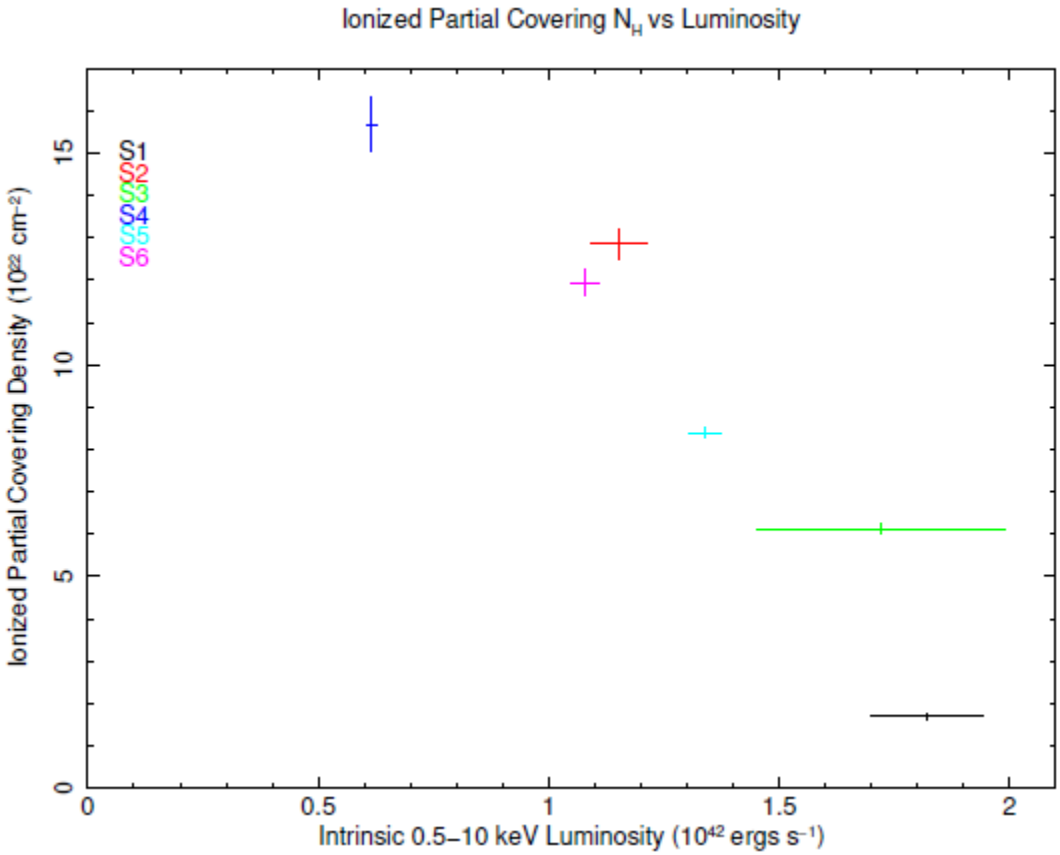

Figure 3.25: Ionized partial coverer column density plotted against intrinsic luminosity. Displays a general negative correlation.

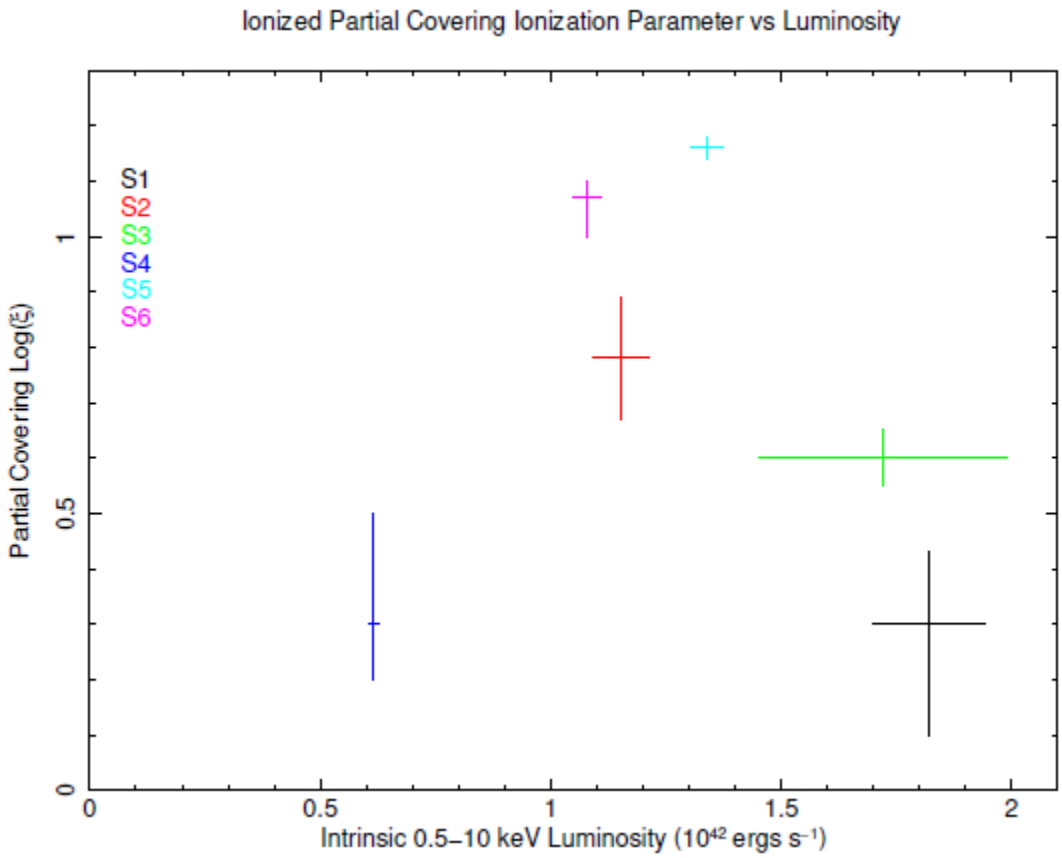

Figure 3.26: Ionized partial coverer ionization parameter plotted against intrinsic luminosity. No obvious trend is shown.

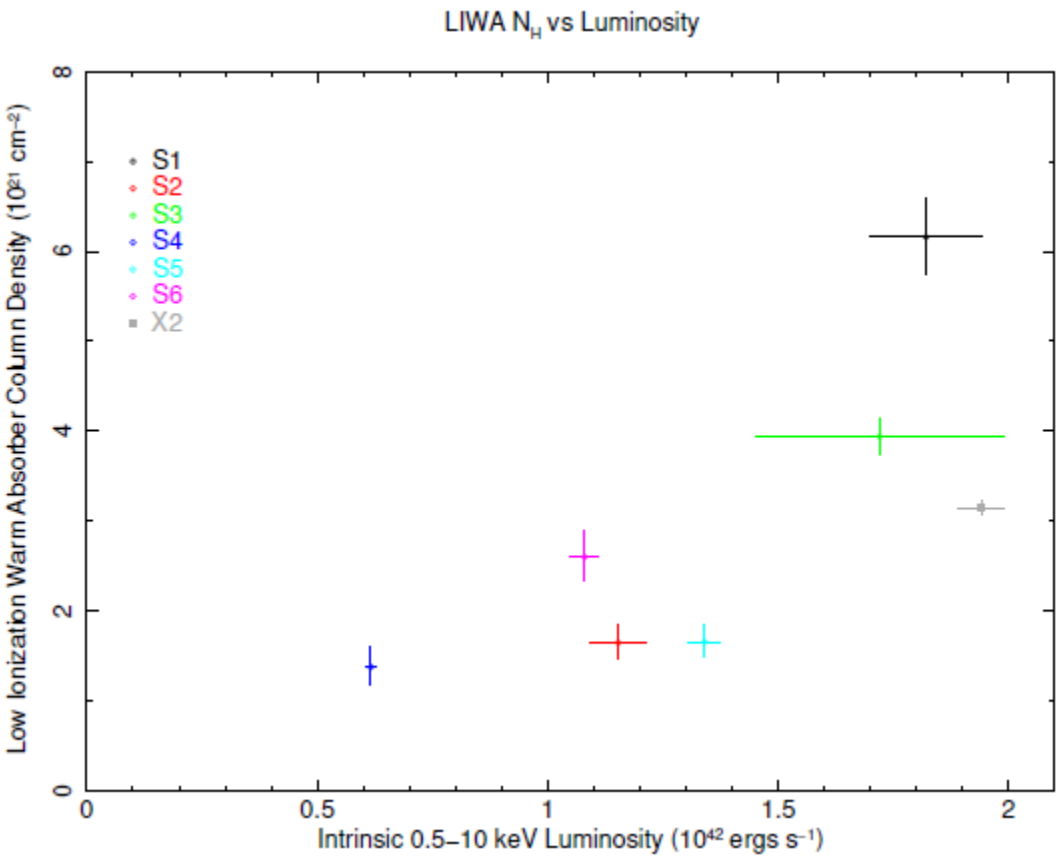

Figure 3.27: Low ionization warm absorber column density plotted against intrinsic luminosity. Displays a positive correlation.

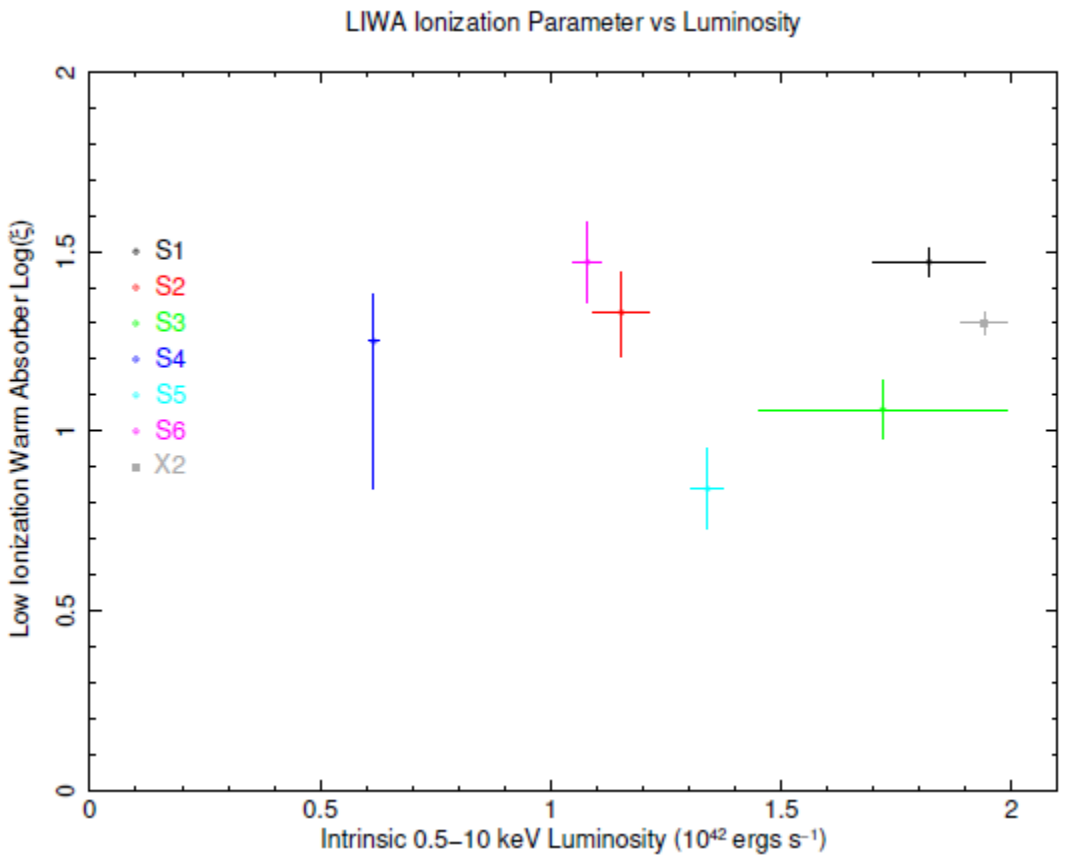

Figure 3.28: Low ionization warm absorber ionization parameter plotted against intrinsic luminosity. Displays no correlation.

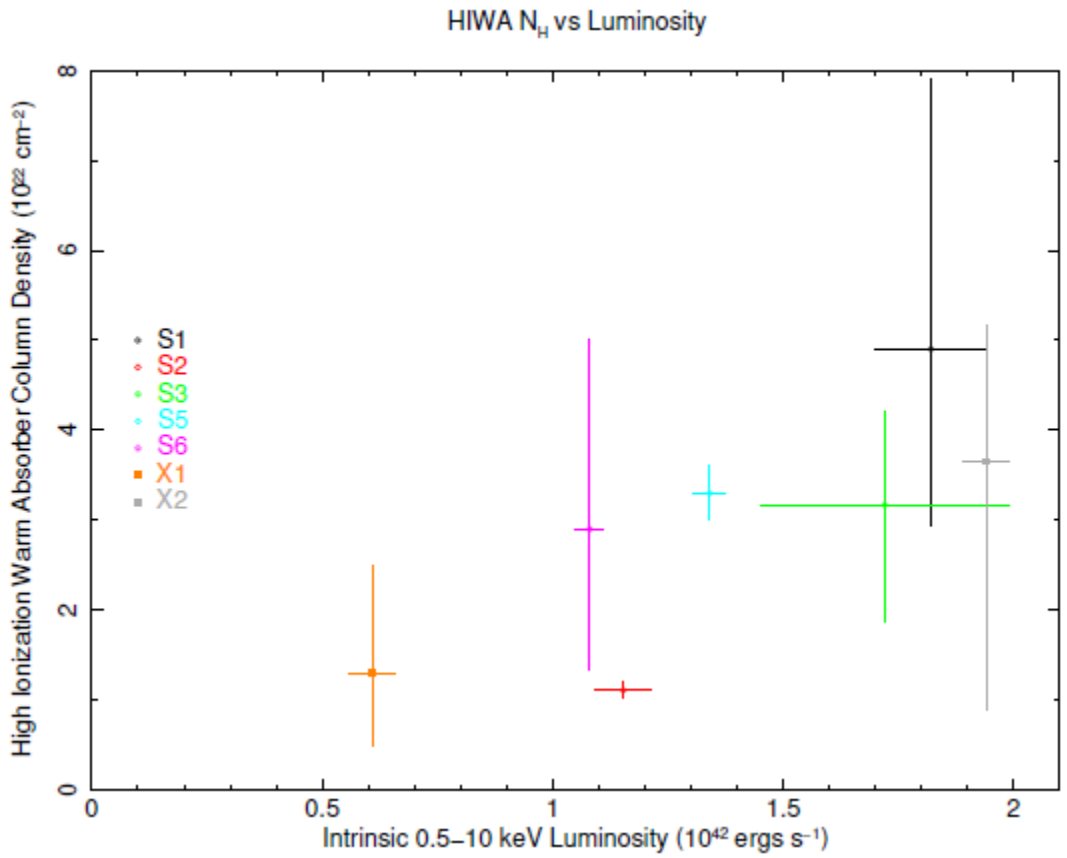

Figure 3.29: High ionization warm absorber ionization parameter plotted against intrinsic luminosity. Displays a positive correlation.

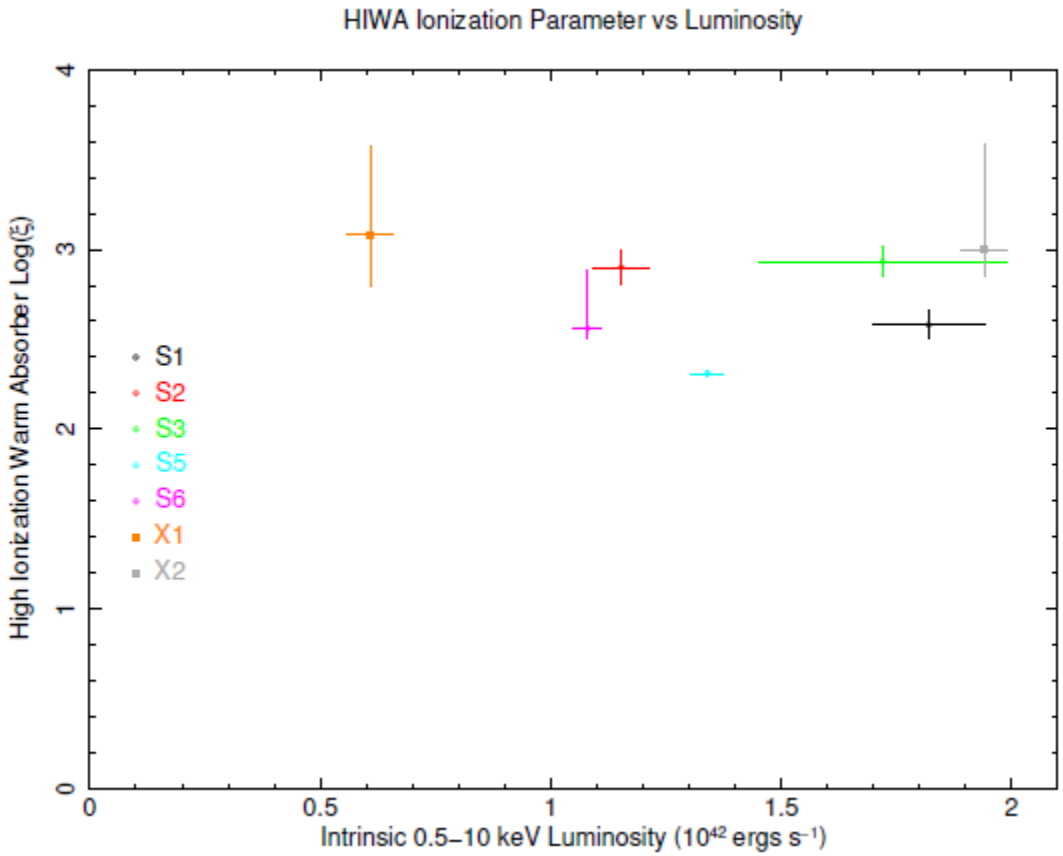

Figure 3.30: High ionization warm absorber ionization parameter plotted against intrinsic luminosity. Displays no correlation.

NGC 3227 TIME AVERAGED ANALYSIS PART II: THE NUSTAR AND LATER XMM-NEWTON OBSERVATIONS

This chapter is a modification of "Combined Analysis of X-Ray Spectra of NGC 3227 - Paper II", a paper submitted to The Astrophysical Journal. While much of it is taken from the paper, additions have been made such as the RGS Section 4.4.3. Some other portions of the paper have been removed for this dissertation, including much of the Introduction section, in order to avoid unnecessary repetition of parts from Chapter 3.

4.1 Introduction

The goal of our work is to create a model than can explain the broad behaviour of the source across multiple satellites and observations. After the work presented in Chapter 3 was carried out, our efforts turned to applying the model we presented in Section 3.5.2 to more recent observations of NGC 3227. For this general model to hold true, it must be able to explain subsequent observations that were not yet analyzed. Adjustments to the model, such as a change in the properties of absorbing material in the line of sight, are acceptable so long as the primary continuum mechanisms remain consistent. Thus, we take the model formed in Chapter 3 and apply it to the later observations concerned in this chapter.

In November and December 2016 the XMM-Newton and NuStar observatories took six joint observations of NGC 3227. The source was observed further by NuStar in January 2017. Turner et al. (2018) formed models for the last two observations, focusing on an occultation event that took place during the final observation. Lobban et al. (2020) considered all of these observations and constructed flux-resolved models for the campaign. Their main focus was variability studies, including the time lag behavior among different components.

Section 4.2 explains the data reduction and Section 4.3 gives timing analysis, while Section 4.4 presents the spectral analysis. Section 4.5 presents our unified physical model

which is consistent with Chapter 3 and the more recent observations, and comparison with other work. Summary and concluding remarks are given in Section 4.6.

4.2 Observations and Data Reduction

A summary of observation start times and exposure times is given in Table 4.1 for both XMM-Newton and NuStar. The six XMM-Newton and the first six NuStar observations were part of a joint campaign in late 2016. Note that while both XMM-Newton and NuStar observed the source on the same day during the campaign, the start times of the two missions are not equal (see Table 4.1). The last NuStar observation took place separately one and a half months after the end of the campaign.

The range of 0.3 - 10 keV was used for the European Photon Imaging Camera (EPIC) pn (Strüder et al. 2001) for the XMM-Newton observations. The Metal Oxide Semi-conductor (MOS) (Turner et al. 2001) cameras were not used as this dissertation focuses on the pn camera. The 1.7 - 2.1 keV range was omitted on the pn camera to eliminate calibration uncertainties in the region. For NuStar, the 10 - 50 keV range was used for both the Focal Plane Modules A and B (FPMA, FPMB, Harrison et al. (2013)) when paired with an XMM-Newton observation. For the final NuStar observation the 3 - 50 keV range was used for both the FPMA and FPMB.

Similar to Chapter 3, all Observational Data Files (ODF) were downloaded using the w3browse HEASARC tool from the NASA website. The observations are labeled with an "X" prefix if performed by XMM-Newton and an "N" prefix if observed by NuStar. The observations are numbered in sequential order based on the date of observation including both the joint campaign observations and the two previous observations 0101040301 (X1) and 0400270101 (X2). For consistency across all observations we analyzed throughout this dissertation, we continue the order with observation 078252201 labeled as X3 and the subsequent observations following the same labeling scheme. The NuStar observations

begin with 60202002002 labeled as N3 in order to keep consistent with the corresponding XMM-Newton observation for the campaign. Since the XMM-Newton and first six NuStar observations are taken together and used simultaneously in fitting, we refer to the combination of both observations as XN (e.g. combined 078252201 and 60202002002 are XN3).

XMM-Newton ODF data are processed using the xmmextractor command as included in Scientific Analysis System (SAS) version 16.0.0. NuStar ODF data are processed using the nuproducts command included with HEAsoft. All XMM-Newton observations used circular regions of 25" for the source and background. The source region was centered on the source while the background region was offset to avoid light from both NGC 3227 and NGC 3226. All NuStar observations used circular regions of 70" for the source and background with an appropriate background offset.

Keeping consistent with Chapter 3, our models adopt $H_o = 70, q_o = 0.0$, and $\Lambda_o = 0.73$. In each model all components are attenuated with a neutral hydrogen column density of $N_H = 1.99 \times 10^{20}$ cm^{-2} reported by the Galactic Column Density HEASARC tool (Angelini & Sabol 2021), with data taken from Kalberla et al. (2005). All fit parameters are given in the source rest frame and errors are reported at the 90% confidence level ($\Delta\chi^2 = 2.7$) unless otherwise stated.

4.3 Timing Analysis

4.3.1 Light Curves

The lights curves for each observation were extracted. The energy bands used were 0.3 - 10 keV for the XMM-Newton pn and 3 - 70 keV for the NuStar FPMA. For the XMM-Newton observations the 0.3 - 10 keV range was further split into 0.3 - 2 keV (soft) and 2 - 10 keV (hard) bands. Figures 4.1 - 4.6 display the light curves and hardness ratios for the six XMM-Newton observations and Figures 4.7 - 4.13 display the light curves for the seven NuStar

observations. In Figures 4.1, 4.2, and 4.6 we notice that the variability of each observation tends to increase when the flux is higher compared to lower flux regions of the observation. Furthermore, this variability is greatest in the soft band compared to the hard band. This is consistent with the results from Chapter 3, where the higher flux XMM-Newton and Suzaku observations displayed more variability. The flux of each observation should be high enough for time resolved analysis to be relevant (see Chapter 5). In particular, X5 displayed a sharp peak in flux during the latter half of the observation which will be studied further in Chapter 5.

Figures 4.7 - 4.12 show that in general the NuStar light curves mirror the results from the XMM-Newton observations, though with the appropriate time delay - compare, e.g., the two peaks in Figure 4.1 and Figure 4.7. The last NuStar observation, N9, appears to have two flares in about the first half of the observation but otherwise have flux levels consistent with the other observations (see Figure 4.13).

4.3.2 Flux-Flux Plot

The flux-flux plot for the XMM-Newton pn camera is shown in Figure 4.14. Compared to Figures 3.9 and 3.10 of Chapter 3, we note that all of observations take place exclusively in the high state. The first five observations show very similar characteristics to the X2 observation analyzed previously. We note that during X5, X7, and X8 when there are stronger flares the soft emission is stronger, which again indicates that flare emissions are softer.

The final observation, X8, displays a relatively higher soft count rate while the hard band (2 - 10 keV) is brighter than the typical trend of the rest of the observations. This feature can be explained by a removal of ionized absorbing material from the line of sight during the later half of the X8 observation. Ionized absorbers are more relevant in the 0.3 - 2 keV band than in the 2 - 10 keV band. Without the material absorbing the continuum,

the count rate of the soft band would increase while leaving the hard band more constant. This explanation is consistent with the work presented by Turner et al. (2018) and our own analysis of the observation (see Section 4.4).

4.4 Spectral Analysis

We carried out the spectral analysis of the pn data from the six XMM-Newton and the FPMA and FPMB data from the seven NuStar observations. All spectral fits were performed in XSPEC 12.10.1f. The method of spectral fitting is identical to Chapter 3, Section 3.5, except that NuStar data are also included. Initially, the 2.1 - 10 keV range of the XMM-Newton pn data was fitted. After that fitting, the 10 - 50 keV data from NuStar's both FPMA and FPMB were included. For N9, the 3 - 50 keV data from the FPMA and FPMB were used. Once the 2.1 - 50 keV model from the combined XMM-Newton and NuStar observations was formed, the result was extended to the soft band of the 0.3 - 1.7 keV of the XMM-Newton pn data. Then, the additional model components were added to form the final best fit for the 0.3 - 50 keV model for the broad band combined observations.

4.4.1 Hard 2.1 - 50 keV Band Analysis

The XMM-Newton 2.1 - 10 keV pn spectral fits began with a simple power law (model "zpowerlw") with galactic absorption (model "phabs"). Note that all redshifted model components are set to the redshift of NGC 3227 (z = 0.00386). Residuals below 3 keV were reduced with the addition of a local neutral absorber (model "zphabs"), and Fe Kα residuals near 6.4 keV were modeled with a gaussian (model "zgauss").

After the XMM-Newton 2.1 - 10 keV pn model was formed, the NuStar 10 - 50 keV FPMA and FPMB data were introduced. In order to simultaneously use the pn, FPMA, and FPMB data a constant (model "constant") was introduced to account for cross calibration. This constant was fixed to 1 for the pn and allowed to vary between 0.9 and 1.1 for both the

FPMA and FPMB. Residuals consistent with reflection were obvious. The power law and gaussian were replaced with an accretion disk reflection model with hard photon power law (model "Xillver" Garcia et al. (2013)). The model was then ready for the inclusion of the lower energy pn data (see next section).

For NuStar's N9 observation there were no pn data from XMM-Newton to be used simultaneously. Thus, the Xillver model was immediately applied (see Figure 4.15a). The calibration constant was fixed to 1 for the FPMA and allowed to vary between 0.9 and 1.1 for the FPMB. Absorption residuals remained which were reduced using a neutral absorber (Figure 4.15b). This formed an extremely good fit of the data ($\Delta\chi^2$/DOF = 566.32/562). Note that the density of the neutral absorber is much higher than in the other observations (see Table 4.2). Attempting to add warm absorber models proved fruitless as the fitting rejected them in favor of the neutral absorber. This observation took place one and half months after the N8 observations. The warm absorbers should be present but many of the features of warm absorption are more relevant below 3 keV than above it. It is likely that the lower ionization warm absorbers described previously can be added to the neutral absorption for N9, as that would cause the apparent density of the neutral absorber to increase. Alternatively, a particularily thick neutral cloud could have drifted into the line of sight in the fourty two days between the N8 and N9 observations.

4.4.2 Phemenological 0.3 - 50 keV Broad Band Analysis

Once the 2.1 - 50 keV data were modeled, we extended the pn data down to 0.3 keV. The 1.7 - 2.1 keV range of the pn data was omitted due to calibration uncertainties. In most of the observations positive residuals below 1.7 keV existed, implying the necessity of a soft excess component. An additional soft power law of index $\Gamma > 3$ was added to each observation which significantly improved the fit. Negative residuals around 0.7 - 0.9 keV remained which are consistent with warm absorption. We used an XSTAR table (XSTAR

v2.39; Kallman (2021)) generated by the "xstar2xspec" command. For all XSTAR tables, an α parameter equivalent to the hard photon index was used. One warm absorber proved insufficient, so a second warm absorber at higher ionization was added. Henceforth, these two are referred to as the low ionization warm absorber (LIWA) and high ionization warm absorber (HIWA). There still remained some absorption residuals. Similar to Lobban et al. (2020), a third warm absorber was added where the log of the ionization parameter is negative (NIWA). Afterwards, there existed positive residuals around 0.7 - 0.9. To model these we used a diffuse gas emission model, "mekal" (Liedahl et al. 1995; Mewe et al. 1985, 1986). The parameters are the temperature, hydrogen density in cm^{-3} which was kept at the default value of 1, elemental abundances, and the normalization. The included elements are C, N, O, Ne, Mg, Al, Si, S, Ar, Ca, Fe, and Ni and were all set to solar abundance. The normalization is given by Equation 4.1

$$Norm._{mek} = \frac{10^{-14}}{4\pi D^2} \int n_e n_H \, dV \tag{4.1}$$

where D is the distance to the source and n_e and n_H are the electron and H densities in cm^{-3}.

The final 0.3 - 50 keV model was thus formed. The observation XN6 required some additional absorption around 0.9 keV, and so an absorption edge was added. This feature is part of the warm absorbers and it is similar to the absorption edge applied for the X2 observation in Markowitz et al. (2009) and Chapter 3.

There was an exception in the XN8 observation. We were not able to form a good fit of the full time averaged spectrum. Absorption features in the early part of the observation are too different from the later half to form a single model for the full observation. In order to model this observation we cut it in half temporally. The first half of the observation is labeled as XN8 Low and the last half is labeled as XN8 High. Turner et al. (2018) studied

this observation in much more detail and described that as a cloud of absorbing material passing through the line of sight during the first half of this observation. The total density of the absorbers was lower in XN8 High than in XN8 Low. Our results are consistent with the analysis by Turner et al. (2018).

Progressive residuals are given for all broad band observations in Figures 4.16 - 4.22, and model parameters for all observations are given in Table 4.2. P-values for the fits are also displayed in Table 4.2 and are particularily good for observations XN4, XN5, XN7, XN8 Low, and N9. The observations XN3 and XN8 High had rougher p-values, and XN6 strugged to get a good fit.

4.4.3 XMM-Newton RGS Analysis

We approached the RGS analysis for the later XMM-Newton observations in the same manner as we did for X2 in Chapter 3. First, we apply a photoabsorbed power law to the spectrum and record obvious emission lines. Then, we replace the simple power law with the model formed in Section 4.4.2 to the spectrum. The lines detected across the six observations were C VI Lyα (368 eV), Ca XI (407 eV), N VI (430 eV), C VI Lyβ (436 eV), N VII (500 eV), O VII (574 eV), O VIII Lyα (653 eV), Fe XVII (735 eV and 775 eV), O VII (775 eV), Fe XVIII (853 eV and 875 eV), Ne IX (922 eV), Ne X (1022 eV), and Mg XI (1352 eV). However, we were unable to witness all of them in each observation. The C VI Lyα and Lyβ were seen in all observations. Observation X4 detected Ca XI and N VI. All except X3 detected N VII and the 574 eV O VII line. The O VII Lyα was detected by all. The observation X7 was able to detect Fe XVII at 735 and 775 eV although the 775 line is likely blended with an O VII line at the same energy. Fe XVIII was detected at 853 eV by X3 and 875 eV by X4 and X7. Ne IX was detected by all at 922 eV. Ne X was detected at 1022 eV by X3, X5, X7, and X8. Only X7 was able to detect Mg XI at 1352 keV.

Once the model formed in Section 4.4.2 (broad band model) was applied to each

spectrum, we froze the parameters of the Xillver model as we did previously for X2. Other parameters were initially allowed to vary. Most spectra were insensitive to the HIWA, so it was fixed to the Section 4.4.2 model parameters in observations X3, X5, X6, and X7. The densitiy of the NIWA was similarily tempermental and fixed to the Section 4.4.2 model in observations X3, X6, X7, and X8. As was seen in the previous chapter, the fits were generally rougher than the pn and NuStar model. The fit statistics were χ^2/DOF = 991.92/886 for X3, 1494.96/1444 for X4, 2161.75/1999 for X5, 2158.86/1939 for X6, 3295.44/2862 for X7, and 2517.54/1931 for X8.

The neutral absorption remained the same order of magnitude and differed by up to 2×10^{20} cm^{-2}, remaining largely consistent with the broad band model. The two observations that did not fix the HIWA to last section's model were X4 and X8. For X4, the best fit value for the density was lower than the broadband model but their error bars overlap. The ionization parameter is very similar. For X8, the density did not change from the X8 Low best fit and the ionization parameter was almost the same as its value in X8 High. This is reasonable as the RGS data was not split in half temporally, instead using the entire observation. The NIWA density was fixed in most of the observations but varied in X4 and X5. The error bars did not overlap for X4 but were within 2.1 $\times$ 10^{21} cm^{-2}. Error bars overlapped for X5. The ionization parameter of the NIWA was lower in all observations except X7, where it was higher. In all situations, the difference in NIWA ionization parameters between the RGS and broadband models are < 1, with the largest discrepancy being X4. The LIWA density generally increased with time during the observations, a trend not displayed in the broadband model. As such, it's likely an artifact of the fitting and not a characteristic of the source itself. The observations X3 and X4 density best fits were lower than the broadband model while the X6 and X7 densities were higher. The X5 density was somewhat higher but not to the extent of the other observations. The density for X8 was between the X8 Low and X8 High broad band model values as expected.

The soft power law index was more variable. While most of the values remained above $\Gamma = 3$, X3 markedly had a low best fit value for $\Gamma = 2.84$. Fixing this value to the broad band model significantly worsened the fit with $\delta\chi^2 = +123.89$. This was the largest inconsistency between the broad band and RGS model fits. The error bars do not quite overlap for the X4, X5, and X7 observations, but the difference is < 0.30. The Γ for X6 and X8 were similar to the broad band model. The mekal temperatures were largely consistent, with the error bars overlapping in observations X3, X5, and X6. The observations X4 and X7 had a lower best fit value than the broad band model but the descrepancy was < 30 eV. The observation X8 displayed the largest descrepancy of ~ 50 eV. In the broad band model, the best fit mekal temperature was the highest of all of the observations while here it is in line with the values from other observations. Forcing the value of the temperature to similar to the broad band model (kT = 230 eV) yeilded a worsening of the fit only by $\delta\chi^2 = 21.97$, so this descrepancy can be explained by the relative insensitivity of the mekal model by values differing by 10s of eVs.

With the exception of X3's low power law index, the differences between the broad band and RGS models are relatively small and can be explained by the data being collected by different instruments. Model parameters for the RGS fits are displayed in Table 4.3. Residuals and detected lines are shown in Figures 4.23 - 4.28.

4.4.4 Alternative Models for Soft Excess

The soft excess present in the XMM-Newton observations was modeled with a steep power law in Section 4.4.2. As an alternative to the power law model, we consider blackbody, warm Comptonization, and thermal bremsstralung as possible explanations for this emission. For information on the parameters and equations of these models refer to Section 3.6.

The soft power law was replaced with a redshifted blackbody (model "zbbody"). This produced some success with $\chi^2/DOF = 1203.35/1070$ for XN3, 1855.39/1705 for XN5,

2028.92/1774 for XN6, 1776.22/1690 for XN7, 1120.73/1057 for XN8 Low, and 1287.11/1205 for XN8 High. However, XN4 was not able to achieve a succesful fit with χ^2/DOF = 2009.77/1531. Furthermore, the resulting blackbody temperatures were kT = 90 - 200 eV while physically reasonable temperatures are around kT = 10 eV (see Bechtold et al. (1987); Gierliński & Done (2004)). For these reasons this model was abandoned.

A warm Componization model ("compST", Sunyaev & Titarchuk (1980)) was then applied. Soft emission is due to reprocessing of UV or EUV photons emitted by the disk by the warm atmosphere of the inner regions of the disk. This model was successful in explaining the soft excess in Chapter 3. Fits were found for all observations (χ^2/DOF = 771.43/708 for XN3, 1273.91/1204 for XN4, 1453.30/1392 for XN5, 1605.29/1438 for XN6, 1437.01/1409 for XN7, 909.40/943 for XN8 Low, and 1150.72/1057 for XN8 High). Fit parameters are listed in Table 4.4.

A thermal bremsstralung model ("zbremss") was also considered. It produced succesful fits with χ^2/DOF = 1201.01/1068 for XN3, 1711.40/1533 for XN4, 1857.88/1703 for XN5, 2032.62/1772 for XN6, 1810.55/1692 for XN7, 1058.21/1056 for XN8 Low, and 1299.88/1207 for XN8 High. However, the temperatures were inconsistent, ranging from kT = 170 eV to 670 eV. Combined with the difficulty this model displayed in Chapter 3, we consider this model to be unlikely.

4.5 Discussion

4.5.1 The Broad Band Unified Model

In Chapter 3 we analyzed the data of NGC 3227 from earlier major observations, six by Suzaku and two by XMM-Newton, obtained during the period of 2000 - 2008. That led to our unified model consistent with all these observations by two different missions. This chapter, that work was extended to the more recent observation campaign utilizing both the XMM-Newton and NuStar which was carried out in 2016 and 2017. The purpose of our

work is to obtain a broad band universal model consistent with all those observations by multiple missions over the longer period. We examined whether our earlier model applies to the more recent multiple observations by not only XMM-Newton, but also NuStar. That is useful because the NuStar provides a superior and wider range of the higher energy bands beyond 10 keV, which is more sensitive than the Suzaku data used in the previous chapter.

In the current studies, we first note that the source was in a high state during all observations. Compare, e.g., the current flux-flux plots in Figure 4.14 with those in Figure 3.10. Furthermore, comparing current Figures 4.1 - 4.13 with the light curves of S1 and X2 in Chapter 3 (Figures 3.1 and 3.8) both in the high state, it is noted that in both cases the source is highly variable and similar. In Chapter 3 it was noted that the hard power law index generally increases with luminosity (see Figure 3.22). That agrees with our current results with the hard power law index mostly around 1.6 - 1.8 (see Table 4.2), as expected when the source is stronger. The data of all current observations require the soft excess, as expected since all of them are in the high state. Also similar to Chapter 3, we find that here the soft excess is consistent with both steep power law and warm Compton model (see Sections 4.4.2 and 4.4.4).

The flux-flux plot of Figure 4.14 is similar mostly to the high state case in Chapter 3. One exception is X8, the last of the 2016 XMM-Newton and NuStar campaign. The difference is that the X8 exhibits a more gradual slope. The soft emission is relatively less for a given hard flux, as compared with the rest of the observations (see Figure 4.14). That is consistent with the interpretation by some other authors, e.g., Turner et al. (2018) and Lobban et al. (2020), that this is due to the additional absorption of the soft emission by the passing of a cloud through the line of sight.

The observation N9 is the last solo NuStar observation in 2017. It is still in the high state but the soft excess (which is to appear at less than $\sim$ 1 keV) is missing because the NuStar spectrum does not cover the soft bands below 3 keV. Otherwise, the primary

power law emission is similar to the rest of the observations, with $\Gamma = 1.73$, as expected in the high state. The effect of the surrounding material is, however, simpler where the neutral absorption dominates (see Figure 4.15 and Table 4.2). The change of the surrounding material is quite reasonable because this observation was made about one and a half months after the last of the 2016 campaign and the features of warm absorption are more apparent below the FPMA and FPMB's minimum sensitive energy.

A major difference between the current results and Chapter 3 is that the effects of the surrounding material are more complex in Chapter 3, where different observations often showed different absorption and emission features. Our current case is somewhat simpler with less additional complex features. The observation XN6 is the only one that requires additional absorption. That is understandable noting that the current case is all in the high state where, in our model, the coronal primary emission region is larger and hence the outer portion of the emission region is covered by the outer less dense portion of the line-of-sight clouds, which can be less complicated than the central region. Another difference is that the current case shows three warm absorbers, the LIWA, HIWA, and additional third NIWA, instead of two which was the case previously. However, these differences of the features caused by the surrounding material can be expected quite well because the current set of observations took place eight years after those in Chapter 3, and the environment can change easily during those years.

In conclusion, the unified physical model for the central engine offered in Chapter 3 is still valid in the current case with the recent observations.

4.5.2 Comparison With Other Work

Comparison with the older work was covered in detail in Chapter 3, and therefore we restrict our discussion mainly to the latest papers. Lobban et al. (2020) carried out mainly the X-ray variability analysis of the data from the same observations which are used in our

current studies, the 2016 XMM-Newton and NuStar observation campaign and the 2017 NuStar observation. Turner et al. (2018) concentrated on the last two observations of the 2016 campaign. During all these observations NGC 3227 was in the bright state. Their primary emission from the central source consists of a power law with Γ of 2 in Turner et al. (2018) and with 1.4 - 1.7 in Lobban et al. (2020), with a blackbody (Turner et al. 2018) or a Comptonized disk blackbody (Lobban et al. 2020) added as a soft excess. The primary emission model by Lobban et al. (2020) is essentially consistent with our model at the bright state, while the Turner et al. (2018) model is somewhat simpler.

Both of these authors agree with our finding on the primary emission from the center: (i) softer when brighter behavior of the power law component, (ii) the bulk of the short variability being continuum driven, and (iii) presence of a strong variable soft excess. The effects of the surrounding material are also similar, though the method adopted was somewhat different. We adopted the method from Chapter 3 which essentially follows Markowitz et al. (2009).

The major difference between the work by Lobban et al. (2020) and our current work is the difference of our focus, goal and approach. Our focus is the extension of the time-averaged spectral studies of Chapter 3 to the sets of new observations. Our goal is to test the unified physical model proposed in Chapter 3 (see Section 3.8.1). On the other hand, the interest and content of Lobban et al. (2020) are different, the time variability studies, including the time-lag problem, etc. These authors adopted mainly the flux-resolved analysis. On the other hand, they did not adopt (except for the X7 observation) the time-averaged spectral analysis, the major method we adopted. Also, Lobban et al. (2020) used the PEXRAV reflection model which is inferior to the more modern Xillver model that we used.

4.6 Summary and Concluding Remarks

The studies in Chapter 3 are extended to the later observations of NGC 3227 in the 2016 XMM-Newton plus NuStar campaign and the 2017 NuStar observation, by carrying out the time-averaged spectral analysis for these more recent observations. Combined with the Chapter 3 results we constructed a universal physical model for NGC 3227 which is valid for all observations of this source during the long 2000 to 2017 period by multiple X-ray observatories covered by both Chapter 3 and Chapter 4.

Chapter 4 Tables

Table 4.1: XMM-Newton and NuStar X3 - X8 and N3 - N9 observation summary: Start times (UTC) and exposure times (ks) are given.

Observation	Year	Start Time (UTC)	Total Exposure Times (ks)
078252201 (X3)	2016	Nov. 09 12:51:03	92 .0
078252301 (X4)	2016	Nov. 25 03:36:31	74 .0
078252401 (X5)	2016	Nov. 29 02:48:55	84.0
078252501 (X6)	2016	Dec. 01 17:00:00	87.0
078252601 (X7)	2016	Dec. 05 21:29:20	86.6
078252701 (X8)	2016	Dec. 09 14:28:03	87.9
60202002002 (N3)	2016	Nov. 09 13:16:08	49.8
60202002004 (N4)	2016	Nov. 25 09:26:08	42.5
60202002006 (N5)	2016	Nov. 29 16:31:08	39.7
60202002008 (N6)	2016	Dec. 01 10:31:08	41.8
60202002010 (N7)	2016	Dec. 05 09:31:08	40.9
60202002012 (N8)	2016	Dec. 09 08:36:08	39.3
60202002014 (N9)	2017	Jan. 21 23:51:09	47.6

Table 4.2: The Broad band 0.3 - 70 keV time averaged model parameters from the combined XMM-Newton and NuStar observations XN3 - N9.

Component	Parameter	XN3	XN4	XN5	XN6	XN7	XN8 Low	XN8 High	N9
Neutral Absorption	N_H $\left(10^{20} cm^{-2}\right)$	$2.75^{+0.26}_{-0.26}$	$6.15^{+0.29}_{-0.31}$		$9.27^{+0.29}_{-0.29}$	$4.05^{+0.17}_{-0.17}$	$7.50^{+0.17}_{-0.16}$	$7.98^{+0.25}_{-0.25}$	$309.30^{+0.23}_{-0.22}$
Xillver[a]	Γ_{Hard}	$1.55^{+0.02}_{-0.02}$	$1.48^{+0.01}_{-0.01}$	$1.59^{+0.01}_{-0.01}$	$1.70^{+0.01}_{-0.01}$	$1.70^{+0.01}_{-0.01}$	$1.69^{+0.01}_{-0.01}$	$1.81^{+0.01}_{-0.01}$	$1.73^{+0.01}_{-0.01}$
	Log ξ	< 1.32	< 1.02	< 1.18	< 0.09	$1.32^{+0.07}_{-0.13}$	< 0.40	$1.31^{+0.10}_{-0.24}$	$1.51^{+0.18}_{-0.79}$
	Reflection Fraction	$0.95^{+0.09}_{-0.08}$	< 0.58	$0.79^{+0.04}_{-0.04}$	$0.88^{+0.05}_{-0.06}$	$0.71^{+0.05}_{-0.04}$	$0.87^{+0.07}_{-0.07}$	$0.67^{+0.07}_{-0.07}$	$0.80^{+0.05}_{-0.05}$
	Norm. $\left(10^{-4}\right)$	$1.74^{+0.02}_{-0.02}$	$1.63^{+0.01}_{-0.01}$	$1.70^{+0.05}_{-0.05}$	$2.06^{+0.01}_{-0.01}$	$2.37^{+0.01}_{-0.01}$	$2.19^{+0.01}_{-0.01}$	$2.69^{+0.02}_{-0.02}$	$3.43^{+0.03}_{-0.03}$
Fe Kα Correction[b]	σ		$6.52^{+0.02}_{-0.02}$						
	Norm. $\left(10^{-5}\right)$		$2.31^{+0.39}_{-0.39}$						
Soft Power Law[a]	Γ_{Soft}	$3.80^{+0.03}_{-0.03}$	$3.72^{+0.03}_{-0.03}$	$3.83^{+0.02}_{-0.02}$	$3.84^{+0.03}_{-0.03}$	$3.73^{+0.02}_{-0.02}$	$3.76^{+0.02}_{-0.02}$	$3.75^{+0.03}_{-0.03}$	
	Norm. $\left(10^{-3}\right)$	$14.18^{+0.20}_{-0.20}$	$2.53^{+0.04}_{-0.04}$	$4.58^{+0.06}_{-0.06}$	$3.46^{+0.06}_{-0.06}$	$5.95^{+0.07}_{-0.07}$	$16.74^{+0.19}_{-0.19}$	$8.02^{+0.12}_{0.12}$	
Mekal[c]	kT (eV)	$156.44^{+8.14}_{-6.72}$	$187.08^{+7.84}_{-7.02}$	$179.86^{+4.17}_{-3.93}$	$180.43^{+12.40}_{-15.25}$	$199.81^{+7.71}_{-6.47}$	$234.76^{+3.59}_{-3.49}$	$227.94^{+5.49}_{-4.94}$	
	Norm. $\left(10^{-3}\right)$	$12.13^{+1.04}_{-1.04}$	$0.84^{+0.13}_{-0.13}$	$2.25^{+0.25}_{-0.26}$	$0.80^{+0.21}_{-0.21}$	$1.81^{+0.21}_{-0.20}$	$15.86^{+0.54}_{-0.53}$	$4.80^{+0.34}_{-0.34}$	
Negative Ion. Warm Abs.	N_H $\left(10^{21} cm^{-2}\right)$	$3.36^{+1.30}_{-1.06}$	$3.32^{+1.42}_{-1.01}$	$2.65^{+0.17}_{-0.17}$	> 4.63	$0.84^{+0.02}_{-0.02}$	> 0.28	> 4.36	
	Log ξ	$-1.28^{+0.01}_{-0.01}$	$-1.92^{+0.05}_{-0.05}$	$-0.59^{+0.02}_{-0.02}$	$-1.82^{+0.13}_{-0.09}$	$-1.01^{+0.07}_{-0.01}$	$-1.94^{+0.03}_{-0.04}$	$-1.90^{+0.05}_{-0.06}$	
Low Ion. Warm Abs.	N_H $\left(10^{21} cm^{-2}\right)$	$3.18^{+0.18}_{-0.18}$	$2.07^{+0.18}_{-0.21}$	$2.27^{+0.10}_{-0.09}$	$2.87^{+0.09}_{-0.09}$	$2.87^{+0.13}_{-0.12}$	$17.38^{+0.57}_{-0.56}$	$4.55^{+0.26}_{-0.28}$	
	Log ξ	$0.17^{+0.02}_{-0.02}$	< 0.07	$1.08^{+0.06}_{-0.06}$	$1.13^{+0.03}_{-0.03}$	$1.05^{+0.04}_{-0.05}$	$1.03^{+0.01}_{-0.01}$	$1.00^{+0.02}_{-0.02}$	
High Ion. Warm Abs.	N_H $\left(10^{21} cm^{-2}\right)$	$66.65^{+7.13}_{-6.62}$	$1.80^{+0.17}_{-0.34}$	$14.64^{+3.60}_{-2.89}$	$47.19^{+11.13}_{-9.18}$	$21.41^{+0.23}_{-0.21}$	$121.13^{+9.75}_{-8.79}$	$67.47^{+2.60}_{-2.54}$	
	Log ξ	$2.59^{+0.02}_{-0.02}$	$2.60^{+0.10}_{-0.09}$	$2.86^{+0.02}_{-0.02}$	$2.90^{+0.01}_{-0.01}$	$2.77^{+0.02}_{-0.02}$	$2.60^{+0.01}_{-0.01}$	$2.49^{+0.01}_{-0.01}$	
Absorption Edge	Energy (keV)				$0.94^{+0.02}_{-0.02}$				
	Depth $\left(10^{-2}\right)$				$7.42^{+1.14}_{-1.14}$				
FPMA Calibration	Constant	$0.96^{+0.02}_{-0.02}$	$1.07^{+0.02}_{-0.02}$	$1.03^{+0.02}_{-0.02}$	$1.09^{+0.01}_{-0.02}$	$1.07^{+0.02}_{-0.02}$	$1.06^{+0.01}_{-0.02}$	$1.07^{+0.03}_{-0.03}$	
FPMB Calibration	Constant	$1.01^{+0.02}_{-0.02}$	$1.10_{-0.01}$	$1.03^{+0.02}_{-0.02}$	$1.09^{+0.01}_{-0.02}$	$1.10_{-0.01}$	$1.08^{+0.02}_{-0.01}$	$1.08^{+0.03}_{-0.03}$	$1.00^{+0.01}_{-0.01}$
	χ^2/DOF	762.36/709	1279.78/1205	1456.53/1398	1855.69/1707	1565.95/1490	1289.20/1300	1166.22/1058	566.32/562
	P-value	0.0807	0.0660	0.1347	0.0065	0.0837	0.5790	0.0110	0.44125

[a]Xillver and Power law normalizations are photons $\mathrm{keV}^{-1}\mathrm{cm}^{-2}\mathrm{s}^{-1}$ at 1 keV.

[b]Gaussian normalization is total photons $\mathrm{cm}^{-2}\mathrm{s}^{-1}$ in the line of sight.

[c]Mekal normalization is $10^{-14}/4\pi(D_A(1+z))^2) \int n_e n_H \, dV$ where D_A is the angular diameter distance to the source (cm), n_e and n_H are the electron and H densities (cm^{-3}), respectively.

Table 4.3: XMM-Newton X3-X8 RGS model parameters. Some parameters of the NIWA and HIWA are fixed to the Section 4.4.2 model.

Component	Parameter	X3	X4	X5	X6	X7	X8
Neutral Absorption	N_H $\left(10^{20} cm^{-2}\right)$	< 4.03	$4.22^{+1.21}_{-1.21}$		$7.94^{+0.74}_{-0.74}$	$4.61^{+0.43}_{-0.43}$	$8.69^{+0.67}_{-0.67}$
Soft Power Law[a]	Γ_{Soft}	$2.84^{+0.11}_{-0.04}$	$3.96^{+0.19}_{-0.19}$	$3.58^{+0.11}_{-0.11}$	$3.80^{+0.12}_{-0.12}$	$3.35^{+0.08}_{-0.08}$	$3.69^{+0.11}_{-0.11}$
	RGS1 Norm. $\left(10^{-3}\right)$	$21.96^{+0.26}_{-0.26}$	$1.25^{+0.08}_{-0.08}$	$4.15^{+0.13}_{-0.13}$	$4.34^{+0.46}_{-0.44}$	$10.43^{+0.32}_{-0.28}$	$8.02^{+0.30}_{-0.30}$
	RGS2 Norm. $\left(10^{-3}\right)$	$20.43^{+0.30}_{-0.28}$	$1.30^{+0.09}_{-0.09}$	$3.60^{+0.14}_{-0.14}$	$4.38^{+0.48}_{-0.46}$	$10.42^{+0.32}_{-0.32}$	$7.99^{+0.32}_{-0.32}$
Mekal[b]	kT (eV)	$183.30^{+23.78}_{-21.67}$	$141.32^{+9.50}_{-15.45}$	$175.18^{+13.27}_{-17.78}$	$176.09^{+12.67}_{-24.76}$	$155.24^{+18.74}_{-12.72}$	$178.04^{+1.04}_{-2.25}$
	RGS1 Norm. $\left(10^{-3}\right)$	$0.95^{+0.36}_{-0.35}$	$1.49^{+0.22}_{-0.22}$	$0.96^{+0.19}_{-0.19}$	$1.32^{+0.26}_{-0.25}$	$2.11^{+0.34}_{-0.34}$	$2.17^{+0.41}_{-0.41}$
	RGS2 Norm. $\left(10^{-3}\right)$	$1.43^{+0.55}_{-0.49}$	$0.73^{+0.51}_{-0.51}$	$0.70^{+0.35}_{-0.35}$	< 0.84	$1.83^{+0.85}_{-0.85}$	$2.22^{+0.77}_{-0.77}$
Negative Ion. Warm Abs.	N_H $\left(10^{21} cm^{-2}\right)$	$3.36^{+1.30}_{-1.06}(fixed)$	$1.10^{+0.15}_{-0.18}$	$2.93^{+0.40}_{-0.38}$	$> 4.63(fixed)$	$0.84^{+0.02}_{-0.02}(fixed)$	$> 4.36(fixed)$
	Log ξ	$-1.08^{+0.01}_{-0.02}$	$-1.05^{+0.14}_{-0.15}$	$-0.22^{+0.06}_{-0.06}$	$-1.52^{+0.10}_{-0.17}$	$-1.31^{+0.03}_{-0.03}$	$-1.61^{+0.10}_{-0.16}$
Low Ion. Warm Abs.	N_H $\left(10^{21} cm^{-2}\right)$	$0.72^{+0.05}_{-0.05}$	$0.60^{+0.20}_{-0.16}$	$2.13^{+0.37}_{-0.33}$	$3.71^{+0.45}_{-0.42}$	$4.53^{+0.38}_{-0.37}$	$5.58^{+0.61}_{-0.58}$
	Log ξ	$0.37^{+0.21}_{-0.16}$	$0.38^{+0.26}_{-0.26}$	$1.49^{+0.08}_{-0.08}$	$1.39^{+0.05}_{-0.05}$	$1.28^{+0.03}_{-0.03}$	$1.39^{+0.05}_{-0.04}$
High Ion. Warm Abs.	N_H $\left(10^{21} cm^{-2}\right)$	$66.65^{+7.13}_{-6.62}(fixed)$	$0.83^{+0.70}_{-0.39}$	$14.64^{+3.60}_{-2.89}(fixed)$	$47.19^{+11.13}_{-9.18}(fixed)$	$21.41^{+0.23}_{-0.21}(fixed)$	$121.13^{+23.76}_{-4.19}$
	Log ξ	$2.59^{+0.02}_{-0.02}(fixed)$	$2.54^{+0.25}_{-0.25}$	$2.86^{+0.02}_{-0.02}(fixed)$	$2.90^{+0.01}_{-0.01}(fixed)$	$2.77^{+0.02}_{-0.02}(fixed)$	$2.48^{+0.03}_{-0.03}$
	χ^2/DOF	991.92/886	1494.96/1444	2161.75/1999	2158.86/1939	3295.44/2862	2517.54/1931

[a]Power law normalization is photons keV^{-1}cm^{-2}s^{-1} at 1 keV.

[b]Mekal normalization is $10^{-14}/4\pi(D_A(1+z))^2) \int n_e n_H \, dV$ where D_A is the angular diameter distance to the source (cm), n_e and n_H are the electron and H densities (cm^{-3}), respectively.

Table 4.4: XN3 - XN8 warm comptonization model parameters.

Component	Parameter	XN3	XN4	XN5	XN6	XN7	XN8 Low	XN8 High
Neutral Absorption	N_H $\left(10^{20} cm^{-2}\right)$	$4.85^{+0.49}_{-0.48}$	$5.64^{+0.38}_{-0.37}$	$4.28^{+0.23}_{-0.24}$	$8.33^{+0.32}_{-0.33}$	$4.46^{+0.26}_{-0.26}$	$7.73^{+0.69}_{-0.62}$	$7.72^{+0.50}_{-0.50}$
Xillver[a]	Γ_{Hard}	$1.73^{+0.01}_{-0.01}$	$1.51^{+0.01}_{-0.01}$	$1.70^{+0.01}_{-0.01}$	$1.74^{+0.01}_{-0.01}$	$1.77^{+0.01}_{-0.01}$	$1.73^{+0.01}_{-0.01}$	$1.74^{+0.01}_{-0.01}$
	Log ξ	$1.07^{+0.22}_{-0.12}$	< 1.13	$1.06^{+0.18}_{-0.30}$	$1.29^{+0.38}_{-0.34}$	$1.35^{+0.04}_{-0.03}$	$< 1.42^{+0.22}_{-0.33}$	$1.00^{+0.05}_{-0.24}$
	Reflection Fraction	$1.03^{+0.09}_{-0.07}$	$0.61^{+0.13}_{-0.21}$	$0.91^{+0.06}_{-0.05}$	$0.90^{+0.05}_{-0.04}$	$0.85^{+0.04}_{-0.04}$	$0.89^{+0.06}_{-0.06}$	$0.69^{+0.07}_{-0.06}$
	Norm. $\left(10^{-4}\right)$	$2.07^{+0.02}_{-0.02}$	$1.55^{+0.01}_{-0.01}$	$1.80^{+0.01}_{-0.01}$	$2.20^{+0.01}_{-0.01}$	$2.25^{+0.01}_{-0.01}$	$2.16^{+0.01}_{-0.01}$	$2.45^{+0.01}_{-0.01}$
Fe Kα Correction[b]	Norm. $\left(10^{-5}\right)$		$1.75^{+0.35}_{-0.36}$					
Comptonized Component[c]	kT (eV)	$355.42^{+6.43}_{-6.18}$	$324.96^{+5.41}_{-4.81}$	$300.47^{+2.29}_{-2.30}$	$307.88^{+3.19}_{-3.23}$	$318.49^{+3.19}_{-2.55}$	$330.77^{+7.85}_{-8.31}$	$200.00^{+3.62}_{-3.81}$
	Depth	$19.26^{+0.27}_{-0.26}$	$20.44^{+0.23}_{-0.23}$	$20.11^{+0.12}_{-0.12}$	$19.42^{+0.16}_{-0.17}$	$17.09^{+0.13}_{-0.12}$	$16.07^{+0.29}_{-0.30}$	$25.16^{+0.51}_{-0.53}$
	Norm. $\left(10^{-3}\right)$	$10.42^{+0.16}_{0.16}$	$1.93^{+0.04}_{-0.04}$	$4.24^{+0.06}_{-0.06}$	$4.06^{+0.09}_{-0.09}$	$3.48^{+0.05}_{-0.05}$	$3.46^{+0.07}_{-0.07}$	$3.23^{+0.05}_{-0.05}$
Mekal[d]	kT (eV)	$103.61^{+12.10}_{-8.61}$	$120.70^{+17.99}_{-10.52}$	$199.71^{+6.23}_{-5.34}$	$231.04^{+15.43}_{-11.53}$	$180.15^{+11.62}_{-16.14}$	$232.38^{+4.20}_{-3.89}$	$235.18^{+4.90}_{-4.41}$
	Norm. $\left(10^{-3}\right)$	$20.08^{+3.56}_{-3.56}$	$1.79^{+0.33}_{-0.33}$	$2.11^{+0.22}_{-0.22}$	$1.01^{+0.65}_{-0.66}$	$0.97^{+0.25}_{-0.26}$	$7.87^{+0.35}_{-0.35}$	$4.80^{+0.22}_{-0.22}$
Negative Ion. Warm Abs.	N_H $\left(10^{21} cm^{-2}\right)$	$2.13^{+0.08}_{-0.07}$	$0.87^{+0.07}_{-0.07}$	$0.63^{+0.03}_{-0.03}$	> 5.60	$0.79^{+0.04}_{-0.04}$	$8.71(frozen)$	$7.44(frozen)$
	Log ξ	$-1.21^{+0.02}_{-0.02}$	$-0.92^{+0.07}_{-0.07}$	$-1.00^{+0.06}_{-0.03}$	$-1.54^{+0.04}_{-0.06}$	$-1.01^{+0.07}_{-0.02}$	< -1.86	$-2.00^{+0.01}_{-0.20}$
Low Ion. Warm Abs.	N_H $\left(10^{21} cm^{-2}\right)$	$3.00^{+0.24}_{-0.25}$	$1.19^{+0.18}_{-0.16}$	$3.68^{+0.16}_{-0.15}$	$3.66^{+0.17}_{-0.16}$	$1.86^{+0.06}_{-0.05}$	$11.83^{+0.27}_{-0.21}$	$5.30^{+0.29}_{-0.29}$
	Log ξ	$0.59^{+0.07}_{-0.06}$	$0.63^{+0.11}_{-0.11}$	$0.46^{+0.02}_{-0.02}$	$1.12^{+0.05}_{-0.05}$	$1.03^{+0.04}_{-0.08}$	$1.04^{+0.01}_{-0.01}$	$1.00^{+0.02}_{-0.06}$
High Ion. Warm Abs.	N_H $\left(10^{21} cm^{-2}\right)$	$72.14^{+7.23}_{-6.74}$	$2.00^{+0.28}_{-0.26}$	$9.19^{+1.91}_{-1.59}$	$13.73^{+5.97}_{-4.13}$	$2.77^{+0.13}_{-0.10}$	$68.58^{+5.99}_{-4.37}$	$29.39^{+2.68}_{-3.70}$
	Log ξ	$2.62^{+0.02}_{-0.02}$	$2.67^{+0.10}_{-0.10}$	$2.83^{+0.03}_{-0.03}$	$2.91^{+0.02}_{-0.02}$	$1.72^{+0.04}_{-0.04}$	$2.66^{+0.01}_{-0.01}$	$2.72^{+0.02}_{-0.02}$
FPMA Calibration	Constant	$1.01^{+0.02}_{-0.02}$	$1.07^{+0.01}_{-0.01}$	$1.09^{+0.01}_{-0.01}$	$1.10_{-0.01}$	$1.10_{-0.01}$	$1.10_{-0.02}$	$1.04^{+0.02}_{-0.02}$
FPMB Calibration	Constant	$1.05^{+0.02}_{-0.02}$	$1.10_{-0.01}$	$1.09^{+0.01}_{-0.01}$	$1.10_{-0.01}$	$1.10_{-0.01}$	$1.10_{-0.01}$	$1.06^{+0.02}_{-0.02}$
	χ^2/DOF	771.43/708	1273.91/1204	1453.30/1392	1605.29/1438	1437.01/1409	909.40/943	1150.72/1057
	P-value	0.0489	0.0791	0.0672	0.0004	0.2958	0.6453	0.0230

[a]Xillver and Power law normalizations are photons $\mathrm{keV}^{-1}\mathrm{cm}^{-2}\mathrm{s}^{-1}$ at 1 keV.

[b]Gaussian normalization is total photons $\mathrm{cm}^{-2}\mathrm{s}^{-1}$ in the line of sight.

[c]CompST normalization is $Nf/4\pi D^2$ where N is the total number of photons, D is the distance, $f = z(z+3)y^2/\Gamma(2x+4)/\Gamma(z)$, z is the spectral index, y is the injected photon energy in units of temperature, and Γ is the incomplete gamma function.

[d]Mekal normalization is $10^{-14}/4\pi(D_A(1+z))^2) \int n_e n_H \, dV$ where D_A is the angular diameter distance to the source (cm), n_e and n_H are the electron and H densities (cm^{-3}), respectively.

Chapter 4 Figures

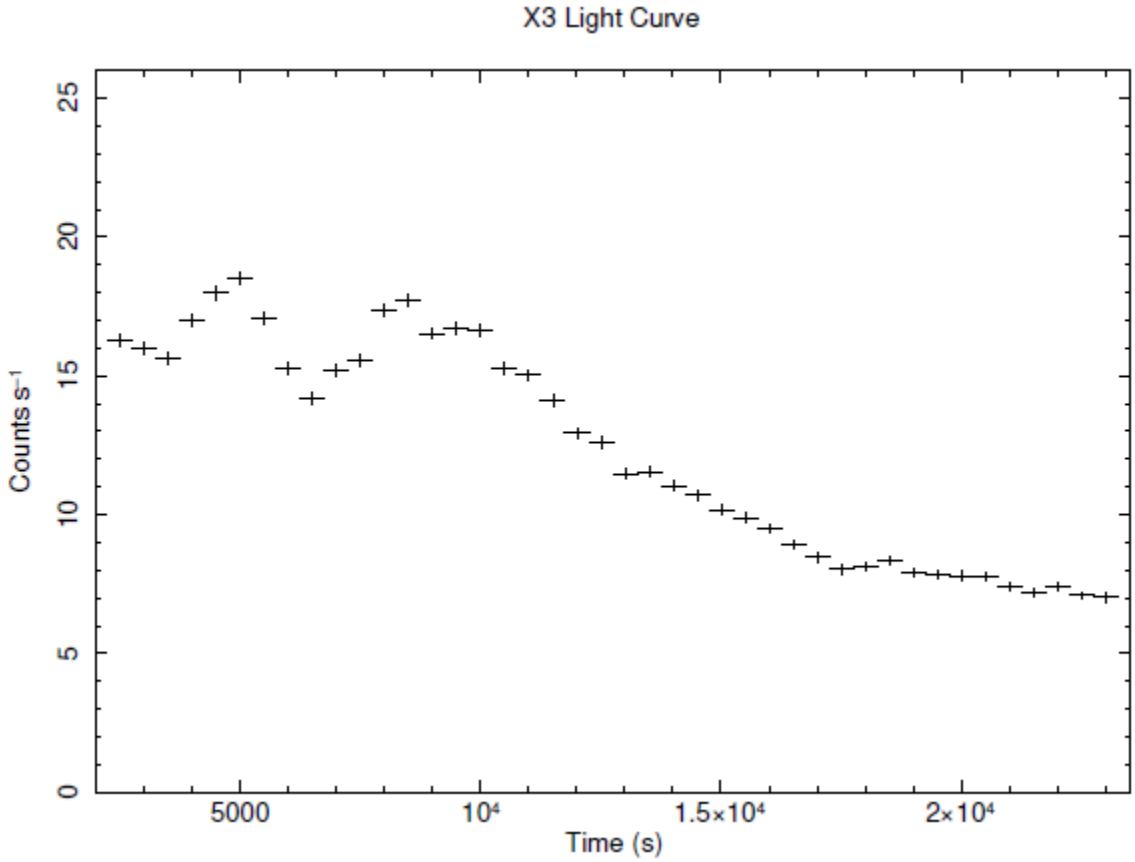

Figure 4.1: XMM-Newton observation X3 pn light curve.

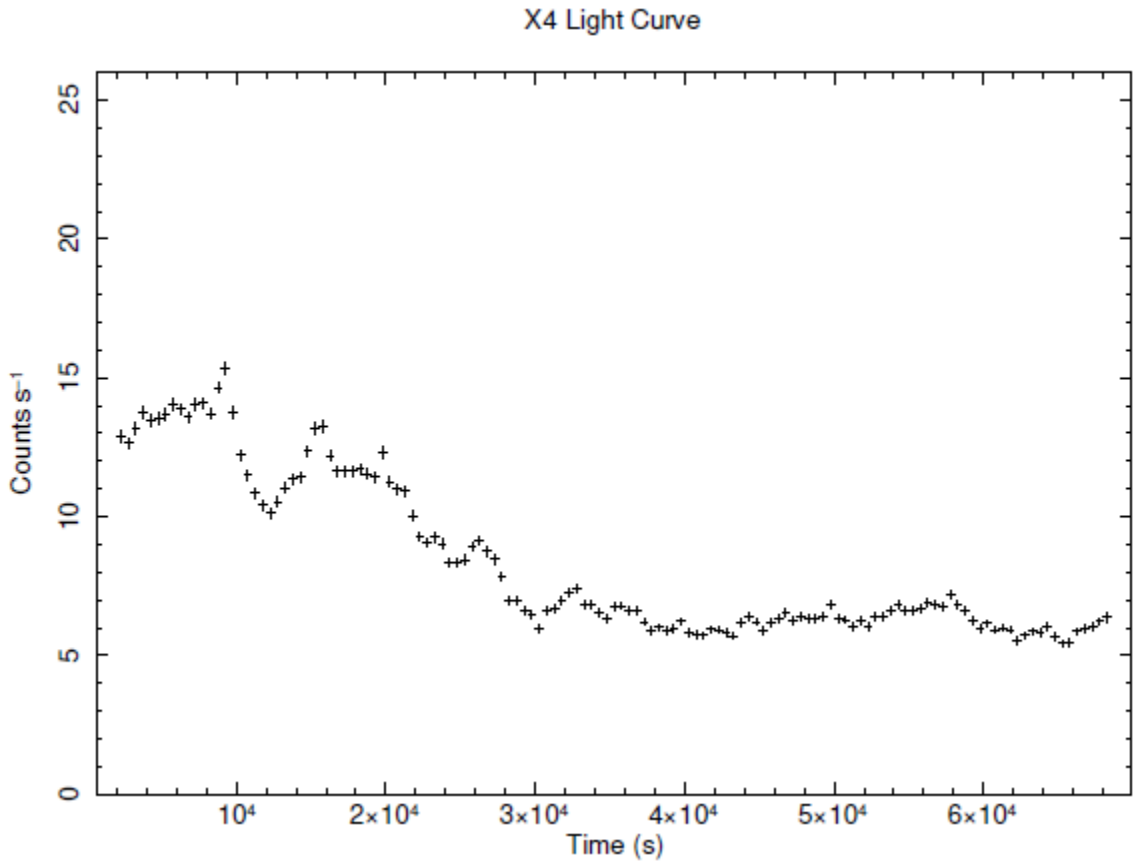

Figure 4.2: XMM-Newton observation X4 pn light curve.

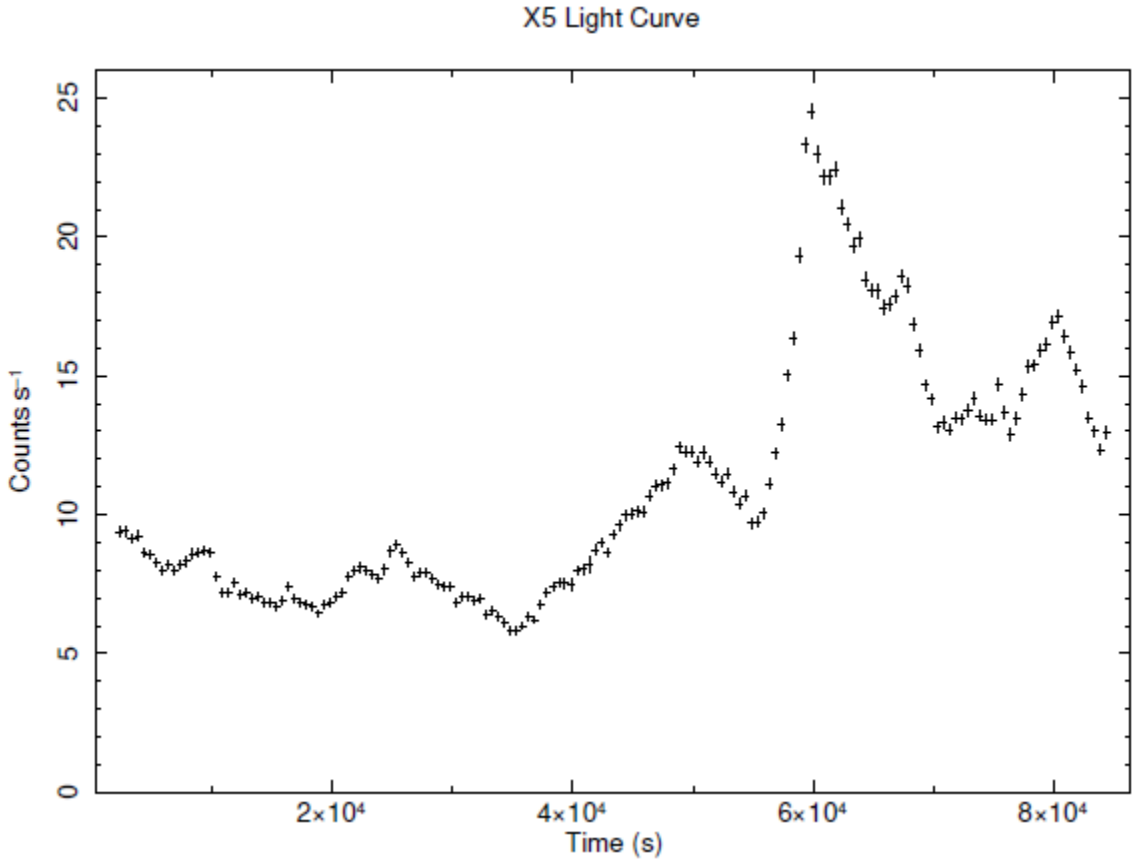

Figure 4.3: XMM-Newton observation X5 pn light curve.

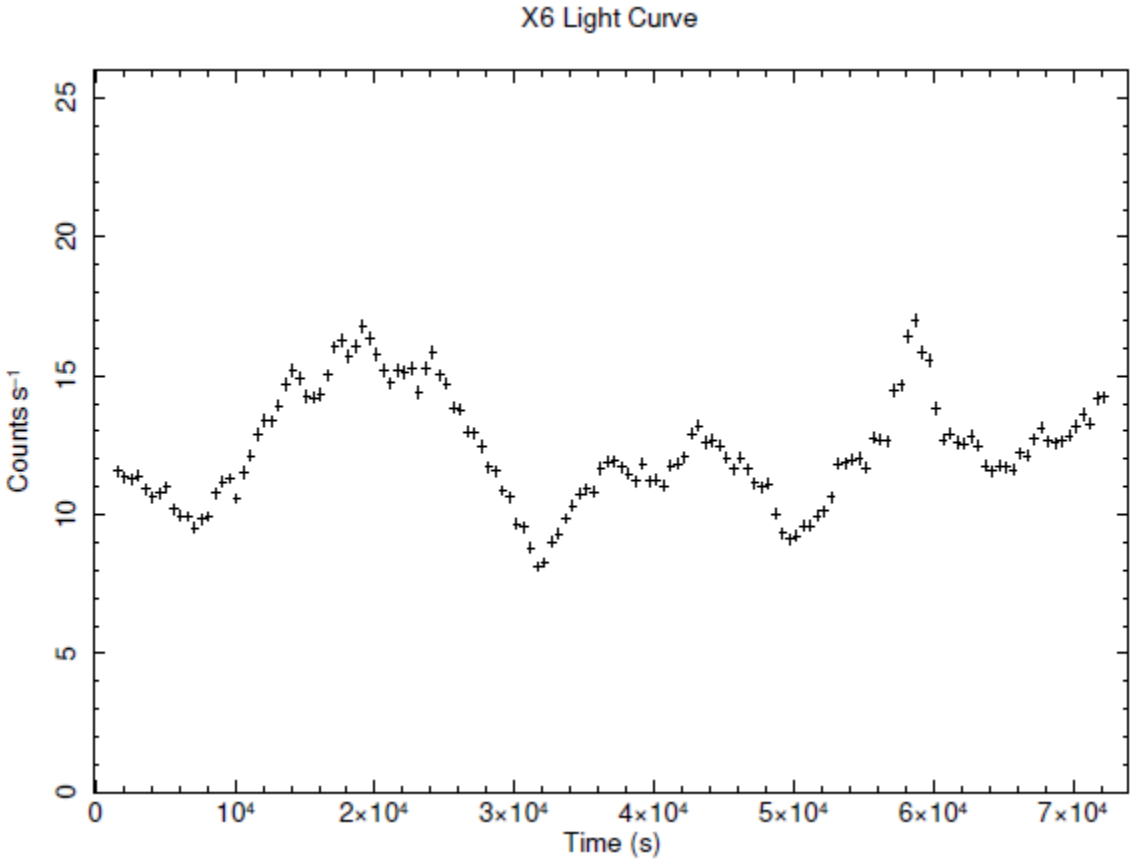

Figure 4.4: XMM-Newton observation X6 pn light curve.

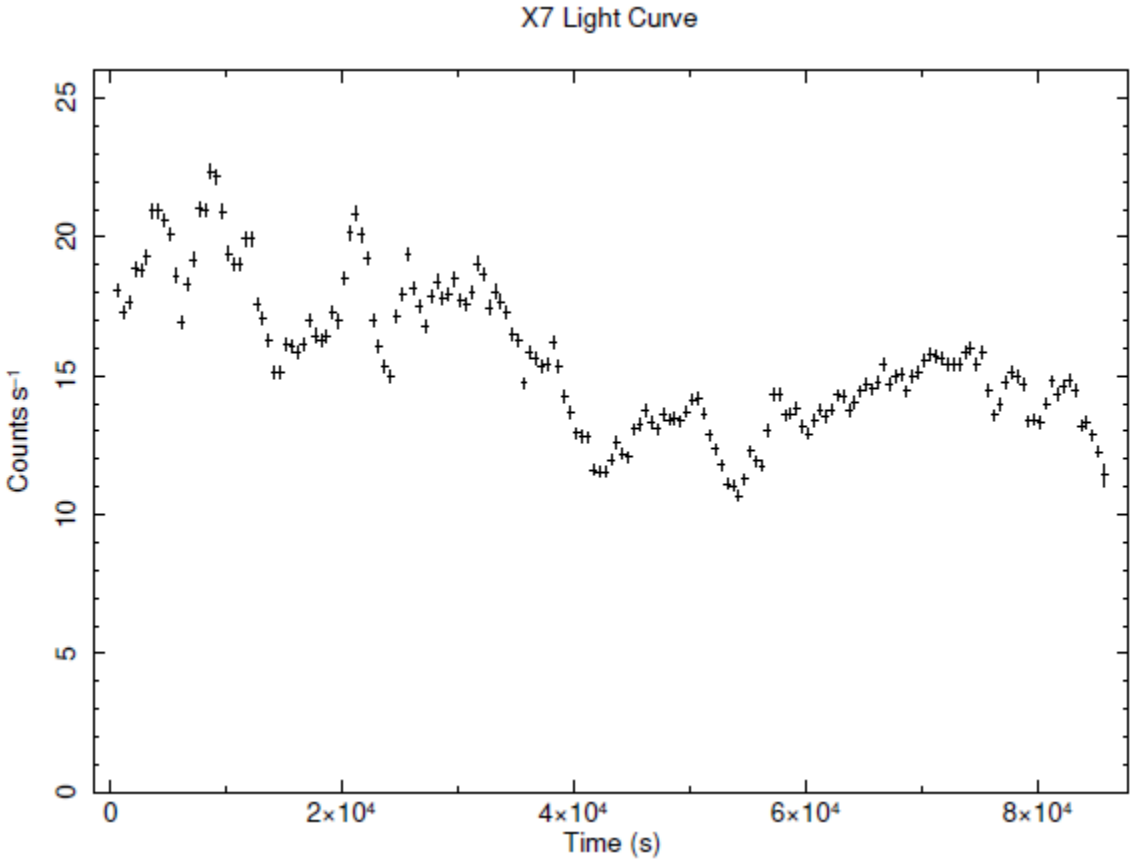

Figure 4.5: XMM-Newton observation X7 pn light curve.

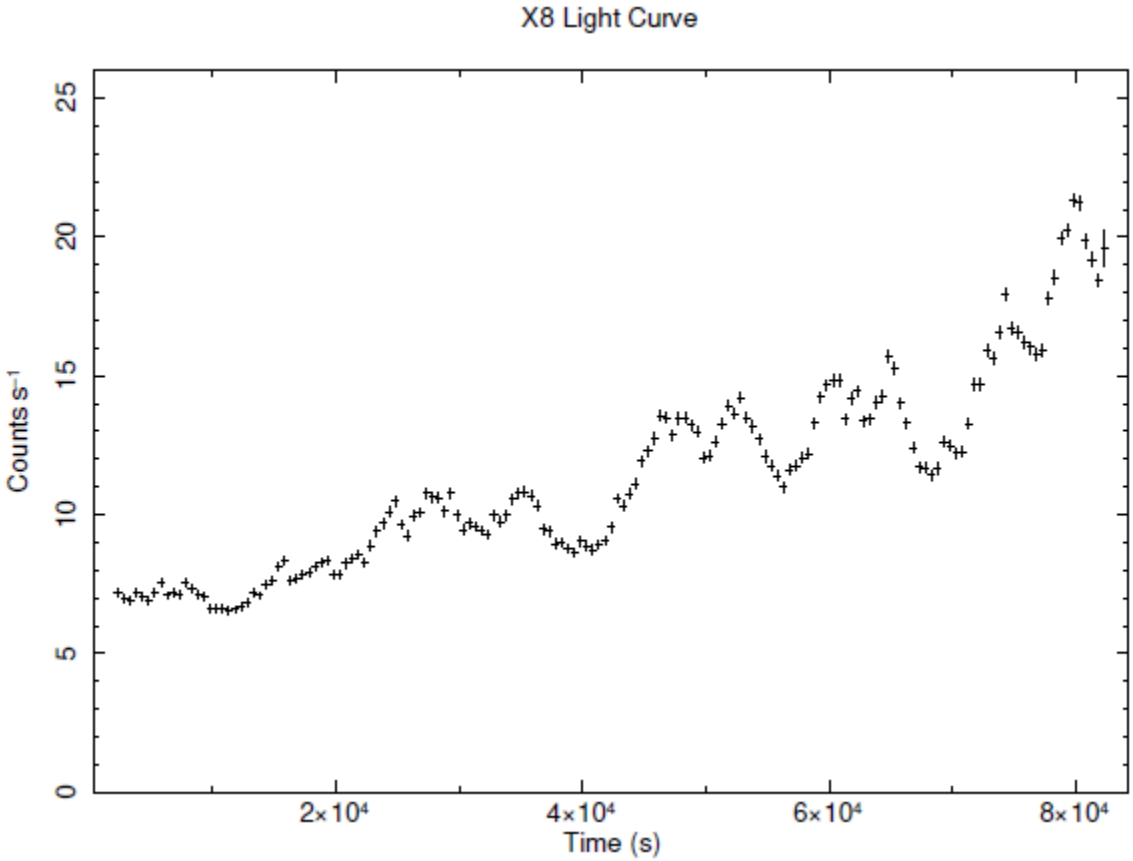

Figure 4.6: XMM-Newton observation X8 pn light curve.

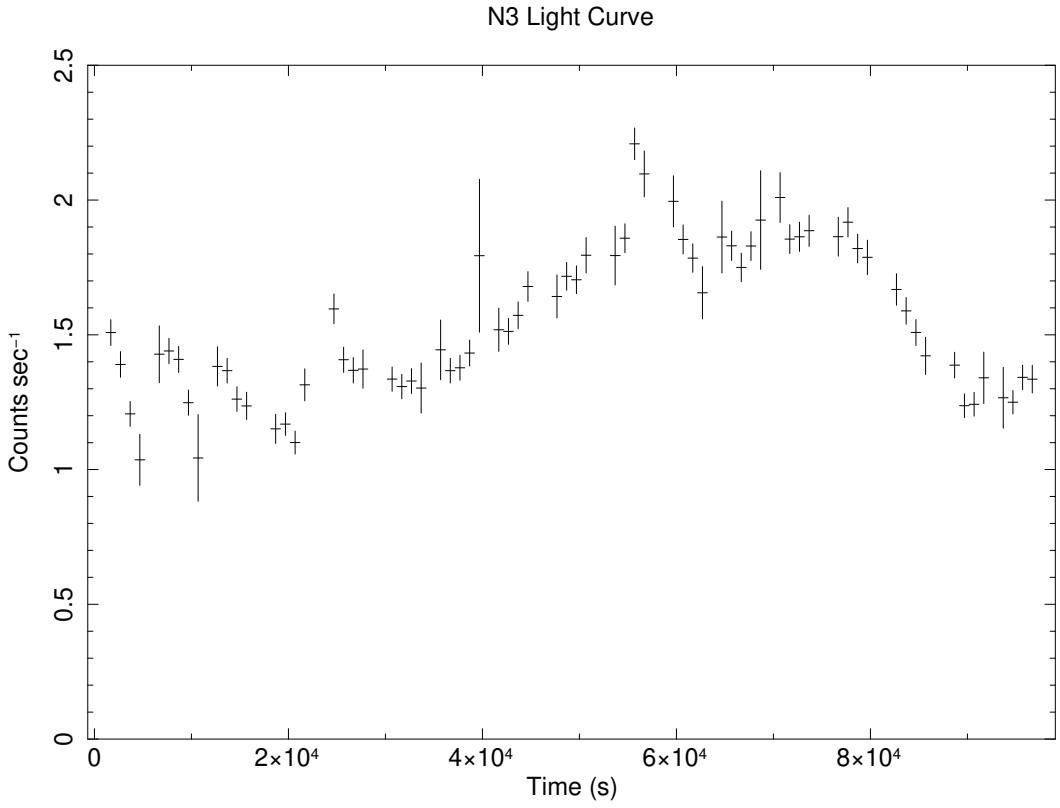

Figure 4.7: NuStar observation N3 FPMA light curve.

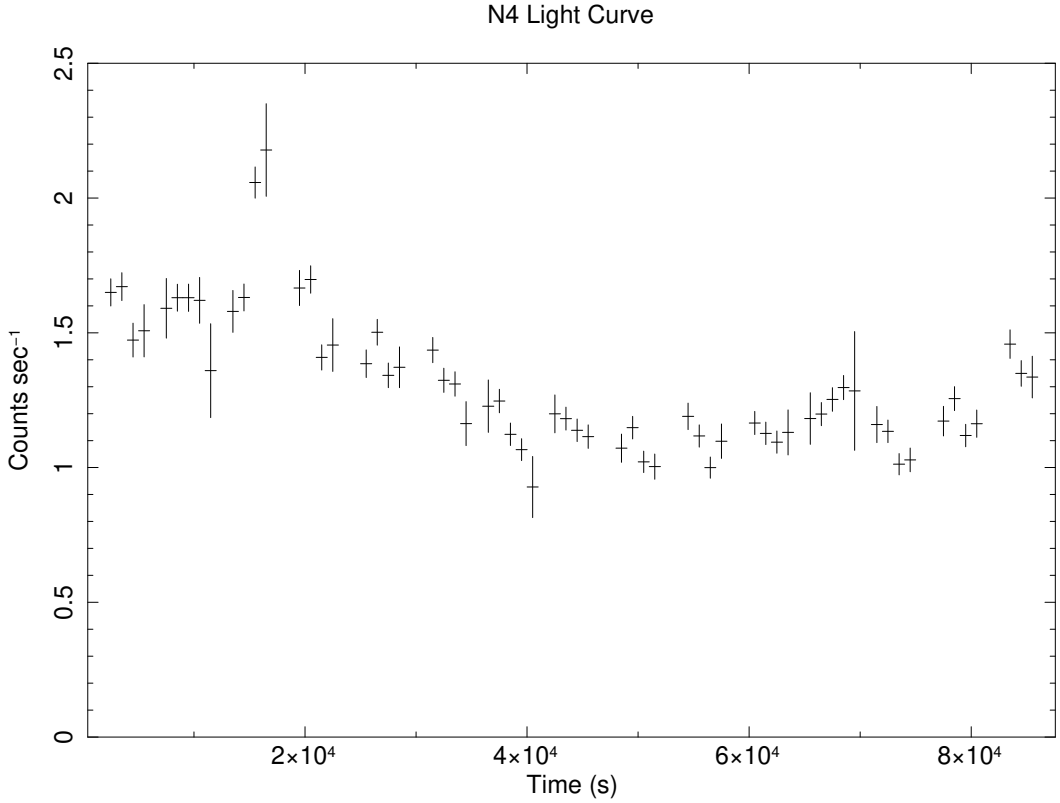

Figure 4.8: NuStar observation N4 FPMA light curve.

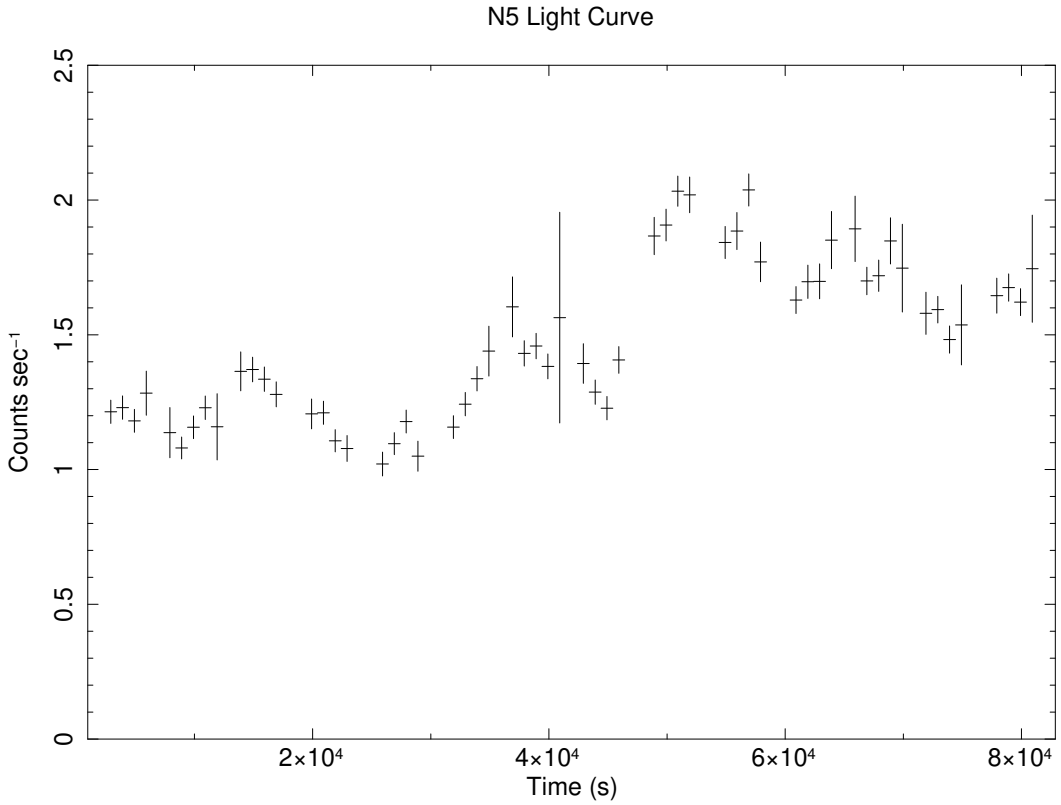

Figure 4.9: NuStar observation N5 FPMA light curve.

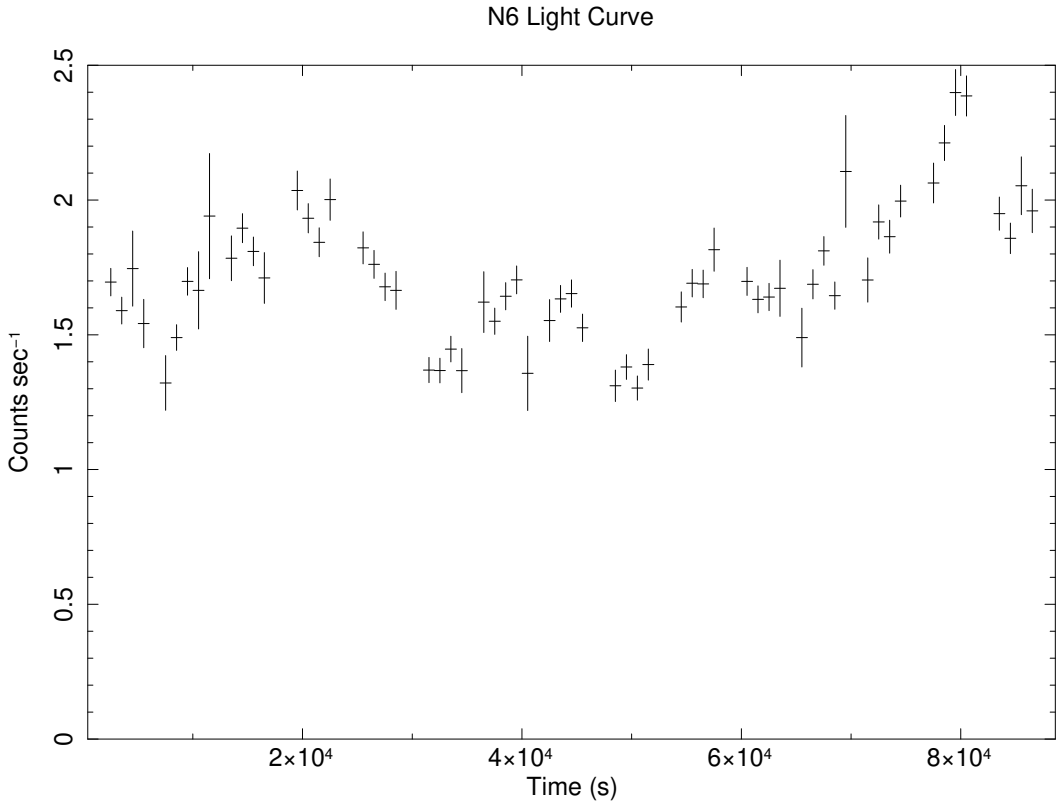

Figure 4.10: NuStar observation N6 FPMA light curve.

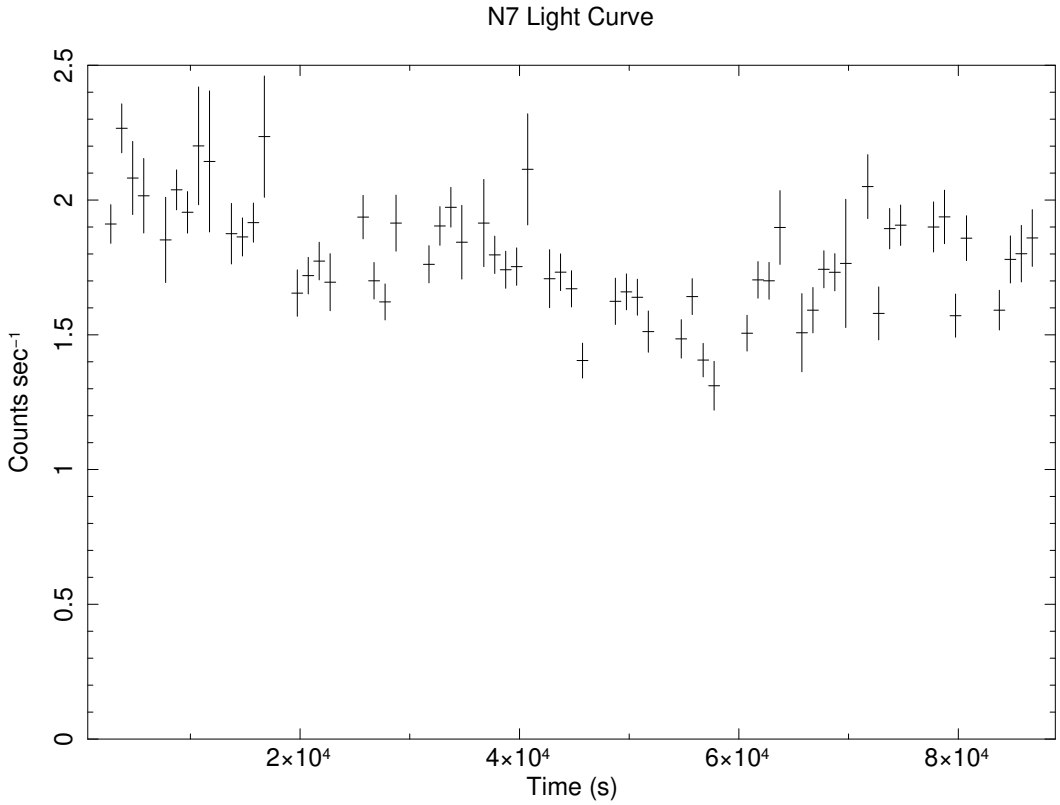

Figure 4.11: NuStar observation N7 FPMA light curve.

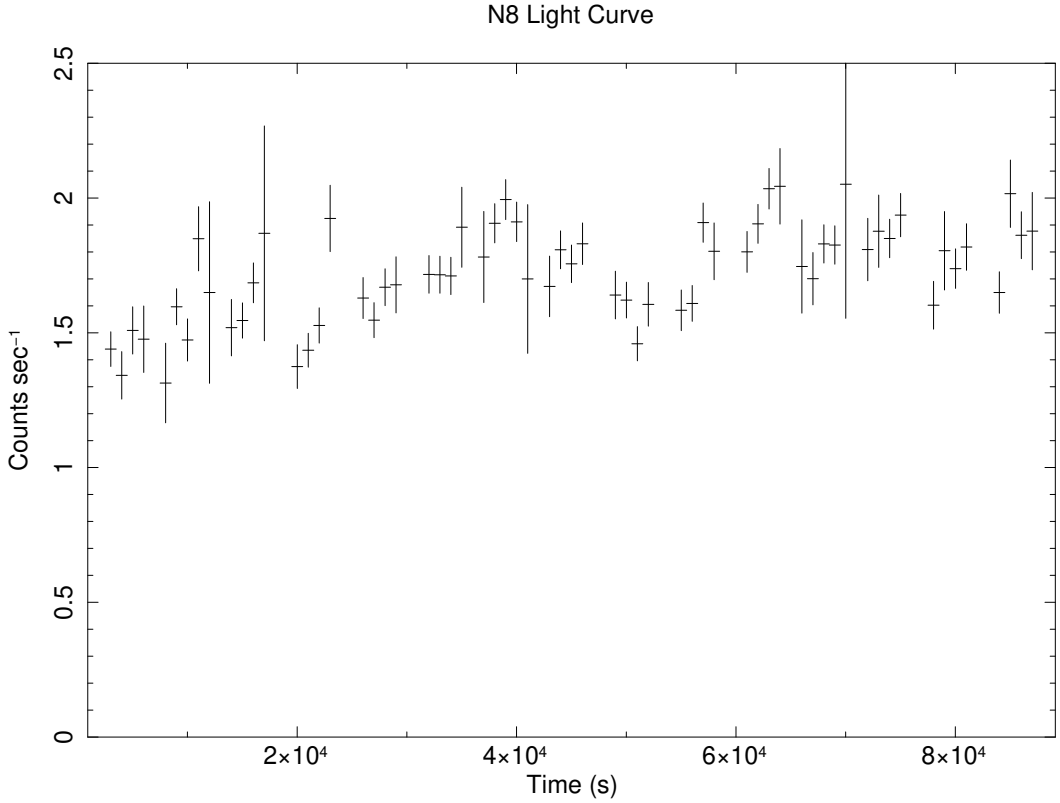

Figure 4.12: NuStar observation N8 FPMA light curve.

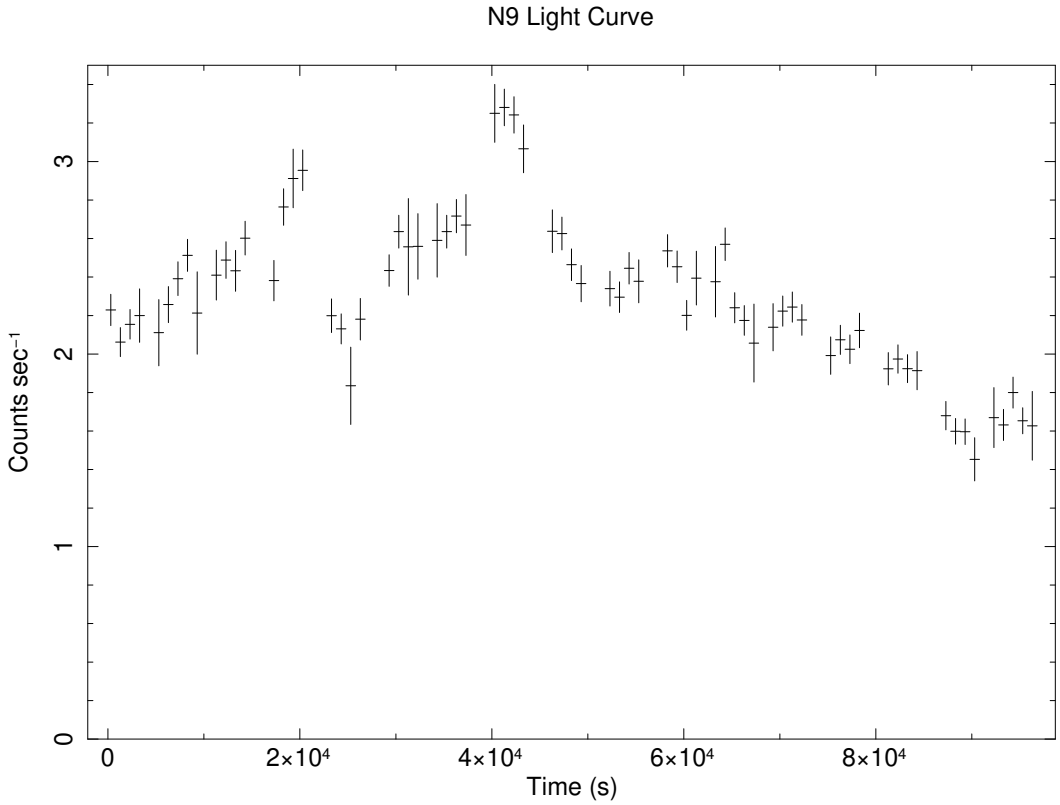

Figure 4.13: NuStar observation N9 FPMA light curve.

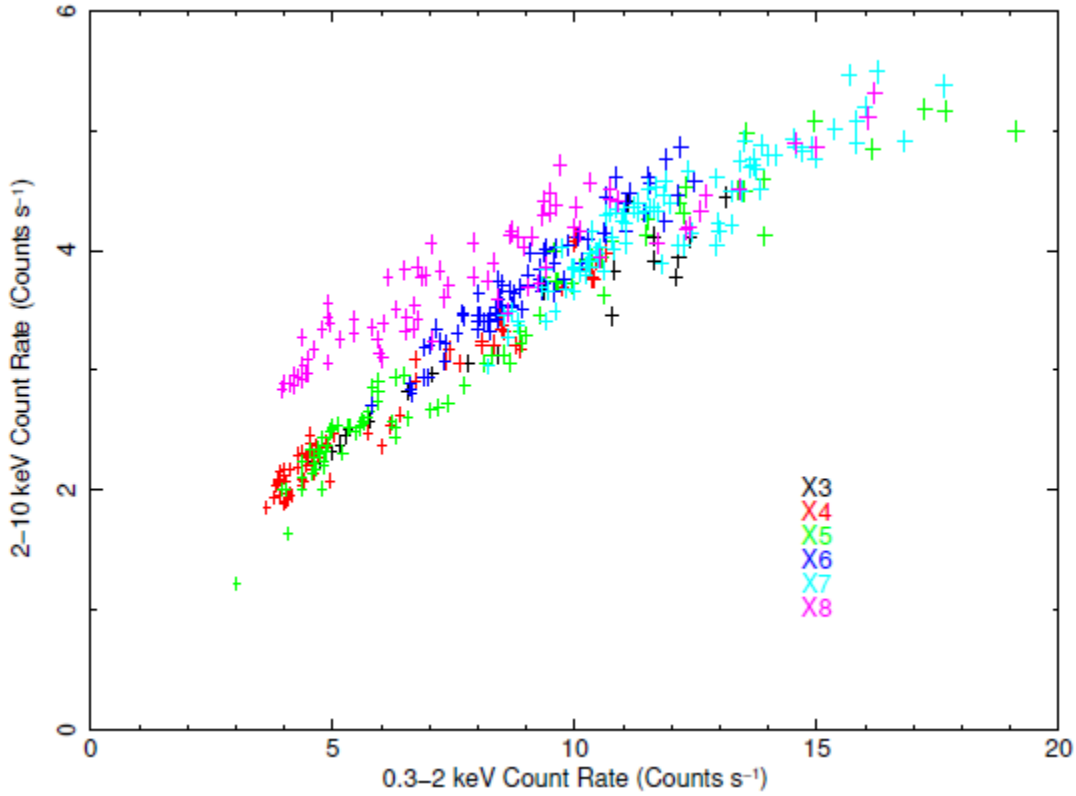

Figure 4.14: XMM-Newton X3-X8 pn flux-flux plot. All observations take place in the high state.

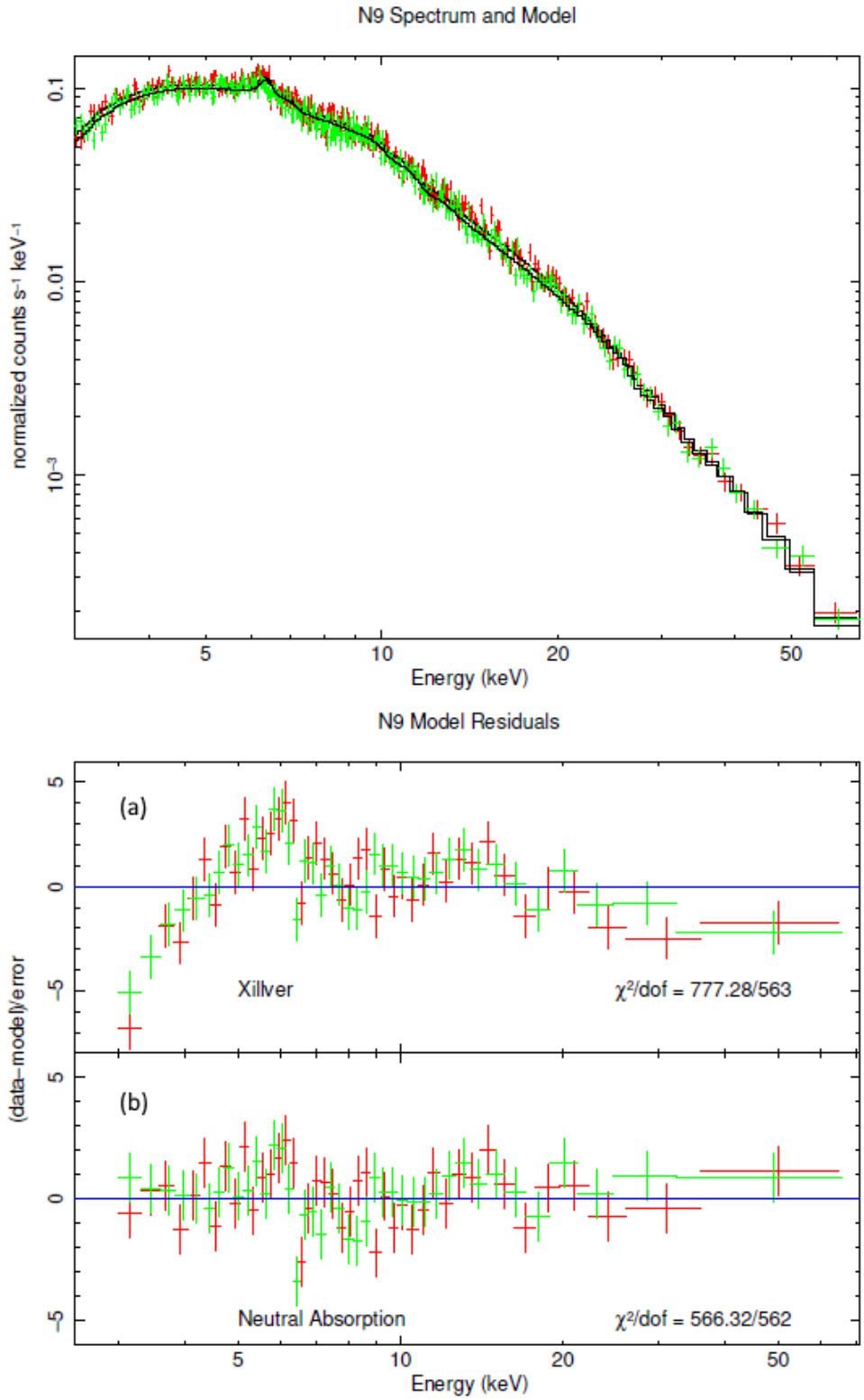

Figure 4.15: NuStar observation N9 spectrum and fit residuals. The FPMA and FPMB data are red and green respectively. Panel (a) shows the disc reflection and power law (Xillver) model with galactic absorption while panel (b) displays the residuals once local neutral absorption was added.

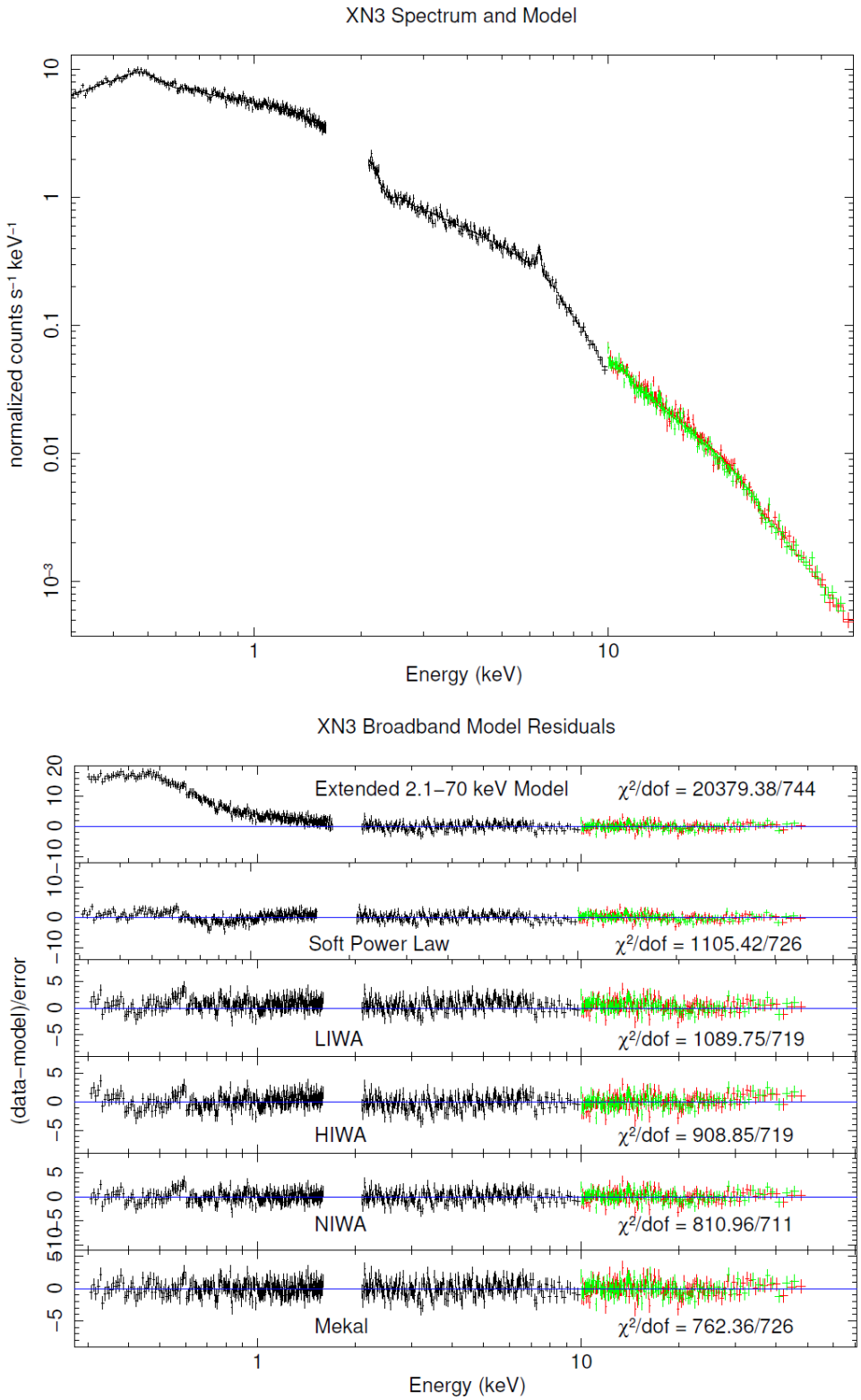

Figure 4.16: XMM-Newton and NuStar observation XN3 spectrum and fit residuals. Pn data are black, FPMA data are red, and FPMB data are green.

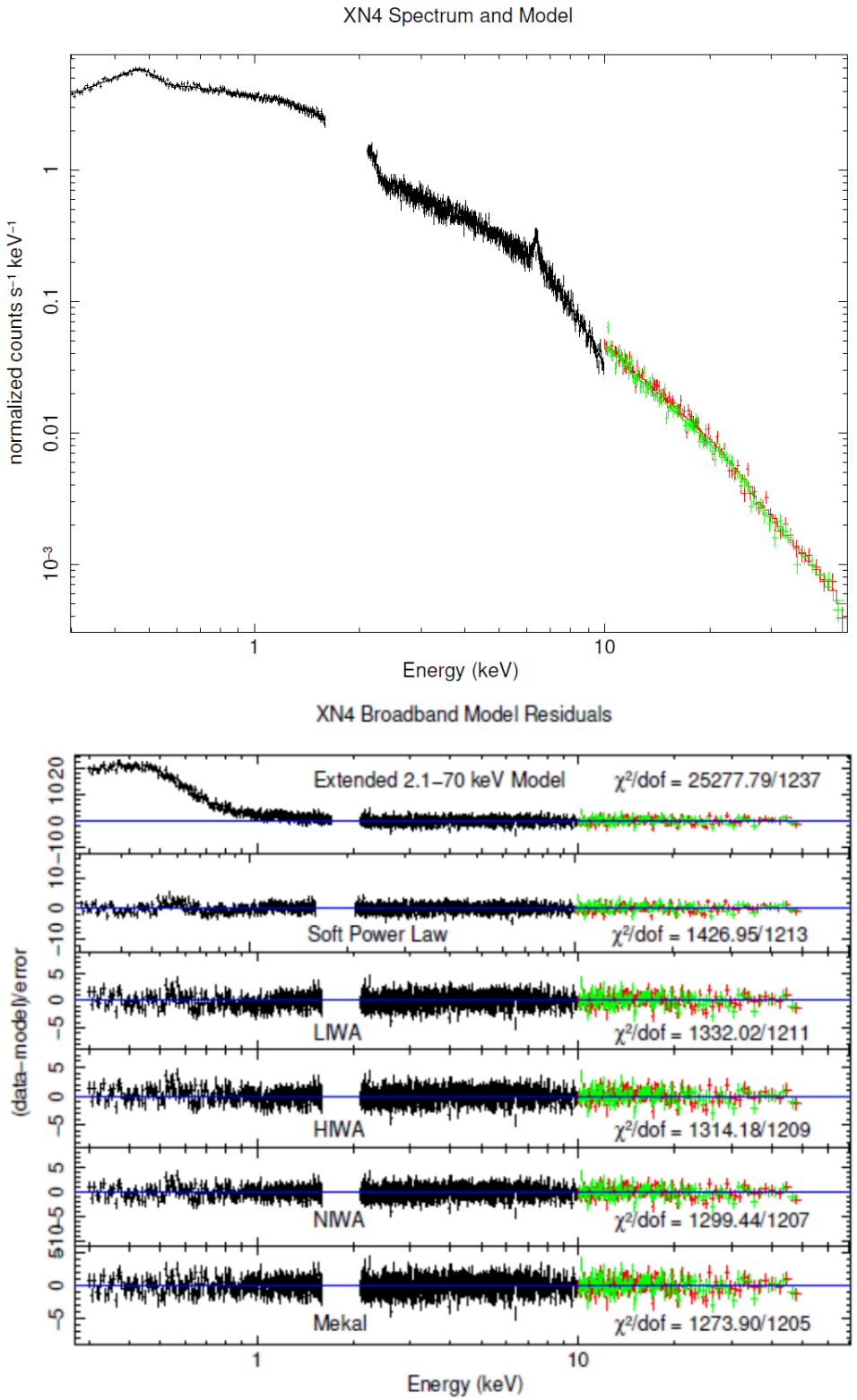

Figure 4.17: XMM-Newton and NuStar observation XN4 spectrum and fit residuals. Pn data are black, FPMA data are red, and FPMB data are green.

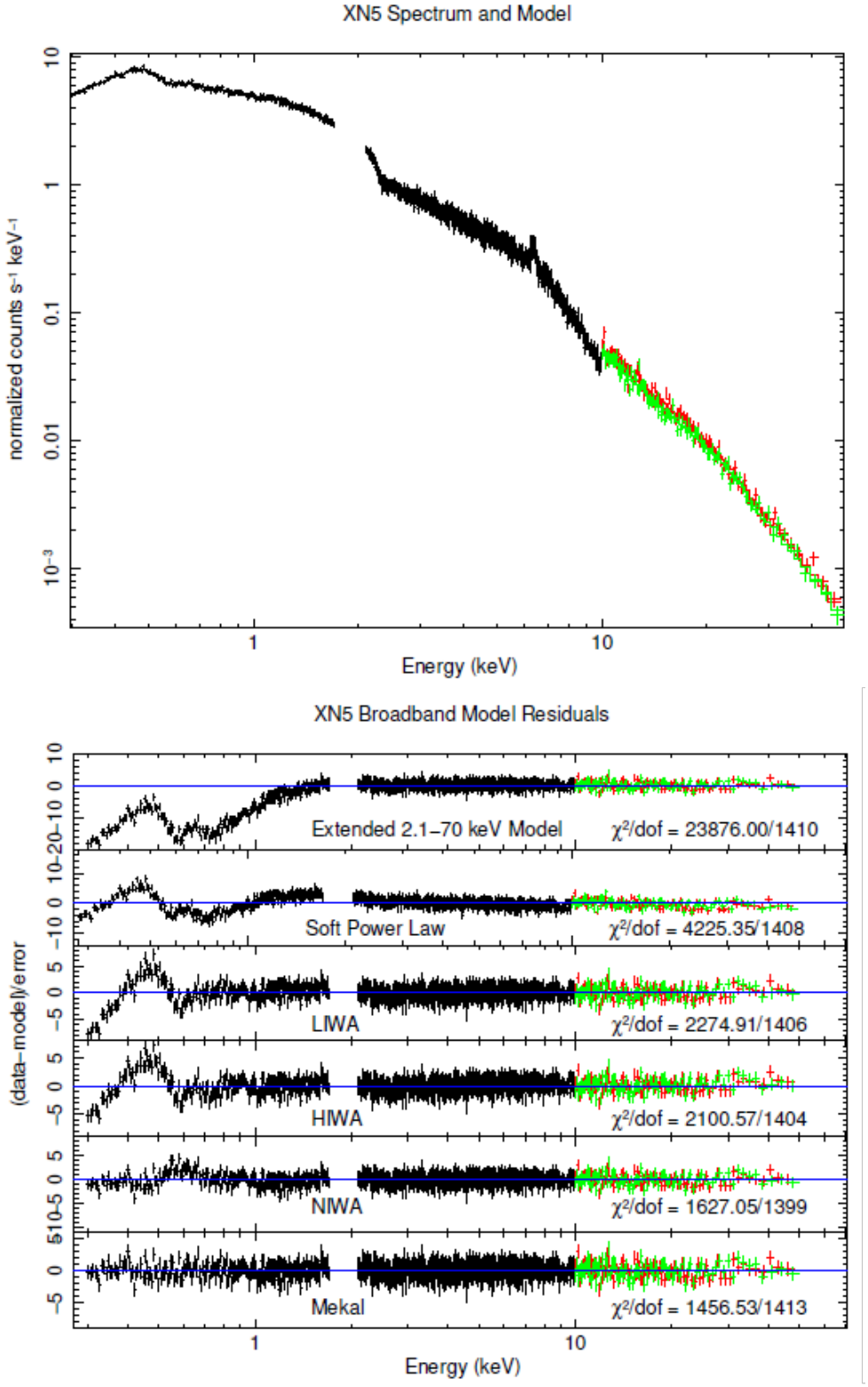

Figure 4.18: XMM-Newton and NuStar observation XN5 spectrum and fit residuals. Pn data are black, FPMA data are red, and FPMB data are green.

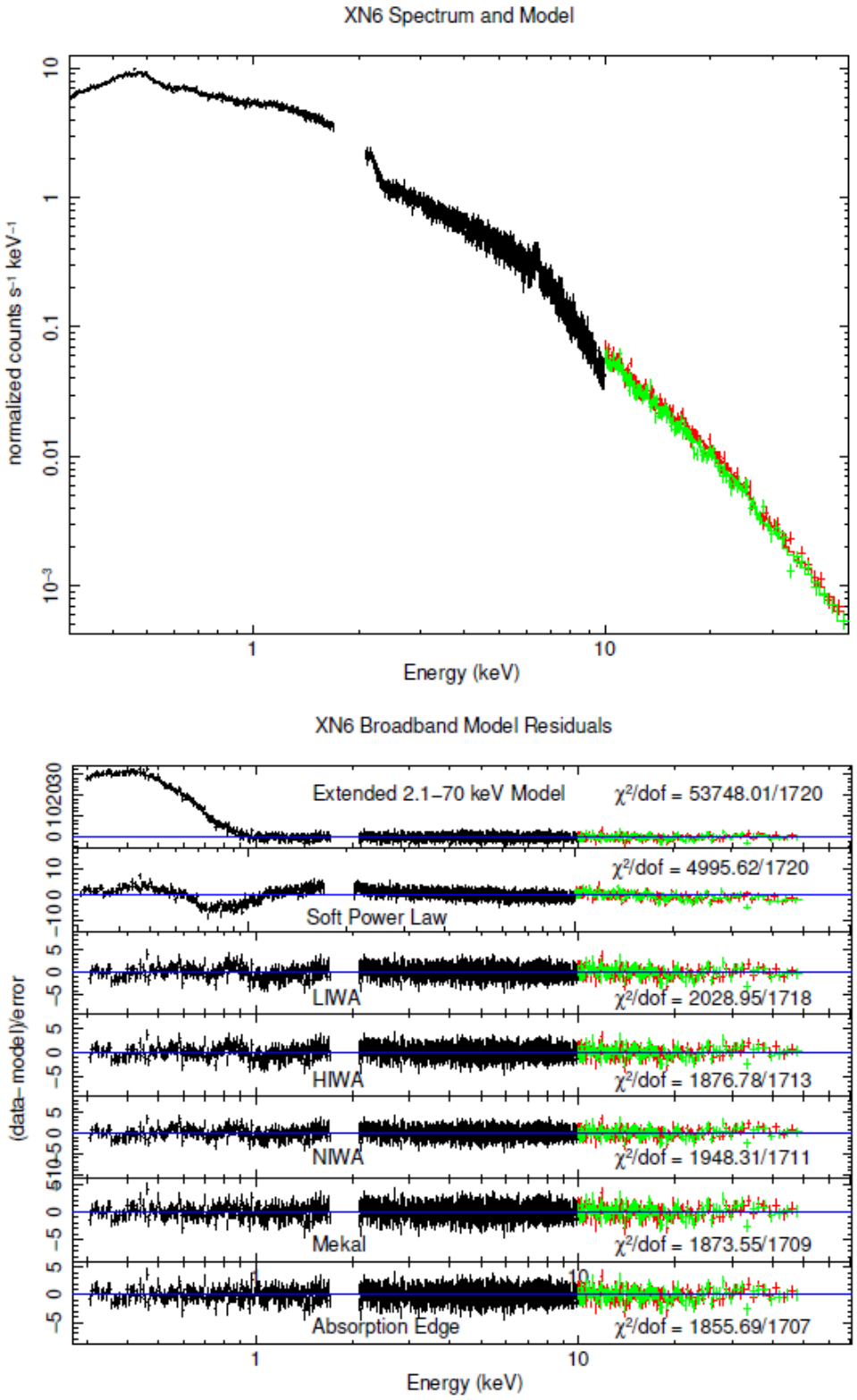

Figure 4.19: XMM-Newton and NuStar observation XN6 spectrum and fit residuals. Pn data are black, FPMA data are red, and FPMB data are green.

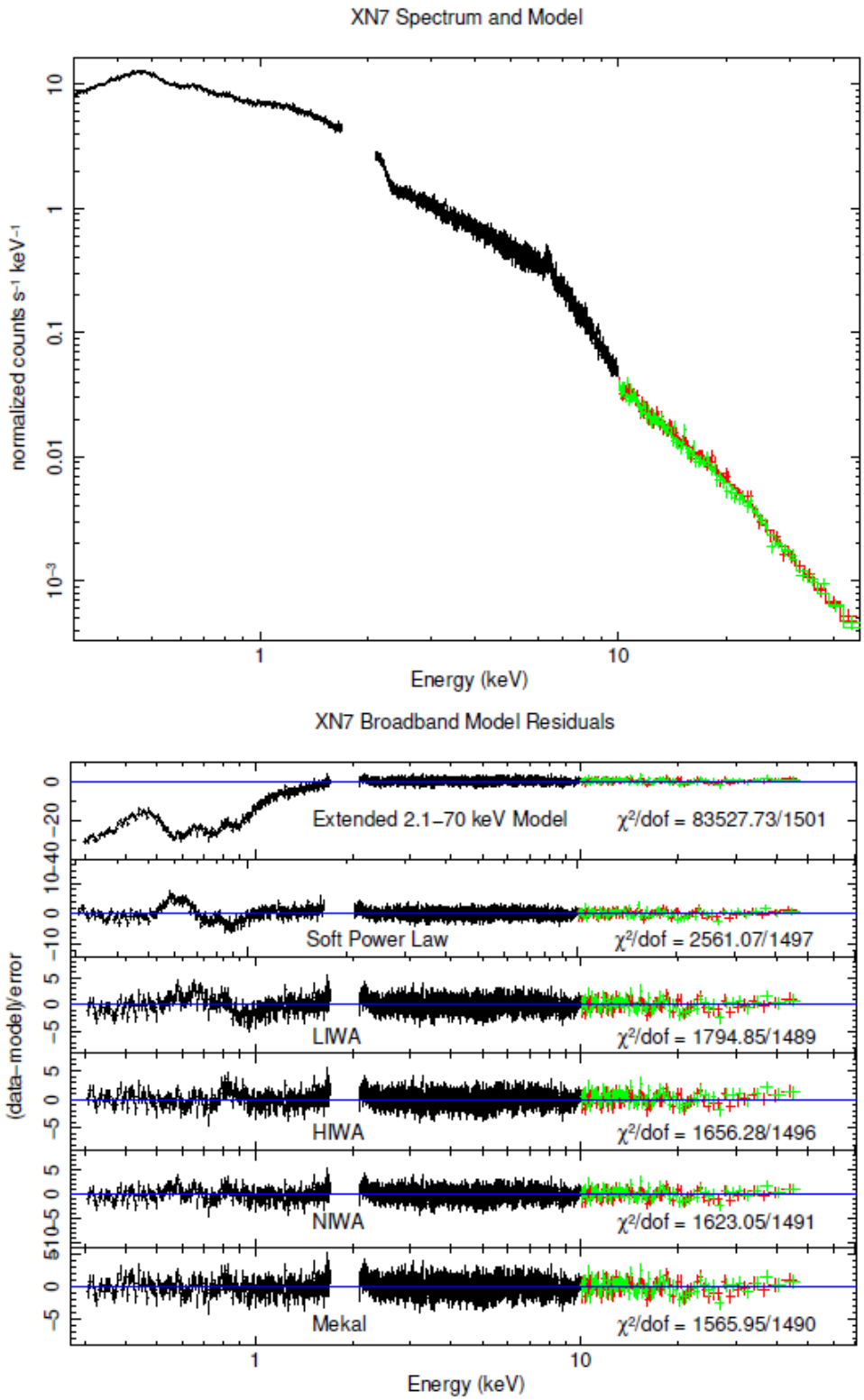

Figure 4.20: XMM-Newton and NuStar observation XN7 spectrum and fit residuals. Pn data are black, FPMA data are red, and FPMB data are green.

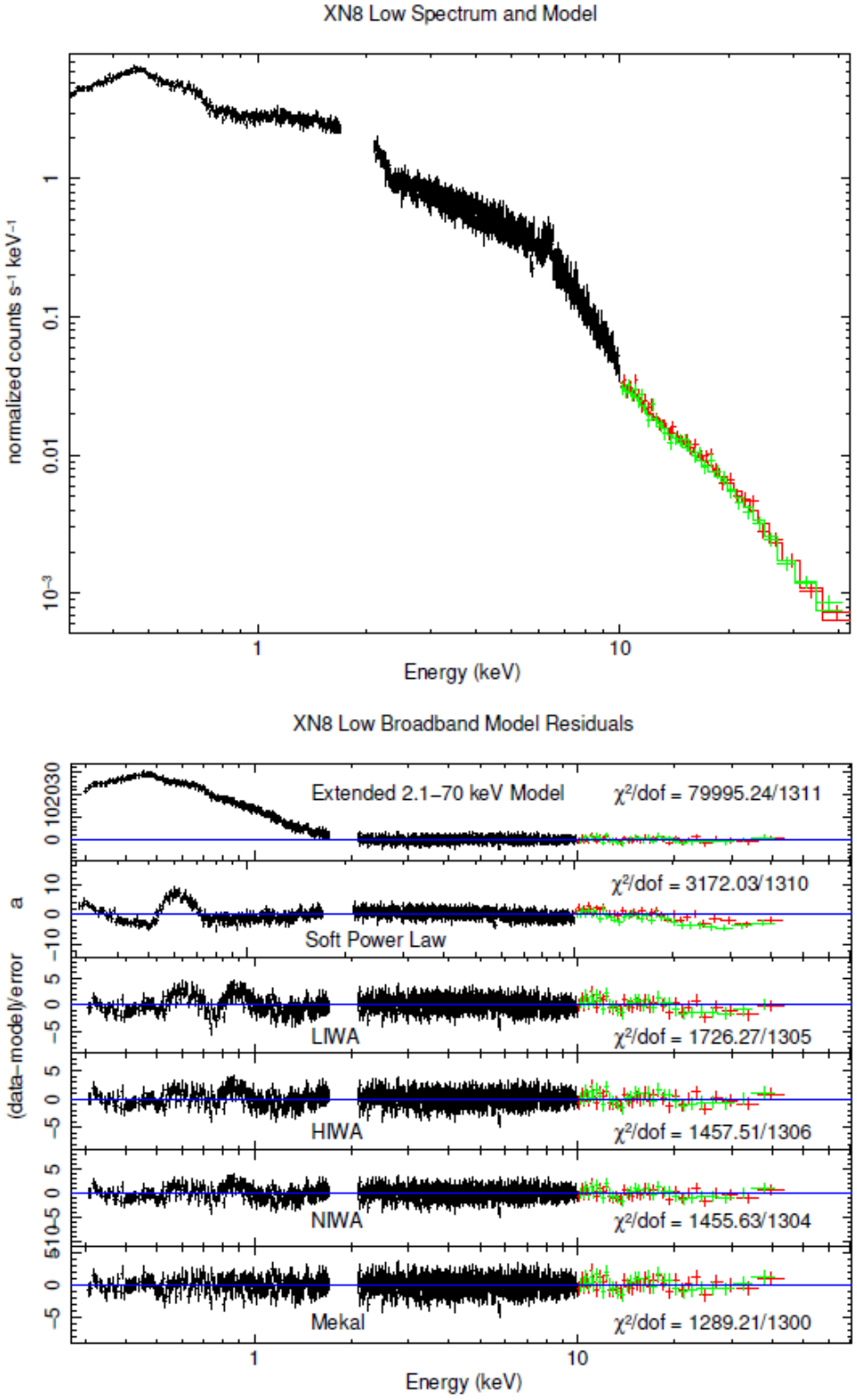

Figure 4.21: XMM-Newton and NuStar observation XN8 Low spectrum and fit residuals. Pn data are black, FPMA data are red, and FPMB data are green.

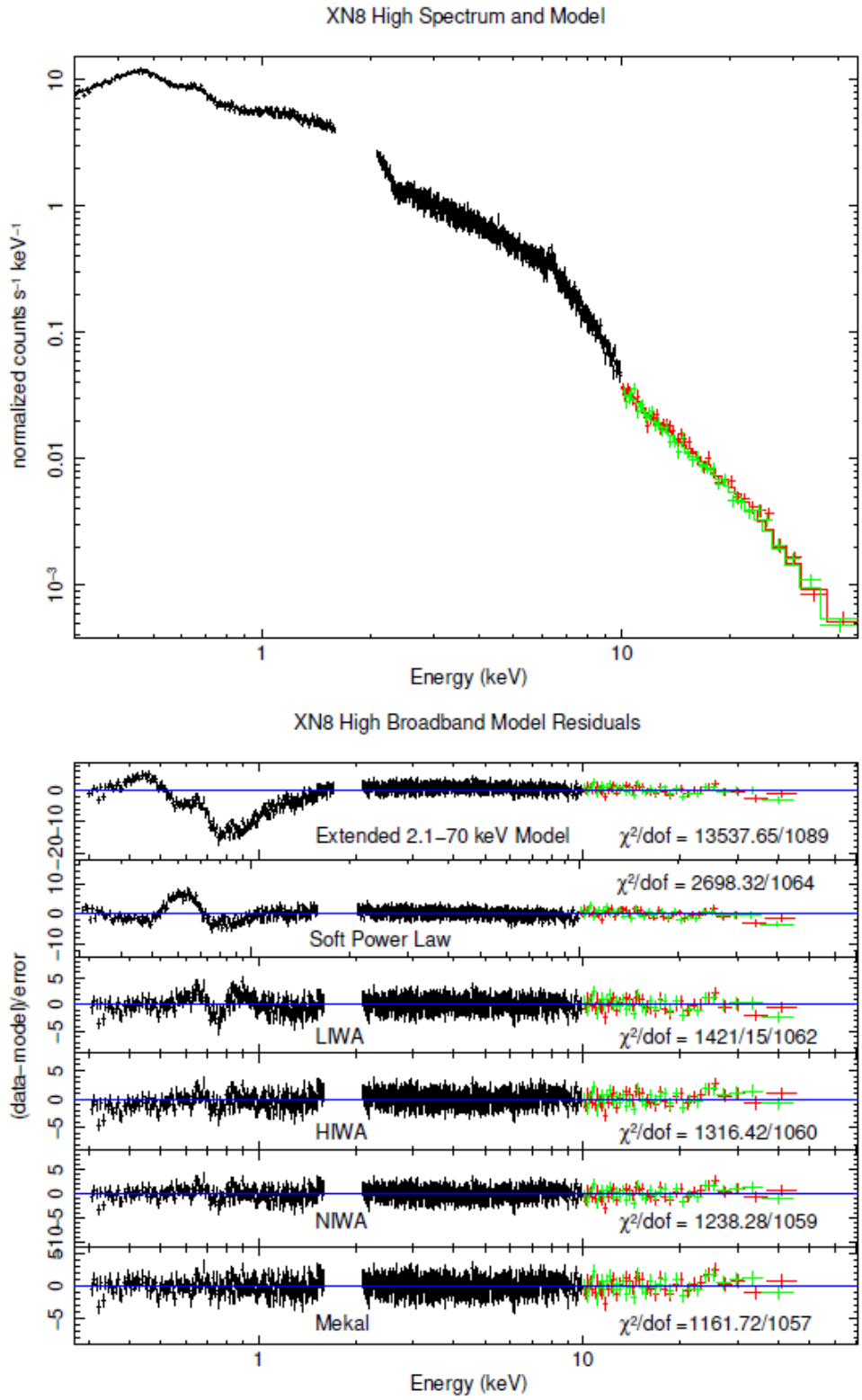

Figure 4.22: XMM-Newton and NuStar observation XN8 High spectrum and fit residuals. Pn data are black, FPMA data are red, and FPMB data are green.

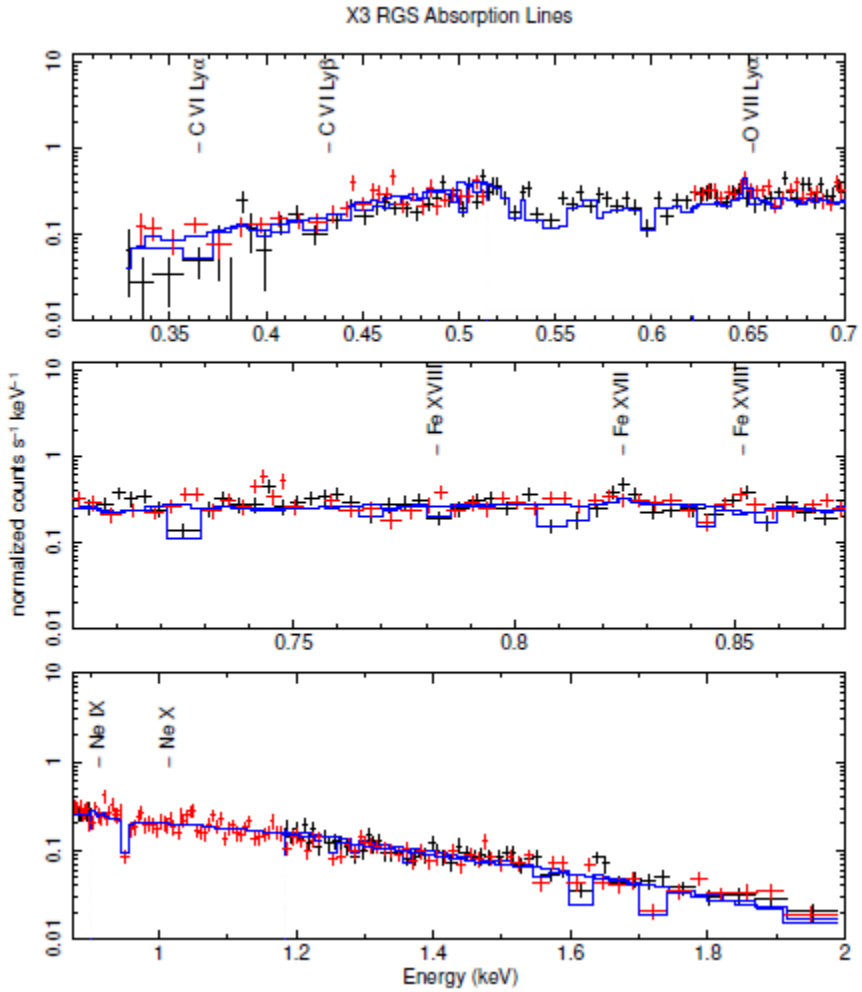

Figure 4.23: Absorption lines detected during the X3 RGS analysis. The 0.3 - 2 keV band is split into three regions. The top panel is 0.3 - 0.7 keV, the middle panel is 0.7 - 0.875, and the bottom panel is 0.875 - 2 keV. RGS1 data are black, RGS2 data are red, and the model is blue.

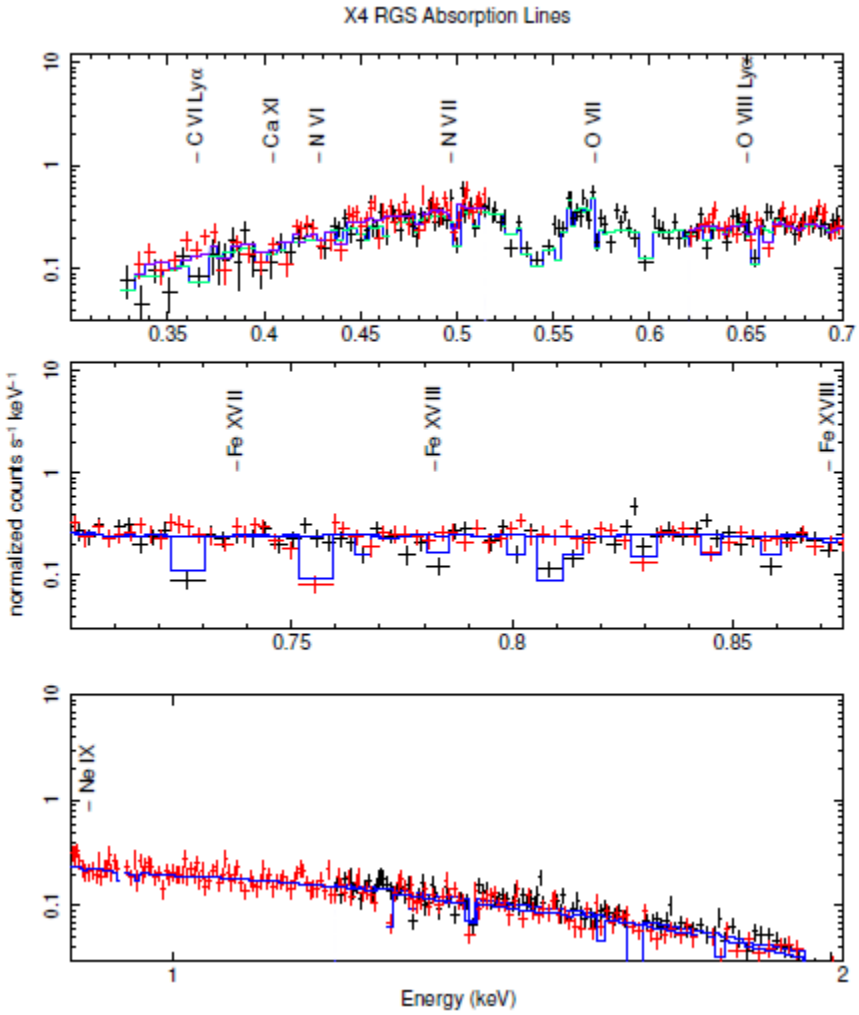

Figure 4.24: Absorption lines detected during the X4 RGS analysis. The 0.3 - 2 keV band is split into three regions. The top panel is 0.3 - 0.7 keV, the middle panel is 0.7 - 0.875, and the bottom panel is 0.875 - 2 keV. RGS1 data are black, RGS2 data are red, and the model is blue.

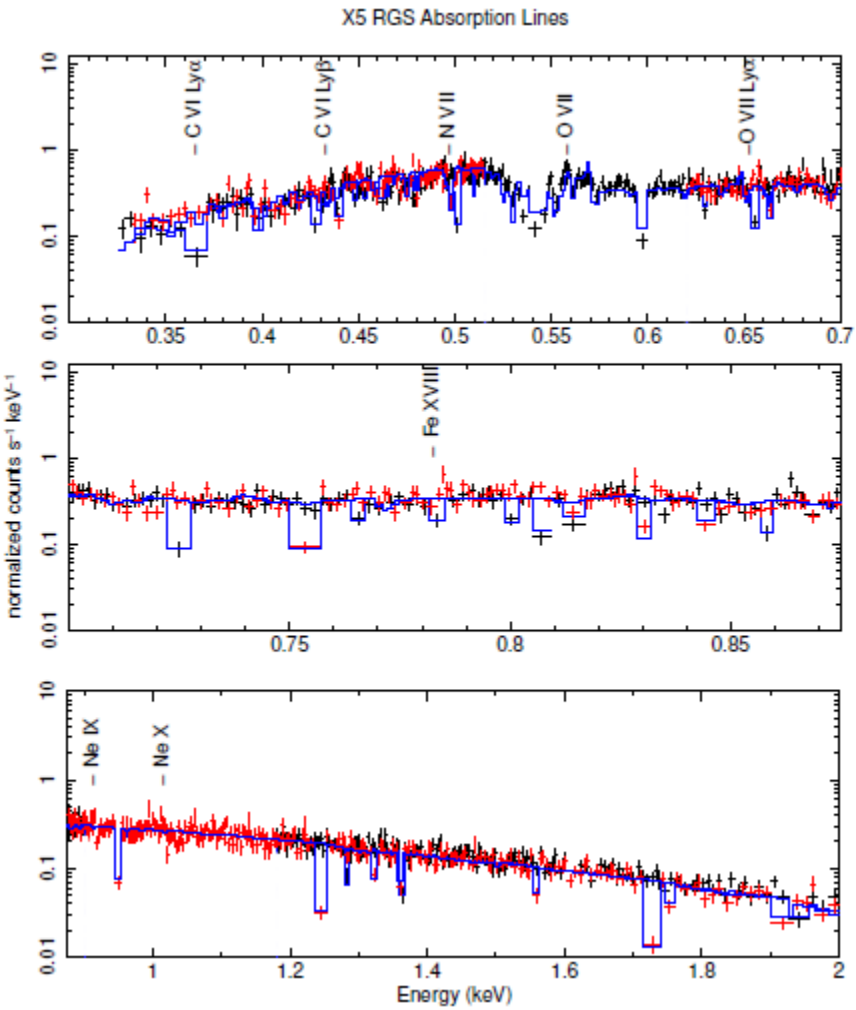

Figure 4.25: Absorption lines detected during the X5 RGS analysis. The 0.3 - 2 keV band is split into three regions. The top panel is 0.3 - 0.7 keV, the middle panel is 0.7 - 0.875, and the bottom panel is 0.875 - 2 keV. RGS1 data are black, RGS2 data are red, and the model is blue.

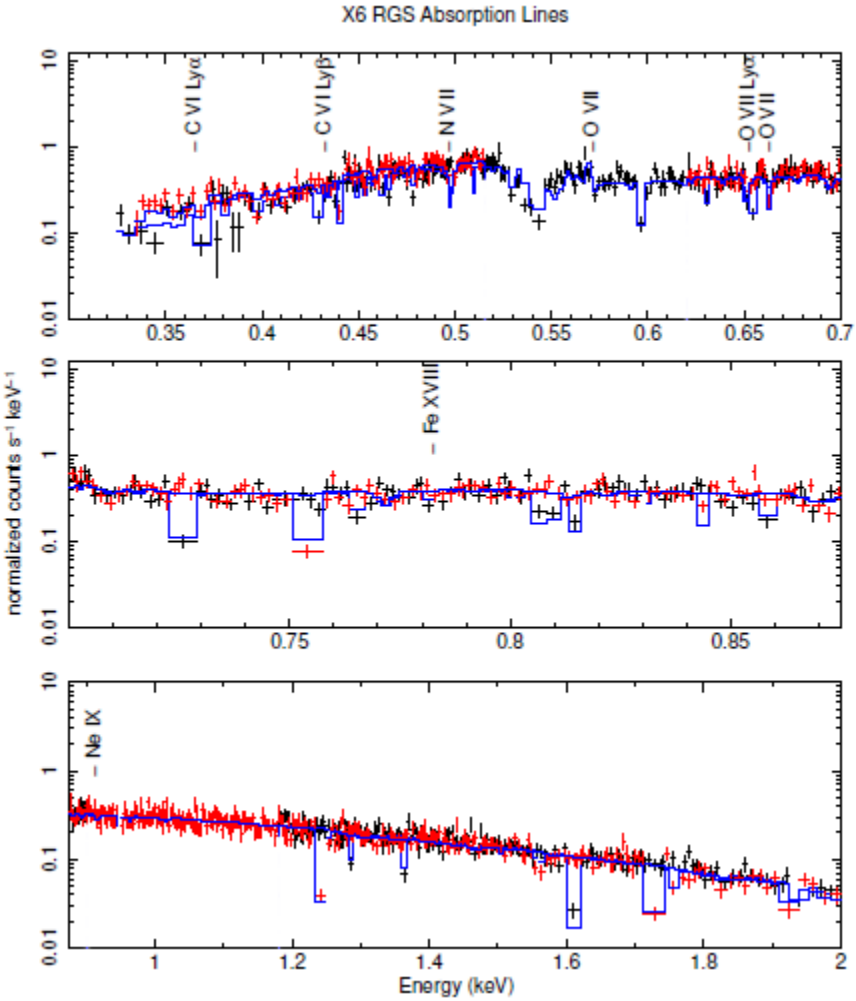

Figure 4.26: Absorption lines detected during the X6 RGS analysis. The 0.3 - 2 keV band is split into three regions. The top panel is 0.3 - 0.7 keV, the middle panel is 0.7 - 0.875, and the bottom panel is 0.875 - 2 keV. RGS1 data are black, RGS2 data are red, and the model is blue.

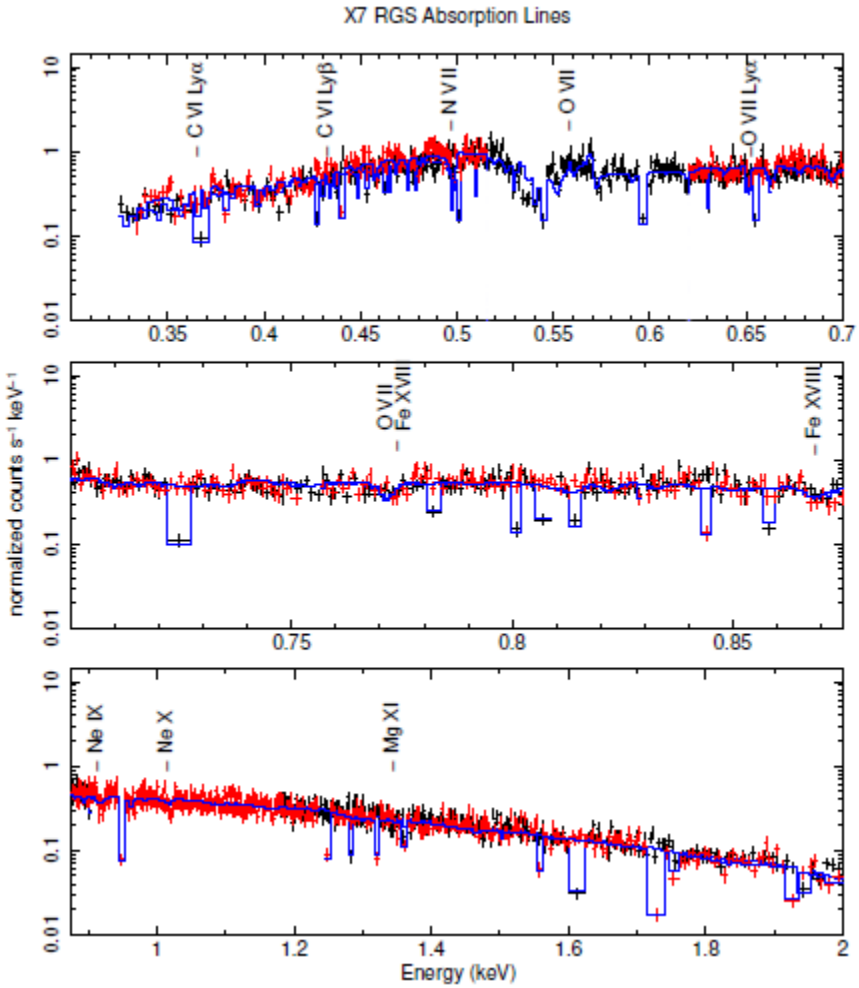

Figure 4.27: Absorption lines detected during the X7 RGS analysis. The 0.3 - 2 keV band is split into three regions. The top panel is 0.3 - 0.7 keV, the middle panel is 0.7 - 0.875, and the bottom panel is 0.875 - 2 keV. RGS1 data are black, RGS2 data are red, and the model is blue.

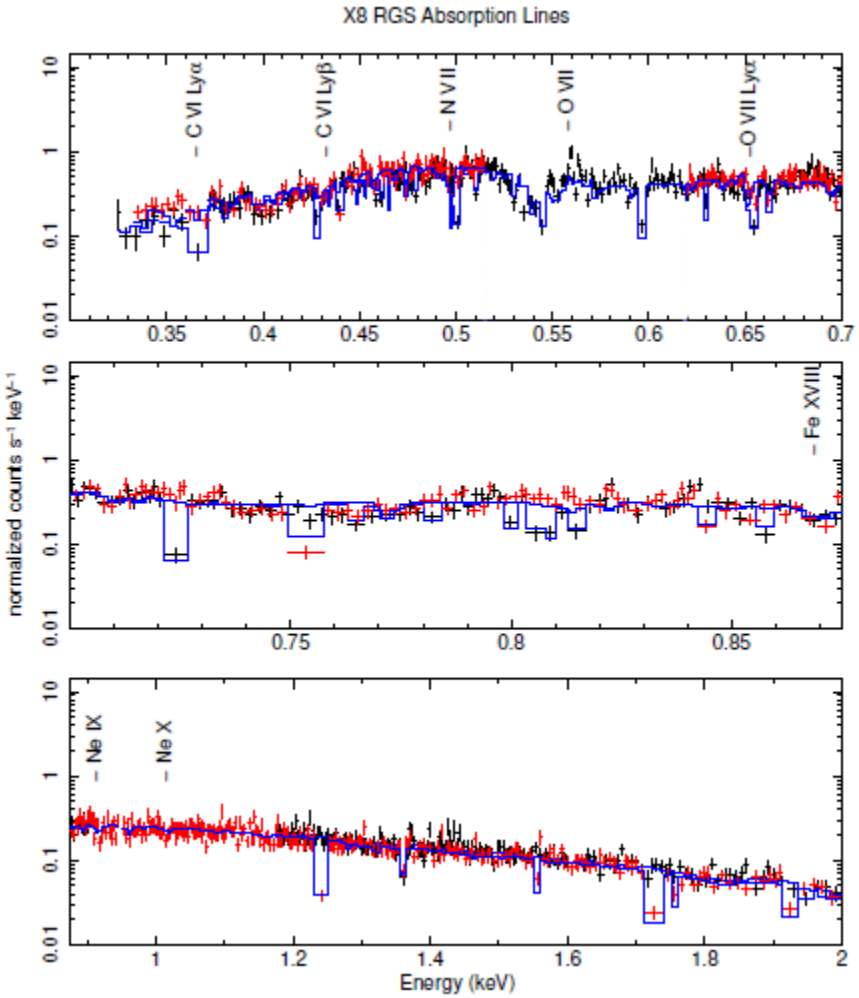

Figure 4.28: Absorption lines detected during the X38RGS analysis. The 0.3 - 2 keV band is split into three regions. The top panel is 0.3 - 0.7 keV, the middle panel is 0.7 - 0.875, and the bottom panel is 0.875 - 2 keV. RGS1 data are black, RGS2 data are red, and the model is blue.

NGC 3227 TIME RESOLVED ANALYSIS

In this chapter we explore time resolved analysis of the high flux observations presented previously. The observations S1, X2, and all XMM-Newton observations of the 2016 campaign are used. The other Suzaku observations and X1 did not have sufficiently high flux for time resolved analysis to be performed. The purpose of this analysis is to observe how the behaviour of the source changes over the course of the observation. In addition, it allows us to study events within the observation more carefully. In particular, the transition from the low branch to the high branch exhibited by S1 and the sharp increase in flux during the later half of X5 are of interest. The majority of the short term variability takes place in the soft (0.3 - 2 keV) band. As such, NuStar is unable to observe this region. For this reason, NuStar is not included in this chapter.

Light curves with hardness ratios are presented, which are divided into the time regions within the observation. To avoid confusion with the light curves present in Chapters 3 and 4, these new figures will be referred to as "ratio light curves". The ratio light curves are displayed in Figures 5.1 - 5.8. To create the ratio light curves, we first took each observation and formed the soft band (0.5 - 2 keV for S1 and 0.3 - 2 keV for the XMM-Newton observations) and hard band (2 - 10 keV) light curves. Then, we divided the hard band light curve by the soft band light curve to form the hardness ratio. Each figure contains three panels. The top panel is the soft band light curve, the middle panel is the hard band light curve, and the bottom panel is the hardness ratio. Each region is labeled sequencially with an "R" to define it as a time region using the observation as a prefix. For example, the second time region of X4 is labeled X4R2.

Time regions were chosen by the behaviour of the hardness ratio. For example, X5 is split into four time regions. The first region (X5R1) has a flat hardness ratio (see Figure 5.5). The hardness ratio decreases during X5R2. A sharp dip in the hardness ratio is seen

in X5R3 and the ratio returns to a stable state in X5R4. Once the time regions had been chosen, spectra of each region were created using XSELECT. Initially, the time averaged models found in Chapters 3 and 4 were applied to each region. Then, the model parameters were allowed to vary and the models were fit. The parameters of the best fits are displayed in Tables 5.1 - 5.8.

5.1 S1 Time Resolved Analysis

Previously in Chapter 3, the S1 observation flux-flux plot (see Figure 3.9) displayed a distinct two branch structure. The other Suzaku observations took place during the low state, while S1 spent time in both high and low states during the observation. The S1 ratio light curve is shown in Figure 5.1. The observation begins in the low state (SR1), spends some time transitioning (SR2 and SR3), then rapidly advances to the high state (SR4 and SR5). Comparing the top and middle panels of Figure 5.1, we see that the soft and hard band have mirrored behaviour with the soft emission varying more strongly. This corresponds to a drop in the hardness ratio throughout the observation (Figure 5.1 bottom panel). Model parameters for fits of all of the regions are displayed in Table 5.1.

The density and covering fraction of the partial coverer was highest in the low flux state (SR1) and lowest in the high flux states (SR4 and SR5). The best fit Xillver reflection fraction also dropped during the observation. In the low state (SR1), the 0.922 keV Ne IX line seen in other observations breifly appeared, but faded when the flux increased. The lower flux regions (SR1 and SR2) did not require a soft excess component unlike the high state (SR4 and SR5). The warm absorbers remained largely consistent, although there was some fluctuation in the density of the LIWA.

5.2 X2 Time Resolved Analysis

The flux of X2 varied periodically thoughout the observation as seen by the ratio light curve of the observation (Figure 5.2). Model parameters for the time resolved fits are listed in Table 5.2. The hardness ratio remained largely stable throughout the observation as seen by Figure 5.2 bottom panel. Many of the best fit model parameters also remained consistent including the neutral absorber, the LIWA, the Xillver ionization parameter and reflection fraction, and the soft power law. The Xillver hard power law was low in X2R1, increased and peaked in X2R3, then dropped for the rest of the observation. This behaviour was also seen during the time resolved analysis of Markowitz et al. (2009) (see their Figure 13). The HIWA density was unstable and was fixed to the time averaged model for the best fits. The HIWA ionization parameter was consistent although only lower limits were found for X2R1, X2R3, and X2R4. The absorption edge was consistent except for X2R3 where it vanished. This is most likely an artifact of fitting. Overall, the time resolved results agree with the time averaged analysis and the time resolved analysis performed by Markowitz et al. (2009).

5.3 X3 Time Resolved Analysis

The observation X3 ratio light curve is displayed in Figure 5.3 and the time resolved model parameters are listed in Table 5.3. The general behaviour is higher flux during the first two regions and lower flux during the last two. Many of the parameters including Xillver ionization parameter and reflection fraction, the soft power law, the NIWA parameters, and the HIWA parameters remained consistent throughout the observation. Referring to Figure 5.3, the flux drops somewhat throughout the observation. This corresponds to a drop in the hard power law index as the observation progresses, consistent with other observations. The density of the neutral absorber appears to drop during the observation, but the fit is somewhat insensitive to this value. Fixing the neutral absorber density to the time averaged

model ($N_H = 4.85 \times 10^{20}\text{cm}^{-2}$) yeilded $\Delta\chi^2/DOF = +6.99$ for X3R1, $\Delta\chi^2/DOF = +15.38$ for X3R2, $\Delta\chi^2/DOF = +12.33$ for X3R3, and $\Delta\chi^2/DOF = +0.14$ for X3R4.

Recall that the mekal model is emission from a diffuse plasma as described in Section 4.4.2. The mekal plasma temperature also appears to decrease during the observation. Fixing the mekal temperature to the time averaged model (kT= 103.61 eV) yeilded $\Delta\chi^2/DOF = +33.53$ for X3R1, $\Delta\chi^2/DOF = +21.61$ for X3R2, and $\Delta\chi^2/DOF = +19.33$ for X3R3. The mekal temperature for the X3R4 best fit was consistent with the time averaged value.

5.4 X4 Time Resolved Analysis

The observation X4 lacked interesting features in its time resolved analysis. The X4 ratio light curve is displayed in Figure 5.4 and the time resolved model parameters are listed in Table 5.4. Similar to X3, X4 begins at higher flux and drops off during the observation while remaining in the high state (see Figure 5.4). The Xillver hard power law drops and the reflection fraction rises from the beginning of the observation as expected by the behaviour of the light curve. All other parameters of Xillver remain consistent. The neutral absorber, all three warm absorbers, and mekal remain consistent thoughout the observation within error bars. The soft power law was also consistent except for X4R2, where the best fit had a lower value for the soft power law index compared to other regions. Fixing the X4R2 value of the soft power law index to the time averaged value ($\Gamma = 3.72$) yeilded $\Delta\chi^2/DOF = +7.24$, so this is a result of aquiring a best fit rather than the source behaving differently during this time region.

5.5 X5 Time Resolved Analysis

During the observation X5, the soft flux substantially increases during X5R3. The hard flux also increases during this time but to a smaller degree. The X5 ratio light curve

is displayed in Figure 5.5 and the time resolved model parameters are listed in Table 5.5. Throughout the observation, the soft power law index and warm absorbers displayed stable behaviour. Mekal was also largely stable except in the X5R3 where the best fit temperature was higher. Fixing this parameter to the time averaged value worsened the fit by only $\Delta\chi^2 = +9.36$ so this remains consistent. For Xillver, the index of the hard power law increased with flux as seen previously. Values of the Xillver ionization parameter agree with each other and the time averaged value although in most regions only the upper limit was found. We also see the general decrease in reflection fraction with increasing flux, also noting that the last two regions X5R3 and X5R4 could only find upper limits. The flux increase during X5R3 will be discussed in greater detail in Section 5.9.

5.6 X6 Time Resolved Analysis

The observation X6 ratio light curve is displayed in Figure 5.6 and the model parameters are listed in Table 5.6. From Figure 5.6, the source appears to exhibit periodic flux variability with a period of $\sim 2\times10^4$ seconds. The Xillver parameters, soft power law, neutral absorber, NIWA, and HIWA remained consistent throught the observation within error bars. The fits were insensitive to the NIWA column density, so it was fixed to the time averaged value ($7.45 \times 10^{21}\mathrm{cm}^{-2}$). The LIWA density remained consistent although higher than the time averaged value. The LIWA ionizaiton parameter was lower than the time averaged value across all time regions. Fixing the LIWA ionization parameter value to the time averaged model showed a significant decrease in goodness of fit for the first two regions with $\Delta\chi^2/DOF = +40.65$ for X6R1 and $\Delta\chi^2/DOF = +61.48$ for X6R2, but not for the last two regions with $\Delta\chi^2/DOF = +3.85$ for X6R3 and $\Delta\chi^2/DOF = +12.09$ for X6R4. The mekal temperature also was higher in X6R2 and fixing it to the time averaged value worsened the fit by $\Delta\chi^2/DOF = +23.68$. With these results, the LIWA ionization state may have increased during the observation but otherwise it remained stable.

5.7 X7 Time Resolved Analysis

The observation X7 produced the most stable parameters during the time resolved analysis of the 2016 campaign. The X7 ratio light curve is displayed in Figure 5.7 and the model parameters are listed in Table 5.7. The light curve was more bright and variable in the first two regions compared to the last two. However, this behaviour did not manifest in the model parameters. The Xillver parameters, soft power law, mekal parameters, LIWA, and HIWA parameters remained consistent across all regions and consistent with the time averaged model within error bars. The NIWA ionization parameter was also consistent. The only exception was the best fit value of the NIWA density in X7R3 being higher than the other regions. Fixing the NIWA density to the time averaged value ($0.84 \times 10^{20} \mathrm{cm}^{-2}$) yeilded $\Delta\chi^2/DOF = +37.83$.

5.8 X8 Time Resolved Analysis

The observation X8 was characterized by a drop in the density of absorbing material during the observation as discussed in Chapter 4 and Turner et al. (2018). The X8 ratio light curve is displayed in Figure 5.8 and the model parameters are listed in Table 5.8. Observing Figure 5.8, the hard band shows some increase but is largely stable. The soft band rises in flux substantially which results in a clear decrease in the hardness ratio throughout the observation. Since we split this observation in half in Chapter 4, we will compare the X8R1 and X8R2 models to the XN8 Low model and the X8R3 and X8R4 models to the XN8 High model. We also refer to the Chapter 4 model as time averaged to keep consistency with the rest of this chapter despite XN8 being split in half temporally.

The results are consistent with the Chapter 4 analysis. Most parameters are either within error bars of the Chapter 4 models or the error bars nearly overlap. The neutral absorber was slightly below error bars for the first two regions and within error bars for the

last two regions. Both the Xillver hard power law index and reflection fraction fluctuates, but we note that the XN8 Low values are between the best fit values X8R1 and X8R2, and the XN8 High values are between the best fit values for X8R3 and X8R4 (see Tables 4.2 and 5.8) for both of these parameters. Mekal parameters and the soft power law remained consistent throughout the observation. The time resolved models were insensitive to the NIWA density, so its value was fixed to the Chapter 4 model (8.71×10^{21} cm^{-2} for XN8 Low and 7.74×10^{21} cm^{-2} for XN8 High). The NIWA ionization parameter remained consistent. The LIWA density drops off by an order of magnitude between X8R2 and X8R3, consistent with Chapter 4. The HIWA density was lower than the Chapter 4 models but the fits are less sensitive to changes in HIWA density compared to the neutral absorber or LIWA. Fixing the time resolved values to the time averaged model yeilds $\Delta\chi^2/DOF = +23.56$ for X8R1, $\Delta\chi^2/DOF = +2.07$ for X8R2, $\Delta\chi^2/DOF = +0.88$ for X8R3, and $\Delta\chi^2/DOF = +21.72$ for X8R4. The HIWA ionization parameter remained consistent.

5.9 Discussion

First, we note that our time averaged models presented in Chapter 3 and 4 were able to successfully model time resolved regions with minor alterations. Thus, our model is capable of explaining the behavior of the source on both short and long time scales. Some of the observations (X2 and X4) produced time resolved results that confirmed the time average model but did not improve our understanding of the observation.

The time resolved analysis of S1 produced trends that appeared in Chapter 3's Luminosity and Model Parameter Relation section (Section 3.7). As the source increased in luminosity, the partial covering density and covering fraction decreased, the Xillver power law index increased while the reflection fraction decreased, and the inclusion of a soft power law became necessary. This shows that the behavior present on longer time scales ($\sim$1 week) is also present on time scales within an observation (10s of ks). The S1 time resolved analysis

also reinforces the idea that the only major addition to the low state model to explain the source at a high state is the inclusion of a soft excess component.

The observation X3 produced an apparent drop in the mekal plasma temperature during the observation. From the changes in $\Delta\chi^2$ presented in Section 5.3, this is reasonably statistically significant. A drop in mekal temperature would decrease the soft emission, a characteristic seen during the observation. We consider a cooling of the plasma temperature during the observation partially responsible for the decrease in soft flux. The remainder of the soft flux drop corresponds to a significant decrease in soft power law normalization during X3R4.

The observation X5 produced a sharp increase in flux during X5R3 that warranted additional investigation. Note that the normalization of the soft power law significantly increased during X5R3, implying that a soft power law component is largely responsible for the flare (Table 5.5). In addition, the flux is stable during the earlier part of the observation (Figure 5.5). This provides us with an opportunity to isolate the spectrum of the flare by subtracting the spectrum of X5R1 from X5R3. In this manner, the stable components are subtracted and the variable components (primarily the flare) remain. We then apply the time averaged XN5 model to the spectrum and fit.

The stable components proved to be both Xillver and mekal, leaving the flare to be modeled entirely by an absorbed soft power law. Model parameters are listed in Table 5.9 and the spectrum is shown in Figure 5.9. The soft power law had a markedly lower index ($\Gamma = 2.37$) than the soft power law generally responsible for the soft emission. This may be the cause for the total soft power law index to drop during the fitting of X5R3 (see Table 5.5). The density of the HIWA was significantly larger than the time averaged model ($89.14 \times 10^{21}\mathrm{cm}^{-2}$ vs $14.64 \times 10^{21}\mathrm{cm}^{-2}$) but the fit was fairly insensitive to this parameter. Fixing the parameter to the time averaged value worsened the fit by $\Delta\chi^2 = +12.52$. The HIWA ionization parameter was within error bars. Both parameters of the LIWA were within

error bars. The NIWA density was somewhat lower than expected. Fixing it to the time averaged value worsens the fit by $\Delta\chi^2 = +2.06$ so this should not be an issue. The NIWA ionization parameter was slightly higher than expected but it is consistent when considering error bars. Absorption features are thus consistent with the time averaged model and the time resolved models. Since the X5 flare is modeled with a power law between the soft and hard power laws present in the time averaged and time resolved analyses, we propose this event occurs in addition to the processes responsible for the two power laws. This could be caused by short increase in accretion rate due to a significant mass of material infalling.

The observation X6 produced a statistically significant descrepancy in LIWA ionization parameters between the time averaged model and regions X6R1 and X6R2. This could not be resolved by shifting the values of other parameters. As such, we may have observed an increase in the ionization of the absorbing cloud modeled as the LIWA during this observation.

The observation X7 produced an increase in the NIWA density during X7R3. Referring to Figure 5.7, we notice a dip in flux during the middle of X7R3. This dip is most obvious in the soft band (top panel), but also exists in the hard band (middle panel) as evidenced by the stable hardness ratio (bottom panel). Due to the shortness of the timescale, it is unlikely that additional absorbing material entered or left the line of sight. We interpret this as a momentary decrease in the size of the emission region. Akin to the partial covering trends displayed in Section 3.7, a decrease in the size of the emission region could cause the emitted flux to cease being absorbed by a low density portion of the cloud. As a result, the apparent density would increase.

In Chapter 4, we needed to split XN8 in half in order to model it. This chapter further splits XN8 Low and XN8 High into two regions each. However, the additional division did not reveal anything we did not observe previously. The LIWA density dramatically reduces between X8R2 and X8R3. The in-depth analysis performed by Turner et al. (2018) modeled

this behaviour as a lowly ionized partial covering absorber drifting out of the line of sight during the observation. Their model kept the density constant while allowing the covering fraction to vary. The covering fraction dramatically reduced during the observation and this approach successfully modeled this behaviour. Since we are using a fully covering warm absorber, it instead manifests as a drop in column density of the absorber. The stability of the mekal parameters and the soft power law during X8 imply that the increase in flux is due to the removal of material only, compared to an increase in emission region responsible for the low state to high state transition displayed by S1.

5.10 Summary and Concluding Remarks

Overall, the time resolved analysis is consistent with the time averaged analysis performed in Chapters 3 and 4. The observation S1 was able to observe the source in the low and high states. Consistent with the other Suzaku observations, the low states did not require a soft power law while the high states did. The observation X2 showed variations in the hard power law that agreed with Markowitz et al. (2009). The observation X3 may have observed a cooling of the plasma responsible for the emission modeled by mekal. The observation X4 did not produce interesting results. The observation X5 contained a flare in X5R3 that produced a soft emission spectrum. This was modeled by a power law with an index between the values of the soft and hard power laws. The observation X6 witnessed an increased in the LIWA ionization. The observation X7 observed a brief decrease of the emission region during X7R3. The observation X8 remained consistent with our Chapter 4 analysis and Turner et al. (2018).

Chapter 5 Tables

Table 5.1: S1 XIS time resolved parameters.

Component	Parameter	S1R1	S1R2	S1R3	S1R4	S1R5
Ionized Partial Covering	N_H $\left(10^{22} cm^{-2}\right)$	$6.48^{+0.46}_{-0.45}$	$1.81^{+0.14}_{-0.13}$	$1.74^{+0.11}_{-0.10}$	$1.14^{+0.23}_{-0.22}$	$1.31^{+0.50}_{-0.38}$
	Log ξ	$1.08^{+0.10}_{-0.26}$	$0.66^{+0.15}_{-0.14}$	$0.30^{+0.20}_{-0.28}$	< 0.95	< 0.65
	Covering Fraction	$0.68^{+0.01}_{-0.01}$	$0.55^{+0.01}_{-0.01}$	$0.62^{+0.04}_{-0.04}$	$0.32^{+0.06}_{-0.06}$	$0.15^{+0.04}_{-0.04}$
Xillver[a]	Γ_{Hard}	$1.60^{+0.02}_{-0.02}$	$1.60^{+0.01}_{-0.01}$	$1.57^{+0.03}_{-0.03}$	$1.64^{+0.03}_{-0.03}$	$1.71^{+0.02}_{-0.02}$
	Log ξ	< 1.08	$0.34^{+0.07}_{-0.12}$	$1.54^{+0.23}_{-0.37}$	< 1.32	$1.00^{+0.12}_{-0.48}$
	Reflection Fraction	< 1.26	$1.19^{+0.12}_{-0.12}$	$0.62^{+0.11}_{-0.11}$	$0.63^{+0.17}_{-0.15}$	$0.62^{+0.12}_{-0.12}$
	XIS 0 & 3 Norm. $\left(10^{-4}\right)$	$1.34^{+0.02}_{-0.02}$	$1.72^{+0.02}_{-0.02}$	$1.88^{+0.02}_{-0.02}$	$2.06^{+0.03}_{-0.03}$	$2.44^{+0.03}_{-0.03}$
	XIS 1 Norm. $\left(10^{-4}\right)$	$1.28^{+0.03}_{-0.03}$	$1.63^{+0.02}_{-0.02}$	$1.75^{+0.03}_{-0.03}$	$1.91^{+0.04}_{-0.04}$	$2.35^{+0.04}_{-0.04}$
Ne IX Emission	XIS 0 & 3 Norm. $\left(10^{-4}\right)$	< 2.37				
	XIS 1 Norm. $\left(10^{-4}\right)$	$4.00^{+2.81}_{-2.81}$				
High Ion. Warm Abs.	N_H $\left(10^{21} cm^{-2}\right)$	$51.11^{+20.99}_{-15.69}$	$45.34^{+4.71}_{-4.39}$	> 50.25	$50.01^{+16.19}_{-12.28}$	> 46.99
	Log ξ	$2.36^{+0.02}_{-0.02}$	$2.24^{+0.01}_{-0.01}$	$2.70^{+0.14}_{-0.14}$	$2.34^{+0.03}_{-0.03}$	$2.81^{+0.13}_{-0.13}$
Low Ion. Warm Abs.	N_H $\left(10^{21} cm^{-2}\right)$	$7.69^{+0.87}_{-0.73}$	$3.24^{+0.19}_{-0.30}$	$9.37^{+1.32}_{-1.22}$	$4.89^{+0.88}_{-0.77}$	$6.01^{+0.62}_{-0.59}$
	Log ξ	$1.52^{+0.05}_{-0.05}$	$1.36^{+0.05}_{-0.05}$	$1.56^{+0.08}_{-0.06}$	$1.46^{+0.13}_{-0.11}$	$1.46^{+0.07}_{-0.06}$
Soft Power Law[a]	Γ_{Soft}			$3.30^{+0.30}_{-0.29}$	$3.30^{+0.69}_{-0.63}$	$3.29^{+1.22}_{-1.01}$
	XIS 0 & 3 Norm. $\left(10^{-3}\right)$			$1.52^{+0.24}_{-0.24}$	$0.58^{+0.29}_{-0.29}$	$0.69^{+0.28}_{-0.24}$
	XIS 1 Norm. $\left(10^{-3}\right)$			$1.17^{+0.23}_{-0.23}$	$1.12^{+0.28}_{-0.28}$	$0.69^{+0.24}_{-0.24}$
Fe Absorption Edge	τ	< 0.11	$0.06^{+0.04}_{-0.04}$	$0.10^{+0.05}_{-0.05}$	$0.08^{+0.06}_{-0.06}$	$0.11^{+0.05}_{-0.05}$
	χ^2/DOF	226.71/189	522.03/499	500.39/203	353.17/336	643.38/595
	P-value	0.0316	0.2298	0.5244	0.2491	0.0850

[a]Xillver and Power law normalizations are photons $\mathrm{keV}^{-1}\mathrm{cm}^{-2}\mathrm{s}^{-1}$ at 1 keV.

Table 5.2: X2 pn time resolved parameters.

Component	Parameter	X2R1	X2R2	X2R3	X2R4	X2R5
Neutral Absorption	N_H $\left(10^{20} cm^{-2}\right)$	$8.67^{+0.93}_{-1.00}$	$10.25^{+0.37}_{-0.38}$	$9.43^{+0.46}_{-0.47}$	$10.58^{+0.46}_{-0.47}$	$10.40^{+0.53}_{-0.55}$
Xillver[a]	Γ_{Hard}	$1.47^{+0.01}_{-0.01}$	$1.57^{+0.01}_{-0.01}$	$1.64^{+0.01}_{-0.01}$	$1.56^{+0.01}_{-0.01}$	$1.59^{+0.01}_{-0.01}$
	Log ξ	$1.40^{+0.30}_{-0.26}$	$1.30^{+0.04}_{-0.16}$	$1.09^{+0.02}_{-0.22}$	$1.29^{+0.04}_{-0.15}$	< 1.03
	Reflection Fraction	$0.62^{+0.09}_{-0.09}$	$0.73^{+0.07}_{-0.06}$	$0.89^{+0.09}_{-0.10}$	$0.66^{+0.08}_{-0.09}$	$0.78^{+0.09}_{-0.09}$
	pn Norm. $\left(10^{-4}\right)$	$3.23^{+0.02}_{-0.02}$	$2.58^{+0.01}_{-0.01}$	$2.28^{+0.01}_{-0.01}$	$2.55^{+0.01}_{-0.01}$	$2.59^{+0.01}_{-0.01}$
High Ion. Warm Abs.	N_H $\left(10^{21} cm^{-2}\right)$	$36.51(fixed)$	$36.51(fixed)$	$36.51(fixed)$	$36.51(fixed)$	$36.51(fixed)$
	Log ξ	> 2.54	$3.00^{+0.94}_{-0.24}$	> 2.68	> 2.88	$2.97^{+0.91}_{-0.21}$
Low Ion. Warm Abs.	N_H $\left(10^{21} cm^{-2}\right)$	$3.56^{+0.20}_{-0.19}$	$3.90^{+0.13}_{-0.13}$	$3.99^{+0.18}_{-0.17}$	$3.46^{+0.16}_{-0.16}$	$3.05^{+0.15}_{-0.14}$
	Log ξ	$1.31^{+0.06}_{-0.06}$	$1.33^{+0.04}_{-0.04}$	$1.30^{+0.05}_{-0.04}$	$1.32^{+0.05}_{-0.05}$	$1.38^{+0.06}_{-0.06}$
Soft Power Law[a]	Γ_{Soft}	$3.80^{+0.09}_{-0.09}$	$3.80^{+0.03}_{-0.03}$	$3.80^{+0.05}_{-0.05}$	$3.80^{+0.04}_{-0.04}$	$3.80^{+0.05}_{-0.05}$
	pn Norm. $\left(10^{-3}\right)$	$1.48^{+0.03}_{-0.03}$	$2.72^{+0.03}_{-0.03}$	$3.15^{+0.04}_{-0.04}$	$2.91^{+0.03}_{-0.03}$	$2.54^{+0.03}_{-0.03}$
Absorption Edge	Energy (keV)	$0.85^{+0.03}_{-0.03}$	$0.85^{+0.01}_{-0.01}$		$0.84^{+0.01}_{-0.02}$	$0.84^{+0.01}_{-0.01}$
	τ	$0.14^{+0.03}_{-0.03}$	$0.15^{+0.01}_{-0.01}$		$0.12^{+0.02}_{-0.02}$	$0.14^{+0.02}_{-0.02}$
	χ^2/DOF	681.15/626	1087.32/1020	768.69/692	788.64/758	777.37/741
	P-value	0.0626	0.0703	0.0223	0.2137	0.1718

[a]Xillver and Power law normalizations are photons keV^{-1}cm^{-2}s^{-1} at 1 keV.

Table 5.3: X3 pn time resolved parameters.

Component	Parameter	X3R1	X3R2	X3R3	X3R4
Neutral Absorption	N_H $\left(10^{20} cm^{-2}\right)$	$7.23^{+0.46}_{-0.46}$	$2.68^{+0.47}_{-0.45}$	$2.69^{+0.48}_{-0.46}$	< 0.82
Xillver[a]	Γ_{Hard}	$1.73^{+0.03}_{-0.03}$	$1.62^{+0.04}_{-0.04}$	$1.53^{+0.04}_{-0.04}$	$1.55^{+0.06}_{-0.06}$
	Log ξ	< 1.7	< 2.03	< 2.36	< 1.31
	Reflection Fraction	$1.16^{+0.24}_{-0.24}$	< 0.99	< 1.26	< 1.43
	pn Norm. $\left(10^{-4}\right)$	$2.26^{+0.03}_{-0.03}$	$2.64^{+0.04}_{-0.04}$	$2.26^{+0.04}_{-0.04}$	$1.45^{+0.04}_{-0.04}$
Mekal[b]	kT (eV)	$181.61^{+11.59}_{-13.62}$	$149.49^{+11.41}_{-8.71}$	$152.63^{+15.14}_{-10.07}$	$103.94^{+11.48}_{-13.41}$
	pn Norm. $\left(10^{-3}\right)$	$7.52^{+1.87}_{-1.87}$	$29.84^{+3.60}_{-3.60}$	$17.10^{+3.72}_{-2.19}$	$17.80^{+3.13}_{-3.13}$
High Ion. Warm Abs.	N_H $\left(10^{21} cm^{-2}\right)$	$66.70^{+20.79}_{-16.26}$	$76.32^{+10.99}_{-10.90}$	$87.82^{+9.17}_{-8.61}$	$88.76^{+13.09}_{-23.56}$
	Log ξ	$2.73^{+0.04}_{-0.04}$	$2.49^{+0.04}_{-0.04}$	$2.44^{+0.03}_{-0.03}$	$2.61^{+0.07}_{-0.06}$
Low Ion. Warm Abs.	N_H $\left(10^{21} cm^{-2}\right)$	$2.61^{+0.41}_{-0.39}$	$3.55^{+0.24}_{-0.25}$	$3.63^{+0.24}_{-0.25}$	$1.13^{+0.33}_{-0.35}$
	Log ξ	$0.74^{+0.06}_{-0.06}$	$0.15^{+0.03}_{-0.03}$	$0.13^{+0.03}_{-0.03}$	< 0.82
Neg Ion. Warm Abs.	N_H $\left(10^{21} cm^{-2}\right)$	> 3.91	$2.78^{+1.06}_{-0.89}$	$2.36^{+1.07}_{-0.68}$	$1.61^{+1.04}_{-0.25}$
	Log ξ	$-1.32^{+0.02}_{-0.02}$	$-1.17^{+0.02}_{-0.02}$	$-1.19^{+0.02}_{-0.02}$	> -0.62
Soft Power Law[a]	Γ_{Soft}	$3.80^{+0.05}_{-0.05}$	$3.86^{+0.04}_{-0.05}$	$3.87^{+0.04}_{-0.05}$	$3.57^{+0.24}_{-0.26}$
	pn Norm. $\left(10^{-3}\right)$	$14.52^{+0.47}_{-0.47}$	$27.08^{+0.57}_{-0.57}$	$16.40^{+0.37}_{-0.37}$	$2.82^{+0.25}_{-0.25}$
	χ^2/DOF	382.96/391	401.44/376	367.88/375	132.25/98
	P-value	0.6047	0.1757	0.5937	0.0121

[a]Xillver and Power law normalizations are photons $\mathrm{keV}^{-1}\mathrm{cm}^{-2}\mathrm{s}^{-1}$ at 1 keV.

[b]Mekal normalization is $10^{-14}/4\pi(D_A(1+z))^2) \int n_e n_H \, dV$ where D_A is the angular diameter distance to the source (cm), n_e and n_H are the electron and H densities (cm^{-3}), respectively.

Table 5.4: X4 pn time resolved parameters.

Component	Parameter	X4R1	X4R2	X4R3	X4R4	X4R5
Neutral Covering	N_H $\left(10^{20} cm^{-2}\right)$	$5.00^{+0.71}_{-0.73}$	$5.78^{+0.57}_{-0.57}$	$3.88^{+0.73}_{-0.72}$	$5.79^{+1.18}_{-1.27}$	$3.43^{+1.04}_{-0.11}$
Xillver[a]	Γ_{Hard}	$1.72^{+0.01}_{-0.01}$	$1.54^{+0.02}_{-0.02}$	$1.41^{+0.02}_{-0.02}$	$1.47^{+0.02}_{-0.02}$	$1.50^{+0.02}_{-0.02}$
	Log ξ	< 0.80	< 1.34	< 1.59	$1.00^{+0.15}_{-0.36}$	$0.68^{+0.34}_{-0.36}$
	Reflection Fraction	$0.98^{+0.14}_{-0.14}$	< 0.99	$1.09^{+0.17}_{-0.17}$	$1.42^{+0.18}_{-0.18}$	$1.57^{+0.19}_{-0.18}$
	pn $\left(10^{-4}\right)$	$1.88^{+0.02}_{-0.02}$	$1.95^{+0.02}_{-0.02}$	$1.89^{+0.02}_{-0.02}$	$1.67^{+0.02}_{-0.02}$	$1.55^{+0.02}_{-0.02}$
Mekal[b]	kT (eV)	$152.62^{+28.49}_{-32.76}$	$140.25^{+57.78}_{-67.38}$	$145.58^{+33.65}_{-32.78}$	$154.26^{+27.08}_{-23.08}$	$186.05^{+19.06}_{-31.13}$
	pn Norm. $\left(10^{-3}\right)$	$1.34^{+0.59}_{-0.59}$	$0.69^{+0.43}_{-0.43}$	$2.57^{+0.50}_{-0.50}$	$0.67^{+0.30}_{-0.30}$	$0.86^{+0.24}_{-0.24}$
High Ion. Warm Abs.	N_H $\left(10^{21} cm^{-2}\right)$	$1.78^{+0.32}_{-0.61}$	$2.84^{+0.76}_{-0.62}$	$0.91^{+0.61}_{-0.42}$	$0.99^{+0.46}_{-0.40}$	$0.82^{+0.37}_{-0.28}$
	Log ξ	$2.51^{+0.02}_{-0.02}$	$2.61^{+0.12}_{-0.12}$	$2.64^{+0.53}_{-0.37}$	$2.36^{+0.68}_{-0.69}$	$2.17^{+0.51}_{-0.76}$
Low Ion. Warm Abs.	N_H $\left(10^{21} cm^{-2}\right)$	$1.04^{+0.19}_{-0.16}$	$1.84^{+0.28}_{-0.39}$	$1.87^{+0.09}_{-0.09}$	$1.23^{+0.32}_{-0.26}$	$1.80^{+0.19}_{-0.32}$
	Log ξ	$1.01^{+0.23}_{-0.24}$	< 0.17	$1.08^{+0.10}_{-0.17}$	$0.72^{+0.38}_{-0.32}$	$0.40^{+0.19}_{-0.17}$
Neg Ion. Warm Abs.	N_H $\left(10^{21} cm^{-2}\right)$	$1.08^{+0.09}_{-0.10}$	> 1.71	$1.47^{+0.05}_{-0.05}$	$2.96^{+1.06}_{-0.82}$	$4.11^{+1.27}_{-1.02}$
	Log ξ	$-1.00^{+0.08}_{-0.10}$	$-1.92^{+0.29}_{-0.13}$	$-0.97^{+0.04}_{-0.07}$	$-1.79^{+0.08}_{-0.08}$	$-1.77^{+0.06}_{-0.06}$
Soft Power Law[a]	Γ_{Soft}	$3.80^{+0.07}_{-0.07}$	$3.36^{+0.07}_{-0.07}$	$3.81^{+0.06}_{-0.06}$	$3.80^{+0.14}_{-0.13}$	$3.80^{+0.12}_{-0.11}$
	pn Norm. $\left(10^{-3}\right)$	$2.80^{+0.12}_{-0.12}$	$3.62^{+0.10}_{-0.10}$	$2.16^{+0.08}_{-0.08}$	$0.82^{+0.06}_{-0.06}$	$0.80^{+0.06}_{-0.06}$
	χ^2/DOF	568.97/524	537.24/486	435.57/392	413.66/379	421.18/379
	P-value	0.0851	0.0537	0.0637	0.1063	0.0665

[a]Xillver and Power law normalizations are photons $\mathrm{keV}^{-1}\mathrm{cm}^{-2}\mathrm{s}^{-1}$ at 1 keV.

[b]Mekal normalization is $10^{-14}/4\pi(D_A(1+z))^2) \int n_e n_H \, dV$ where D_A is the angular diameter distance to the source (cm), n_e and n_H are the electron and H densities (cm^{-3}), respectively.

Table 5.5: X5 pn time resolved parameters.

Component	Parameter	X5R1	X5R2	X5R3	X5R4
Xillver[a]	Γ_{Hard}	$1.43^{+0.01}_{-0.01}$	$1.59^{+0.02}_{-0.02}$	$1.66^{+0.01}_{-0.01}$	$1.62^{+0.02}_{-0.02}$
	Log ξ	$0.39^{+0.14}_{-0.10}$	< 1.40	< 1.37	< 2.03
	Reflection Fraction	$1.07^{+0.10}_{-0.10}$	$0.81^{+0.15}_{-0.14}$	< 0.76	< 0.71
	pn Norm. $\left(10^{-4}\right)$	$1.59^{+0.01}_{-0.01}$	$1.55^{+0.02}_{-0.02}$	$2.02^{+0.02}_{-0.02}$	$2.06^{+0.02}_{-0.02}$
Mekal[b]	kT (ev)	$171.08^{+6.29}_{-10.26}$	$179.96^{+8.26}_{-8.26}$	$199.95^{+8.77}_{-7.28}$	$180.88^{+12.36}_{-10.16}$
	pn Norm. $\left(10^{-3}\right)$	$1.64^{+0.30}_{-0.30}$	$2.16^{+0.52}_{-0.52}$	$4.29^{+0.58}_{-0.58}$	$2.61^{+0.70}_{-0.70}$
High Ion. Warm Abs.	N_H $\left(10^{21} cm^{-2}\right)$	$15.92^{+8.60}_{-5.86}$	$15.32^{+10.86}_{-6.39}$	$29.33^{+27.79}_{-16.90}$	$10.42^{+14.49}_{-7.54}$
	Log ξ	$2.84^{+0.03}_{-0.03}$	$2.85^{+0.05}_{-0.05}$	$2.94^{+0.02}_{-0.02}$	$2.89^{+0.05}_{-0.05}$
Low Ion. Warm Abs.	N_H $\left(10^{21} cm^{-2}\right)$	$2.26^{+0.19}_{-0.18}$	$2.26^{+0.26}_{-0.24}$	$3.12^{+0.28}_{-0.26}$	$2.26^{+0.23}_{-0.21}$
	Log ξ	$0.95^{+0.15}_{-0.05}$	$1.09^{+0.14}_{-0.17}$	$1.18^{+0.08}_{-0.08}$	$1.09^{+0.19}_{-0.20}$
Neg Ion. Warm Abs.	N_H $\left(10^{21} cm^{-2}\right)$	$2.65^{+0.25}_{-0.33}$	$2.64^{+0.30}_{-0.38}$	$3.24^{+0.12}_{-0.13}$	$2.66^{+0.33}_{-0.50}$
	Log ξ	$-0.53^{+0.04}_{-0.04}$	$-0.58^{+0.05}_{-0.05}$	$-0.50^{+0.04}_{-0.03}$	$-0.66^{+0.05}_{-0.05}$
Soft Power Law[a]	Γ_{Soft}	$3.77^{+0.03}_{-0.03}$	$3.83^{+0.05}_{-0.05}$	$3.75^{+0.03}_{-0.03}$	$3.83^{+0.05}_{-0.05}$
	pn Norm. $\left(10^{-3}\right)$	$3.28^{+0.07}_{-0.07}$	$4.20^{+0.13}_{-0.13}$	$10.32^{+0.19}_{-0.19}$	$5.80^{+0.18}_{-0.18}$
	χ^2/DOF	759.69/721	504.83/516	727.99/675	538.64/521
	P-value	0.0830	0.4437	0.0358	0.2592

[a]Xillver and Power law normalizations are photons $\mathrm{keV}^{-1}\mathrm{cm}^{-2}\mathrm{s}^{-1}$ at 1 keV.

[b]Mekal normalization is $10^{-14}/4\pi(D_A(1+z))^2) \int n_e n_H \, dV$ where D_A is the angular diameter distance to the source (cm), n_e and n_H are the electron and H densities (cm^{-3}), respectively.

Table 5.6: X6 pn time resolved parameters.

Component	Parameter	X6R1	X6R2	X6R3	X6R4
Neutral Covering	N_H $\left(10^{20} cm^{-2}\right)$	$7.73^{+0.41}_{-0.41}$	$6.75^{+0.45}_{-0.46}$	$8.76^{+0.31}_{-0.31}$	$7.85^{+0.48}_{-0.48}$
Xillver[a]	Γ_{Hard}	$1.65^{+0.01}_{-0.01}$	$1.67^{+0.01}_{-0.01}$	$1.68^{+0.01}_{-0.01}$	$1.73^{+0.02}_{-0.02}$
	Log ξ	< 1.32	$1.30^{+0.06}_{-0.45}$	< 1.12	< 1.22
	Reflection Fraction	$0.78^{+0.12}_{-0.12}$	$0.96^{+0.12}_{-0.13}$	$0.95^{+0.11}_{-0.10}$	< 0.99
	pn Norm. $\left(10^{-4}\right)$	$2.29^{+0.02}_{-0.02}$	$2.23^{+0.02}_{-0.02}$	$2.06^{+0.01}_{-0.01}$	$2.14^{+0.02}_{-0.02}$
Mekal[b]	kT (ev)	$187.86^{+9.83}_{-8.10}$	$238.10^{+17.60}_{-13.05}$	$195.09^{+8.78}_{-7.18}$	$181.60^{+10.67}_{-11.80}$
	pn Norm. $\left(10^{-3}\right)$	$2.97^{+0.54}_{-0.54}$	$1.88^{+0.31}_{-0.31}$	$2.99^{+0.43}_{-0.43}$	$3.10^{+0.73}_{-0.73}$
High Ion. Warm Abs.	N_H $\left(10^{21} cm^{-2}\right)$	$47.47^{+18.06}_{-13.76}$	$27.07^{+21.08}_{-11.61}$	$51.30^{+12.25}_{-9.79}$	$74.89^{+21.60}_{-17.10}$
	Log ξ	$2.85^{+0.02}_{-0.02}$	$2.88^{+0.03}_{-0.03}$	$2.84^{+0.02}_{-0.02}$	$2.81^{+0.02}_{-0.02}$
Low Ion. Warm Abs.	N_H $\left(10^{21} cm^{-2}\right)$	$3.01^{+0.30}_{-0.26}$	$4.05^{+0.66}_{-0.60}$	$3.38^{+0.23}_{-0.21}$	$3.15^{+0.27}_{-0.25}$
	Log ξ	$0.44^{+0.03}_{-0.03}$	$0.43^{+0.04}_{-0.03}$	$0.84^{+0.04}_{-0.04}$	$0.61^{+0.05}_{-0.05}$
Neg Ion. Warm Abs.	N_H $\left(10^{21} cm^{-2}\right)$	$7.45(fixed)$	$7.45(fixed)$	$7.45(fixed)$	$7.45(fixed)$
	Log ξ	$-1.71^{+0.07}_{-0.12}$	> -1.85	$-1.67^{+0.05}_{-0.06}$	$-1.75^{+0.10}_{-0.24}$
Soft Power Law[a]	Γ_{Soft}	$3.86^{+0.04}_{-0.04}$	$3.80^{+0.05}_{-0.05}$	$3.80^{+0.03}_{-0.03}$	$3.77^{+0.05}_{-0.05}$
	pn Norm. $\left(10^{-3}\right)$	$6.14^{+0.16}_{-0.16}$	$5.51^{+0.13}_{-0.13}$	$6.11^{+0.13}_{-0.13}$	$6.17^{+0.20}_{-0.20}$
Absorption Edge	Energy (keV)	$0.86^{+0.04}_{-0.03}$	$0.87^{+0.03}_{-0.03}$	$0.95^{+0.09}_{-0.05}$	$0.89^{+0.03}_{-0.03}$
	τ	$0.07^{+0.02}_{-0.02}$	$0.10^{+0.02}_{-0.02}$	$0.04^{+0.02}_{-0.02}$	$0.14^{+0.03}_{-0.03}$
	χ^2/DOF	666.84/610	594.46/582	784.14/731	567.19/515
	P-value	0.0550	0.3512	0.0768	0.0554

[a]Xillver and Power law normalizations are photons $\mathrm{keV}^{-1}\mathrm{cm}^{-2}\mathrm{s}^{-1}$ at 1 keV.

[b]Mekal normalization is $10^{-14}/4\pi(D_A(1+z))^2) \int n_e n_H \, dV$ where D_A is the angular diameter distance to the source (cm), n_e and n_H are the electron and H densities (cm^{-3}), respectively.

Table 5.7: X7 pn time resolved parameters.

Component	Parameter	X7R1	X7R2	X7R3	X7R4
Neutral Covering	N_H $\left(10^{20} cm^{-2}\right)$	$4.30^{+0.32}_{-0.33}$	$4.04^{+0.35}_{-0.36}$	$4.00^{+0.34}_{-0.35}$	$4.21^{+0.39}_{-0.40}$
Xillver[a]	Γ_{Hard}	$1.77^{+0.01}_{-0.01}$	$1.75^{+0.01}_{-0.01}$	$1.70^{+0.01}_{-0.01}$	$1.68^{+0.01}_{-0.01}$
	Log ξ	$1.37^{+0.15}_{-0.22}$	$1.04^{+0.28}_{-0.33}$	< 1.41	< 1.40
	Reflection Fraction	$0.73^{+0.09}_{-0.08}$	$0.89^{+0.10}_{-0.11}$	$0.78^{+0.10}_{-0.10}$	$0.81^{+0.11}_{-0.11}$
	pn Norm. $\left(10^{-4}\right)$	$2.40^{+0.01}_{-0.01}$	$2.30^{+0.01}_{-0.01}$	$2.08^{+0.01}_{-0.01}$	$2.43^{+0.02}_{-0.02}$
Mekal[b]	kT (ev)	$233.68^{+20.04}_{-14.15}$	$201.00^{+15.25}_{-10.84}$	$215.78^{+12.76}_{-14.26}$	$210.95^{+10.80}_{-9.91}$
	pn Norm. $\left(10^{-3}\right)$	$1.46^{+0.28}_{-0.28}$	$2.34^{+0.45}_{-0.45}$	$2.58^{+0.34}_{-0.34}$	$2.91^{+0.39}_{-0.39}$
High Ion. Warm Abs.	N_H $\left(10^{21} cm^{-2}\right)$	$18.86^{+5.19}_{-4.10}$	$29.22^{+5.01}_{-5.94}$	$28.73^{+5.74}_{-7.08}$	$20.40^{+4.48}_{-3.71}$
	Log ξ	$2.82^{+0.02}_{-0.02}$	$2.76^{+0.02}_{-0.02}$	$2.81^{+0.02}_{-0.02}$	$2.74^{+0.03}_{-0.03}$
Low Ion. Warm Abs.	N_H $\left(10^{21} cm^{-2}\right)$	$3.31^{+0.40}_{-0.36}$	$2.86^{+0.27}_{-0.24}$	$3.69^{+0.41}_{-0.39}$	$3.35^{+0.37}_{-0.33}$
	Log ξ	$1.13^{+0.08}_{-0.07}$	$1.01^{+0.08}_{-0.05}$	$1.08^{+0.07}_{-0.06}$	$1.00^{+0.05}_{-0.05}$
Neg Ion. Warm Abs.	N_H $\left(10^{21} cm^{-2}\right)$	$0.74^{+0.04}_{-0.05}$	$0.91^{+0.04}_{-0.05}$	$1.34^{+0.08}_{-0.08}$	$0.81^{+0.06}_{-0.06}$
	Log ξ	$-1.00^{+0.10}_{-0.03}$	$-1.01^{+0.10}_{-0.03}$	$-1.19^{+0.02}_{-0.02}$	$-1.05^{+0.03}_{-0.04}$
Soft Power Law[a]	Γ_{Soft}	$3.80^{+0.04}_{-0.03}$	$3.80^{+0.04}_{-0.04}$	$3.80^{+0.04}_{-0.04}$	$3.80^{+0.04}_{-0.04}$
	pn Norm. $\left(10^{-3}\right)$	$6.86^{+0.11}_{-0.11}$	$6.08^{+0.14}_{-0.14}$	$5.89^{+0.12}_{-0.12}$	$5.38^{+0.13}_{-0.13}$
	χ^2/DOF	718.69/780	691.79/717	753.19/680	679.87/671
	P-value	0.9427	0.6010	0.0265	0.3977

[a]Xillver and Power law normalizations are photons $\mathrm{keV}^{-1}\mathrm{cm}^{-2}\mathrm{s}^{-1}$ at 1 keV.

[b]Mekal normalization is $10^{-14}/4\pi(D_A(1+z))^2) \int n_e n_H \, dV$ where D_A is the angular diameter distance to the source (cm), n_e and n_H are the electron and H densities (cm^{-3}), respectively.

Table 5.8: X8 pn time resolved parameters.

Component	Parameter	X8R1	X8R2	X8R3	X8R4
Neutral Covering	N_H $\left(10^{20} cm^{-2}\right)$	$6.58^{+0.38}_{-0.39}$	$6.51^{+0.35}_{-0.35}$	$7.82^{+0.37}_{-0.38}$	$7.87^{+0.31}_{-0.32}$
Xillver	Γ_{Hard}	$1.65^{+0.02}_{-0.02}$	$1.77^{+0.02}_{-0.02}$	$1.84^{+0.01}_{-0.01}$	$1.73^{+0.01}_{-0.01}$
	Log ξ	< 1.75	< 1.68	< 1.44	$1.38^{+0.25}_{-0.25}$
	Reflection Fraction	$0.76^{+0.13}_{-0.12}$	$0.97^{+0.14}_{-0.13}$	$0.71^{+0.11}_{-0.11}$	$0.56^{+0.09}_{-0.09}$
	pn Norm. $\left(10^{-4}\right)$	$2.22^{+0.02}_{-0.02}$	$2.19^{+0.02}_{-0.02}$	$2.33^{+0.02}_{-0.02}$	$2.46^{+0.01}_{-0.01}$
Mekal[b]	kT (ev)	$237.70^{+6.16}_{-5.49}$	$237.45^{+6.21}_{-5.58}$	$224.13^{+8.07}_{-7.12}$	$218.49^{+6.24}_{-6.54}$
	pn Norm. $\left(10^{-3}\right)$	$11.97^{+0.80}_{-0.80}$	$10.97^{+0.78}_{-0.78}$	$5.91^{+0.63}_{-0.63}$	$4.05^{+0.39}_{-0.39}$
High Ion. Warm Abs.	N_H $\left(10^{21} cm^{-2}\right)$	$80.88^{+8.08}_{-7.51}$	$109.71^{+27.14}_{-11.43}$	$72.69^{+2.58}_{-2.54}$	$49.91^{+4.22}_{-3.97}$
	Log ξ	$2.56^{+0.02}_{-0.02}$	$2.63^{+0.02}_{-0.02}$	$2.35^{+0.01}_{-0.01}$	$2.64^{+0.01}_{-0.01}$
Low Ion. Warm Abs.	N_H $\left(10^{21} cm^{-2}\right)$	$16.16^{+1.22}_{-0.99}$	$14.96^{+0.54}_{-0.53}$	$4.56^{+0.39}_{-0.43}$	$4.33^{+0.32}_{-0.33}$
	Log ξ	$1.01^{+0.01}_{-0.01}$	$1.05^{+0.01}_{-0.01}$	$1.00^{+0.03}_{-0.04}$	$1.00^{+0.03}_{-0.04}$
Neg Ion. Warm Abs.	N_H $\left(10^{21} cm^{-2}\right)$	$8.71(fixed)$	$8.71(fixed)$	$7.74(fixed)$	$7.74(fixed)$
	Log ξ	> -1.94	> -1.94	$-1.71^{+0.05}_{-0.06}$	$-1.95^{+0.07}_{-0.45}$
Soft Power Law[a]	Γ_{Soft}	$3.87^{+0.04}_{-0.04}$	$3.74^{+0.04}_{-0.04}$	$3.70^{+0.04}_{-0.04}$	$3.80^{+0.04}_{-0.03}$
	pn Norm. $\left(10^{-3}\right)$	$10.01^{+0.03}_{-0.03}$	$11.41^{+0.29}_{-0.29}$	$8.79^{+0.23}_{-0.23}$	$7.00^{+0.13}_{-0.13}$
	χ^2/DOF	631.58/602	612.08/597	753.53/660	806.04/772
	P-value	0.1954	0.3256	0.0066	0.1919

[a]Xillver and Power law normalizations are photons keV^{-1}cm^{-2}s^{-1} at 1 keV.

[c]Mekal normalization is $10^{-14}/4\pi(D_A(1+z))^2) \int n_e n_H \, dV$ where D_A is the angular diameter distance to the source (cm), n_e and n_H are the electron and H densities (cm^{-3}), respectively.

Table 5.9: X5 flare spectrum model parameters.

Component	Parameter	X5 Flare
Soft Power Law[a]	Γ	$2.37^{+0.02}_{-0.02}$
	pn Norm. $\left(10^{-3}\right)$	$8.68^{+0.11}_{-0.11}$
High Ion. Warm Abs.	N_H $\left(10^{21} cm^{-2}\right)$	$89.14^{+30.40}_{-19.00}$
	Log ξ	$2.60^{+0.04}_{-0.04}$
Low Ion. Warm Abs.	N_H $\left(10^{21} cm^{-2}\right)$	$2.07^{+0.25}_{-0.24}$
	Log ξ	$1.21^{+0.11}_{-0.11}$
Neg. Ion. Warm Abs.	N_H $\left(10^{21} cm^{-2}\right)$	$1.71^{+0.05}_{-0.05}$
	Log ξ	$-0.47^{+0.09}_{-0.09}$
	χ^2/DOF	567.69/561
	P-value	0.4134

[a] Power law normalization is photons $\mathrm{keV}^{-1}\mathrm{cm}^{-2}\mathrm{s}^{-1}$ at 1 keV.

Chapter 5 Figures

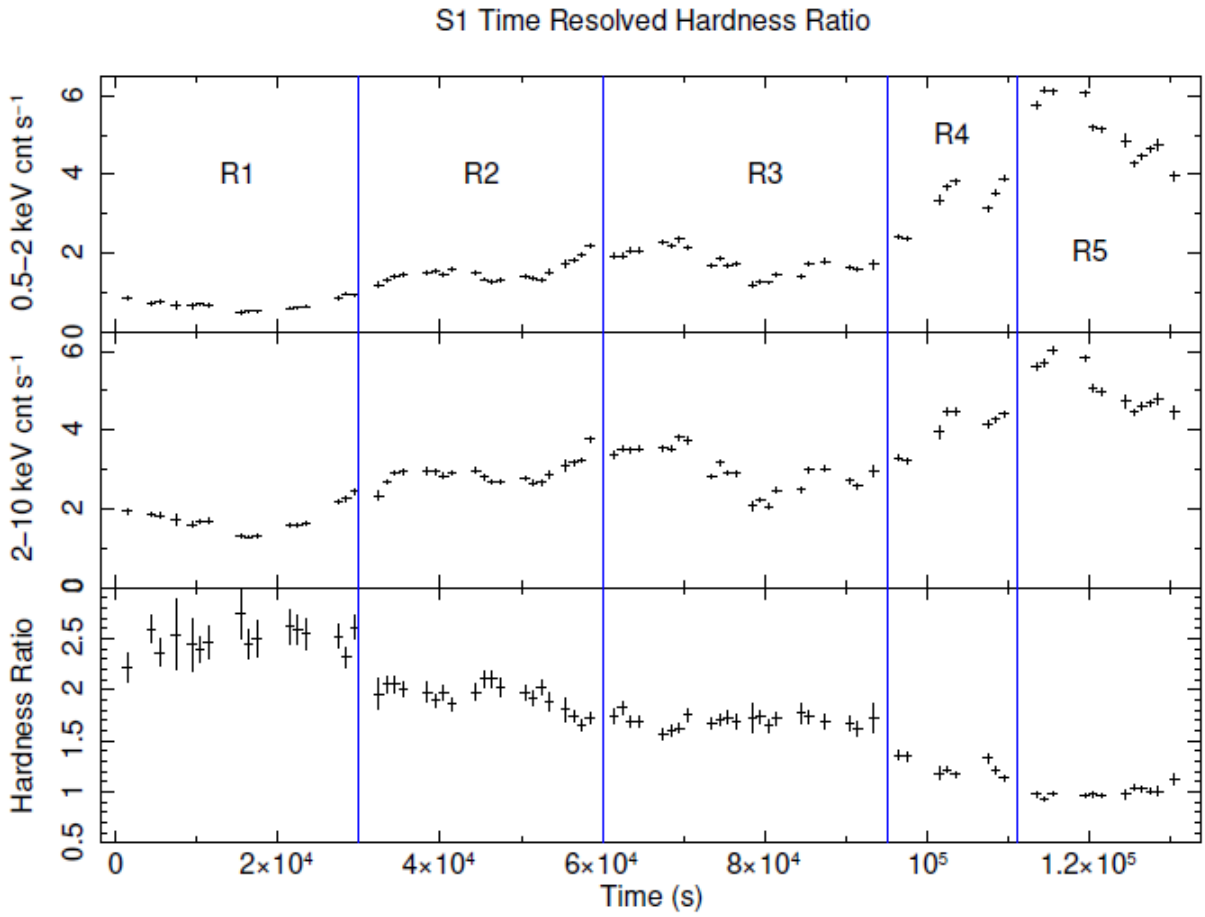

Figure 5.1: S1 Hardness Ratio and Time Regions.

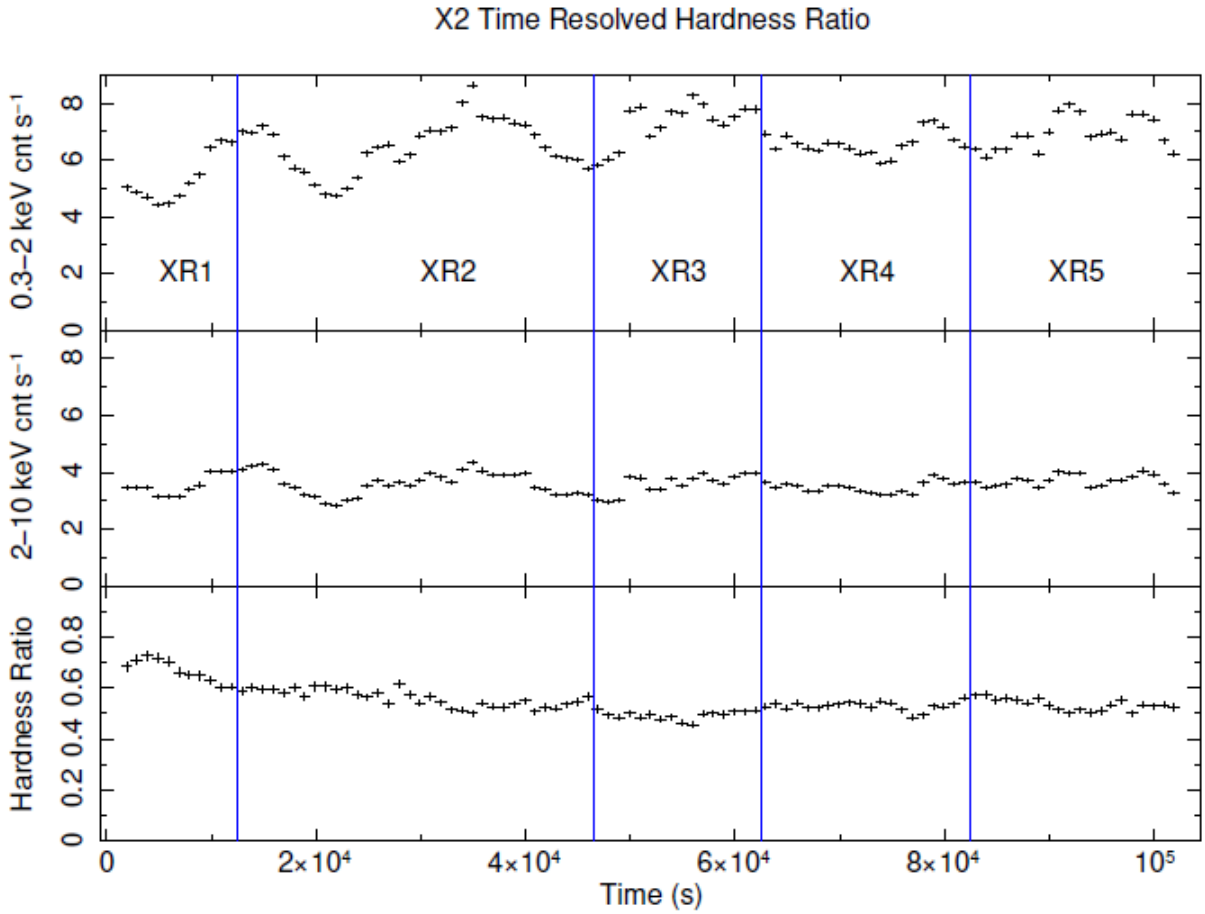

Figure 5.2: X2 Hardness Ratio and Time Regions.

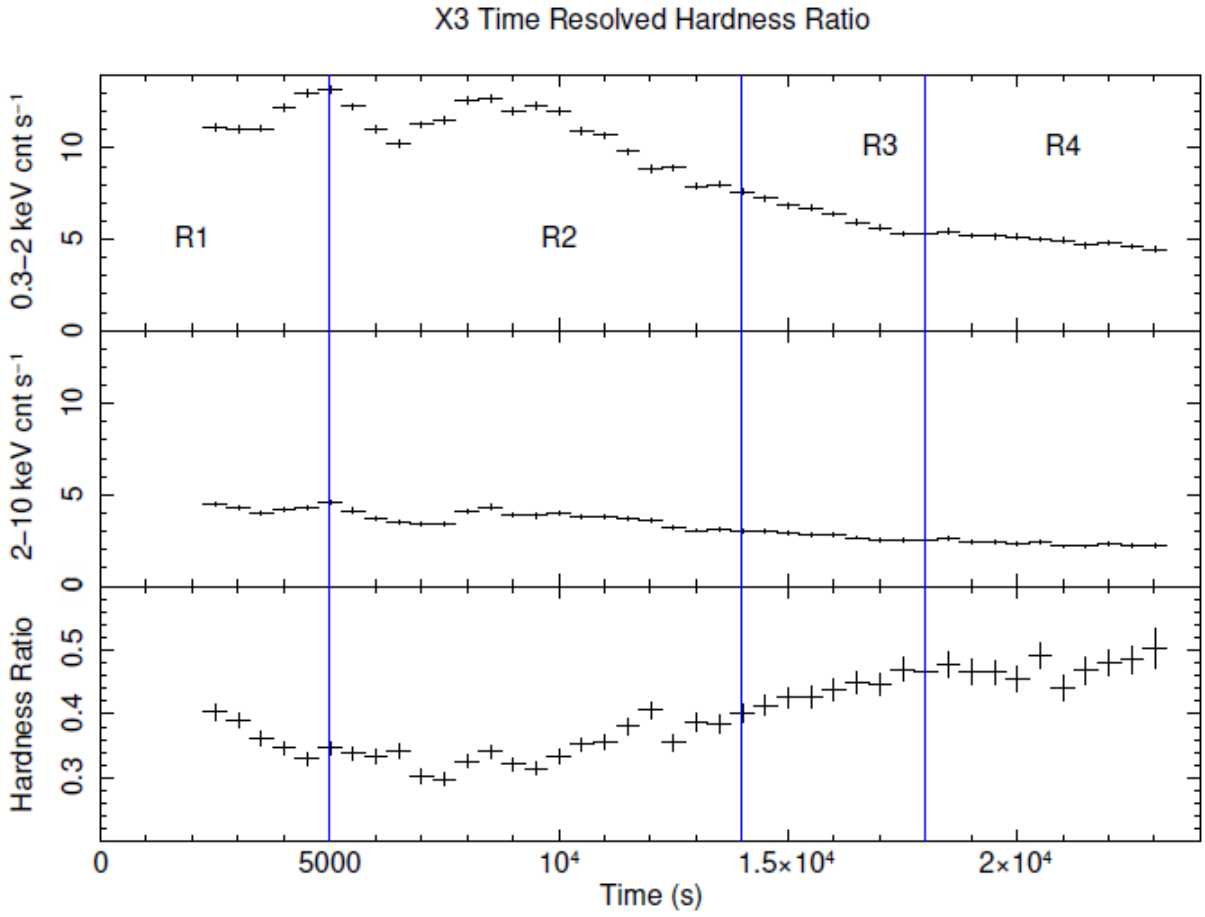

Figure 5.3: X3 Hardness Ratio and Time Regions.

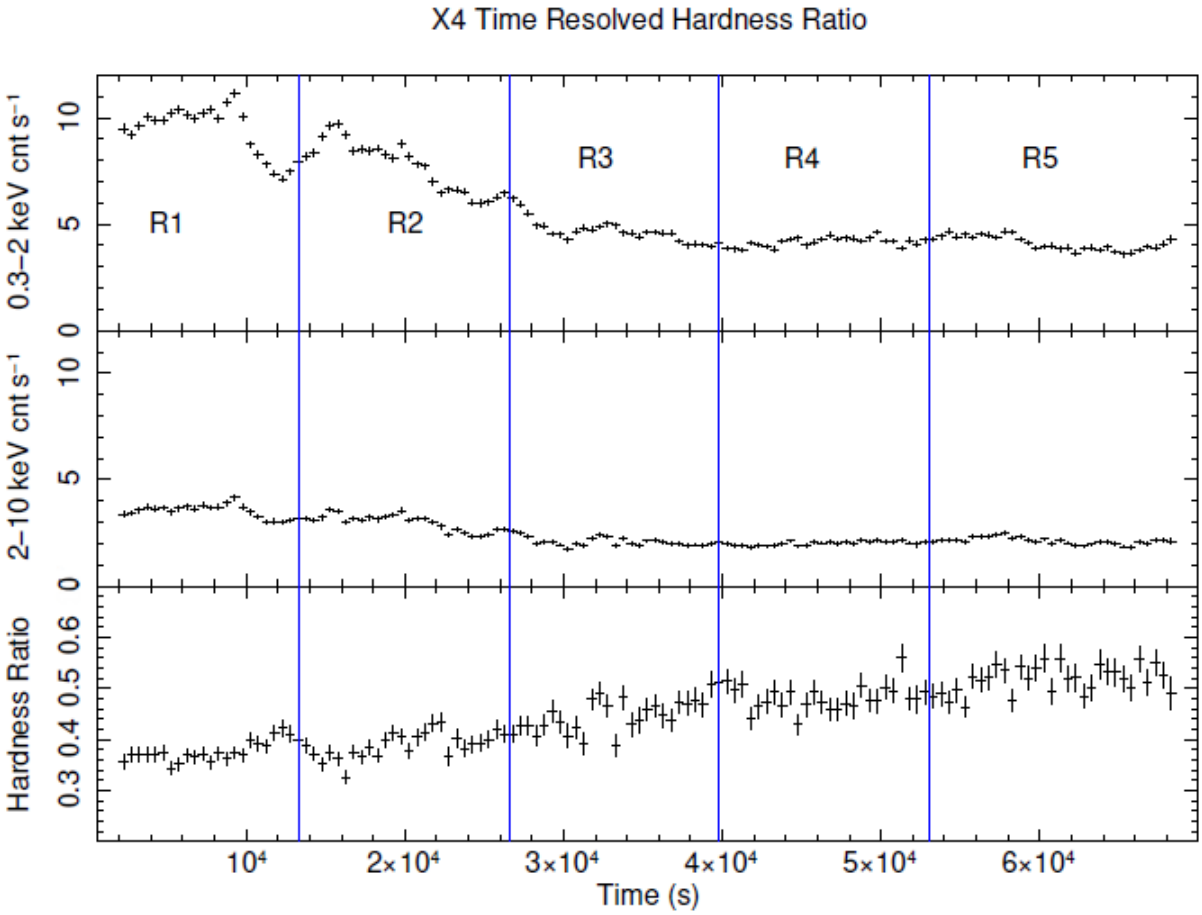

Figure 5.4: X4 Hardness Ratio and Time Regions.

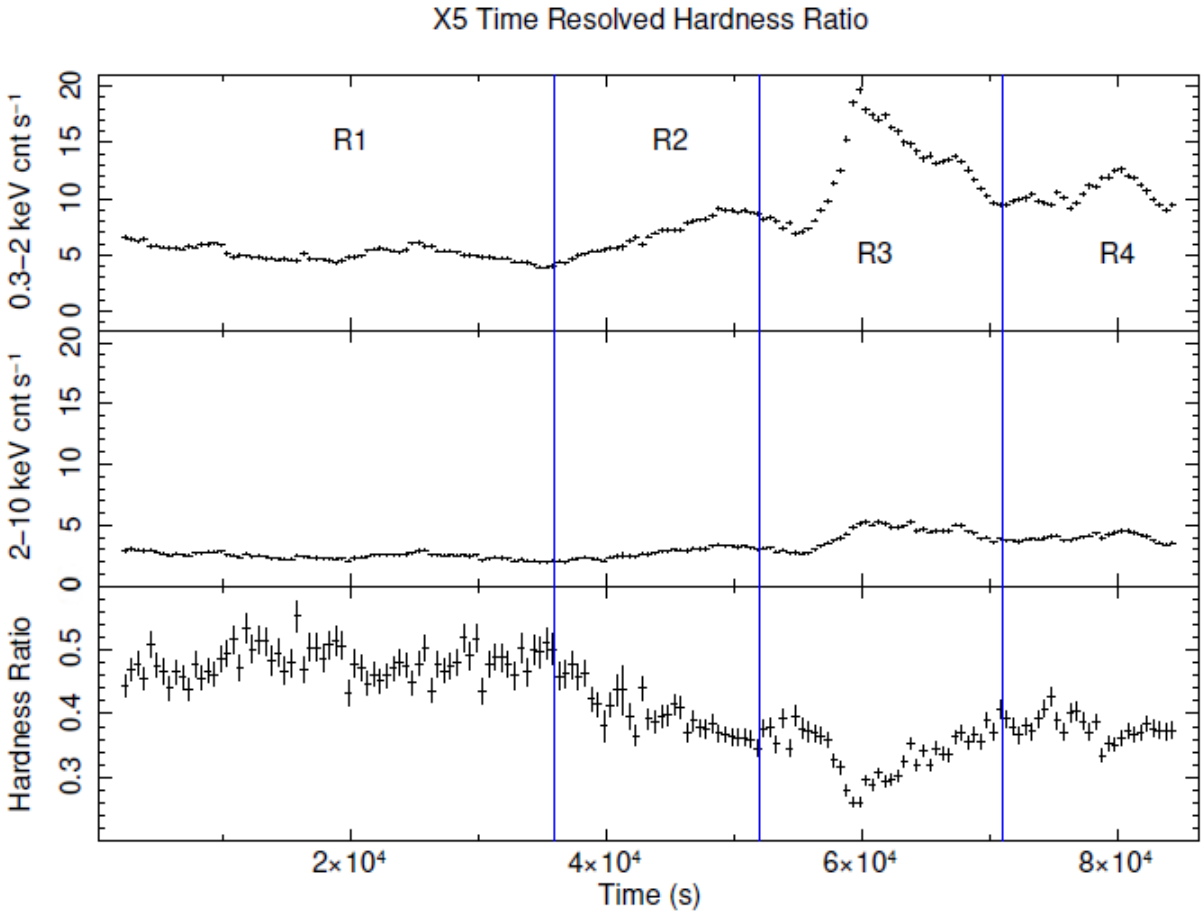

Figure 5.5: X5 Hardness Ratio and Time Regions.

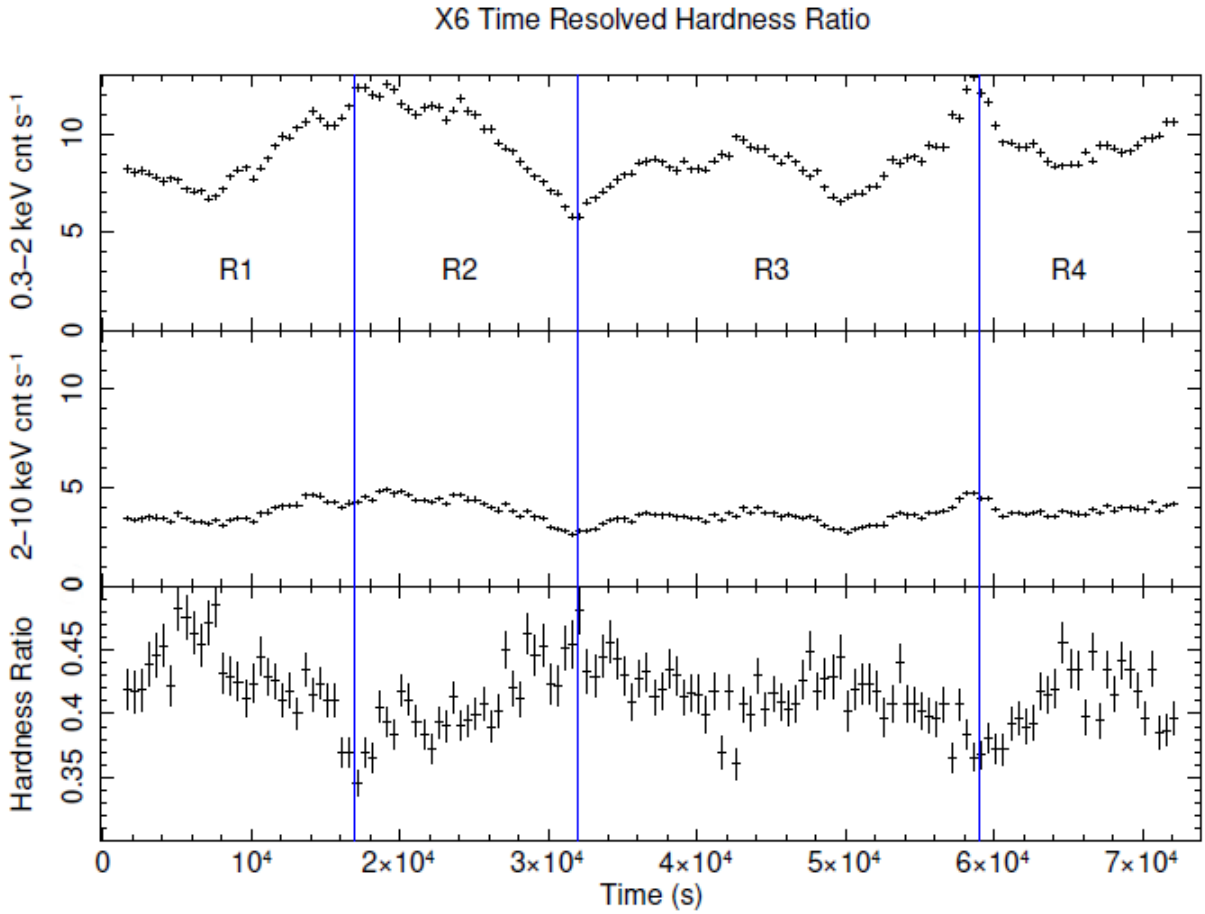

Figure 5.6: X6 Hardness Ratio and Time Regions.

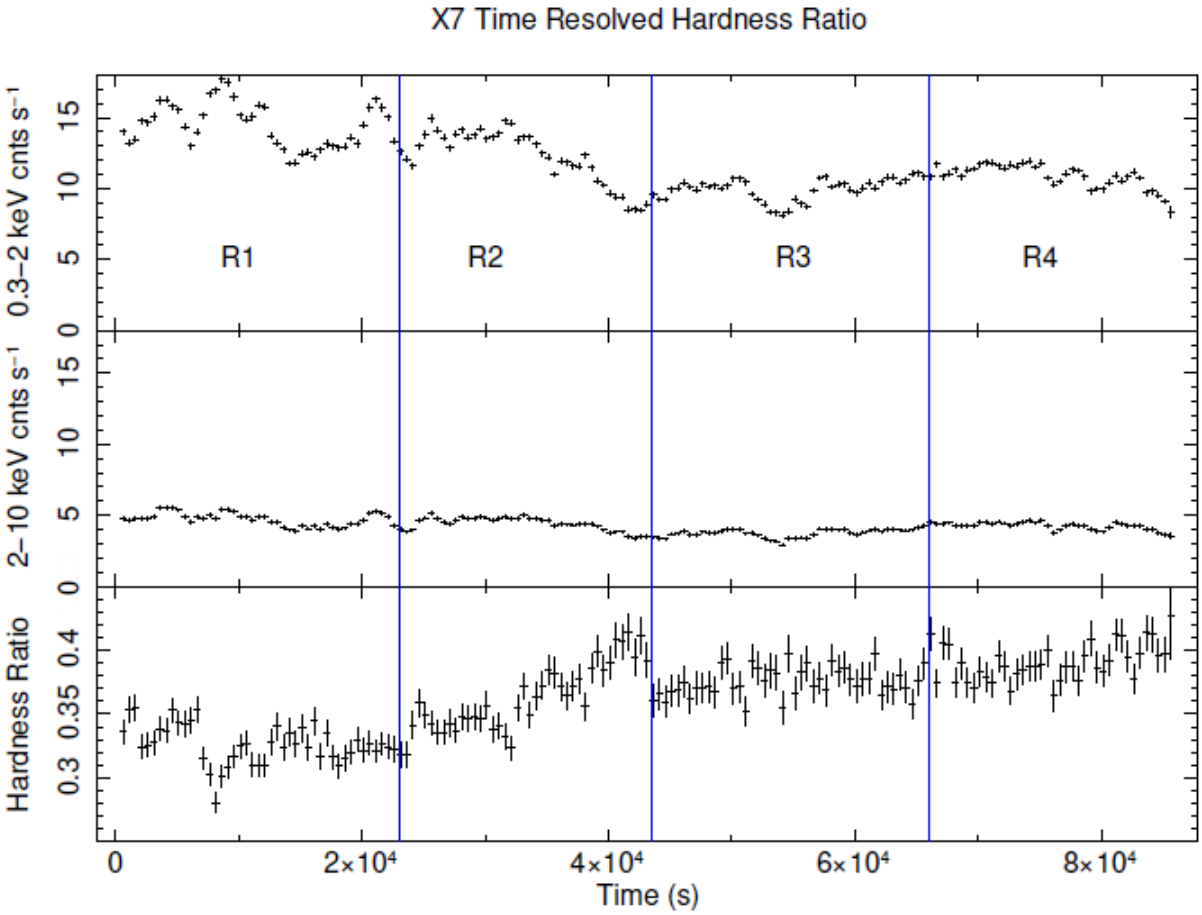

Figure 5.7: X7 Hardness Ratio and Time Regions.

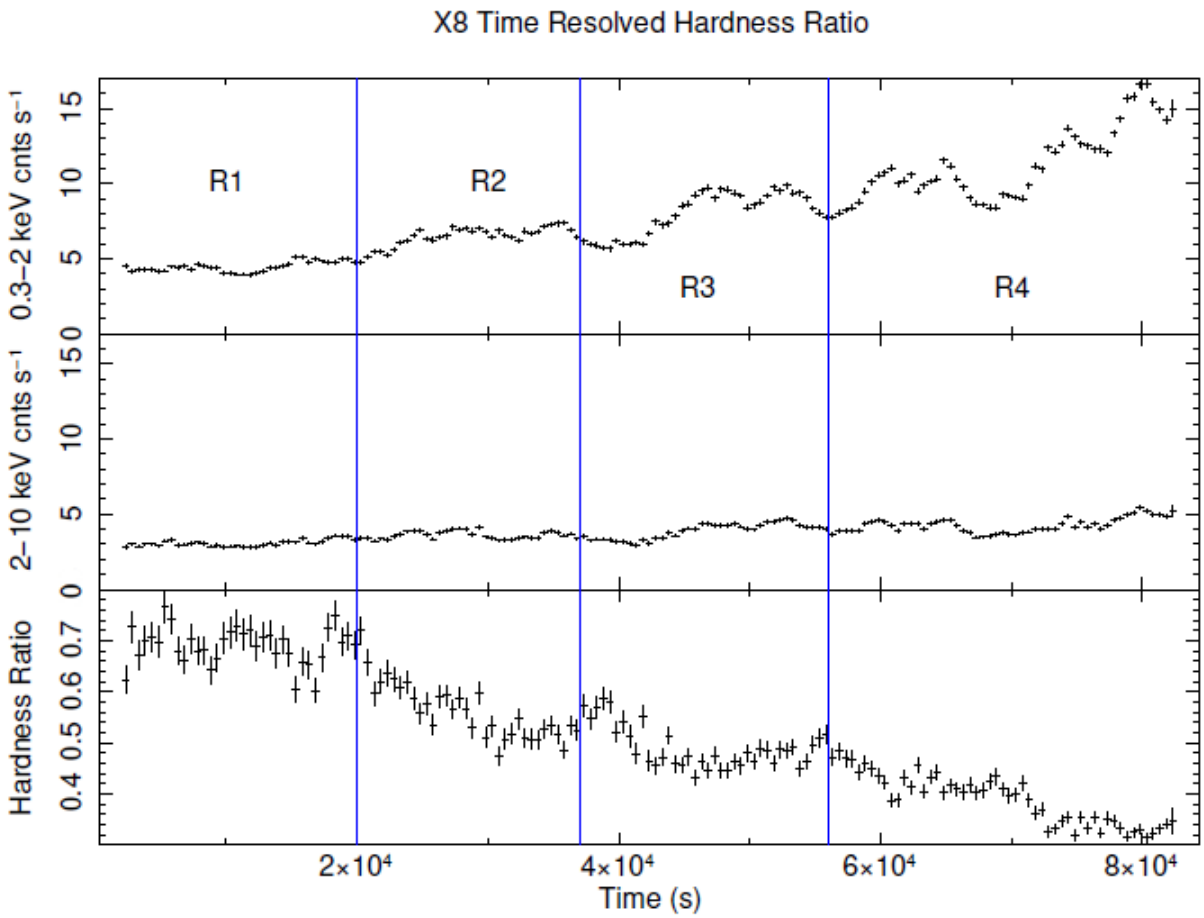

Figure 5.8: X8 Hardness Ratio and Time Regions.

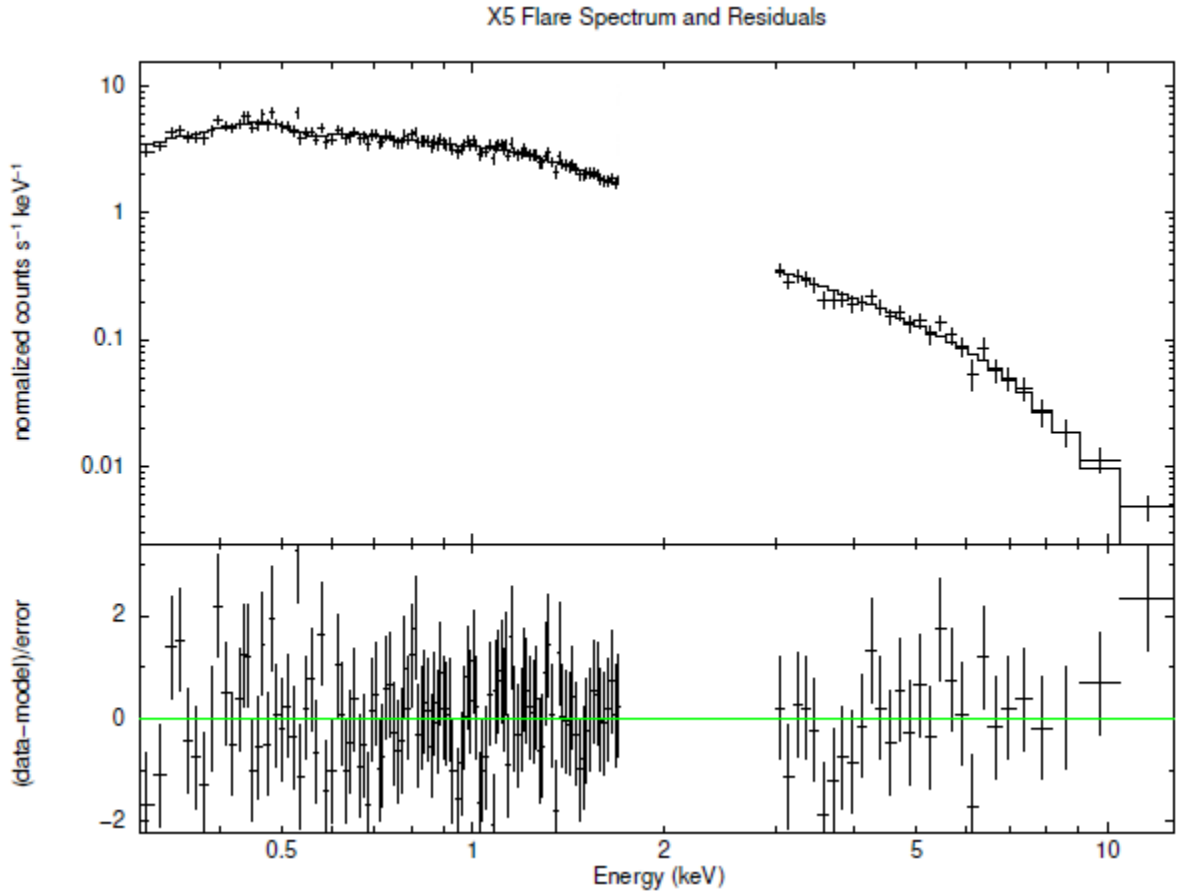

Figure 5.9: X5 Flare Spectrum.

CONCLUSION

The active galactic nucleus NGC 3227 is a highly variable source that has been studied and modeled by multiple authors. We have formed a model capable of explaining the spectral behaviour of the source in low, moderate, and high flux states. Our model consists of the following components: a hard photon power law, a reflection component, multiple absorbers at different ionization levels, various emission lines, and a soft excess component for the higher flux observations. We consider these components to represent the following physical structures.

1. The hard photon power law is due to thermally emitted photons from the disc undergoing inverse Compton scattering off of the hot electrons in a corona above the disk.

2. The reflection component is the hard power law reflecting off of the disk.

3. The complex absorption features are due to multiple clouds at different distances to the central engine. The higher ionized ones are closer, possibly in the broad line region. The lower ionized or neutral ones are further away in the narrow line region. These clouds have a degree of tangential velocity relative to the line of sight which allows the clouds to drift into and out of the line of sight given sufficiently long time scales.

4. The emission lines are successfully modeled by emission from a hot, diffuse gas. The Ne IX line could also originate from the star forming regions of the torus.

5. The soft excess component, while usually modeled as a soft power law, can be explained by inverse Compton scattering. This is produced by a separate population of electrons that are cooler than the coronal electrons. This population exists closer to the disk in a warm disk atmosphere.

With this model, the primary spectral differences between observations can be explained by a combination of varying accretion rates and absorption features. As the accretion rate increases, it pumps additional energy into the corona. This allows a larger portion of the

corona to contribute to the hard power law emission in a meaningful way. In this manner, the size of the effective emission region increases. With the increase in emission region size, a larger area of absorbing clouds along the line of sight are illuminated. Since our absorber models use a uniform density, they average dense and diffuse portions of the absorbers into a single value. This interpretation explains the behaviour of the partial covering absorber during the Suzaku observations. Although we are observing the same clouds during campaigns, there exists the possibility that particularily dense portions of the clouds can enter and exit the line of sight during the campaign. This explains the large decrease in the density of the absorbers during the XN8 observation.

In addition, the photons released by increased accretion also shine upon the disk atmosphere. These photons undergo inverse compton scattering off of the electrons present in the atmosphere and produce the soft excess component. While the electrons in the atmosphere are present during the low state, they do not have sufficient energy to contribute to the overall spectrum in a significant way. Thus, the soft excess component is necessary for high state observations but not for low state observations.

We have succeded in creating the most robust model to date. Our model has sufficient flexibility to explain the spectrum of all of the observations contained within this thesis while maintaining consistency and physical plausability. Compared to previous efforts, it utilizes a higher number of observations (21), a larger number of satellites (3), and a longer timespan of data (2000 - 2017). It does so while using the full energy band (0.3 - 50 keV). Thus, it is the most complete spectral modeling campaign of this source.

This model provides a useful starting point for modeling subsequent observations. With this model formed, the typical behaviour of the source (e.g. S2 for low state, X4 for high state) is determined. This allows abberant spectral features (e.g. S4 spectrum, X5 flare) to be clearly identified. From the RGS analysis, necessary components of the composition of absorbing clouds are revealed. The drop in covering density during XN8 implies significant

tangential velocity of these absorbers. Our model shows that the hard power law index fluxuates between 1.4 - 1.8 in our best fit models. Should a spectral fit initially have that parameter below the lower bound, it implies that heavy absorption is needed. If the index is above the upper bound, then it is likely contaminated with the process responsible for the soft excess emission. The strength of the Fe Kα line also yeilds lower limits on the strength of the reflection in this system.

Furthermore, we can compare the model to other AGN. This model can provide a starting point for observations of similar sources, thus reducing the time and effort required to successfully model them. In addition, it could help identify differences between NGC 3227 and other AGN. If this model is unable to properly describe another source, then critical parameter(s) must be different in that source. This could include significantly different characteristics of absorbing clouds, strength of reflection, and source of the soft excess. Also consider if this model is applied to a radio loud source that has some similarities to NGC 3227 (e.g. inclination angle, accretion rate). If differences between radio loud and quiet sources appear in the X-ray band, this model could help identify them.

Future work includes applying and adapting this model to observations that were not analyzed in this dissertation. Two XMM-Newton observations made public at the end of 2020 and two NuStar observations made public in early 2021 are of immediate interest. Otherwise, future observations of the source in the relevant energy bands can be used to further test this model.

REFERENCES CITED

Abdo, A. A., Ackermann, M., Ajello, M., et al. 2010, ApJSS, 188, 406

Ackermann, M., Ajello, M., Allafort, A., et al. 2012, ApJ, 747, 104

Adams, T. F. 1977, ApJSS, 33, 19A

Anderson, J. M., & Ulvestad, J. S. 2005, ApJ, 627, 674A

Angelini, L., & Sabol, E. J. 2021, Online nH Galactic Column Density Tool, `heasarc.gsfc.nasa.gov/cgi-bin/Tools/w3nh/w3nh.pl`

Antonucci, R. 1993, ANRAA, 31, 473

Arnaud, K. A. 1996, Astronomical Data Analysis Software and Systems V, eds. Jacoby G. & Barnes J., ASP Conf. Series Vol. 101, p17

—. 2018, "Statistical Methods in XSPEC", The XSPEC Wiki, `https://asd.gsfc.nasa.gov/XSPECwiki/statistical_methods_in_XSPEC`

Balucinska-Church, M., & McCammon, D. 1992, ApJ, 400, 699B

Barthel, P. 1991, "Active Galaxies and Quasistellar Objects, Interrelations of Variours Types", In Maran, S. P. ed. *Astronomy and Astrophysics Encyclopedia*, Wiley

Barthel, P. D., Vestergaard, M., & Lonsdale, C. J. 2000, A&A, 354, 7

Barvainis, R. 1987, ApJ, 320, 537

—. 1993a, ApJ, 412, 513B

—. 1993b, ApJ, 412, 513

Bechtold, J., Czerny, B., Elvis, M., Fabbiano, G., & Green, R. F. 1987, ApJ, 314, 699B

Begelman, M. C. 2014, 26th Solvay Conference on Physics: "Astrophysics and Cosmology", eds. Blandford, R. and Sevrin, A., World Scientific

Blandford, R. D., & Königl, A. 1979, ApJ, 232, 34B

Blandford, R. D., & Rees, M. J. 1978, Phys. Scri., 17, 3

Blandford, R. D., & Znajek, R. L. 1977, MNRAS, 179, 433B

Blumenthal, G. R., & Gould, R. J. 1970, Rev. Mod. Phys., 42, 237

Boissay, R., Ricci, C., & Paltani, S. 2016, A&A, 588, A70

Boller, T., Brandt, W. N., & Fink, H. 1996, A&A, 305, 53B

Bonzini, M., Padovani, P., Mainieri, V., et al. 2013, MNRAS, 436, 3759

Brandt, W. N., Fabian, A. C., & Pounds, K. A. 1996, MNRAS, 278, 326B

Brinkman, A., Aarts, h., den Boggende, A., et al. 1998, in "Proceedings of the First XMM Workshop: Science with XMM", ESTEC, Noordwijk, The netherlands, ed. Dahlem M.

Buisson, D. J. K., Lohfink, A. M., Alston, W. N., & Fabian, A. C. 2016, MNRAS, 464, 3194

Cheng, H., Liu, B. F., Liu, J., et al. 2020, ANRAS, 495, 1158

Clark, D. A., Bridle, A. H., Burns, J. O., Perley, R. A., & Norman, M. L. 1992, ApJ, 385, 173

Cohen, R. D. 1983, ApJ, 273, 489C

Crenshaw, D. M., Kraemer, S. B., Bruhweiler, F. C., & Ruiz, J. R. 2001, ApJ, 555, 633C

Cuno, H. 1929, Astron. Nach., 236, 233H

Dauser, T., García, J., Walton, D. J., et al. 2016, A&A, 590, A76

Davies, R. I., Thomas, J., Genzel, R., et al. 2006, ApJ, 646, 754D

den Herder, J. W., Brinkman, A. C., Kahn, S. M., et al. 2001, A&A, 365, L7

Done, C., Mulchaey, J. S., Mushotzky, R. F., & Arnaud, K. A. 1992, ApJ, 395, 275

Draine, B. T., & Lee, H. M. 1984, ApJ, 285, 89D

Edelson, R. A., & Malkan, M. A. 1986, ApJ, 308, 59E

Elvis, M., Maccacaro, T., Wilson, A. S., et al. 1978, MNRAS, 183, 129

ESA. 2019, "XMM-Newton Orbit/Navigation", https://sci.esa.int/web/xmm-newton/-/31349-orbit-navigation

—. 2021a, "The XMM-Newton Spacecraft", https://www.cosmos.esa.int/web/xmm-newton/technical-details-spacecraft

—. 2021b, "The Service Module", https://www.cosmos.esa.int/web/xmm-newton/xmm-svm

—. 2021c, "The Telescopes of XMM-Newton", https://www.cosmos.esa.int/web/xmm-newton/technical-details-mirrors

—. 2021d, "The european Photon Imaging Camera (EPIC) Onboard XMM-Newton", https://www.cosmos.esa.int/web/xmm-newton/technical-details-epic

—. 2021e, "The Reflection Grating Spectrometer (RGS) Onboard XMM-Newton", https://www.cosmos.esa.int/web/xmm-newton/technical-details-rgs

—. 2021f, "The XMM-Newton Optical Monitor", https://www.cosmos.esa.int/web/xmm-newton/technical-details-om

Fanaroff, B. L., & Riley, J. M. 1974, MNRAS, 167, 31P

Fanti, R., C., F., Schilizzi, R. T., et al. 1990, A&A, 231, 333F

Fath, E. A. 1909, PASP, 21, 138F

Ferrando, P., Arnaud, M., Bouére, A., et al. 1999, Astron. Nachr., 320, 379

Foschini, L., Berton, M., Caccianiga, A., et al. 2015, A&A, 575, A13

Garcia, J., Dauser, T., Reynolds, C. S., et al. 2013, ApJ, 768, 146G

George, I. M., Mushotzky, R., Turner, T. J., et al. 1998, ApJ, 509, 146G

Gierliński, M., & Done, C. 2004, MNRAS, 349, L7

—. 2006, MNRAS, 371, L16

Gondoin, P., Orr, A., Lumb, D., & Siddiqui, H. 2003, A&A, 397, 883

Gondoin, P., van Katwijk, K., Aschenbach, B., et al. 1994, Proc. SPIE, 2209, 438

González-Delgado, R. M. G., & Pérez, E. 1997, MNRAS, 284, 931

Goodall, C. V., Butler, G., & Mahmoud, S. M. 2001, J. of Aero. Eng., 215, 175

Greenstein, J. L., & Schmidt, M. 1964, ApJ, 140, 1G

Guilbert, P. W., & Rees, M. J. 1988, MNRAS, 233, 475

Gunn, J. E., & Peterson, B. A. 1965, ApJ, 142, 1633G

Gursky, H., Kellog, E. M., Leong, C., Tananbaum, H., & Giacconi, R. 1971, ApJ, 165L, 43G

Haardt, F., & Maraschi, L. 1991, ApJ, 380L, 51H

Haardt, F., Maraschi, L., & Ghisellini, G. 1994, ApJ, 432L, 95H

Haba, Y., Liebmann, A. C., Fukumura, K., Kunieda, H., & Tsuruta, S. 2008, PASJ, 60, 1257

Halpern, J. P. 1984, ApJ, 281, 90H

Hardcastle, M. J., & Croston, J. H. 2020, New Astron. Rev., 88, 101539

Harrison, F. A., Cook, W. R. Miyasaka, H., & McLean, R. 2010, Semiconductor Radiation Detection Systems (Doca Raton, FL: CRC PRESS)

Harrison, F. A., Craig, W. W., Christensen, F. E., et al. 2013, ApJ, 770, 103

Heckman, T. M. 1980, A&A, 87, 152H

—. 1987, IAUS, 121, 421H

Heckman, T. M., & Best, P. N. 2014, ARAA, 52, 589

Imanishi, M. 2002, ApJ, 569, 44

Jansen, F., Lumb, D., Altieri, B., et al. 2001, A&A, 365, L1

JAXA. 2003, "ASTRO-EII Launched Into Space - Summer 2005", `global.jaxa.jp/article/special/xray/p4_e.html`

Jin, C., Ward, M., & Done, C. 2012, MNRAS, 422, 3268

Kalberla, P. M. W., Burton, W. B., Hartmann, D., et al. 2005, A&A, 440, 775K

Kallman, T. R. 2021, "XSTAR: A Spectral Analysis Tool", NASA Goddard Space Flight Center, `https://heasarc.gsfc.nasa.gov/xstar/docs/html/xstarmanual.html`

Kamae, T., Ezawa, H., Yasushi, F., et al. 1996, Proc. SPIE, 2806, 314

Kara, E., Steiner, J. F., Fabian, A. C., et al. 2019, Nature, 565, 198K

Karzas, W. J., & Latter, R. 1961, ApJS, 6, 167K

Kaspi, S., Brandt, W. N., George, I. M., et al. 2002, ApJ, 643, L168

Kellermann, K. I., & Owen, F. N. 1988a, "Relativistic Beaming", Published in "Galactic and Extragalactic Radio Astronomy", 2nd edition, eds. Verschuur, G. L. and Kellerman, K. I.

—. 1988b, "Jets, Lobes, and Hot Spots", Published in "Galactic and Extragalactic Radio Astronomy", 2nd edition, eds. Verschuur, G. L. and Kellerman, K. I.

—. 1988c, Published in "Galactic and Extragalactic Radio Astronomy", 2nd edition, eds. Verschuur, G. L. and Kellerman, K. I.

Kellogg, E., Baldwin, J. R., & Koch, D. 1975, ApJ, 199, 299K

Khachikian, E. Y., & Weedman, D. W. 1974, ApJ, 192, 581K

Kitamoto, S., Kohmura, T., Yamamoto, N., et al. 2004, Proc. SPIE, 5168, 376K

Komossa, S. 2002, Workshop on X-ray Spectroscopy of AGN with Chandra and XMM-Newton, MPE Garching, Dec. 3

Komossa, S., & Fink, H. 1997, A&A, 327, 483

Koratkar, A., & Blaes, O. 1999, PASP, 111, 1

Koyama, K., Tsunemi, H., Dotani, T., et al. 2007, PASJ, 59, S23

Kraemer, S. B., George, I. M., Turner, T. J., & Crenshaw, D. M. 2000, ApJ, 535, 53K

Kunieda, H., Ishida, M., Endo, T., et al. 2001, App. Opt., 40, 553

Laor, A. 1991, ApJ, 376, 90L

Liedahl, D. A., Osterheld, A. L., & Goldstein, W. H. 1995, ApJ, 438L, 115L

Lightman, A. P., & White, T. R. 1988, ApJ, 335, 57

Lobban, A. P., Turner, T. J., Reeves, J. N., Braito, V., & Miller, L. 2020, MNRAS, 494, 5056

Machalski, J., Koziel-Wierzbowska, D., Jamrozy, M., & Saikia, D. J. 2008, ApJ, 679, 149M

Maeda, Y., Someya, K., Ishida, M., Hayashida, K., & Mori, H. 2008, JAXA-ISAS Suzaku Memo, 15 July 2008

Maini, A., Prandoni, I., Norris, R. P., Giovannini, G., & Spitler, L. R. 2016, A&A, 589, L3

Markowitz, A., Reeves, J. N., George, I. M., et al. 2009, ApJ, 691, 922

Mason, K. O., Breeveld, A., Much, R., et al. 2001, A&A, 365, L36

Mathur, S. 2000, MNRAS, 314, L17

Mathur, S., Fields, D., Peterson, B. M., & Grupe, D. 2012, ApJ, 754, 146

Matthews, T. A., & Sandage, A. R. 1963, ApJ, 138, 30M

McKinney, J. C., & Gammie, C. F. 2004, ApJ, 611, 977

Mewe, R., Gronenschild, E. H. B. M., & van den Oord, G. H. J. 1985, A&A, 62, 197M

Mewe, R., Lemen, J. R., & van den Oord, G. H. J. 1986, A&A, 65, 511M

Miniutti, G., & Fabian, A. C. 2004, MNRAS, 349, 1435

Mitsuda, K. 2003, "Suzaku XIS2", X-ray Astronomy Group at ISAS, `www.astro.isas.jaxa.jp/suzaku/news/2006/1123/`

—. 2009, "Anomaly in XIS0", X-ray Astronomy Group at ISAS, `www.astro.isas.jaxa.jp/suzaku/news/2009/0702/`

Mitsuda, K., Bautz, M., Inoue, H., et al. 2007, PASJ, 59, S1

Mori, H., Iizuka, R., Shibata, R., et al. 2005, PASJ, 57, 245

Mundell, C. G., Pedlar, A., Axon, D. J., Meaburn, J., & Unger, S. W. 1995, MNRAS, 277, 641M

Mushotzky, R. F., Done, C., & Pounds, K. A. 1993, ARA&A, 31, 717

Mushotzky, R. F., Marhsall, F. E., Boldt, E. A., Holt, S. S., & Serlemitsos, P. J. 1980, ApJ, 235, 377

Nakazawa, K., Kamae, T., Makishima, K., et al. 1999, Proc. SPIE, 3765, 148

Netzer, H. 2004, ApJ, 604, 551

—. 2015, ARAA, 53, 365

Netzer, H., Turner, T. J., & George, L. M. 1994, ApJ, 435, 106

Newman, J., Tsuruta, S., Liebmann, A. C., Kunieda, H., & Haba, Y. 2021, ApJ, 907, 45

Noda, H., Makishima, K., Yamada, S., et al. 2014, ApJ, 794, 2N

Oke, J. B., & Gunn, J. E. 1974, ApJ, 189, L5

Osterbrock, D. E. 1978, Phys. Scr., 17, 137

Osterbrock, D. E., & Ferland, G. J. 2006, Astrophysics of Gaseous Nebulae and Active Galactic Nuclei, 2nd ed., *University Science Books*

Osterbrock, D. E., & Koski, A. T. 1976, MNRAS, 176, 61P

Osterbrock, D. E., & Martel, A. 1993, ApJ, 414, 552

Padovani, P. 2011, MNRAS, 411, 1547

Pearson, K. 1895, Proc. Royal Soc. London, 58, 240

Pearson, T. 1995, "The QDP/PLT User's Guide", California Institute of Technology

Peterson, B. M., Ferrarese, L., Gilbert, K. M., et al. 2004, ApJ, 613, 682P

Pigot, C., Sauvageot, J., Ferrando, P., & Belsole, E. 2000, Proc. SPIE, 4140

Ptak, A., Yaqoob, T., Serlemitsos, P. J., Mushotzky, R., & Otani, C. 1994, ApJ, 436, L31

Release, J. P. 2015, "X-ray Astronomy Satellite 'Suzaku"'Completes Scientific Mission", `https://global.jaxa.jp/press/2015/08/20150826_suzaku.html`

Release, N. N. 2012, "NASA's NuSTAR Mission Lifts Off", Caltech, https://www.nustar.caltech.edu/news/nustar120613

Rodrìguez-Ardila, A., & Viegas, S. M. 2003, MNRAS, 340, L33

Ross, R. R., & Fabian, A. C. 1993, MNRAS, 261, 74

—. 2005, MNRAS, 358, 211R

Ross, R. R., Fabian, A. C., & Young, A. J. 1999, MNRAS, 306, 461

Rubin, V. C., & Ford, W. K. 1968, ApJ, 154, 431R

Rudnick, L., & Edgar, B. K. 1984, ApJ, 279, 74R

Sako, M., Khan, S. M., Behar, E., et al. 2001, A&A, 365, L168

Sanders, D. B. 1999, Active Galactic Nuclei and Related Phenomena, IAUS, Vol. 194, eds. Terzian, Y., Weedman, D. and Khachikian, E., p. 25

Saxton, R. D., Turner, M. J. L., Williams, O. R., et al. 1993, MNRAS, 262, 63

Schmidt, M. 1963, Nature, 197, 1040

Schmitt, J. L. 1968, Nature, 218, 663S

Serlemitsos, P. J., & Soong, Y. 1996, Ap&SS, 239, 117

Serlemitsos, P. J., Soong, Y., Chan, K., et al. 2007, PASJ, 59, S9

Seyfert, C. K. 1943, ApJ, 97, 28S

Shakura, N. I., & Sunyaev, R. A. 1973, A&A, 24, 337

Sheilds, G. 1978, Nature, 272, 706

Shull, J. M., & van Steenberg, M. E. 1985, ApJ, 294, 599S

Slipher, V. M. 1917, Lowell Observatory Bulletin, 3, 59S

Spearman, C. 1904, Am. J. Psychol., 15, 72

Stenbrugge, K. C., Kaastra, J. S., de Vries, C. P., & Edelson, R. 2003, A&A, 402, 477

Strüder, L., Briel, U., Dennerl, K., et al. 2001, A&A, 365, L18

Sujová, I., Hudec, R., & Munz, F. 2008, PoS, BLAZARS2008, 065

Sunyaev, R. A., & Titarchuk, L. G. 1980, A&A, 86, 121S

Takahashi, T., Abe, K., Endo, M., et al. 2007, PASJ, 59, S35

Tashiro, M. S., Kamae, T., Makishima, K., et al. 2002, IEEE Trans. Nucl. Sci., 49, 1893

Tennant, A. F. 1991, The QDP/PLT User's Guide, NASA Technical Memorandum 4301

Tucker, W., Kellog, E., Gursky, H., & Tananbaun, H. 1973, ApJ, 180, 715T

Turner, M. J. L., Abbey, A., Arnaud, M., et al. 2001, A&A, 365, L27

Turner, T. J., Reeves, J. N., Lobban, A., & Miller, L. 2018, MNRAS, 481, 2470

Ulrich, M.-H. 1984, MNRAS, 230, 121

Urry, C. M., & Pdovani, P. 1995, PASP, 107, 715

Urry, M. C. 2003, In Active Galactic Nuclei: From central Engine to Host Galaxy, eds. Collin, S., Combes, F., Shiosman, I., vol. 290 of Astronomical Society of the Pacific Conference Series

Villa, G. E., Abbey, A. F., Arnaud, M., et al. 1996, Proc. SPIE, 2808, 402

Walton, D. J., Nardini, E., Fabian, A. C., Gallo, L. C., & Reis, R. C. 2013, MNRAS, 428, 2901

Winge, C., Peterson, B. M., Horne, K., et al. 1995, ApJ, 445, 680

Yan, M., Sadeghpour, H. R., & Dalgarno, A. 1998, ApJ, 496, 1044Y

Yang, Q., Xie, F., Yuan, F., et al. 2014, MNRAS, 447, 1692

Zaroubi, S. 2013, Published in The First Galaxies, Astrophysics and Space Science Library, Vol. 396, Springer

Zdziarski, A. A., Johnson, W. N., Done, C., Smith, D., & McNaron-Brown, K. 1995, ApJL, 438, L63

Zhong, X., & Jiancheng, W. 2013, ApJ, 773, 23Z

APPENDICES

APPENDIX A

ABBREVIATIONS AND INITIALISMS

ACU	Analog Control Unit
AE	Analog Electronics
AGN	Active Galactic Nucleus
BB	Black Body
BBB	Big Blue Bump
BGO	Bismuth Germanate Crystal
BI	Back Illuminated
BLR	Broad Line Region
CCD	Charge-coupled Device
CDS	Correlated Double Sample
CFRP	Carbon Fiber Reinforced Plastic
CPU	Central Processing Unit
CSG	Clock Sequence Generator
DE	Digital Electronics
DOF	Degrees of Freedom
DP	Data Processor
DPP	Data Pre-processor
EEPROM	Electrically Erasable Programmable Read-only Memory
EEV	English Electric Valve
EMAE	EPIC MOS Analogue Electronics
EMCR	EPIC MOS Control and Recognition Unit
EMDH	EPIC MOS Data Handling System
EMVC	EPIC MOS Voltage Controller
EPIC	European Photon Imaging Camera
ERH	ERM Harness
ERM	EPIC Radiation Monitor
ERMD	ERM Detection Head
ERME	ERM Electronics
ESA	European Space Agency
EUV	Extreme Ultraviolet
FI	Front Illuminated
FITS	Flexible Image Transport System
FOV	Field of View
FPA	Focal Plane Assembly
FPMA	Focal Plane Module A
FPMB	Focal Plane Module B
FR-1	Fanaroff & Riley Class 1
FR-2	Fanaroff & Riley Class 2
FSRQ	Flat Spectrum Radio Quasar
FWZI	Full Width at Zero Intensity
GFRP	Glass Fiber Reinforced Polymer
GSO	Gadolinium Silicate Crystal
HEAO-1	High Energy Astrophysics Observatory - 1

HEASARC	High Energy Astrophysics Science Archive Research Center
HEAsoft	High Energy Astrophysics Software Suite
HIWA	High Ionization Warm Absorber
HPQ	High Polarisation Quasar
HXD	Hard X-ray Detector
IC	Instrument Controller
IGM	Intergalactic Medium
IR	Infrared
IRR	Ionized Relativistic Reflection
ISCO	Innermost Stable Circular Orbit
JAXA	Japan Aerospace Exploration Agency
LINER	Low Ionization Emission-line Region Galaxy
LIWA	Low Ionization Warm Absorber
MOS	Metal Oxide Semiconductor
MPU	Main Processing Unit
MSP	Mirror Support Platform
NASA	National Aeronautics and Space Administration
NGC	New General Catalogue
NIWA	Negative Ionization Warm Absorber
NLR	Narrow Line Region
NLS1	Narrow Line Seyfert 1
NuStar	Nuclear Spectroscopic Telescope Array
OBF	Optical Block Filter
OBDH	On-board Data Handling
ODF	Observational Data File
OM	Optical Monitor
OVV	Optically Violently Variable Quasar
PCB	Polychlorinated Biphenyl Board
PH	Pulse Height
PIM	Peripheral Interface Module
PPU	Pixel Processing Unit
PSU	Power Supply Unit
QSO	Quasi-stellar Object
QSR	Quasi-stellar Radio Source
RAE	RGS Analogue Electronic Unit
RDE	RGS Digital Electronic Unit
RFC	RGS Focal Plane Camera
RGA	Reflection Grating Array
RGS	Reflection Grating Spectrometer
RIAF	Radiatively Inefficient Accretion Flow
SAS	Scientific Analysis System
SRAM	Statistic-random Access Memory
SVM	Service Module

TCE	Thermo-electric Cooler Control Electronics
TEC	Thermo-electric Cooler
TPU	Transient Processing Unit
UTA	Unresolved Transition Array
UV	Ultraviolet
VRO	Virmillion River Radio Observatory
WPU	Well Processing Unit
XIMAGE	X-ray Imaging Package
XIS	X-ray Imaging Spectrometer
XMM-Newton	X-ray Multi Mirror Mission
XRS-2	X-ray Spectrometer - 2
XRT	X-ray Telescope
XSPEC	X-ray Spectral Fitting Package

APPENDIX B

XSPEC MODELS USED

ZBBODY
A redshifted blackbody spectrum.

$$A(E) = \frac{K \times 8.0525(E[1+z])^2 dE}{(1+z)(kT)^4(exp[E(1+z)/kT]-1)} \tag{B.1}$$

- kT Temperature in keV.
- z Redshift.
- K Normalization given by the following equation:

$$Norm._{bb} = \frac{L_{39}}{D_{10}(1+z)^2} \tag{B.2}$$

Where L_{39} is luminosity in 10^{39} ergs s^{-1}, D_{10} is distance in 10 kpc, and z is the redshift.

ZBREMSS
Thermal bremsstrahlung spectrum based on the Kellogg et al. (1975) polynomial fits to the Karzas & Latter (1961) numerical values. Assumed He abundance is 8.5 % of the H abundance.

- kT Plasma temperature in keV.
- z Redshift.
- K Normalization given by the following equation:

$$Norm._{bremss} = \frac{3.02 \times 10^{-15}}{4\pi D^2} \int n_e n_i \, dV \tag{B.3}$$

Where D is the distance to the source, n_e is the electron number density, and n_i is the ion number density.

COMPST
A Comptonization spectrum of cool photons on hot electrons from Sunyaev & Titarchuk (1980).

- kT Temperature in keV.
- τ Optical depth.
- K Normalization given by the following equations:

$$Norm._{comp} = \frac{Nf}{4\pi d^2} \tag{B.4}$$

Where N is the total number of photons from the source, d is the distance from the source, and f is the factor given by Equation 3.7.

$$f = \frac{\alpha(\alpha+3)y^2\Gamma(\alpha)}{\Gamma(2\alpha+4)} \tag{B.5}$$

Where α is the spectral index, y is the injected photon energy in units of temperature, and Γ is the incomplete gamma function.

KDBLUR

A convolution model to relativistically smooth a spectrum from an accretion disk around a rotating black hole. Convolves in the Laor (1991) shape.

- $Index$ Power law dependence of emissivity (scales as R^{-Index}).
- Rin_G Inner radius in units of GM/c^2.
- $Rout_G$ Outer radius in units of GM/c^2.
- $Incl$ Inclination of the disk in degrees.

MEKAL

Emission spectrum from hot, diffuse gas based on the model calculations of Mewe et al. (1985, 1986) with Fe L calculations by Liedahl et al. (1995).

- kT Plasma temperature in keV.
- n_H Hydrogen density in cm^{-3}.
- *Abundanc* Metal abundances. Included elements are C, N, O, Ne, Na, Mg, Al, Si, S, Ar, Ca, Fe, and Ni.
- z Redshift.
- *switch* Determines whether the spectrum is calculated by running the mekal code (0), by interpolating a mekal table (1), or by interpolating the AtomDB data (2).
- K Normalization given by the following equation:

$$K = \frac{10^{-14}}{4\pi D^2} \int n_e n_H \, dV \tag{B.6}$$

Where D is the distance to the source and n_e and n_H are the electron and H densities in cm^{-3}.

PHABS, ZPHABS

Neutral photoelectric absorption model. The cross sections, $\sigma(E)$, are taken from Balucinska-Church & McCammon (1992) with He cross section from Yan et al. (1998). This model ignores Thomson scattering.

$$M(E) = exp[-n_{H\sigma}(E[1+z])] \tag{B.7}$$

- n_H Equivalent hydrogen column density in 10^{22} atoms cm^{-2}.
- z Redshift. Set to zero in phabs.

REFLIONX

Reflected spectrum off of an optically thick atmosphere of constant density illuminated by a power law radiation spectrum. See Ross & Fabian (2005); Ross et al. (1999).

- $Fe/solar$ Abundance of Fe relative to solar value.
- Γ Photon index of illuminating spectrum.
- ξ Ionization parameter where $\xi = 4\pi F/n_H$, where F is the illuminating flux and n_H is the H number density.
- K Normalization given by total photons keV^{-1} cm^{-2} s^{-1} evaluated at 1 keV.

XILLVER

X-ray reflected spectrum from accretion disks from Garcia et al. (2013).

- Γ Photon index of the illuminating spectrum.
- A_{fe} Iron abundance with respect to solar value.
- E_{cut} Exponential high-energy cutoff for the power law.
- $log(\xi)$ Ionization given by $\xi = 4\pi F/n$.

- z Redshift.
- $Incl$ Viewing angle with respect to the disk's normal.
- $refl_{frac}$ Reflection fraction defined in the frame of the source as the ratio of coronal intensity illuminating the disk to the coronal intensity that reaches the observer.
- K Normalization in total photons keV^{-1} cm^{-2}s^{-1}.

For ξ, f is the flux of the illuminating radiation and n is the gas density in units of $n = 10^{15}$cm^{-3}

XSTAR TABLE MODELS

Ionized absorption models formed by running the XSTAR code. Once created, they have three parameters when used in XSPEC.

- $column$ Hydrogen column density in cm^{-2}.
- $log(\xi)$ Log of the ionization parameter given by $\xi = \frac{L}{nr^2}$.
- z Redshift.

For ξ, L is the integrated incident luminosity, n is the density of the material, and r is the distance of the material from the illuminating source.

ZEDGE

Redshifted absorption edge.

$$M(E) = 1 \quad \text{for} \quad E \leq E_c \tag{B.8}$$

$$M(E) = exp(-\tau[E(1+z)/E_c]^3) \quad \text{for} \quad E \geq E_c \tag{B.9}$$

- E_c Threshold energy.
- τ Absorption depth at the threshold.

ZGAUSS

Simple redshifted gaussian line profile.

$$A(E) = K\frac{1}{\sigma \times \sqrt{2\pi}} exp\left(\frac{-(E[1+z] - E_i)^2}{2\sigma^2}\right) \tag{B.10}$$

- E_i Line energy in keV.
- σ Line width in keV.
- z Redshift.
- K Source frame total photons cm^{-2} s^{-1} in the line of sight.

ZPOWERLW
Redshifted photon power law.

$$A(E) = K[E(1+z)]^{-\Gamma} \tag{B.11}$$

- Γ Photon index.
- z Redshift.
- K Normalization in total photons keV^{-1} cm^{-2}s^{-1}.

ZXIPCF
Redshifted ionized partial covering absorption model that uses a grid of XSTAR models. The absorber covers a fraction f of the source while the remaining fraction $(1-f)$ is seen directly.

- n_H Equivalent hydrogen column density in 10^{22} atoms cm^{-2}.
- $log(\xi)$ Log of the ionization parameter given by $\xi = \frac{L}{nr^2}$.
- f Covering Fraction.
- z Redshift.

For ξ, L is the integrated incident luminosity, n is the density of the material, and r is the distance of the material from the illuminating source (Done et al. 1992).